MAGNETIC MONITORING APPROACH TO KINETICS OF PHASE TRANSFORMATIONS IN MULTICOMPONENT ALLOY SYSTEMS

A THESIS SUBMITTED TO
THE GRADUATE SCHOOL OF NATURAL AND APPLIED SCIENCES
OF
MIDDLE EAST TECHNICAL UNIVERSITY

BY

NAGEHAN DUMAN

IN PARTIAL FULFILLMENT OF THE REQUIREMENTS
FOR
THE DEGREE OF DOCTOR OF PHILOSOPHY
IN
METALLURGICAL AND MATERIALS ENGINEERING

MARCH 2012

Approval of the thesis:

MAGNETIC MONITORING APPROACH TO KINETICS OF PHASE TRANSFORMATIONS IN MULTICOMPONENT ALLOY SYSTEMS

submitted by **NAGEHAN DUMAN** in partial fulfillment of the requirements for the degree of **Doctor of Philosophy in Metallurgical and Materials Engineering Department, Middle East Technical University** by,

Prof. Dr. Canan Özgen
Dean, Graduate School of **Natural and Applied Sciences** _____

Prof. Dr. Tayfur Öztürk
Head of Department, **Metallurgical and Materials Eng.** _____

Prof. Dr. Amdulla O. Mekhrabov
Supervisor, **Metallurgical and Materials Eng. Dept., METU** _____

Prof. Dr. M. Vedat Akdeniz
Co-Supervisor, **Metallurgical and Materials Eng. Dept., METU** _____

Examining Committee Members:

Prof. Dr. A. Şakir Bor
Metallurgical and Materials Eng. Dept., METU _____

Prof. Dr. Amdulla O. Mekhrabov
Metallurgical and Materials Eng. Dept., METU _____

Assoc. Prof. Dr. Arcan F. Dericioğlu
Metallurgical and Materials Eng. Dept., METU _____

Assoc. Prof. Dr. İlker Küçük
Physics Dept., Uludağ University _____

Assist. Prof. Dr. Y. Eren Kalay
Metallurgical and Materials Eng. Dept., METU _____

Date : 09 March 2012

I hereby declare that all information in this document has been obtained and presented in accordance with academic rules and ethical conduct. I also declare that, as required by these rules and conduct, I have fully cited and referenced all material and results that are not original to this work.

Name, Last name : Nagehan Duman

Signature :

ABSTRACT

MAGNETIC MONITORING APPROACH TO KINETICS OF PHASE TRANSFORMATIONS IN MULTICOMPONENT ALLOY SYSTEMS

Duman, Nagehan
Ph.D., Department of Metallurgical and Materials Engineering
Supervisor : Prof. Dr. Amdulla O. Mekhrabov
Co-Supervisor : Prof. Dr. M. Vedat Akdeniz

March 2012, 222 pages

It is of great importance for a materials scientist both from fundamental and applicability aspects to have better understanding of solid-state phase transformations and its kinetics responsible for micro-/nano-structure development in alloys and corresponding physical and mechanical properties. Transformation kinetics can be analyzed by various experimental techniques such as thermal analysis, laborious electron microscopy combined with extensive image analysis or by measuring changes in electrical resistivity, specimen volume and relative intensities of diffraction lines caused by the phase transformation. Beyond these conventional techniques, this dissertation provides a novel magnetic monitoring approach to study the isothermal kinetics of phase transformations in multicomponent alloy systems involving measurable changes in overall magnetic moment as the transformation proceeds.

This dissertation focuses on understanding the microstructural evolution, macro- and micro-alloying behavior, magnetic properties, thermal characteristics, mechanical properties and kinetics of solid-state transformations, i.e. nanoscale precipitation and nanocrystallization, in nickel aluminides and Fe-based bulk amorphous alloys. Microstructural characterization of alloys was done by X-ray diffraction, scanning electron microscopy and transmission electron microcopy techniques. Magnetic properties were analyzed by vibrating sample magnetometry whereas thermal characteristics were evaluated by differential scanning calorimetry. Mechanical properties of alloys were determined by microhardness measurements and compression tests.

The influence of Fe macroalloying and 3d transition metal microalloying on the microstructure and properties of Ni-Al-Fe alloys were studied for as-cast and annealed states and it is shown that desired microstructure and related properties can be obtained by proper selection of the type and concentration of macro- or micro-alloying elements together with an appropriate annealing procedure. Thermomagnetic characterization reveals the nanoscale precipitation of a ferromagnetic second phase with annealing. In conjunction with saturation magnetization dependence on annealing, an optimum temperature is identified where nanoscale precipitates impart the highest extent of precipitation strengthening. The isothermal kinetics of ferromagnetic second phase precipitation reveals invariant Avrami exponents close to unity, indicating that nanoscale precipitation is governed by a diffusion-controlled growth process with decreasing growth rate, which closely resembles continuous precipitation kinetics.

Appropriate annealing of the Fe-based bulk amorphous alloy precursor produced by suction casting demonstrated extremely fine microstructures containing uniformly distributed and densely dispersed nanocrystals inside a residual amorphous matrix. In order to have better understanding of nanocrystallization mechanisms, kinetic parameters were determined via

isothermal magnetic monitoring and non-isothermal differential scanning calorimetry where excellent agreement was obtained in Avrami exponent and activation energy. Analyzing the local kinetics, the nanocrystalline phase was found to evolve through distinct transformation regimes during annealing which were discussed on the basis of transformation kinetics theory and microscopical investigations on each characteristic transformation regime.

Keywords: Nickel Alloys, Bulk Metallic Glasses, Microstructure, Phase Transformations, Kinetics

ÖZ

ÇOK BİLEŞENLİ ALAŞIM SİSTEMLERİNDE
FAZ DÖNÜŞÜM KİNETİĞİNE MANYETİK İZLEME YAKLAŞIMI

Duman, Nagehan
Doktora, Metalurji ve Malzeme Mühendisliği Bölümü
Tez Yöneticisi : Prof. Dr. Amdulla O. Mekhrabov
Ortak Tez Yöneticisi : Prof. Dr. M. Vedat Akdeniz

Mart 2012, 222 sayfa

Katı halde gerçekleşen faz dönüşümleri ve bu dönüşümlerin kinetiği, metalik malzemelerde mikro-/nano-yapı oluşumu ve dolayısıyla fiziksel ve mekanik özelliklerde belirleyici rol oynaması nedeniyle malzeme bilimi açışından büyük önem arz etmektedir. Dönüşüm kinetiğinin belirlenmesinde, termal analizler, elektron mikroskopisi ve elektriksel direnç, hacim veya kırınım şiddeti ölçümleri gibi birçok deneysel yöntem kullanılabilmektedir. Sıralanan tüm geleneksel yaklaşımların ötesinde, bu tez çalışmasında çok bileşenli alaşım sistemlerinin faz dönüşüm kinetiği, dönüşüm sürecinde malzemenin toplam manyetik momentindeki değişimlerin izlenmesi prensibine dayanan bir manyetik ölçüm yaklaşımı sayesinde belirlenmiştir.

Bu çalışmada, nikel alüminitler ve demir-tabanlı iri-hacimli amorf alaşımların mikroyapısı, makro- ve mikro-alaşımlama özellikleri, manyetik özellikleri, ısıl karakteristikleri, mekanik özellikleri ve nano-boyutta faz çökelmesi ve nanokristalleşme gibi katı faz dönüşüm olgularının kinetiği incelenmiştir. Alaşımların mikroyapısı X-ışını kırınımı, taramalı elektron

mikroskopisi ve geçirimli elektron mikroskopisi teknikleriyle karakterize edilmiş, manyetik özellikleri titreşimli örnek manyetometresi ile belirlenmiş, ısıl karakteristikleri diferansiyel taramalı kalorimetre ile analiz edilmiş, mekanik özellikleri ise mikro-sertlik ölçümleri ve basma testleriyle incelenmiştir.

Ni-Al tabanlı alaşımların Fe ile makro-alaşımlanması ve 3d geçiş metalleriyle mikro-alaşımlanmasının mikroyapı ve özelliklere olan etkisi incelenmiş, istenilen mikroyapı ve dolayısıyla malzeme özelliklerinin uygun alaşımlama ve tavlama koşullarının belirlenmesiyle mümkün olduğu saptanmıştır. İncelenen Ni-Al-Fe alaşımlarının ısıl-manyetik karakterizasyonu, uygun tavlama sıcaklığında ferromanyetik özelliğe sahip nano-boyutta ikinci faz çökeldiği göstermiştir. Doyum manyetizasyonunun tavlama sıcaklığına bağımlılığı ile paralel olarak, çökelme sertleşmesi etkisinin de en yüksek olduğu optimum bir tavlama sıcaklığı elde edilmiştir. Nano-boyutta çökelen ferromanyetik ikinci fazın eş-sıcaklık faz dönüşüm kinetiği incelendiğinde, Avrami indeksinin alaşım kompozisyonu ve tavlama sıcaklığı gibi parametrelerden bağımsız olarak yaklaşık 1 olduğu anlaşılmıştır. Dolayısıyla, ikinci faz çökelmesinin, sürekli çökelme kinetiğine işaret eden bir azalan büyüme hızına sahip difüzyon-kontrollü büyüme ile gerçekleştiği belirlenmiştir.

Hızlı soğutma ile elde edilen iri-hacimli Fe-tabanlı amorf alaşımın, uygun bir tavlama süreci sayesinde amorf matris içerisinde eşit ve yoğun biçimde dağılmış nanokristal bölgelerden oluşan mikroyapılar oluşturduğu gözlemlenmiştir. Bu nanokristalleşme olgusunun daha net anlaşılabilmesi amacıyla manyetik ölçümler ve diferansiyel taramalı kalorimetre ölçümlerinden faydalanılarak kinetik analizler yapılmıştır. Kinetik analizlerde kullanılan bu iki farklı yöntem ile belirlenen Avrami indeksi ve aktivasyon enerjilerinin büyük oranda örtüşmekte olduğu saptanmıştır. Nanokristalleşmenin lokal kinetiği incelendiğindeyse, nanokristal fazın tavlama esnasında farklı oluşum süreçlerinden geçtiği gözlemlenmiş, bu

süreçler dönüşüm kinetiği teorileri ve mikroskobik incelemelerle açıklanmıştır.

Anahtar Kelimeler: Nikel Alaşımları, İri-hacimli Metalik Camlar, Mikroyapı, Faz Dönüşümleri, Kinetik

To my beloved family

ACKNOWLEDGEMENTS

I would like to express my gratitude to my supervisors Prof. Dr. Amdulla O. Mekhrabov and Prof. Dr. M. Vedat Akdeniz for the support, guidance and encouragement they gave me during this study. I would also like to thank my committee members Assoc. Prof. Dr. İlker Küçük and Assoc. Prof. Dr. Arcan F. Dericioğlu, as well as Prof. Dr. A. Şakir Bor and Assist. Prof. Dr. Y. Eren Kalay for their stimulating contributions to this thesis.

I sincerely acknowledge the former and present members of the NOVALAB group; Mehmet Yıldırım, Mine Kalkanci, Muratahan Aykol, Sultan Aybar, Sıla Süer, Mahsuni Yalçın, Amir Fadaie and Tufan Güngören for making this long journey fun. I would also like to thank Özlem Altıntaş Yıldırım, Halil İbrahim Yavuz, and Nusret Serhat Ün, for their endless friendship.

I am grateful to Evren Tan, Aykut Oğuz Konuk and Kağan Şarlar to their assistance in my studies. It was a pleasure for me to receive significant technical support and guidance from Cengiz Tan, Serkan Yılmaz, Yusuf Yıldırım and Necmi Avcı. I am also thankful to METU Metallurgical and Materials Engineering Department for providing facilities for my research.

I feel myself indebted to my parents, my aunt, my sisters and Nihat Ali Işıtman for their love and endless support throughout my lengthy education.

This work was financially supported by the DPT-ÖYP research funds and TÜBİTAK fellowships.

TABLE OF CONTENTS

Abstract iv

Öz vii

Acknowledgements xi

Table of Contents xii

List of Tables xv

List of Figures xvi

Chapters

1. Introduction **1**

1.1 Intermetallic Compounds 1

1.2 Amorphous Alloys 3

1.3 Research Objectives 5

2. Theoretical Background **6**

2.1 Intermetallic Compounds 6

2.1.1 Solid Solutions and Intermetallic Compounds 6

2.1.2 Strengthening Mechanisms 8

2.1.3 Magnetic Properties 13

2.1.4 The Nickel-Aluminum Intermetallic Compound 16

2.1.5 Alloying Additions to NiAl 20

2.1.6 Alloying NiAl with Fe 23

2.2 Amorphous Alloys 28

2.2.1 History of Metallic Glasses 29

2.2.2 The Glass Transition and Glass Forming Ability 30

2.2.3 Plastic Flow and Deformation of Metallic Glasses 32

2.2.4 Structural Relaxation in Metallic Glasses 33

2.2.5 Crystallization of Amorphous Alloys 34

2.2.6 Magnetic Properties of Amorphous and Nanocrystalline Alloys . 36

2.2.7 Fe-based Bulk Metallic Glasses 37

3. Experimental Procedure **41**
3.1 Raw Materials 41
3.2 Fabrication of Samples 43
3.2.1 Arc Melting 44
3.2.2 Rapid Solidification by Suction Casting 45
3.2.3 Cutting Procedure 46
3.2.4 Annealing Procedure 46
3.3 Characterization Techniques 46
3.3.1 X-ray Diffractometry 46
3.3.2 Scanning Electron Microscopy 47
3.3.3 Transmission Electron Microscopy 48
3.3.4 Differential Scanning Calorimetry 49
3.3.5 Vibrating Sample Magnetometry 50
3.3.6 Microhardness Measurements 51
3.3.7 Mechanical Testing 52

4. Magnetic Monitoring Approach **53**
4.1 Isothermal Transformation Kinetics 53
4.2 Isothermal Magnetic Monitoring 59
4.1 Non-isothermal Transformation Kinetics 61

5. Intermetallic Compounds **65**
5.1 Binary NiAl and Ni_3Al Intermetallic Compounds 68
5.2 Macroalloying NiAl with Fe 71
5.2.1 Microstructure 71
5.2.2 Magnetic Properties 81
5.2.3 Microhardness 89
5.2.4 Mechanical Properties 91
5.2.5 Kinetics of Nanoscale Precipitation by Magnetic Monitoring 98
5.3 Microalloying Effects in Ni–Al–Fe Alloys 109
5.3.1 Microstructure 110
5.3.2 Microhardness and Magnetic Properties 125
5.3.3 Mechanical Properties 131
5.3.4 Kinetics of Nanoscale Precipitation by Magnetic Monitoring 138

6. Amorphous Alloys **146**

6.3 Solidification Behavior 146

6.2 Crystallization Behavior 154

6.3 Non-isothermal Kinetics of Nanocrystallization by DSC 160

6.4 Isothermal Kinetics of Nanocrystallization by Magnetic Monitoring 168

7. Conclusions **186**

References **192**

Appendices **206**

A Kikuchi Maps for Cubic Crystals 206

B Standard Indexed Electron Diffraction Patterns for Cubic Structures .. 208

C Equilibrium Phase Diagrams 212

Curriculum Vitae **218**

LIST OF TABLES

TABLES

Table 2.1 Physical properties of transition-metal aluminides and superalloys. …….. 17

Table 3.1 Compositional purity of alloying elements (wt.%). …… 41

Table 3.2 Chemical compositions (at.%) of NiAl based intermetallics with varying Fe content. …….. 42

Table 3.3 Chemical compositions (at.%) of microalloyed Ni-Al-Fe alloys. ……. 43

Table 3.4 Chemical composition (at.%) of Fe-based amorphous alloys. ……..... 43

Table 4.1 Interpretation of Avrami exponents. ……... 57

Table 5.1 Chemical compositions of $Ni_{50}Al_{50}$ and $Ni_{75}Al_{25}$ alloys. …….. 69

Table 5.2 Nominal and actual composition of samples in at.%. …… 71

Table 5.3 Compositional analysis of phases in as-cast and annealed Ni-Al-Fe alloys. …….. 79

Table 5.4 Nominal and actual composition of Ni-Al-Fe-X samples in at.%. …… 110

Table 5.5 Compositional analysis of phases in as-cast and annealed Ni-Al-Fe-X alloys. …….. 118

LIST OF FIGURES

FIGURES

Figure 1.1 Typical parts made of nickel aluminides; (a) stator blade for gas turbines, (b) thermal tile for combustion chamber lining in gas turbines and (c) fuel injector pins in diesel engines. 2

Figure 1.2 Examples for bulk amorphous alloy products; (a) metal pipe, rod, cast component and golf clubs, (b) bottle and watch cases, and (c) micro geared motor. 4

Figure 2.1 Hypothetical free energy curves in the A-B alloy system showing the restriction of terminal solid solubility in the presence of stable intermetallic compound. 7

Figure 2.2 Substitutional impurities acting as obstacles against dislocation movement; (a) smaller, and (b) larger solute atoms. 9

Figure 2.3 Dislocation-particle interactions showing (a) dislocation cutting through the second phase, (b) dislocation looping around second phase. 11

Figure 2.4 The formation of anti-phase boundary by dislocation glide through ordered precipitates inside a disordered matrix. 12

Figure 2.5 Schematic representation of magnetization behavior and corresponding domain configuration in a single-crystal. 15

Figure 2.6 Ni-Al equilibrium phase diagram. 16

Figure 2.7 Thermal conductivities of single crystal NiAl and Ni-based superalloy compared. 18

Figure 2.8 The structures of ordered NiAl and Ni_3Al superlattices. 18

Figure 2.9 Lattice defects arising from off-stochiometery in β-NiAl compound. 19

Figure 2.10 Observed slip vectors for the B2 NiAl compound. 20

Figure 2.11 Equilibrium phase diagram for Ni-Al-Fe system at 298 K. 24

Figure 2.12 Isothermal section of the Ni-Al-Fe system and a vertical section drawn from Ni-25Al to Fe side showing temperature dependence of stable phases. 25

Figure 2.13 Miscibility gap between ordered and disordered bcc phases in the Ni-Al-Fe system, (a) phase equilibria at 750 °C and (b) a vertical section diagram. 27

Figure 2.14 Concentration profiles of ordered NiAl and Fe-rich disordered bcc phases. 28

Figure 2.15 Schematic representation of (a) long range order in crystalline alloys and (b) short range order in amorphous alloys. 29

Figure 2.16 Variation of thermodynamic properties during first and second-order transitions. 31

Figure 2.17 Schemes for primary and eutectic crystallization reactions from the amorphous state. 35

Figure 2.18 Mechanical properties of bulk metallic glasses. 38

Figure 2.19 Comparison of saturation magnetization and permeability for different types of amorphous and nanocrystalline soft magnetic alloys. 39

Figure 3.1 Fabrication of alloys by arc melting. 44

Figure 3.2 Specimen production by suction casting. 45

Figure 3.3 The differential scanning calorimeter used in thermal analysis. 49

Figure 3.4 The vibrating sample magnetometer used for magnetization measurements. 51

Figure 3.5 Compression test specimens. 52

Figure 4.1 An example illustrating the estimation procedure of maximum magnetization (M_f) values using experimentally determined time-dependent magnetization in VSM. 61

Figure 5.1 SEM micrographs of as –cast alloys; (a-b) $Ni_{50}Al_{50}$, and, (c-d) $Ni_{75}Al_{25}$. 68

Figure 5.2 XRD patterns of as-cast (a) $Ni_{50}Al_{50}$, and, (b) $Ni_{75}Al_{25}$ alloys. 70

Figure 5.3 SEM micrographs of (a) $Ni_{50}Fe_{20}Al_{30}$, (b) $Ni_{50}Fe_{25}Al_{25}$ and (c) $Ni_{50}Fe_{30}Al_{20}$ as-cast alloys, and energy dispersive spectra of $Ni_{50}Fe_{30}Al_{20}$ alloy taken from (d) dendritic region and (e) among dendritic region. 72

Figure 5.4 XRD patterns of (a) $Ni_{50}Fe_{20}Al_{30}$, (b) $Ni_{50}Fe_{25}Al_{25}$ and (c) $Ni_{50}Fe_{30}Al_{20}$ as-cast alloys. 73

Figure 5.5 SEM micrographs of $Ni_{50}Fe_{20}Al_{30}$ alloy annealed for 168 h (a) at 673 K, and (b) at 1073 K, and (c) XRD patterns of annealed alloys. 75

Figure 5.6 SEM micrographs of $Ni_{50}Fe_{25}Al_{25}$ alloy annealed at (a) 673 K and (b) 1073 K, (c) XRD patterns for annealed states. 77

Figure 5.7 SEM micrographs of $Ni_{50}Fe_{30}Al_{20}$ alloy annealed at (a) 673 K and (b) 1073 K, (c) XRD patterns for annealed states. 78

Figure 5.8 Magnetization versus applied field curves of $Ni_{50}Al_{50}$, $Ni_{50}Fe_{20}Al_{30}$, $Ni_{50}Fe_{25}Al_{25}$ and $Ni_{50}Fe_{30}Al_{20}$ alloys. 80

Figure 5.9 Thermomagnetization curves measured in a magnetic field of 500 Oe for (a) $Ni_{50}Fe_{25}Al_{25}$ and (b) $Ni_{50}Fe_{30}Al_{20}$ alloys in the as-cast and annealed states (673 K, 873 K and 1073 K). 82

Figure 5.10 Room temperature saturation magnetization values of $Ni_{50}Fe_{20}Al_{30}$, $Ni_{50}Fe_{25}Al_{25}$ and $Ni_{50}Fe_{30}Al_{20}$ alloys as a function of annealing temperature. 84

Figure 5.11 Thermomagnetization curves measured in a magnetic field of 500 Oe for as-cast $Ni_{50}Fe_{20}Al_{30}$, $Ni_{50}Fe_{25}Al_{25}$ and $Ni_{50}Fe_{30}Al_{20}$ alloys. 85

Figure 5.12 Bright-field TEM micrographs of the $Ni_{50}Fe_{25}Al_{25}$ alloy annealed at 673 K; (a) showing the eutectic and dendritic regions, (b) a larger magnification image of the dendritic region (matrix), (c) fine BCC precipitates and corresponding SAED pattern. 87

Figure 5.13 Microhardness of β-phase quantifying the precipitation hardening effect of nano-sized α-Fe precipitates. 89

Figure 5.14 Suction-cast solidification microstructure of (a) binary NiAl, and, Ni-Al50-x-Fex alloys with (b) x=20 at.%, (c) x=25 at.% and (d) x=30 at.%. 91

Figure 5.15 Compressive stress-strain behavior of alloys showing (a) the effect of Fe content in the as-cast state, and, the effect of annealing on (b) Fe_{20}, (c) Fe_{25} and (d) Fe_{30} alloys. 92

Figure 5.16 (a-b) as-cast binary NiAl at different magnifications, (c) as-cast Fe_{20} alloy, (d) Fe_{20} alloy annealed at 873 K. 93

Figure 5.17 Compressive failure of Fe_{25} alloy showing critical resolved stress maximized on a plane inclined to an angle of around 45° to the loading direction. 94

Figure 5.18 Variation of compressive yield strength with annealing of Ni-Al-Fe alloys. 96

Figure 5.19 Thermomagnetization curves of alloys above 600 K where the temperatures for isothermal magnetization measurements are marked. 97

Figure 5.20 Time-dependent magnetization curves of (a) $Ni_{50}Fe_{20}Al_{30}$, (b) $Ni_{50}Fe_{25}Al_{25}$ and (c) $Ni_{50}Fe_{30}Al_{20}$ alloys between 800 K and 900 K. 99

Figure 5.21 Rate of magnetization at different measurement times as a function of temperature in isothermal VSM experiments. The curves correspond to the $Ni_{50}Fe_{25}Al_{25}$ alloy. 100

Figure 5.22 Representative example of time-dependent magnetization above the optimum isothermal temperature. The curves correspond to the $Ni_{50}Fe_{25}Al_{25}$ alloy. 101

Figure 5.23 Correlation between average rates of magnetization and micro-hardness of the primary β-phase. 103

Figure 5.24 Bright field TEM micrographs and corresponding selected area diffraction patterns of $Ni_{50}Fe_{25}Al_{25}$ alloy at annealed (a) 673 K, and (b) 873 K. 104

Figure 5.25 Avrami plots for (a) $Ni_{50}Fe_{20}Al_{30}$, (b) $Ni_{50}Fe_{25}Al_{25}$ and (c) $Ni_{50}Fe_{30}Al_{20}$ alloys. 105

Figure 5.26 Activation energies of precipitation as monitored by magnetization measurements. 106

Figure 5.27 Magnetically assessed time–temperature dependence of α-phase precipitation in the $Ni_{50}Fe_{25}Al_{25}$ alloy. 107

Figure 5.28 SEM micrographs and EDS line scan analyses of as-cast NiAlFe-*X* alloys where (a) *X* = Co, (b) *X* = Mn, and (c) *X* = V. Insets to SEM images show line scan positions. 109

Figure 5.29 (a) Bright field TEM image of as-cast Ni-25Al-25Fe alloy showing dendritic and interdendritic regions, (b) SAED pattern taken along [011] direction of interdendrite matrix, (c) Dark field image formed using 100 superlattice reflection showing fine ordered γ' precipitates (brighter regions) inside γ-phase matrix. 111

Figure 5.30 XRD patterns of as-cast (a) Ni-25Al-25Fe alloy, and, NiAlFe-*X* alloys where (b) *X* = Mn, (c) *X* = V, and (d) *X* = Co. 113

Figure 5.31 SEM micrographs of annealed NiAlFe-Mn alloy at (a) 673 K, (b) 873 K, and (c) 1073 K, and, (d) corresponding XRD patterns. 115

Figure 5.32 SEM micrographs of annealed NiAlFe-Co alloy at (a) 673 K, (b) 873 K, and (c) 1073 K, and, (d) corresponding XRD patterns. 116

Figure 5.33 SEM micrographs of annealed NiAlFe-V alloy at (a) 673 K, (b) 873 K, and (c) 1073 K, and, (d) corresponding XRD patterns. 117

Figure 5.34 Bright field TEM images and SAED patterns of interdendrite matrix in 873 K annealed NiAlFe-*X* alloys where (a) *X* = Mn, (b) *X* = Co, and (c) *X* = V. 121

Figure 5.35 Bright field TEM images and SAED patterns of γ-phase in 1073 K annealed NiAlFe-*X* alloys where (a) *X* = Mn, (b) *X* = Co, and (c) *X* = V. 123

Figure 5.36 Correlation of (a) microhardness of β-phase, and (b) room temperature saturation magnetization in annealed alloys. 126

Figure 5.37 (a) Bright field TEM image of β-phase NiAlFe-V alloy following annealing at 873 K for 168 h, and (b) corresponding SAED pattern taken along [001] direction of β-phase. 128

Figure 5.38 TEM images of NiAlFe-V alloy annealed at 673 K; (a-b) bright-field micrographs, (c) SAED pattern taken from the interface boundary, (d) dark-field micrograph taken from superlattice reflection of the β-phase, and (e) EDS analyses of grain interiors and interface boundary. 130

Figure 5.39 Suction-cast solidification microstructure of NiAlFe-X alloys where X= (a) Co, (b) Mn and (c) V. 132

Figure 5.40 Compressive stress-strain behavior of alloys showing the influence of microalloying on (a) as-cast alloys and (b) alloys annealed at 673 K. 134

Figure 5.41 Compressive stress-strain behavior of annealed V-modified Ni-Al-Fe alloy. 135

Figure 5.42 Variation of compressive yield strength with annealing of Co, Mn and V microalloyed Ni-Al-Fe alloys. 136

Figure 5.43 Fracture surface images of NiAlFe-V alloy annealed at 673 K. 137

Figure 5.44 Temperature scan magnetization curves of as-cast alloys under an applied magnetic field of 500 Oe from (a) room temperature to 600 K, and (b) above 600 K. 139

Figure 5.45 Isothermal magnetization curves of as-cast NiAlFe-*X* alloys where (a) *X* = Co, (b) *X* = Mn, and (c) *X* = V. 140

Figure 5.46 Avrami plots for as-cast NiAlFe-*X* alloys where (a) *X* = Co, (b) *X* = Mn, and (c) *X* = V. 141

Figure 5.47 Activation energies for nanoscale α-phase precipitation. 143

Figure 5.48 (a) Magnetically assessed TTT diagrams for α-phase precipitation in NiAlFe-*X* alloys, (b) TTT diagrams for Ni-25Al-25Fe and NiAlFe-V alloys showing the influence of V addition on the kinetics of α-phase precipitation. 145

Figure 6.1 XRD patterns of Cu-modified $Fe_{43}Co_{28-x}Ni_xB_{19}Si_5Nb_4$ alloys with different Co/Ni ratios. 147

Figure 6.2 Solidification microstructures of rapidly solidified Cu-modified $Fe_{43}Co_{19}Ni_9B_{19}Si_5Nb_4$ alloy; (a) field-emission SEM secondary electron image, (b) conventional SEM secondary electron image and (c) back-scattered electron image. 149

Figure 6.3 Solidification microstructure of relatively slow-cooled Cu-modified $Fe_{43}Co_{19}Ni_9B_{19}Si_5Nb_4$ alloy. 150

Figure 6.4 Energy dispersive maps (field-emission SEM) of relatively slow-cooled Cu-modified $Fe_{43}Co_{19}Ni_9B_{19}Si_5Nb_4$ alloy. 151

Figure 6.5 Energy dispersive maps (conventional SEM) of relatively slow-cooled Cu-modified $Fe_{43}Co_{19}Ni_9B_{19}Si_5Nb_4$ alloy. 152

Figure 6.6 Energy dispersive line scan from distinguishable regions in relatively slow-cooled Cu-modified $Fe_{43}Co_{19}Ni_9B_{19}Si_5Nb_4$ alloy. 153

Figure 6.7 XRD patterns of relatively slow-cooled Cu-modified $Fe_{43}Co_{28-x}Ni_xB_{19}Si_5Nb_4$ alloy. 154

Figure 6.8 (a) Bright-field TEM image showing the amorphous structure of suction-cast Cu-modified $Fe_{43}Co_{19}Ni_9B_{19}Si_5Nb_4$ alloy, and (b) corresponding SAED pattern. 155

Figure 6.9 DSC heat flow curves of the bulk amorphous Cu-modified $Fe_{43}Co_{19}Ni_9B_{19}Si_5Nb_4$ alloy. 157

Figure 6.10 XRD patterns elucidating the crystallization behavior of the Cu-modified $Fe_{43}Co_{19}Ni_9B_{19}Si_5Nb_4$ amorphous alloy. 158

Figure 6.11 DSC heat flow curves showing crystallization exotherms obtained at different heating rates. 160

Figure 6.12 Kissinger plots and activation energies for different steps of crystallization. 161

Figure 6.13 Plots obtained from different non-isothermal models for the calculation of overall activation energy for α–(Fe,Co) crystallization. 163

Figure 6.14 (a) Transformation rate and (b) transformed fraction curves obtained for different heating rates in DSC. 165

Figure 6.15 Local Avrami exponent, $n(X)$, obtained by non-isothermal DSC analysis at different heating rates. …… 167

Figure 6.16 Local Avrami exponent, $n(T)$, obtained by non-isothermal DSC analysis at different heating rates compared with Ozawa analysis. …….. 168

Figure 6.17 Temperature scan magnetization curve showing successive crystallization of ferromagnetic phases above T_C of amorphous alloy. …….. 169

Figure 6.18 Isothermal magnetization behavior of Cu-modified $Fe_{43}Co_{19}Ni_9B_{19}Si_5Nb_4$ alloy under 500 Oe applied magnetic field. …… 170

Figure 6.19 Transformed fraction curves for α–(Fe,Co) phase calculated by isothermal magnetization measurements. …….. 171

Figure 6.20 Avrami plots for different isotherms revealing three qualitative regions. …….. 172

Figure 6.21 Local Avrami exponents comparing non-isothermal DSC analysis and isothermal magnetization measurements. …….. 173

Figure 6.22 Local Avrami exponent, $n(X)$, calculated at different isotherms compared with non-isothermal JMAK direct extension; (a) initial crystallization regime (b) late crystallization regime, (c) overall crystallization process. …….. 175

Figure 6.23 The classical JMAK treatment as applied to isothermal magnetization compared to a soft-impingement diffusion mechanism represented by a modified JMAK relation. …….. 178

Figure 6.24 Local Avrami exponents calculated by non-isothermal DSC analysis utilizing constant and varying Q_a values. Inset shows the variation of Q_a calculated by classical JMAK as applied to isothermal magnetization compared to constant Q_a derived from Kissinger analysis. ……..... 179

Figure 6.25 TEM images and SAED patterns of Cu-modified $Fe_{43}Co_{19}Ni_9B_{19}Si_5Nb_4$ alloy annealed at 823 K; (a) 900 s annealing, (b) 2400 s annealing, (c-d) SAED pattern and high-resolution micrograph corresponding to 2400 s annealing, (e-f) 10800 s annealing. 182

Figure 6.26 XRD patterns showing the evolution of α–(Fe,Co) nanocrystals during 823 K annealing for different durations. 183

Figure 6.27 Deconvoluted XRD pattern of 873 K annealed alloy showing reflections from amorphous matrix and α–(Fe,Co) nanocrystals. 184

Figure 6.28 Room temperature hysteresis loops of suction-cast and annealed Cu-modified $Fe_{43}Co_{19}Ni_9B_{19}Si_5Nb_4$ alloy. 185

Figure A.1 Kikuchi map for BCC crystal structure. 206

Figure A.1 Kikuchi map for FCC crystal structure. 207

Figure B.2 Standard indexed electron diffraction spot patterns for BCC crystal. 208

Figure B.2 Standard indexed electron diffraction spot patterns for FCC crystal. 210

Figure C.1 Co-Fe equilibrium phase diagram. 212

Figure C.2 Fe-B equilibrium phase diagram. 213

Figure C.3 Fe-Si equilibrium phase diagram. 214

Figure C.4 Fe-Ni equilibrium phase diagram. 215

Figure C.5 Fe-Nb equilibrium phase diagram. 216

Figure C.6 Fe-Cu equilibrium phase diagram. 217

CHAPTER 1

INTRODUCTION

The history of civilization is closely associated with progress in the field of materials research which involves the design and fabrication of novel materials and fundamental understanding of their processing, structure, and property relationships. It is nowadays convenient for a materials scientist to classify alloys as crystalline and amorphous alloys where the former demonstrates long range order between its structural units and periodicity at the atomic scale while the latter lacks crystalline symmetry.

1.1 Intermetallic Compounds

Intermetallic compounds are considered as an advanced class of crystalline alloys where an ordered phase is formed between the atoms of constituent elements. In this particular aspect, intermetallics compounds based on transition metal-aluminides (e.g. nickel-, iron- and titanium-aluminides) have shown promise for high temperature load-bearing applications in aggressive environments.

In order to meet the future requirements of aircraft and aerospace engine performance, new materials must be stronger, lighter and more reliable at high temperature aggressive atmospheres. In this respect, nickel aluminides are strong candidates over the Ni-based superalloys known for their wide commercial use in the manufacturing of aeroengines. Nickel aluminides demonstrate lower density which could enable smaller and lighter

components to be fabricated, higher melting temperature providing diffusion slower controlled kinetics, better oxidation resistance, lower ductile to brittle transition temperature and higher thermal conductivity. Moreover, nickel aluminides are cheaper compared to superalloys since they do not generally require alloying with critical minor metals such as Cr, Mo, Ti and Ta. Examples of engine components made from nickel aluminides are shown in Figure 1.1.

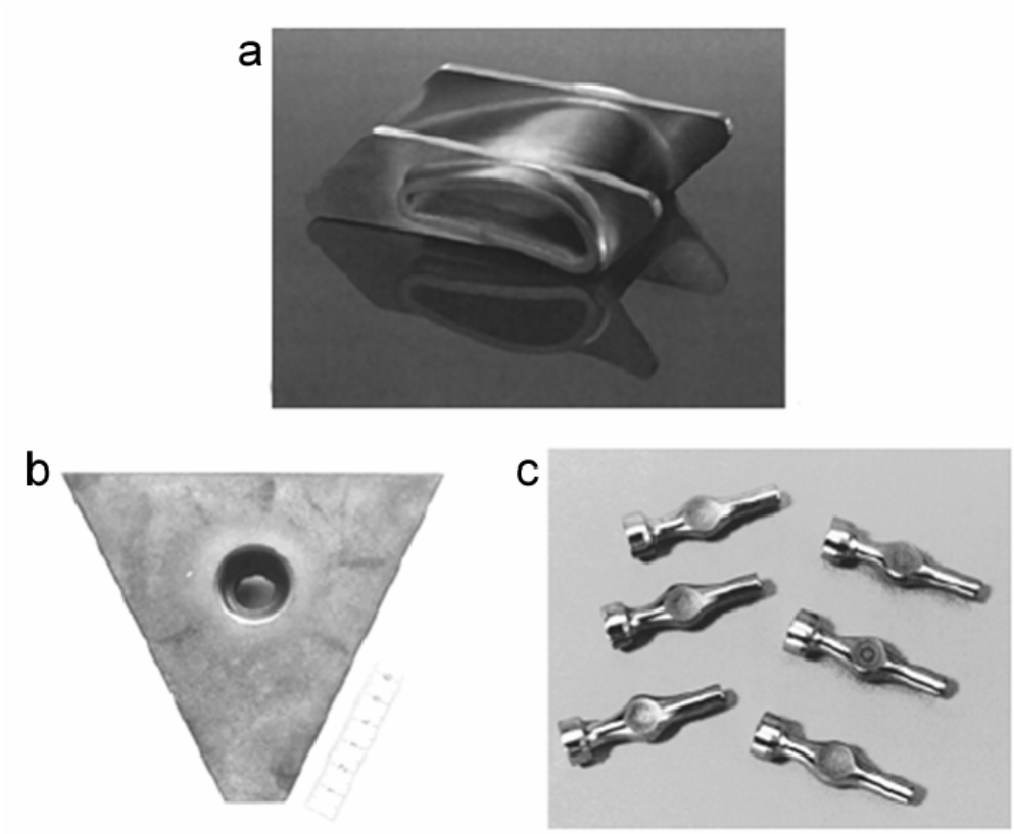

Figure 1.1 Typical parts made of nickel aluminides; (a) stator blade for gas turbines, (b) thermal tile for combustion chamber lining in gas turbines and (c) fuel injector pins in diesel engines.

One single but vital limitation is the low temperature brittleness of nickel aluminides leading to difficulty in damage-tolerant design and low temperature processing using these alloys. Therefore, much effort is being spent to tailor the mechanical properties of nickel aluminides by means of physical metallurgical principles in an attempt to obtain balanced ductility, strength, toughness and impact resistance.

1.2 Amorphous Alloys

Amorphous alloys (metallic glasses), which are new emerging class of materials in glass family, are solids lacking of long range atomic order which provide them with exceptional physical and chemical properties compared to their crystalline counterparts [1-6]. Typically, amorphous alloys are produced by rapid cooling from liquid or gas phase which kinetically hinders crystallization. Since 1960s, purely metallic and metal-metalloid glasses were developed and attracted great research interest to investigate their metallurgical formation which is different from oxide or polymeric glasses.

Among metallic glasses, Fe-based amorphous alloys have drawn much attention owing to their outstanding soft magnetic behavior [7, 8], excellent corrosion resistance [9, 10], and good mechanical properties [11, 12] for potential structural applications such as transformer cores, magnetic shielding, magnetic read-heads. Additionally, metallic glasses will be very convenient for micro- and nano- electromechanical systems where ductility is not vital since the application dimensions are smaller than the plastic zone around propagating crack.

Another interest is the fundamental aspect of crystal formation from amorphous precursors to obtain interesting novel amorphous matrix nanocrystalline alloys. In this respect, it is important to understand the

mechanism of nanocrystallization and corresponding structure-property relationships.

Metallic glasses and amorphous matrix nanocrystalline alloys with the combination of high strength, toughness, hardness and elastic energy storage capability have already been commercialized in the fields of spring, electrode and sporting goods materials (Figure 1.2). Considerable effort is still being spent to fabricate die and cutting tools and soft magnets using metallic glasses. It is therefore obvious that, metallic glasses consisting of amorphous and nanocrystalline phases will be the near future of engineering materials.

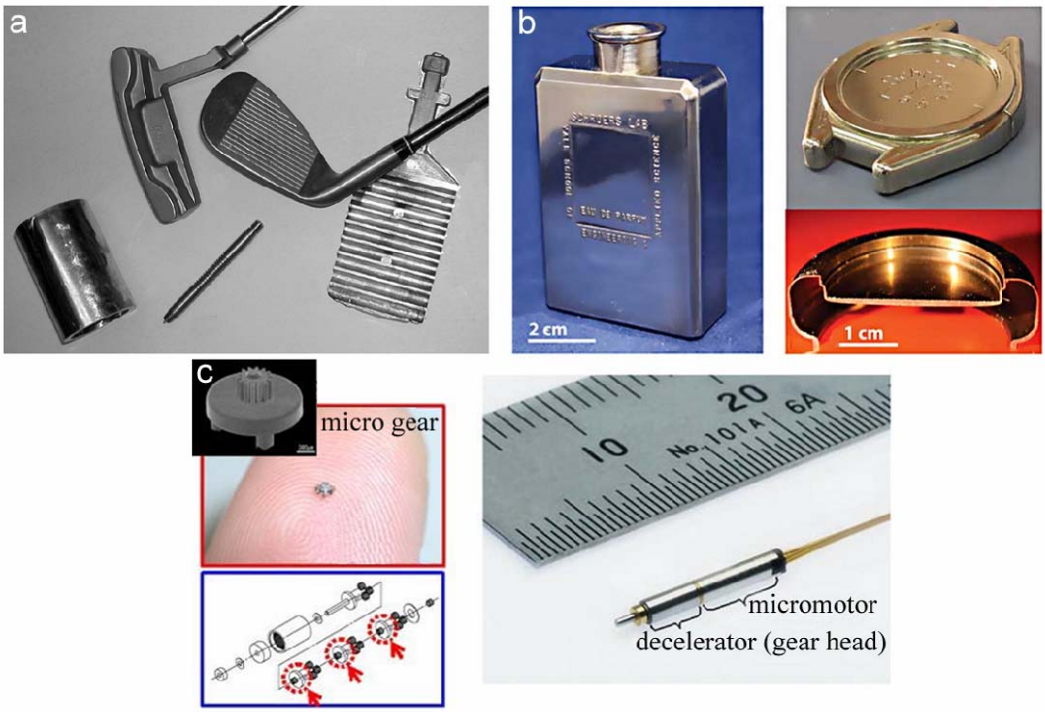

Figure 1.2 Examples for bulk amorphous alloy products; (a) metal pipe, rod, cast component and golf clubs, (b) bottle and watch cases, and (c) micro geared motor.

1.3 Research Objectives

The aim of this dissertation was to understand microstructural evolution, macro- and micro-alloying behavior, magnetic properties, thermal characteristics, mechanical behavior and kinetics of phase transformations, i.e. precipitation and crystallization reactions, in nickel aluminides and Fe-based bulk amorphous alloys. Beyond conventional techniques such as thermal analysis or electron microscopy combined with image analysis, this dissertation provides a novel magnetic monitoring approach to study the isothermal kinetics of phase transformations in multicomponent alloy systems.

This dissertation starts by providing the theoretical background of relevant physical metallurgical principles and a review of previous studies in Chapter 2. Followed by the description of experimental techniques used to fabricate and characterize the studied materials in Chapter 3, this dissertation continues by introducing the magnetic monitoring approach together with fundamentals of transformation kinetics in Chapter 4. The following content of this dissertation is divided into two main chapters which discuss microstructural evolution, mechanical properties and kinetics of precipitation in macro- and micro-alloyed nickel aluminides contained in Chapter 5 and microstructural evolution and kinetics of nanocrystallization in Fe-based bulk amorphous alloys in Chapter 6. Lastly, this dissertation is concluded in Chapter 7 by highlighting the major contributions to the research field of intermetallics and amorphous alloys.

CHAPTER 2

THEORETICAL BACKGROUND

2.1 Intermetallic Compounds

2.1.1 Solid Solutions and Intermetallic Compounds

Whenever atoms of dissimilar elements occupy the sites of a common crystal lattice at various proportions, the resulting phase is termed a *solid solution*. Solid solubility will be governed by factors such as atomic size mismatch of constituent elements (or the elastic strain energy in a solid solution) and chemical affinity of constituent elements (or the electronegative valency effect).

Solid solutions can be thought to be macroscopically homogeneous; however, considerable inhomogeneity might exist in the atomic scale. Random or disordered solid solutions are formed by a statistical distribution of atoms of different elements in lattice sites while ordered solid solutions involve unlike atoms occupying adjoining sites in a crystal lattice. The latter can be termed as a superlattice where like atoms do not prefer being nearest neighbors in the lattice.

Whether a system will be ordered at a given temperature is controlled by the interaction energy between unlike atoms, e.g. systems with strong ordering forces are likely to maintain the ordered arrangement up to higher temperatures. In view of thermodynamics of solid solutions, the ordered state can be viewed as the lower energy state since less favorable like atom interactions are minimized especially at low temperatures where entropy

gain due to disordering is less significant. However, from a practical point of view, deviation from the ideal ordered arrangement is not uncommon due to presence of crystal imperfections, departure from the exact stoichiometric ratios and the presence of alloying elements which disturb atomic ordering.

Considering an A-B alloy system, it can be deduced by constructing a hypothetical free energy vs. temperature plot (Figure 2.1) that the terminal solid solubility of B atoms in A lattice (or the α-phase) is reduced with increasing ability of constituents to form a stable compound (the β-phase).

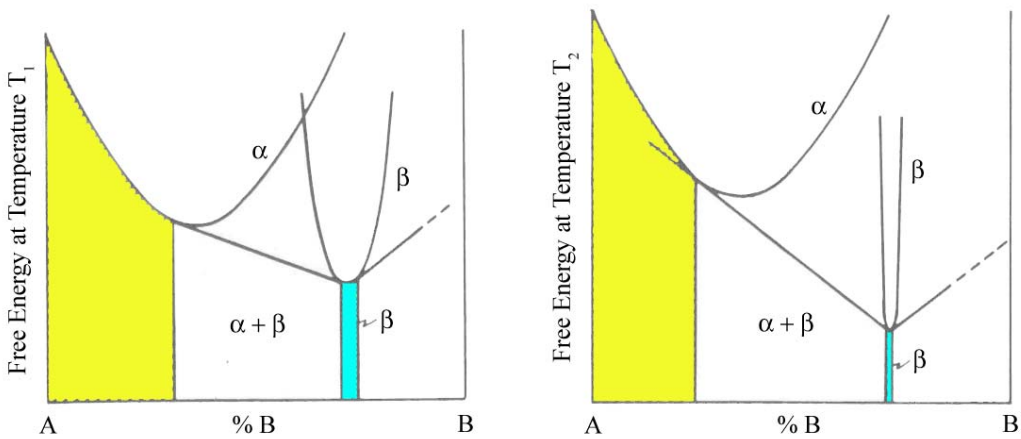

Figure 2.1 Hypothetical free energy curves in the A-B alloy system showing the restriction of terminal solid solubility in the presence of stable intermetallic compound. Adapted from [13].

When the solubility of one component in the other is greatly confined around a stoichiometric composition, the resulting phase is known as an intermediate phase, in other words, an intermetallic compound. An intermetallic compound can be defined as a phase which is formed with a different structure relative to that of its components which enables its explicit differentiation from solid solutions. It is known that intermetallic compounds in binary alloy systems with cubic structure occur in the vicinity

of stoichiometric chemical compositions A_3B, AB and AB_3. The term *intermetallics is* the shortened representation for intermetallic phases or compounds. The strength and type of bonding in intermetallics arise from their electronic configurations and specify the crystal structure of the compound strength of unlike atoms is larger than that of like atoms so that intermetallic formation occurs.

2.1.2 Strengthening Mechanisms

Solid Solution Hardening

Significant changes in the mechanical properties, e.g. critical resolved shear stress for plastic deformation, can be imparted by the addition of secondary or higher order alloying elements where the additional atoms of the alloying element form a substitutional solid solution with the parent metal or alloy.

The formation of a substitutional solid solution can alter the work hardening behavior by inducing a change in the dislocation structure or density. While a change in the latter is only limited to very dilute alloy systems, dislocation arrangement can be greatly altered in the presence of an alloying element which can be explained based on the modification of stacking fault energy. Alloying additions which provide lower stacking fault energies favor the dislocations being dissociated into partial dislocations. This corresponds to a comparable effect on work hardening behavior similar to a decrease in deformation temperature.

Apart from the effect of alloying additions on dislocation arrangement, solid solution hardening mechanisms that arise from interactions between dislocation lines and solute atoms in the lattice can be classified as solute segregation on resting dislocations and solute frictional forces acting on moving dislocations. The phenomenon of dislocation locking is encountered

in the former case by (i) segregation of solute atoms on stacking faults increase their width, (ii) by elastically hindering the dislocation motion by producing an elastic strain field which interacts with that of the dislocation or (iii) by electrostatic locking of the dislocation cores by the generation of extra charges located near solute atom due to valency difference. In additional to solute atoms locking dislocations at rest, a moving dislocation will encounter significant frictional forces by solute atoms lying on the glide plane as depicted in Figure 2.2. The extent of solid solution hardening via dislocation friction is affected by variables such as concentration of solute, mean separation between two solute atoms, whether the solute atom is situated above or below the slip plane, etc.

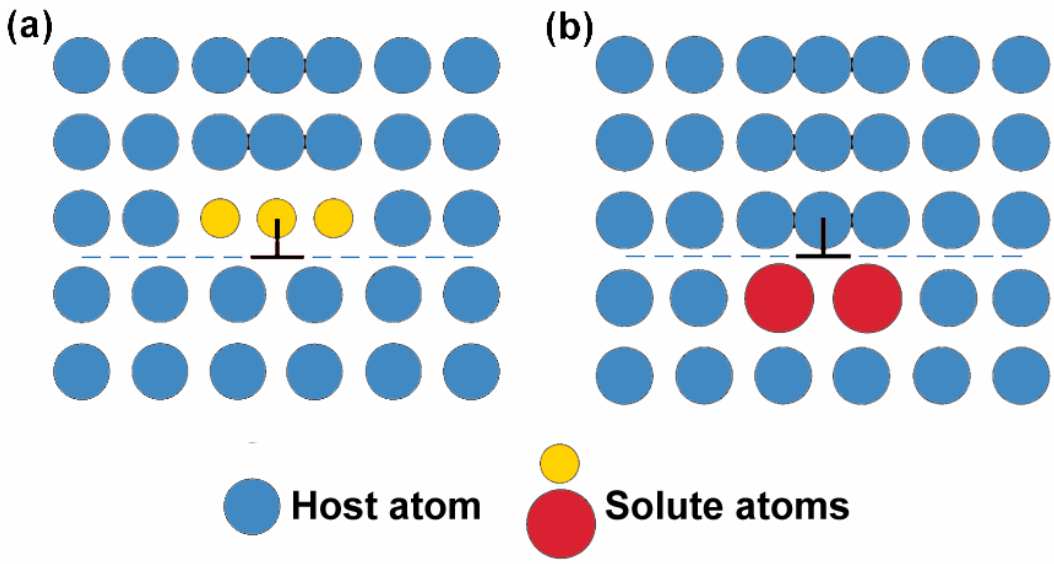

Figure 2.2 Substitutional impurities acting as obstacles against dislocation movement; (a) smaller, and (b) larger solute atoms.

Precipitation Hardening

Since the strength of an alloy is greatly influenced by dislocation generation and mobility of dislocations, formation of second phase precipitates can lead to a remarkable strengthening effect. The gain in the yield strength is dependent on coherency, size, shape, strength and interparticle spacing of the second phase. Dislocation-particle interactions (Figure 2.3) can be grouped depending on the mechanism how a moving dislocation penetrates dispersed second phase particles.

In the case of dislocations cutting a particle at the glide plane and offsetting the particle by an amount equal to the Burger's vector, an increment is required in the shear stress that must be applied to sustain dislocation motion. Moreover, if the glide plane must change in order that a moving dislocation penetrates or cuts through the second phase, the dislocation will encounter an additional frictional stress which results in increased critical resolved shear stress for plastic deformation.

If dislocations can not cut through the second phase particles, formation of dislocation loops is observed indicating that the repulsive force is sufficient to actually stop the dislocation. Dislocation looping around particles requires significant amount of shear stress especially for fine particles and hence small interparticle spacings, and therefore dislocation looping is inoperative with extremely fine precipitates.

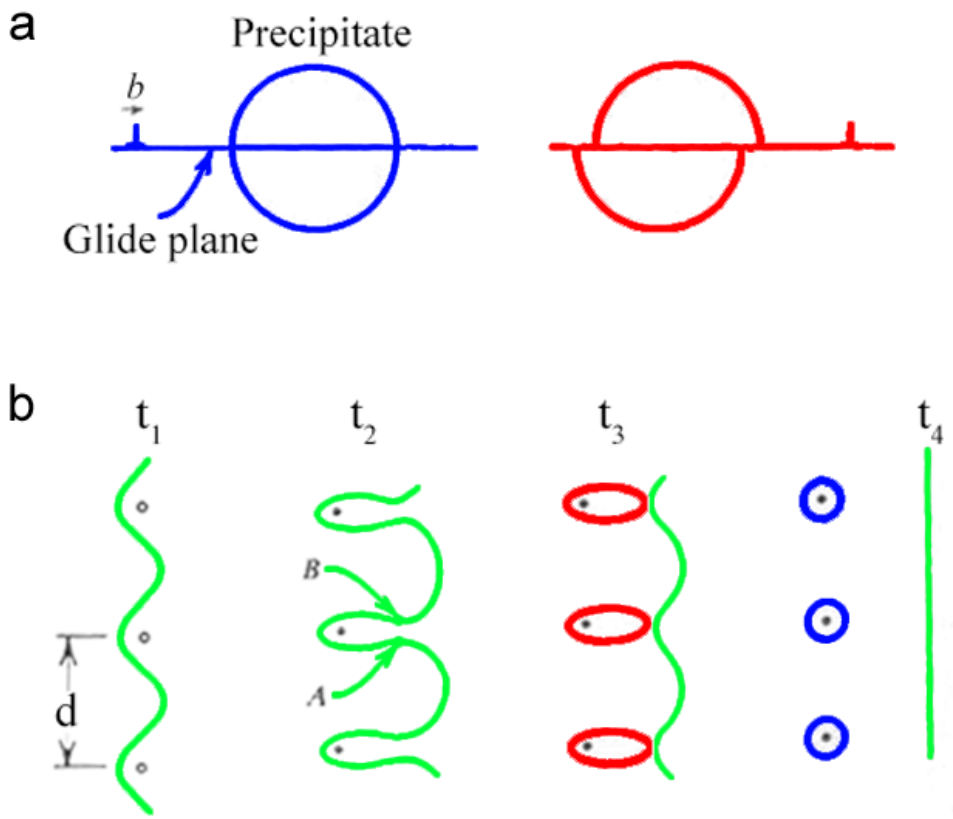

Figure 2.3 Dislocation-particle interactions showing (a) dislocation cutting through the second phase, (b) dislocation looping around second phase.

Long-Range Order Hardening

Intermetallics and solid solutions with long-range order of superlattice structures will actually demonstrate limited dislocation mobility since moving dislocations create disorder across their slip planes and form the so-called anti-phase boundaries as shown in Figure 2.4. Order can be thought to be restored outside the anti-phase domain boundary by pairs of superdislocations lying on the same glide plane. A superdislocation in a perfect superlattice encounters large restraining forces due to the creation of high energy atomic bonds during its glide.

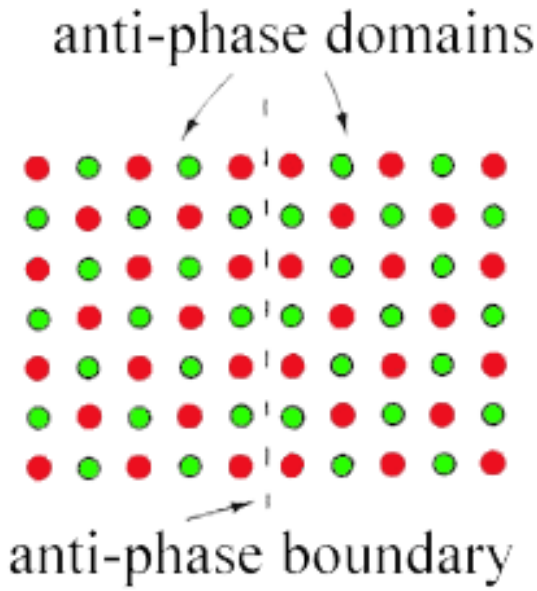

Figure 2.4 The formation of anti-phase boundary by dislocation glide through ordered precipitates inside a disordered matrix.

Of particular interest is the case of coherent or partially coherent ordered precipitates inside a disordered matrix where the penetration of dislocation through the second phase particle will eventually produce an anti-phase boundary due to the disturbance of atomic order on the glide plane. The anti-phase boundary energy is usually very large compared to the coherent boundary energy and therefore anti-phase boundaries are more effective in hindering dislocation motion when dislocations encounter ordered domains inside a disordered matrix.

2.1.3 Magnetic Properties

Magnetism arises from the interaction of electrons with each other and with applied magnetic fields. Electron spin magnetism may cancel itself out in atoms with closed electron shells in which electron orbits are distorted to retain the original internal magnetic field leading to *diamagnetism*. The *d*-shell transition metals, on the other hand, are magnetic atoms due to the uncompensated electron spins and therefore orientation of magnetic moments is observed under an applied magnetic field. While a dilute assembly of such atoms shows *paramagnetism*, in a system where magnetic atoms are close enough so that magnetic electrons interact with magnetic moment of neighboring atoms, cooperative alignment of all spins occur in the lattice. This leads to a spontaneous magnetization termed *ferromagnetism* which involves the alignment of spins of neighboring atoms through exchange forces. The exchange interaction causes a non-zero spontaneous magnetization at zero field which averages to zero net magnetization by considering random orientation of magnetic domains inside the bulk of the material.

Figure 2.5 shows a diagram of the magnetization process and changes in domain configuration of a ferromagnetic material under an applied magnetic field, H. Upon the application of an external field, magnetic domains aligned in favorable directions grow at the expense of unfavorably oriented domains. Increasing the applied magnetic field leads to domain walls starting to move out of the specimen where magnetization (M) direction of the specimen is close to the direction of applied field. Further increasing the applied field reversibly rotates the magnetization of the specimen where it finally matches the applied field direction. That particular point on the M-H curve is termed the saturated magnetic state.

The gradual removal of the applied field results in the hysteresis behavior where the remaining magnetization after complete removal of applied field is

termed the remnant or residual magnetization (M_r), and the magnetic field required to reduce the specimen magnetization to zero is defined as the coercivity, H_c. The maximum attained magnetic moment is called the *saturation magnetization*, M_s. Ferromagnetic materials are best characterized by their susceptibility (χ) or permeability (μ) defined as the slopes on the hysteresis curve. Susceptibility or permeability determines the relative ease of magnetizing a material and hence the specific application field as a magnetic material.

It is possible to identify ferromagnetic materials as hard or soft magnets based on the difficulty in demagnetization by interpreting the hysteresis behavior. Hard magnetic materials are those typically having coercivities greater than 10 kA/m whereas soft magnetic materials show low resistance against magnetization and demagnetization and are characterized by low coercivities < 1 kA/m.

The *Curie transition temperature* (T_C) is defined as the point where ferromagnetic behavior ceases due to thermal fluctuations exceeding the internal molecular field which aligns the atomic magnetic moment along the applied field direction. The exact value of T_C can be determined as the temperature at which the absolute value of the first derivative of magnetization with respect to temperature is maximized.

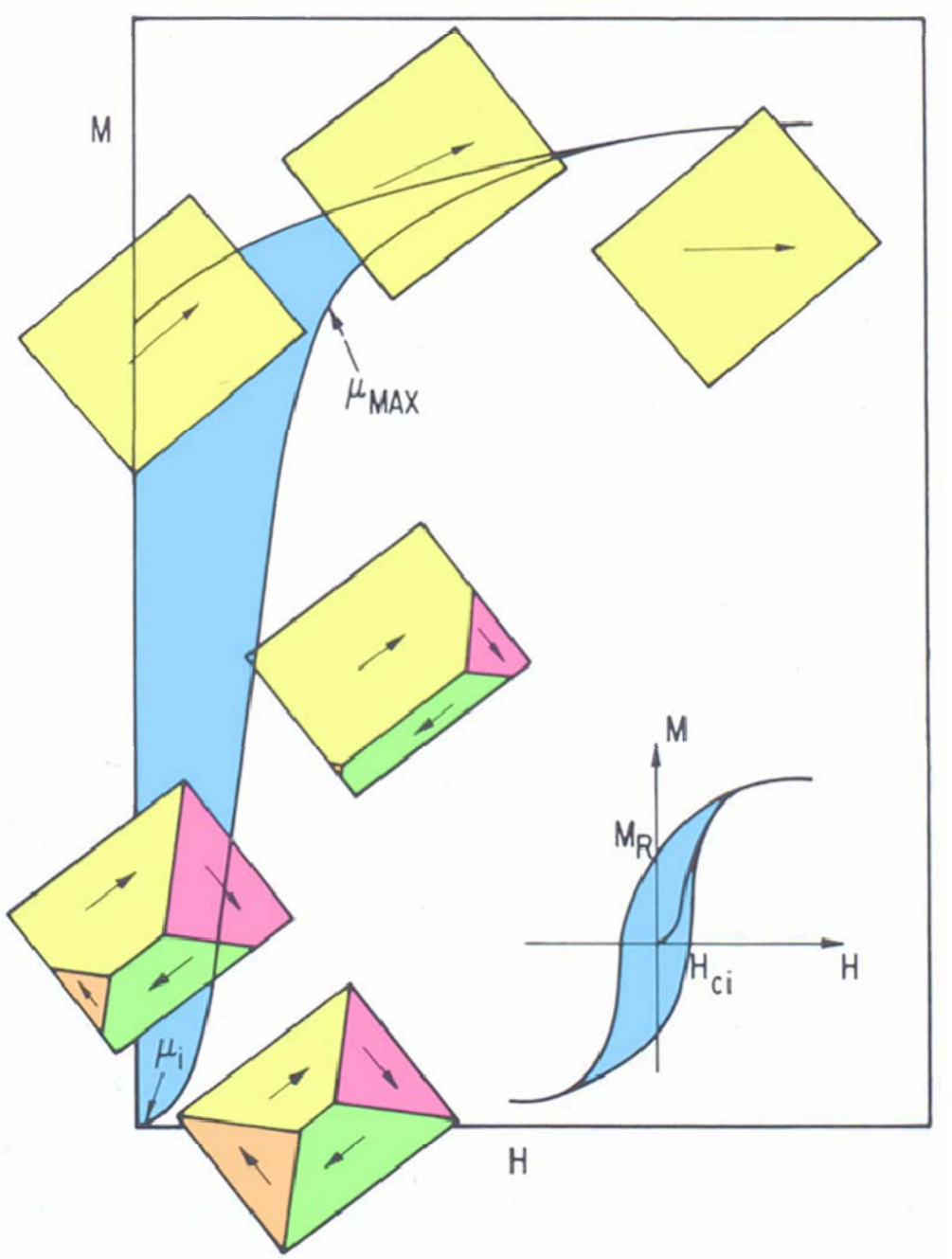

Figure 2.5 Schematic representation of magnetization behavior and corresponding domain configuration in a single-crystal [13].

2.1.4 The Nickel-Aluminum Intermetallic Compound

The nickel-aluminum equilibrium phase diagram contains several intermetallic compounds with different compositions (Figure 2.6). The stoichiometric Ni-Al (NiAl compound) was first evidenced in the beginning of the 20th century with its unusually high melting point.

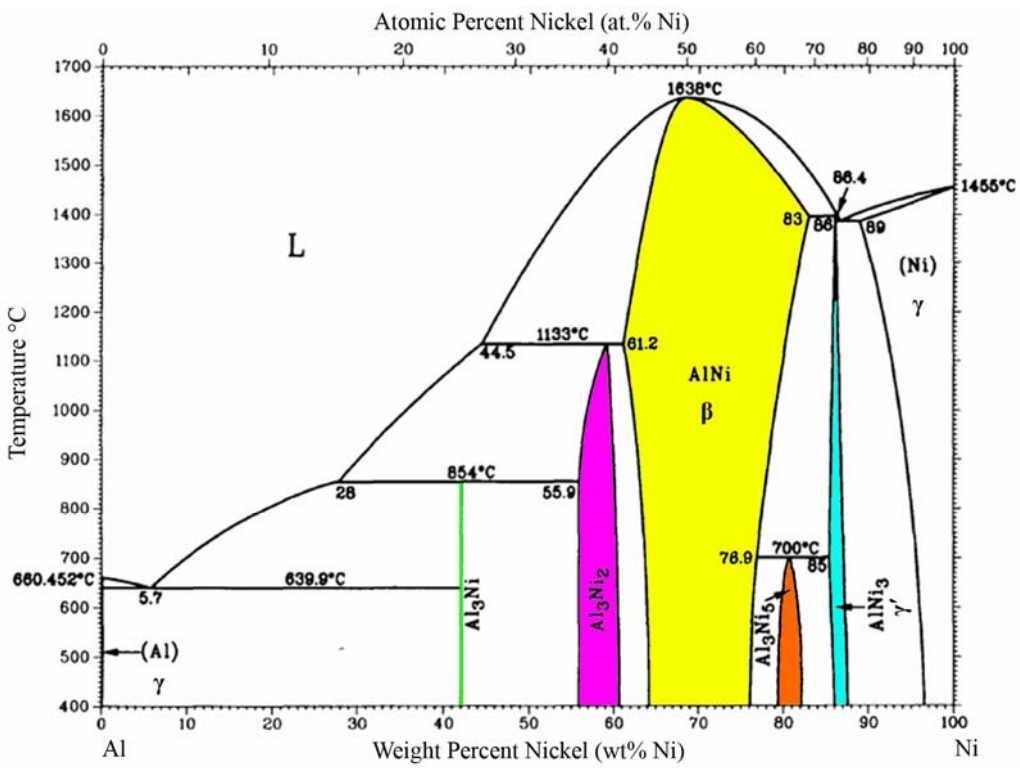

Figure 2.6 Ni-Al equilibrium phase diagram. Adapted from Ref.[14]

In the recent years, the NiAl compound has been drawing much attention as an alternative to Ni-based superalloys for high temperature structural applications. Table 2.1 compares some of the important properties of transition-metal aluminides and nickel-based superalloys. In addition to its high melting temperature (1638 °C) and low density (~6 g/cm^3), the ordered NiAl compound exhibits excellent corrosion and oxidation resistance up to 1300 °C and high thermal conductivity nearly an order of magnitude higher

than that of superalloys (Figure 2.7). Nickel aluminides are relatively inexpensive compared to superalloy counterparts because of strategic and costly minor metals used in the latter. Furthermore, polycrystalline NiAl compound exhibits a significantly low ductile-to-brittle transition temperature in the range 573–873 K when compared to other intermetallic candidates to replace superalloys.

Table 2.1 Physical properties of transition-metal aluminides and superalloys [15-17].

Property	FeAl	Fe_3Al	NiAl	Ni_3Al	γ-TiAl	Ti_3Al	Superalloys
Crystal Structure	B2	$D0_3$	B2	$L1_2$	$L1_0$	$D0_{19}$	$L1_2$/FCC
Melting Temperature (°C)	1330	1540	1638	1390	1440	1180	1450
Density (g/cm3)	5.6	6.7	5.9	7.5	3.8	4.4	8.3
RT Ductility (%)	2.5 - 8	4-8	0-2		1-3	2-5	3-5

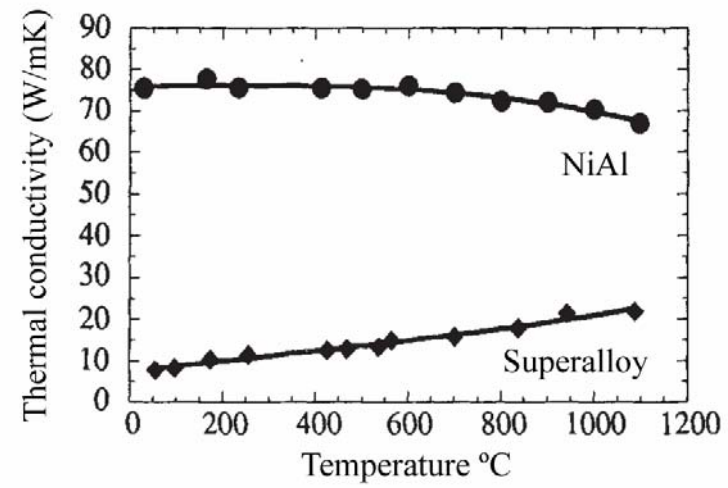

Figure 2.7 Thermal conductivities of single crystal NiAl and Ni-based superalloy compared [2].

The important superlattices (long-range ordered structures) in the Ni-Al system are Ni_3Al and NiAl as depicted in Figure 2.8. The former is designated by $L1_2$ in the Strukturbericht notation where Al atoms reside in 000 positions and Ni atoms in ½½0 positions of the conventional face centered cubic structure. Of particular interest is the latter compound designated by B2 (disordered counterpart is A2) where Ni atoms reside in 000 cube corners and Al atoms in the ½ ½ ½ position.

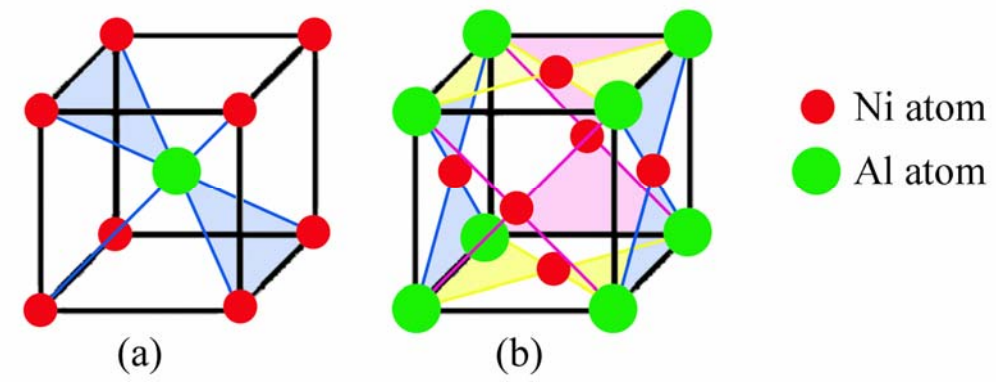

Figure 2.8 The structures of ordered NiAl and Ni_3Al superlattices.

The binary Ni-Al phase diagram in Figure 2.6 suggests that the B2 NiAl compound can also be formed with off-stoichiometric compositions. Different lattice defect structures shown in Figure 2.9 are formed in either side of the stoichiometric compound; Al-rich NiAl is formed by vacancies in the Ni sublattice and Ni-rich NiAl is formed by Ni antistructure atoms occupying the Al sublattice. The deviations from stoichiometry would eventually produce those lattice defects leading to variations in properties such as lattice parameter and mechanical properties of the compound. While moderate solid solution hardening is observed in the Ni-rich side, remarkable increase in the flow stress is evident in the Al-rich side due to vacancy hardening via elastic distortion of the B2 lattice around the atomic defects. It is therefore worth to mention that a good knowledge of the site preference of constituent atoms is required for the interpretation of alloy properties.

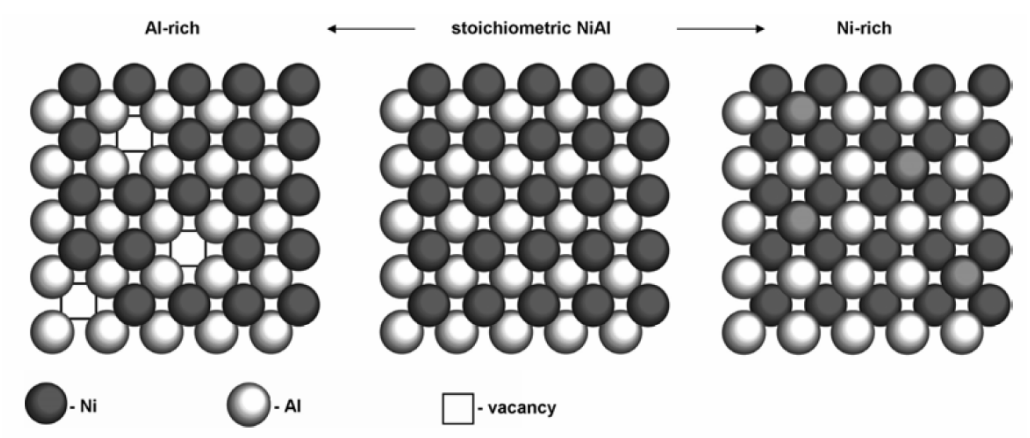

Figure 2.9 Lattice defects arising from off-stochiometery in β-NiAl compound.

The von Mises criterion for plasticity is satisfied when five independent slip systems are operative in disordered alloys. However, the ordered B2-NiAl displays only three independent slip systems as <111> on 110, <110> on 110, and <100> on 110 as shown in Figure 2.10. Thus, it is not expected that

the B2 NiAl alloy shows significant ductility at room temperature. The critical resolved shear stress for <100> dislocations on 110 slip planes is about 70 MPa while that of <111> dislocations is about 600 MPa, and, <110> dislocations are operative only at high temperatures (above 300 °C). Therefore, the deformation of polycrystalline NiAl mostly takes place by <100> slip and fracture occurs intergranularly for stoichiometric NiAl compound whereas transgranular fracture predominates in off-stoichiometric compounds.

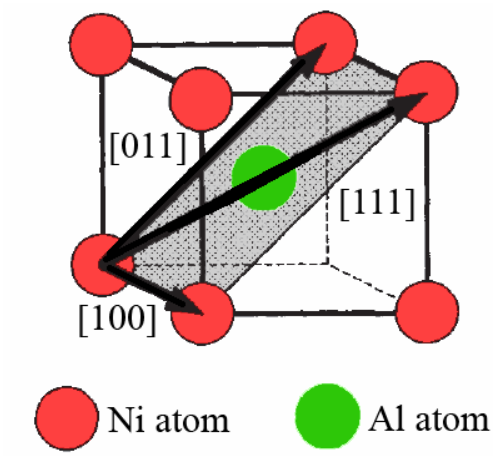

Figure 2.10 Observed slip vectors for the B2 NiAl compound.

2.1.5 Alloying Additions to NiAl

Extensive research has been conducted to understand alloying behavior of various elements in NiAl based intermetallics to clarify their influence on microstructure and mechanical properties.

Alloying additions can have great impact on slip deformation mechanism which directly alters their ductility. Refractory metal alloying of B2 NiAl increases its ductility by reducing the high energy of the anti-phase boundaries [18] that are otherwise responsible for confined activation of less

mobile <111> superdislocations limiting the plasticity of alloy. Macroalloying of NiAl with Cr and Mn can also reduce the antiphase boundary energy [19] which favors activation of <111> dislocations providing five independent slip systems and hence polycrystalline ductility.

Ductility can also be enhanced by the disturbance of the perfect atomic ordering in the NiAl lattice by the incorporation of Cr atoms [18, 20] displaying strong site preference for the Al sublattice. Alloying additions have also been made to NiAl to modify the slip behavior in a way to promote <111> slip and to operate sufficient independent slip systems for plastic deformation [21, 22]. Modification of the slip vector in NiAl by the additions of chromium, vanadium, and manganese were successful however not accompanied by ductility enhancement [23-25].

Alloying additions can have profound effect on ductility by altering the fracture mode from intergranular to transgranular. Doping of stoichiometric NiAl with B, C and Be was also studied [26], and, while B was found to completely suppress intergranular fracture by segregation on grain boundaries, C and Be did not affect the fracture mode.

It was previously reported that the addition of Au improves room temperature ductility and imparts a significant solid solution strengthening effect at elevated temperatures [27]. Similarly, incorporation of 0.5 to 1 at.% Ag to NiAl increased room temperature ductility and compressive strength via solid solution hardening [28]. Remarkable solid solution hardening was observed with of minor Cr addition 1 at.% which increases yield strength by 300%, while larger additions produced α-Cr phase having no predominant contribution from precipitation hardening relative to the solid solution effect [23].

Incorporation of Ta into NiAl was reported [29] to strengthen the alloy through solid solution hardening at low Ta content (< 0.2 at.%) and Laves phase precipitation at high Ta content (> 3 at.%). Sheng et al. [30] related the decrease in mechanical properties of NiAl based alloys with fine precipitation

of an Hf rich phase to the competition of precipitation of Hf rich phase and Heusler phase particles, where the latter seems to have a larger strengthening effect. A decrease in the microhardness with the precipitation of a Cr-rich phase was explained by the change in Al content of Ni-Al-B-Cr alloy [31]. Nb incorporation was shown to strengthen NiAl with precipitation of fine NiAlNb phase which impedes dislocation motion [32].

Guo et al. [33] reported that rare earth elements (Y, Ce, Nd, and Dy) refined the lamellar spacing and increased the room temperature yield strength in addition to compressive ductility of NiAl based eutectic alloy. Minor addition of Dy enhanced the compressive strength and ductility of NiAl-28Cr-5.8Mo-0.2Hf alloy at both room temperature and elevated temperature through lamellar refinement [34]. Improvement of room temperature compressive properties was shown to occur via microstructural refinement of the eutectic phase mixture with the incorporation of Sc into NiAl-Cr(Mo)-0.15Hf alloy [35]. Minor addition of Ga and Mo in NiAl by a mechanical alloying process was shown to provide grain refinement without the formation of a second phase for Ga addition, and second phase compound formation via Mo addition [36].

Whittenberger and Noebe [37] studied Zr additions in the range 0.05 to 0.7 at.% and it was shown that alloys were stronger than binary NiAl at low temperatures and high strain rates.

In a study by Cui et al. [38], minor Hf addition to NiAl/Cr(Mo) eutectic alloy increased the high temperature strength; however, microalloying with Hf was not effective in terms of the alloy's creep resistance.

2.1.6 Alloying NiAl with Fe

The applicability of NiAl compound without ternary or higher order alloying is limited due to poor elevated temperature strength above 823 K [39, 40], brittleness below 600 K caused by large APB energy, and tendency to intergranular brittle fracture at room temperature because of high atomic ordering at the grain boundaries [41-45]. Therefore, many attempts have been made to reduce the brittleness of the NiAl intermetallic compound which can be classified as the modification of slip system by ternary or higher-order alloying [39], grain refinement [27, 46] and incorporation or precipitation of a ductile phase [47, 48]. Although extensive research has been carried out on these alloys, new investigations still continue to reveal the attractive properties of the NiAl alloy system [27, 49-51].

Microalloying NiAl with Fe does not seem to be a remedy against limited ductility since no change of the slip vector can be observed in polycrystalline NiAl [52, 53]. Due to the small atomic size misfit, Fe atoms show substantial site preference for the Ni sublattice which provides slight solute solution hardening. It was also shown that alloying of single β-phase NiAl with 20 at.% Fe was ineffective in promoting <111> slip which in turn did not provide a significant change in room temperature ductility and toughness [42, 54].

On the other hand, favorable microstructures can be developed by alloying NiAl with further increasing amounts of Fe towards the Ni rich region and by employing appropriate annealing procedures [22]. Thus, the incorporation of Fe as a ternary alloying element in NiAl alloys has raised interest, given the specific changes to the material's structural properties. Accordingly, convenient thermal treatments were proposed to produce desired ductile γ-(Ni,Fe) solid solution precipitates which decrease the room temperature brittleness of the B2 NiAl alloys [55, 56]. The volume fraction of this ductile γ-phase has been shown to depend on composition and thermal treatment [57, 58], as can be inferred from the ternary phase diagram and a

vertical section of the Ni-Al-Fe system given in Figure 2.11 and Figure 2.12, respectively.

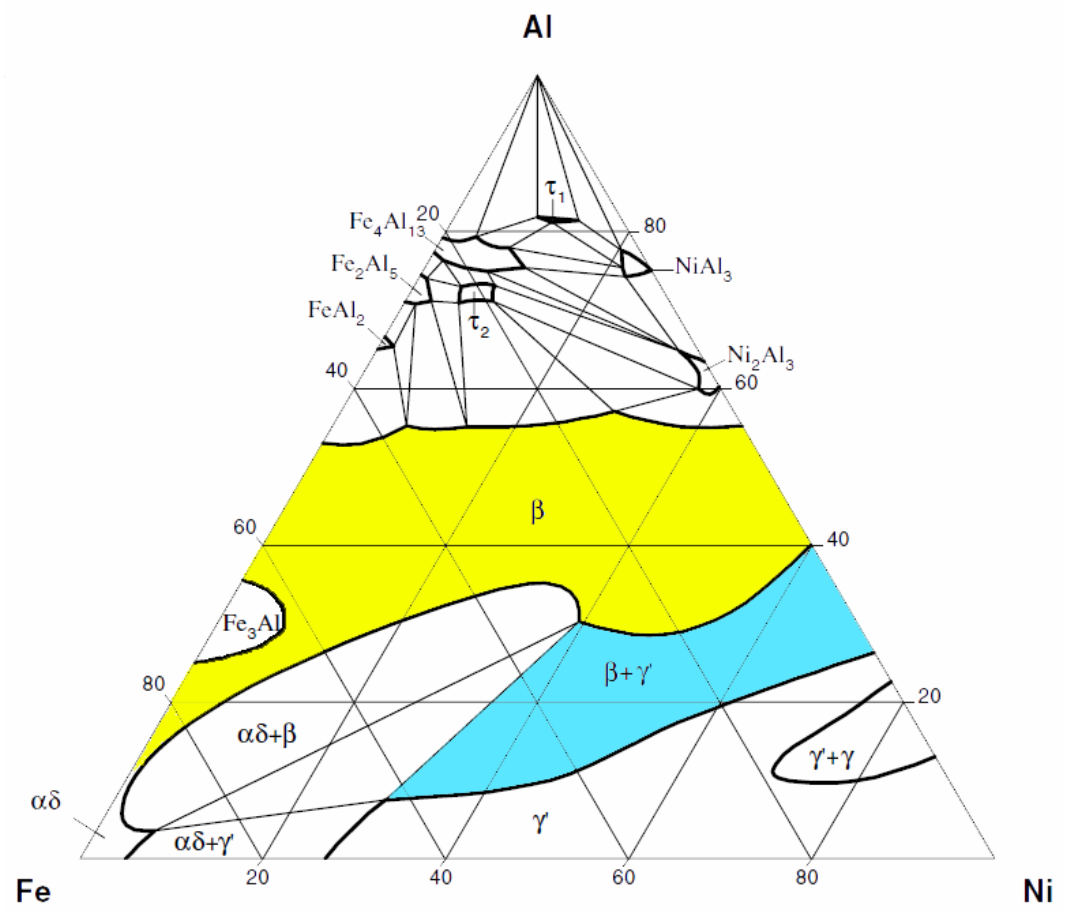

Figure 2.11 Equilibrium phase diagram for Ni-Al-Fe system at 298 K. Adapted from Ref.[59].

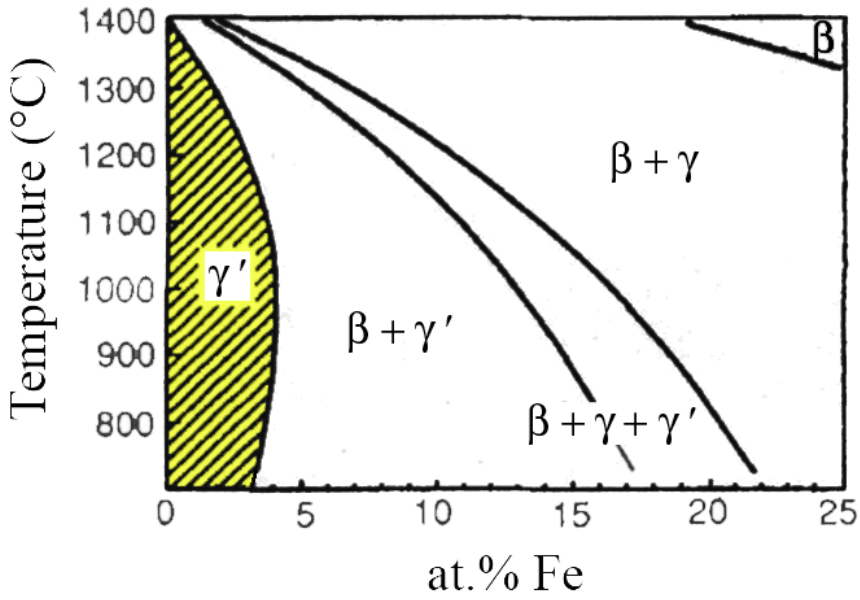

Figure 2.12 Isothermal section of the Ni-Al-Fe system and a vertical section drawn from Ni-25Al to Fe side showing temperature dependence of stable phases. Adapted from Ref.[55].

In addition to room temperature ductilization of NiAl by Fe macroalloying, the high temperature strength of NiAl can also be improved by precipitation hardening. The addition of Fe to the NiAl system was proposed to result in the decomposition of ordered bcc (Ni,Fe)(Al,Fe) phase into an Fe-rich disordered bcc α-phase and NiAl rich ordered bcc phase due to the miscibility gap in the system [54, 60]. The miscibility gap between the ordered and disordered phases extends from the Fe side to the NiAl compound in the Ni-Al binary as shown by the ternary phase diagram in Figure 2.13 calculated by the regular solution model by Bradley [59, 61]. The reexamination of the system by Hao et al. [60] using the diffusion couple method combined with electron microprobe analysis verified the miscibility gap and revealed the equilibrium compositions of Fe-rich and NiAl rich phases formed by the decomposition as shown in Figure 2.14.

Although the disordered Fe-rich bcc phase formed within the miscibility gap is softer compared to the ordered β-matrix, such precipitates were shown to change the slip system so that a higher shear stress is required which strengthens the alloy via precipitation hardening through a dislocation pinning effect [54, 58, 60, 62].

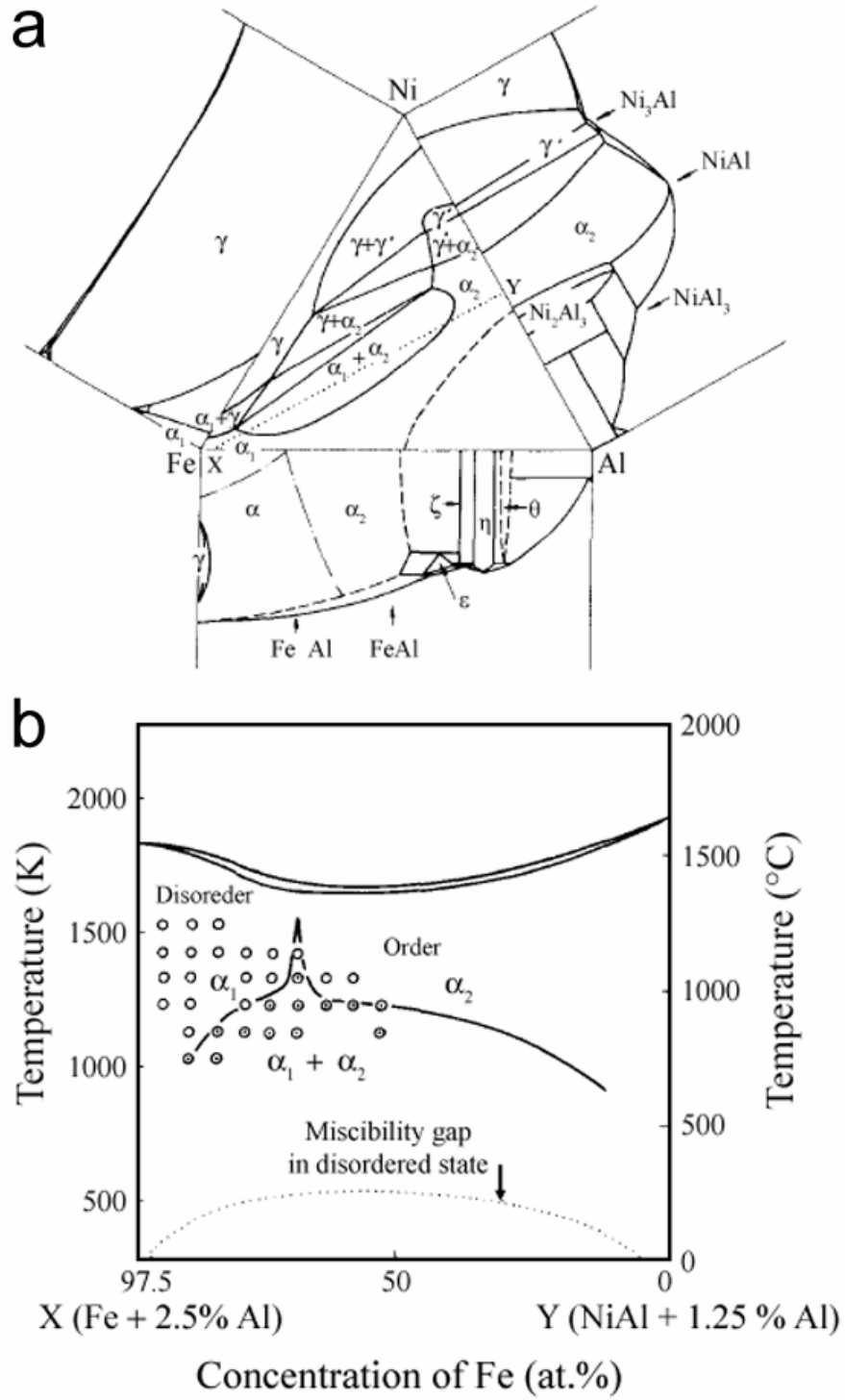

Figure 2.13 Miscibility gap between ordered and disordered bcc phases in the Ni-Al-Fe system, (a) phase equilibria at 750 °C and (b) a vertical section diagram [60, 61].

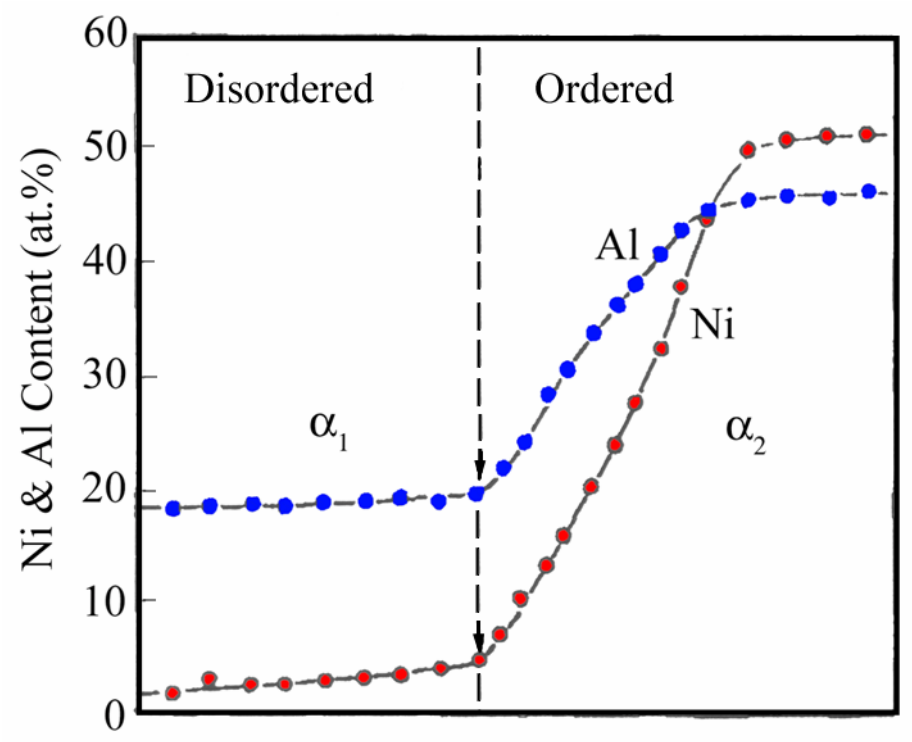

Figure 2.14 Concentration profiles of ordered NiAl and Fe-rich disordered bcc phases. Adapted from Ref. [60].

2.2 Amorphous Alloys

Glass is a general term for a material that is solidified from the melt and has gone through glass transition. Although "glass" and "amorphous solid" are often used as synonyms, a material should exhibit a measurable glass transition to conventionally call it a glass [63]. Metallic glasses are amorphous solids lacking long-range atomic order (Figure 2.15) [64] providing them with exceptional physical properties compared to their crystalline counterparts [5, 65]. Typically, metallic glasses are produced by rapid cooling from liquid or gas phase which kinetically hinders crystallization.

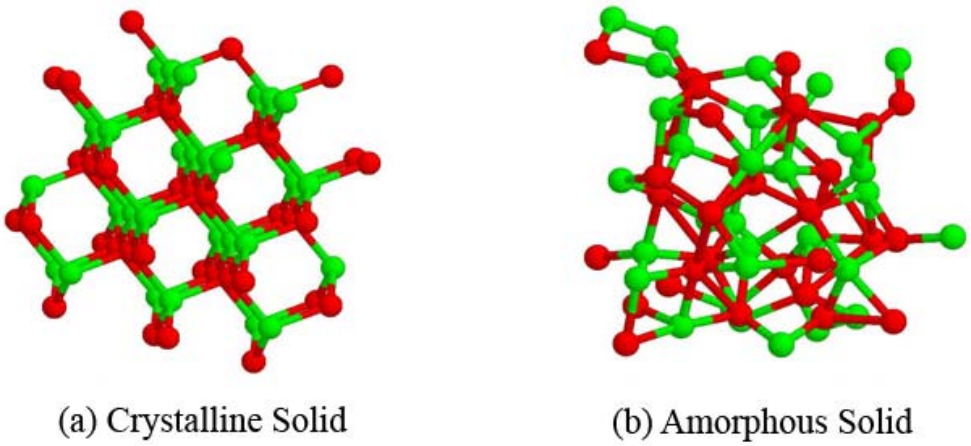

Figure 2.15 Schematic representation of (a) long range order in crystalline alloys and (b) short range order in amorphous alloys.

2.2.1 History of Metallic Glasses

The first metallic glass was discovered by Duwez and coworkers in 1960 [66]. In their study, rapidly quenched $Au_{75}Si_{25}$ alloy appeared to be amorphous due to kinetically hindered nucleation and growth processes. During late 1980's, synthesis of centimeter level bulk metallic glasses was successfully achieved by Turnbull and coworkers [67] for Pd–Ni–P alloy system. Also some solid-state amorphization techniques such as mechanical alloying, ion beam mixing, diffusion induced amorphization in multilayers, hydrogen absorption, and inverse melting had been also developed.

Following 1990s, much research effort was spent to find new alloy compositions and investigate the physical, structural, mechanical and magnetic properties of bulk metallic glass. Recently, bulk metallic glasses (BMGs) showing slower nucleation kinetics have been processed by conventional casting techniques at low cooling rates. Currently, owing to their attractive properties to materials scientists (e.g. superior specific strength, high hardness, high resistance to corrosion, oxidation and wear

[68]), the study and development of bulk metallic glasses are at the cutting edge of metal research because these materials open new opportunities for both fundamental studies and commercial applications. Owing to the relative ease of fabricating metallic glasses into bulk forms, combined with their unique properties, BMGs are attractive for possible applications in aerospace, naval, sports equipment, luxury goods, armor and anti-armor systems, electronic packaging, and biomedical devices.

2.2.2 The Glass Transition and Glass Forming Ability

A thermodynamic transition can be defined as an nth order transition when there is a jump discontinuity in the nth derivative of the Gibbs free energy is with increasing or decreasing temperature. From a thermodynamic point of view, the *glass transition* can be phenomenologically termed as a second order transition where discontinuities in the second derivates of Gibbs free energy (e.g. heat capacity and thermal expansion coefficient) are observed upon the transition as shown in Figure 2.16. However, considering glass transition, these discontinuities do not occur in a perfect manner at a defined temperature but within a (narrow) temperature range which makes the definition of glass transition as a real second-order thermodynamic transition debatable. In addition, glass transition is actually a time-dependent phenomenon where kinetic effects (e.g. heating rate) play a significant role in shifting the glass transition temperature by allowing different relaxation times for the glassy and liquid phases.

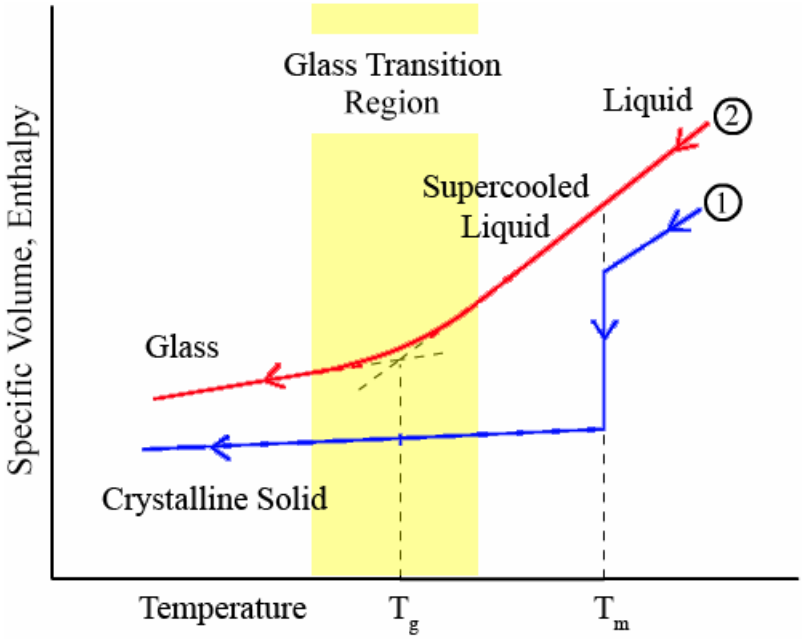

Figure 2.16 Variation of thermodynamic properties during first and second-order transitions.

The stability of the supercooled liquid state, i.e. a frozen-in liquid which bypasses crystallization during solidification, is controlled by the free energy difference of liquid and solid phases below the melting temperature of an alloy. Glass forming ability can be defined as the capability of a liquid to be undercooled into the glassy state and stabilized as solid of certain critical dimension without undergoing crystallization. Predicting the glass forming ability of metallic materials has theoretical and practical importance for the development of bulk metallic glasses. So far, various criteria have been proposed for evaluating the ease of glass formation in metallic systems. Alloys having lower critical cooling rates and larger possible bulk cross-sectional dimensions can be said to have higher glass forming ability. In this respect, the Turnbull criterion for the suppression of crystallization in undercooled melts has so far played a key role. The criteria states that a liquid with T_g/T_l= 2/3 becomes very sluggish in crystallization and can only

crystallize within a very narrow temperature range [69]. Such a liquid can thus be easily undercooled at a lower cooling rate into the glassy state.

In addition to that, following empirical rules were also put forward by Inoue and Johnson [64, 70] as; (i) multi-component alloys of increased complexity and size of crystal unit cells such that configurational entropy of the supercooled liquid phases are increased; (ii) atomic radius mismatch between elements leading to higher packing density and smaller free volume; (iii) negative heat of mixing between the elements, and, (iv) alloy composition close to deep eutectic allowing for the formation of a more stable liquid stable at low temperatures.

2.2.3 Plastic Flow and Deformation of Metallic Glasses

In general, when a stress is applied on a crystalline metallic material, upon overcoming the elastic load carrying barrier referred to as yielding, or in other words, when the critical resolved shear stress is reached on a favorable slip plane, plastic deformation occurs via dislocation motion homogenously throughout the material in an irreversible fashion. Dislocations are line defects, i.e. regions of localized lattice disturbance separating slipped and unslipped regions in a crystal. Movement of dislocations is considered to be the plasticity mechanism (slip) at almost all cases in single crystals or polycrystalline aggregates. Detailed studies have long been performed to develop the “theory of plasticity” in crystalline metals and thus it is rather well understood.

However, in contrast with crystalline metals, metallic glasses are metastable materials exhibiting no long range atomic order, i.e. absence of crystal symmetry. Therefore, they can be considered as free of crystalline defects such as dislocations, and plasticity can not take place homogenously by dislocation motion.

Understating the deformation of metallic glasses yielded separate yet converging theories of inhomogeneous deformation. Plasticity of metallic glasses is perceived to occur through (i) shear transformation zones, (ii) free volume within the glass, and (iii) hypothetical dislocations. Shear transformation zones are planar zones or what is called shear bands exerting localized distortion on the surrounding atoms. Shear strain is accommodated at these zones through localized atomic clusters undergoing intense distortion. Concept of strain accommodation on the basis of free volume model of deformation involves diffuse-like local atomic jumps into larger free volume regions. Lastly, the dislocation model of deformation in metallic glasses considers shear band fronts as dislocation lines that separating distorted and unperturbed regions. Stress intensity at the shear band front activates the shear transformation zones and causes macroscopic deformation. Regardless of by what mechanism shear bands are formed, the initiated bands are unstable due to (i) mismatch in strain rate between perturbed and unperturbed zones, (ii) strain localization within the shear bands, and (iii) adiabatic heating in the vicinity of shear bands due to local free volume perturbations.

2.2.4 Structural Relaxation in Metallic Glasses

A freshly quenched glass, prior to its glass transition, undergoes structural relaxation which involves changes in almost all of its physical properties. This relaxation phenomenon is directly related to the fundamental nature of the glassy state and also the mechanism of glass transition. Structural relaxations are closely associated with the stability of the glassy phase and crystallization processes above the glass transition.

There are a number of studies carried out on polymer glasses using techniques such as dielectric spectroscopy and dynamic thermal mechanical

analysis, vibrational spectroscopy, dilatometry and viscosity measurements. However, due to complexity of molecular structure in high molecular weight polymers which are of more significance to material scientists, fundamental studies of structural relaxation remained largely phenomenological.

On the other hand, structural relaxation of metallic glasses, although not well understood, is thought to depend on structural parameters describing local atomic environment and details of the glassy state. Within this concept, it was proposed that conservative motion of structural defects lead to reversible relaxation whereas annihilation and recombination processes lead to irreversible relaxation. Structural relaxation involves several changes in measurable physical properties such as free volume, Young's Modulus, internal energy, chemical diffusivity and electrical resistivity.

2.2.5 Crystallization of Amorphous Alloys

Metallic glasses as they are prepared are apart from configurational equilibrium and undergo slow structural relaxation towards lower energy metastable amorphous state. The latter metastable amorphous state shows inherent possibility of transformation into a more stable crystalline state. Above the glass transition temperature, crystallization starts by homogenous rather than heterogeneous nucleation since the amorphous/crystalline interface energy is quite low compared to common crystalline materials.

Crystallization of amorphous alloys are generally complicated and do not occur by polymorphous crystallization of a single phase without involving concentration changes. Depending on the alloy composition, amorphous to crystalline transformation typically occur by primary or eutectic crystallization reactions as shown by the schematic diagram in Figure 2.17.

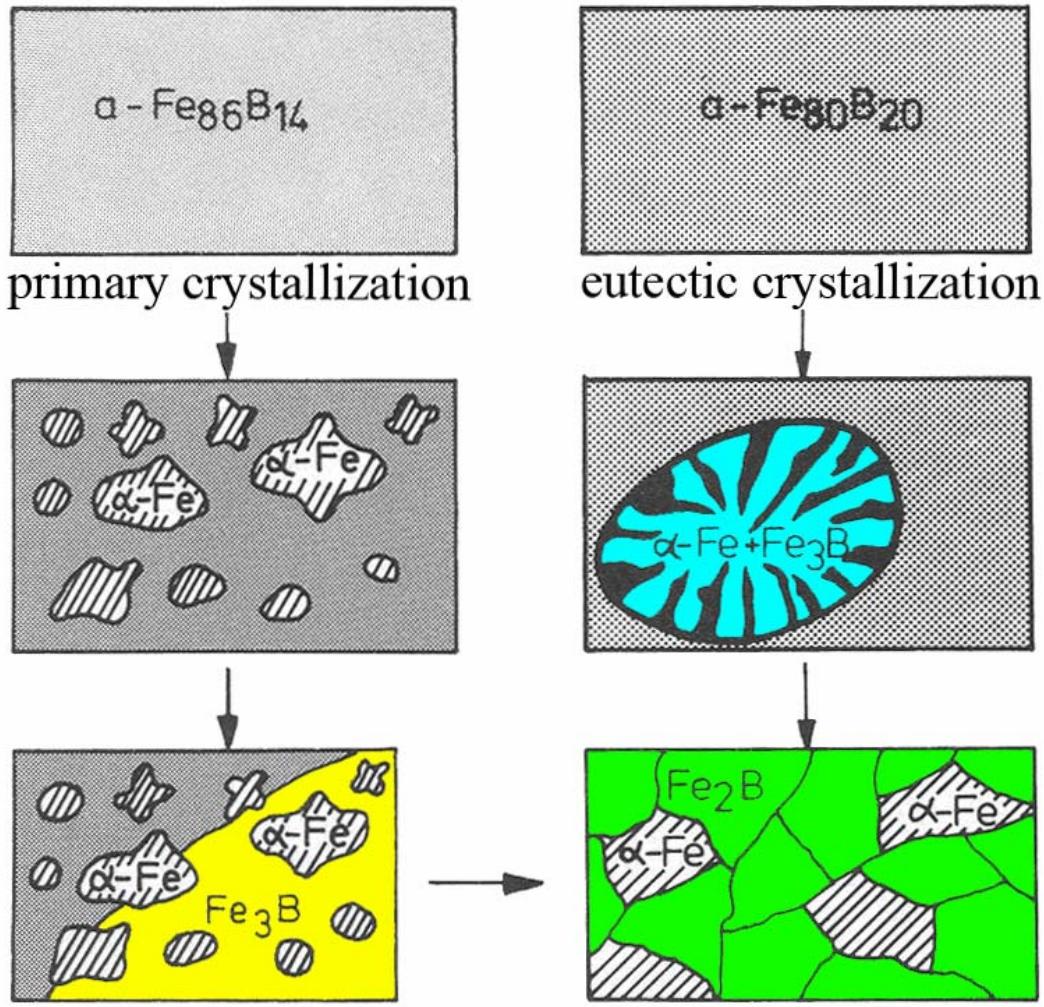

Figure 2.17 Schemes for primary and eutectic crystallization reactions from the amorphous state. Adapted from Ref.[71].

Primary crystallization is a continuous process which proceeds by solute enrichment of the parent amorphous phase until a metastable equilibrium between the primary crystals and the amorphous matrix is established. The eutectic crystallization, on the other hand, occurs by simultaneous formation of two crystalline phases via a discontinuous reaction where primary crystals can act as nucleation centers for both phases.

The transition from amorphous to crystalline state can be tracked by changes in physical properties such as electrical resistivity and saturation magnetization as well as in-situ transmission electron microcopy and X-ray diffraction experiments.

2.2.6 Magnetic Properties of Amorphous and Nanocrystalline Alloys

Magnetic properties of amorphous alloys can be thought to reflect the characteristic of short-range ordering of crystalline counterpart with same chemical composition. Therefore, similar rules will govern their magnetic behavior, yet averaged for randomness. In conventional ferromagnetic materials, saturation magnetization shows a gradual decrease with temperature since atomic thermal vibrational motions are opposing the coupling interactions of atomic magnetic moments which cause misalignment of the magnetic dipole. Magnetization of amorphous alloys is more dependent on temperature than in crystalline alloys, since exchange interactions can be thought to be spread throughout the material due to the amorphous structure. The absence of domain wall pinning grain boundaries or precipitates makes the amorphous alloys show extremely low coercivities. Coercivity goes to a minimum where magnetostriction, i.e. elastic change in dimensions with state of magnetization, ceases. This can be realized either by selecting appropriate alloy composition or low temperature annealing processes to allow for structural relaxation of the glass.

Apart from composition, texture, residual stress and grain shape anisotropy, grain size and its distribution are among the most important factors affecting magnetic properties of polycrystalline ferromagnetic materials. Considerable changes in magnetic behavior are expected when crystallite size approaches the ferromagnetic exchange interaction length. Due to the structural disorder of the interfaces, atoms lying on nanocrystal interfaces possess lower magnetic moment to those inside the bulk of the crystals. A decrease in the grain size in the nanometer range would result in strongly size dependent coercivity where ultimate soft magnetic properties are obtained with crystallite thicknesses below a critical value of about 20 nm. In that case, the local magnetocrystalline anisotropy would lead to coercivity similar to that in amorphous alloys. Ferromagnetic to superparamagnetic transition could also be expected when grain sizes are smaller than a critical value for single magnetic domain formation.

2.2.7 Fe-based Bulk Metallic Glasses

Starting from the early 1990's, there had been tremendous interest on the structure and properties of Pd-, Zr-, Ln-, and Mg- based bulk metallic glasses due to their high glass forming ability and wide supercooled liquid region. In those systems, the maximum diameter of the bulk amorphous alloy that can be produced can reach up to 70 mm and critical cooling rates can be as low as 10^{-1} K/s. The beginning of the new century evidenced considerable attention to extend bulk amorphous alloy systems to cheaper ferrous alloy systems owing to their outstanding soft magnetic behavior [7, 8], excellent corrosion resistance [9, 10], and superior tensile strength [11, 12] for potential structural applications. Figure 2.18 compares the mechanical properties of different bulk metallic glass systems where Fe- and Ni-based systems readily outperform the other known systems.

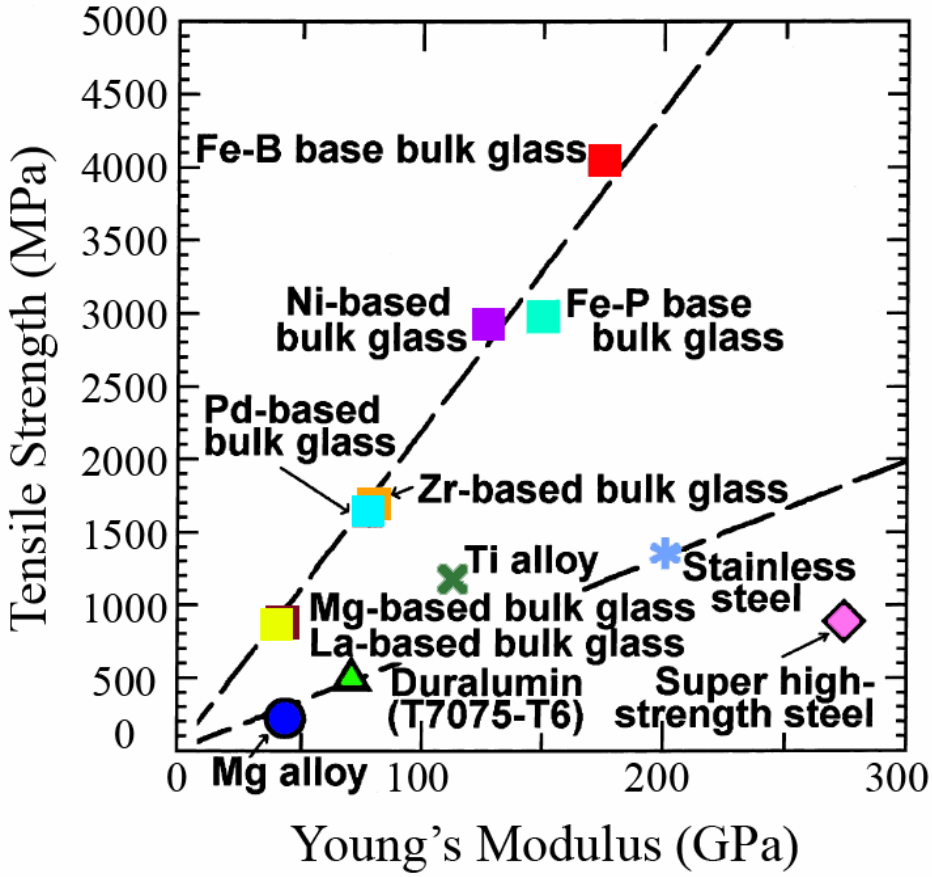

Figure 2.18 Mechanical properties of bulk metallic glasses. Adapted from Ref.[72].

Amorphous alloys are thermodynamically unstable, therefore, a series of changes ascribed to structural relaxation and crystallization occur by annealing [73]. Much of the recent research effort is to tailor the properties of metallic glasses through controlled crystallization of the amorphous precursor. The desired amorphous matrix nanocrystalline structure was obtained in a few glass forming composition classes as; FeZrB(Cu) named as NANOPERM [74, 75], FeCoZrB(Cu) named as HITPERM [76, 77], and FeSiBNbCu named as FINEMET [78]. Among those ferrous alloys, metallic glasses based on the Fe-Si-B FINEMET system [79, 80] proved to be one of the most promising systems demonstrating excellent magnetic properties

such as high permeability, low coercivity and high saturation magnetization as shown in Figure 2.19.

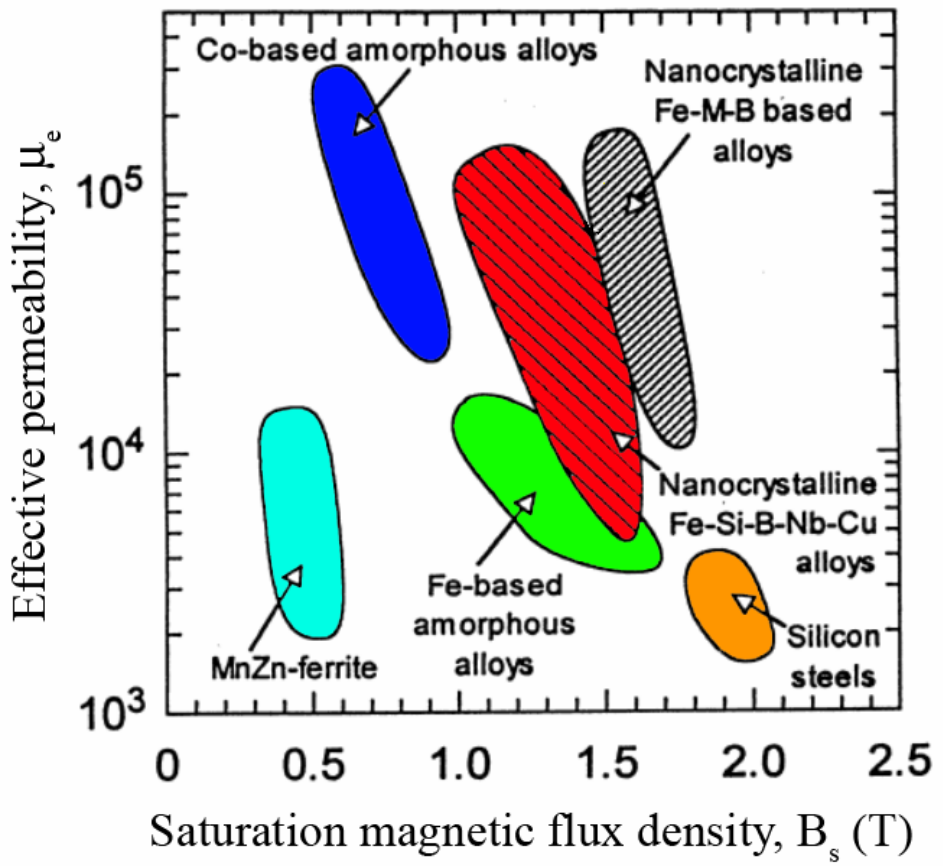

Figure 2.19 Comparison of saturation magnetization and permeability for different types of amorphous and nanocrystalline soft magnetic alloys. Adapted from Ref.[81].

Afterwards, a variety of alloying additions were employed in the Fe-Si-B system to modify glass forming ability as well as nucleation and subsequent growth behavior of crystalline phases. The incorporation of transition metals such as Nb into the Fe-Si-B systems was reported to increase glass forming ability and impede crystallite growth [82, 83] while Co substitution for Fe led to higher Curie temperature for both the amorphous matrix and primary

crystals [84-86]. Additionally, Ni substitution for Co was shown to improve mechanical properties through enhanced shear band formation [87]. Fe-Si-B-Nb alloys that contain a small amount of Cu display ultrafine microstructure of primary crystals inside an amorphous matrix through heterogeneous nucleation effect of Cu clusters formed during structural relaxation of the glass prior to its crystallization [88].

CHAPTER 3

EXPERIMENTAL PROCEDURE

3.1 Raw Materials

In this thesis, high purity elements obtained from Alfa Aeaser were used as alloy constituents. Compositional purities of alloying elements are given in Table 3.1.

Table 3.1 Compositional purity of alloying elements (wt.%).

Element	Grade (wt.%)
Al	99.90
B	99.50
Co	99.90
Cu	99.90
Fe	99.97
Nb	99.60
Ni	99.95
Si	98.50

Studied alloy compositions are classified into three groups as *(i)* $Ni_{50}Fe_xAl_{50-x}$ alloys with varying Fe content (Table 3.2), *(ii)* 3d transition metal microalloyed $Ni_{50}Al_{25}Fe_{24}X_1$ alloys where X = Co, Mn, and V (Table 3.3), and, *(iii)* $[(Fe_{43}Co_{28-x}Ni_x)B_{20}Si_5Nb_4]_{100}Cu_1$ bulk glass forming alloys with varying Ni content (Table 3.4). The alloy compositions of intermetallics were selected based on single phase and two phase regions of the corresponding ternary phase diagram (Figure 2.11) and lattice site preference of the quaternary alloying elements. The compositions of glass forming alloys were chosen according to their high bulk glass forming ability and high thermal stability of the supercooled liquid.

Table 3.2 Chemical compositions (at.%) of NiAl based intermetallics with varying Fe content.

Alloys	Chemical Compositions		
	Ni	Al	Fe
N1	75	25	
N2	50	50	
N3	50	30	20
N4	50	25	25
N5	50	20	30

Table 3.3 Chemical compositions (at.%) of microalloyed Ni-Al-Fe alloys.

Alloys	Chemical Compositions					
	Ni	Al	Fe	Co	Mn	V
N6	50	25	24	1		
N7	50	25	24		1	
N8	50	25	24			1

Table 3.4 Chemical composition (at.%) of Fe-based amorphous alloys.

Alloys	Chemical Compositions						
	Fe	Co	Ni	B	Si	Nb	Cu
ND1	43	9	19	20	5	4	1
ND2	43	14	14	20	5	4	1
ND3	43	19	9	20	5	4	1

3.2 Fabrication of Samples

Samples were produced by first arc-melting and then suction casting whenever required. Samples were then cut standard specimen dimensions using linear precision saw and annealed at appropriate temperatures.

3.2.1 Arc Melting

Master alloys with designed compositions were prepared from high purity elements by arc melting (Edmund Bühler Arc Melter) under zirconium-gettered argon atmosphere (Figure 3.1). Alloyed ingots were re-melted for four times to ensure chemical homogeneity. The arc melting device consists of a high frequency tungsten inert gas DC welding machine connected to a melting chamber with grooved and water cooled copper tray. The chamber vacuum is supplied by a rotary pump and a diffusion pump which can evacuate the chamber down to pressures below 10^{-5} mbar. In a typical procedure, three evacuation processes are followed by high purity argon flushing to completely prevent selective oxidation of alloying elements and to ensure compositional accuracy.

Figure 3.1 Fabrication of alloys by arc melting.

3.2.2 Rapid Solidification by Suction Casting

The pre-alloyed ingots from each studied composition were used for the fabrication of cylindrical rods with a length of 30 mm and diameters of 1–2 mm by suction casting (Edmund Bühler Compact Arc Melter with suction casting option) into a water cooled copper mold (Figure 3.2). Suction casting was used to prepare mechanical test specimens for NiAl based intermetallics and to achieve high cooling rates necessary for glass formation in Cu-modified Fe-Co-Ni-B-Si-Nb alloys.

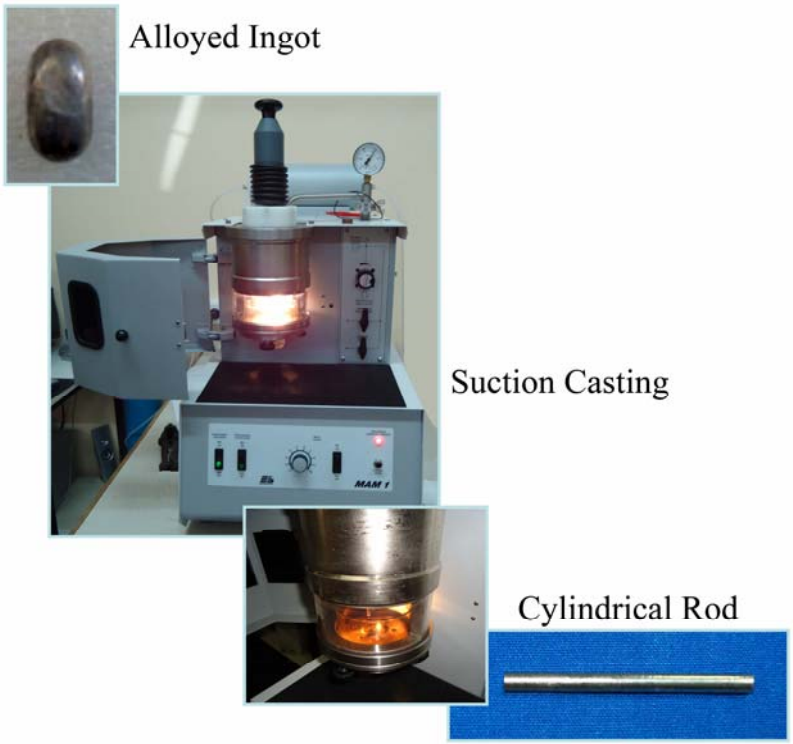

Figure 3.2 Specimen production by suction casting.

3.2.3 Cutting Procedure

In order to prepare specimens for characterization and testing, several slices were cut into required dimensions using a linear precision saw (Buehler IsoMet 5000).

3.2.4 Annealing Procedure

One sample from each alloy was labeled "as-cast". The remaining samples were labeled as "annealed" and placed into quartz tubes filled with argon gas. The alloys were annealed in muffle furnaces at different selected temperatures with ± 5 °C error followed by air cooling.

3.3 Characterization Techniques

In this thesis, various characterization tools were utilized to reveal the microstructural evolution, precipitation and crystallization phenomena, thermal characteristics, magnetic properties and mechanical behavior of studied alloys.

3.3.1 X-ray Diffractometry

Structural characterizations were done via X-ray diffraction (XRD) analysis on a horizontal goniometer device (Rigaku D/MAX 2200 Diffractometer) with Bragg-Brentano focusing optics operating in the $\theta - \theta$ scanning mode. Measurements were done using monochromatic CuKα radiation (40 kV, 40 mA) by continuous scanning over the diffraction angle range $20º < 2\theta < 100º$

with a scanning rate of 2°/min, and step size of 0.02°. Intermetallic alloys were analyzed in bulk slice forms and amorphous alloys in suction-cast rod forms. XRD analyses were performed for qualitative phase identification in intermetallics and annealed amorphous alloys, and also to ensure that bulk glass forming compositions lack long-range atomic order in their as-cast states.

3.3.2 Scanning Electron Microscopy

Microstructural investigations were done using a JEOL JSM 6400 type scanning electron microscope (SEM) and a FEI Nova NanoSEM 430 field-emission gun SEM. NiAl based intermetallic alloys were polished and etched in the following solution: 400 ml hydrochloric acid, 100 ml nitric acid, 100 ml glycerin, 100 ml distilled water, 25 g ferric chloride and 25 g cupric chloride, which was found to yield excellent microstructural resolution. Arc-melted amorphous alloys - prior to suction casting - were polished and etched in nital solution (2% nitric acid) for 2 minutes to observe microstructural features. SEM samples for amorphous alloys - after suction casting - were polished and etched in nital solution (2% nitric acid) for a sufficiently long period (~5 min) to confirm featureless microstructure. The actual chemical compositions of the alloys and compositions of constituent phases in alloys were determined by energy dispersive X-ray spectroscopy attached to scanning electron microscopes (SEM-EDS). Relative amounts (volume fractions) of dendritic and interdendritic regions in intermetallics were analyzed according to the systematic manual point count procedure described in ASTM E562 standards.

3.3.3 Transmission Electron Microscopy

Transmission electron microscopy investigations of intermetallic and amorphous alloys were conducted using a JEOL JEM 2100F type field-emission high-resolution transmission electron microscope operated at 200 kV acceleration voltage. For transmission electron microscopy (TEM) studies of intermetallic alloy samples, precision cut thin foils were first punched to 3 mm diameter discs, ground using SiC paper and finally polished to below 100 μm thickness. The prepared disc shaped foils were dimpled (Fischione Instruments Model 200) followed by twin-jet electropolishing (Fischione Instruments Model 110) in an electrolyte composed of 10 % perchloric acid rest methanol at a temperature of −55 °C and an applied voltage of 11 V. For TEM studies of the amorphous alloy, disc shaped thin foil specimens with 2 mm diameter were reduced to below 100 μm thickness and placed into oyster copper grids. Twin-jet electropolishing was carried out in a solution of 33% nitric acid in methanol at a temperature of -25 °C. All TEM specimens were finally plasma-cleaned (Fischione Instruments Model 1020) prior to transmission electron microscopy investigations.

Several selected area electron diffraction (SAED) single crystal patterns were obtained from different crystallographic zone axes by double-tilting the specimens in TEM according to indexed Kikuchi maps provided in Appendix A. SAED patterns were appropriately labeled using standard single crystal spot patterns given in Appendix B and by constructing corresponding stereographic projections for each zone axis. Superlattice dark field TEM images were recorded by tilting the specimen to the required zone axis and choosing the superlattice reflection which provides the best diffraction contrast. Chemical compositions of observed phases were determined using energy dispersive X-ray spectroscopy attached to the transmission electron microscope (TEM-EDS).

3.3.4 Differential Scanning Calorimetry

Heat flow during heating and cooling was measured by a differential scanning calorimeter (DSC) under flowing high purity argon using a Setaram Setsys 16/18 thermal analyzer (Figure 3.3). Crystallization process of the bulk amorphous alloy was characterized by linear heating runs from room temperature to 1700 K to obtain a set of DSC scans with heating rates ranging from 5 to 40 K/min. Small samples (~15–20 mg) of similar weights were analyzed to avoid sample size effects and to ensure temperature homogeneity throughout samples during DSC analysis.

Figure 3.3 The differential scanning calorimeter used in thermal analysis.

3.3.5 Vibrating Sample Magnetometry

Magnetic properties of alloys, isothermal kinetics of precipitation in intermetallics alloys and crystallization in amorphous alloys were determined using a vibrating sample magnetometer (VSM, ADE Magnetics EV9) shown in Figure 3.4. The Curie transition temperature (T_C) was determined as the minimum point of the temperature derivative of magnetization, dM/dT. Both temperature scan and time dependent (isothermal) magnetization measurements were performed under 500 Oe applied magnetic field. For the kinetics of ferromagnetic phase precipitation in intermetallic alloys, temperature-scan measurements were carried out from room temperature to 973 K at a scan rate of 5 K/min whereas isothermal magnetization experiments were carried out at various temperatures ranging from 750 to 950 K with 25 K increments. Magnetization was measured every 5 K during temperature-scan experiments and every 3 min. during isothermal annealing. For the isothermal kinetics of crystallization in amorphous alloys, temperature scans were recorded within a temperature range from room temperature to 1023 K at a scan rate of 5 K/min. Isothermal runs were performed by first heating the amorphous specimens with a ramp rate of 50 K/min to the prescribed temperatures ranging from 800 K to 875 K where constant annealing periods of 4 h were allowed. Magnetic moments were recorded every 5 K during temperature-scan experiments and every 30 s during isothermal experiments.

Figure 3.4 The vibrating sample magnetometer used for magnetization measurements.

3.3.6 Microhardness Measurements

Vickers microhardness measurements (Hv 0.025) were performed phase-selectively on as-cast and annealed samples by an automated microhardness tester (Shimadzu HMV-2) with an indenter load of 25 g. Averages of microhardness values were reported from at least eight indentations for each specimen.

3.3.7 Mechanical Testing

Room temperature compressive properties of as-cast and annealed alloys were determined on a universal testing machine (Instron 5582, 100 kN) at a constant cross-head speed of $5x10^{-5}$ s^{-1} according to ASTM E9 - 09 standards. Compression test specimens (Figure 3.5) with 2 mm diameter and 3 mm length were cut from suction-cast cylindrical rods by precision cutter and polished prior to testing.

Figure 3.5 Compression test specimens.

CHAPTER 4

MAGNETIC MONITORING APPROACH

4.1 Isothermal Transformation Kinetics

Any extensive rearrangement of atomic structure where the general sense of driving force for such rearrangement is the change in the Gibbs free energy associated with the process can be termed as a *phase transformation*. The spontaneity of a phase transformation will rely on how the free energy of the system is affected by small fluctuations, and, one may consider the energy barrier against transformation of a system towards lower energy state as the atomic diffusion barrier termed as the *activation energy*.

Phase transformations usually start by nucleation of defined centers encountering significant atomic rearrangement within confined volumes. The free energy barrier against nucleation constitutes a negative free energy change term due to the generation of a thermodynamically more stable phase by the transformation and a positive free energy term due to the penalty in forming a new interface between the forming phase and the parent decomposing phase.

In the cases where there is small gain in interfacial energy associated with the nucleation of a new phase, critical nuclei size approaches zero meaning that the transformation occurs simultaneously in all parts of the former phase, which is termed as the *homogenous transformation*. This condition is actually realized for transformations where there exists a diffuse and low energy phase boundary between the newly forming and decomposing phases which could actually be possible for nucleation of a new phase with similar

structure but different composition or lattice parameter compared to the decomposing phase. Examples of such homogenous transformations are decomposition reactions of supersaturated solid solutions and some order-disorder changes.

Most metallurgical reactions are considered as *heterogeneous transformations* meaning that the decomposing regions are microscopically distinguishable during the transformation. In heterogeneous transformations occurring by nucleation and growth, the nucleated phase grows at the expense of the parent phase by atomic jumps at the interphase boundary. Phase transformations occurring by *interface-controlled growth* are those where the rate of growth of the nucleated phase is controlled by atomic jumps only in close vicinity of the interface between two phases, i.e. when the overall growth rate is controlled by the mobility of the interface. On the contrary, heterogeneous transformations taking place via *diffusion-controlled growth* involve long-range transport of atoms towards or away from the growing phase during the course of transformation. For phase transformations where there is appreciable concentration difference between the newly formed phase and the decomposing phase, it is likely that the overall process is dominated by diffusion-controlled growth of nuclei since it requires a large number of jumps per atom to diffuse through long ranges.

The study of kinetics in solid state processes such as phase transformations, crystallization or crystal-growth and precipitation reactions often utilizes the classical Johnson-Mehl-Avrami-Kolmogorov (JMAK) model [89-92] which describes the evolution of transformed volume fraction by;

$$X_t = 1 - \exp(-k(t - t_0)^n) \quad (1)$$

where,

X_t : transformed fraction at time t

k : rate constant

n : Avrami exponent

t_0 : incubation time

Rearranging the JMAK relation yields;

$$\ln(-\ln(1 - X_t)) = n \ln k + n \ln(t - t_0) \quad (2)$$

Provided that the kinetic process of precipitation obeys JMAK theory, double natural logarithmic plot of $1/(1-X_t)$ versus $\ln t$ plot should give a straight line having the slope n and the intercept $n\ln K$. Isothermal transformations which obey $n = 1$ are equivalent to first-order homogenous reactions while values of n other than unity will give sigmoidal shapes with a characteristic slow kinetics at early stages, maximum rate of transformation in intermediate stages and again slowing down kinetics towards the completion of transformation.

It is known that JMAK model constitutes a reasonable approximation for the growth regime, and, analysis of the Avrami exponent provides useful information on the mechanism and geometry of growing precipitates. From a practical point of view, the Avrami exponent from JMAK theory can practically be interpreted by considering;

$$n = i + d.g \tag{3}$$

where,

i: nucleation index reflecting nucleation rate relative to growth
d: dimensionality of growth (geometrical term)
g: growth index reflecting the governing growth mechanism

The nucleation index $i = 0$ corresponds to instantaneous nucleation at all available nucleation centers, $0 < i < 1$ represents decreasing nucleation rate throughout transformation, $i = 1$ corresponds to constant nucleation rate throughout transformation. The growth index is restricted to $g = 1$ for interface-controlled growth and surface reaction controlled growth, or $g = 0.5$ for diffusion-controlled growth. The geometrical term can assume integer values $d = 1$, 2, or 3 corresponding to 1-dimensional (cylinders, needles), 2-dimensional (plates) and 3-dimensional (spherical) growth of nuclei, respectively. A very useful scheme for the interpretation of Avrami exponents to understand phase transformation mechanisms is provided by Christian [93] in Table 4.1.

Table 4.1 Interpretation of Avrami exponents.

Interface controlled growth	**Avrami Exponent**
Increasing nucleation rate	> 4
Constant nucleation rate	4
Decreasing nucleation rate	3 – 4
Zero nucleation rate	3
Grain edge nucleation after site saturation	2
Grain boundary nucleation after site saturation	1

Diffusion controlled growth of precipitates	**Avrami Exponent**
All shapes growing from small dimensions with increasing nucleation rate	> 5
All shapes growing from small dimensions with constant nucleation rate	$2\frac{1}{2}$
All shapes growing from small dimensions with deceasing nucleation rate	$1\frac{1}{2} - 2\frac{1}{2}$
Growth of precipitates with appreciable initial volume	$1 - 1\frac{1}{2}$
Needles and plates of finite dimensions	1
Thickening of very large plates after complete edge impingement	$\frac{1}{2}$
Thickening of needles after complete end impingement	1
Precipitation on dislocations (very early stages)	$\frac{2}{3}$

It has to be noted that the Avrami exponent n should be independent of extent of transformation unless a change in growth geometry, growth index and nucleation index occurs over the course of transformation. Provided that transformation mechanism does not vary throughout the process, slopes of Ln(-Ln(1-X_t)) vs. Ln(t-t_0) plots are taken as an overall value for Avrami exponent (n) as stated above.

However, a constant Avrami exponent throughout whole transformation is not essentially observed for some real cases of phase transformations where significant alterations in the linearity of Avrami plots were observed along the course of transformation. Therefore, determination of local Avrami exponent, $n(X)$, is essential to track the evolution of transformation mechanism throughout the entire process. Isothermal transformation curves can be utilized to calculate the local Avrami exponent, $n(X)$, using Equation (4).

$$n(X) = \frac{\mathrm{d}\left(\mathrm{Ln}\left[-\mathrm{Ln}\left(1-X\right)\right]\right)}{\mathrm{d}\left[\mathrm{Ln}(t\text{-}t_0)\right]} \tag{4}$$

Furthermore, it is possible to estimate the activation energies for a phase transformation using the classical JMAK theory. Imposing an Arrhenius temperature dependence of the rate constant k (Equation 5), different isothermal temperatures can be employed to obtain an overall the activation energy (Q_a) employing the relation;

$$k = k_0 \cdot \exp\left(\frac{-Q_{\mathrm{a,overall}}}{R \cdot T}\right) \tag{5}$$

and by constructing ln$k$ vs. 1/T plots where the slope is -Q_a/RT.

The local activation energy, $Q_a(X)$ can also be calculated using Equation (6) for each transformed fraction by utilizing an Arrhenius thermal dependence of time required to attain a chosen transformed fraction at different isotherms, by taking the slopes $\ln(1/t)$ vs. $(1/T)$ plots.

$$t_{X_t}^{-1} = A \cdot \exp\left(\frac{-Q_a(X)}{R \cdot T} \right) \tag{6}$$

4.2 Isothermal Magnetic Monitoring

One of the most reliable methods for determining magnetization of materials depends on the principle of voltage generated in a coil by a varying magnetic flux. In the vibrating sample magnetometer, magnetic field is measured at a fixed distance from the sample to obtain the magnetic moment of the sample. The principle of measurement relies on varying the field at the coil at the same frequency of an oscillating sample with fixed frequency and small amplitudes. By this means, an AC voltage is produced in the coil which is then converted into a DC signal being proportional to the magnetic moment of the sample. Apart from the disadvantage of small sample sizes, the vibrating sample magnetometer is quite sensitive and versatile allowing for isochronal and isothermal measurements in wide temperature ranges.

Isothermal transformation curves which relate the transformed volume fraction to the time allowed for transformation can be obtained by various experimental techniques such as conventional thermal analysis, careful microscopy combined with image analysis or by measuring changes in electrical resistivity, specimen volume and relative intensities of diffraction lines caused by the phase transformation.

In this thesis, a novel magnetic monitoring approach via vibrating sample magnetometry approach was implemented to the classical JMAK theory to study the kinetics of phase transformations in intermetallics and nanocrystallization in amorphous alloys. In order to analyze transformation kinetics by magnetic monitoring, it is essential that measurable changes in overall magnetic moment are observed as transformation proceeds through a process where newly forming phase shows a distinct temperature dependence of magnetization relative to the decomposing phase. For instance, precipitation of second phase particles with remarkably higher Curie transition temperature relative to the decomposing phase can be given as a widely applicable area where magnetic monitoring could be successfully employed by tracking overall magnetic moments above the Curie transition of the decomposing phase.

In the proposed magnetic monitoring approach, measured values of time dependent magnetization under an applied magnetic field can be implemented in the JMAK theory by relating the fraction transformed X_t to magnetization at time t during annealing (M_t), initial magnetization (M_i) and final magnetization or magnetization at infinite time (M_f or M_∞) as described by the following Equation (7) [103]:

$$X_t = \frac{M_t - M_i}{M_\infty - M_i} \tag{7}$$

An important point to note in this approach is the method used to estimate the value for final magnetization. The experimentally obtained time dependence of magnetization was first least square fit to an exponential rise function and then extrapolated to a sufficiently long time (~8 h). By this means, the maximum attainable fraction of precipitates, taken as $\alpha_t = 1$, is assumed to be reached at such long isothermal holding times, as illustrated in Figure 4.1.

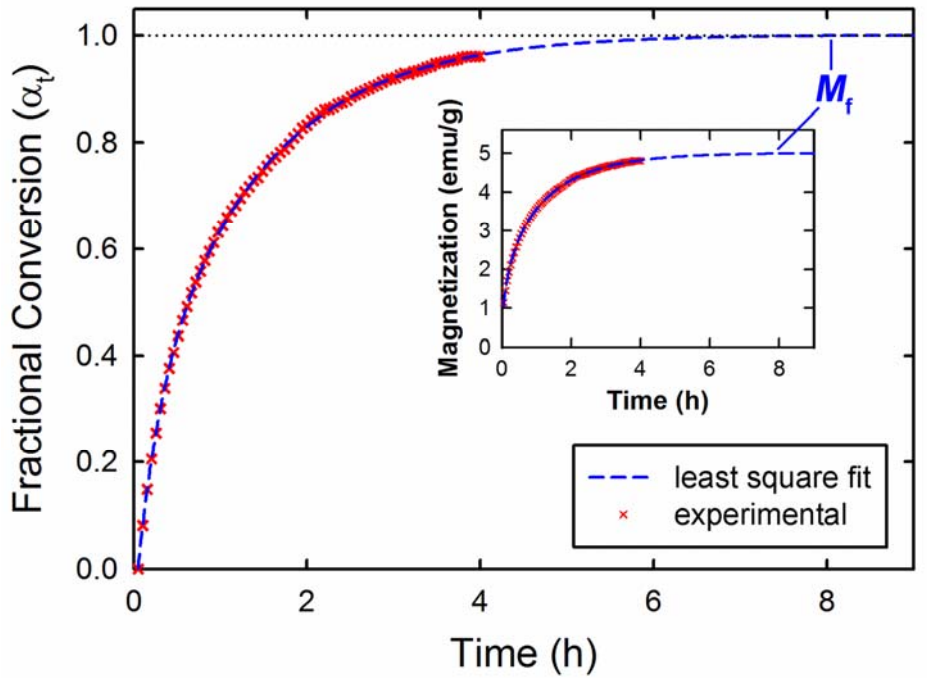

Figure 4.1 An example illustrating the estimation procedure of maximum magnetization (M_f) values using experimentally determined time-dependent magnetization in VSM.

4.3 Non-Isothermal Transformation Kinetics

As an alternative to isothermal analysis of transformation kinetics, conventional isochronal (non-isothermal) thermal analysis approach can be employed which can also yield local Avrami exponents. Non-isothermal techniques are much easier and faster, and yield higher signal-to-noise ratio especially when high heating rates are employed. However, applicability of non-isothermal models to derive local transformation kinetics is questionable since most non-isothermal models are developed based on assumptions that are valid for isothermal regimes.

The transformation rate and transformed fraction can be calculated from non-isothermal heat flow curves through Equation (8) after subtraction of the baseline,

$$\frac{dX_{\mathrm{t}}}{dt} = \frac{d\left(\dfrac{\Delta H}{\Delta H_{\mathrm{total}}}\right)}{dt} = \frac{\phi}{\dfrac{1}{\beta}\displaystyle\int_{T_i}^{T_f} \phi dT} \tag{8}$$

where ϕ is the heat flow, ΔH is the enthalpy change of the process and β is the heating rate.

An adequate way of treating transformation kinetics by non-isothermal approaches lies on the "isokinetic assumption". The isokinetic assumption requires that nucleation and growth rates have same temperature dependence and the transformation is independent of thermal history. Considering the concept of additivity by Cahn [13], the isokinetic assumption is also satisfied when saturation of nucleation sites occurs at early stages during transformation and the growth rate depends only on temperature.

Generalization of the JMAK model to non-isothermal processes was realized by Nakamura et al. [94, 95] under the isokinetic approximation. On this basis, a direct extension of JMAK model to non-isothermal processes has been successfully implemented by Blázquez et al. [96] which yields the local Avrami exponent, $n(X)$, through Equation (9). This direct extension of JMAK is capable of extracting $n(X)$ from a single non-isothermal DSC run, provided that an overall activation energy is estimated for the process.

$$\frac{\mathrm{d}(\mathrm{Ln}[-\mathrm{Ln}(1-X_{\mathrm{t}})])}{\mathrm{d}(\mathrm{Ln}[(T-T_0)/\beta])} = n\left(X\right)\left[1+\frac{Q_a}{RT}\left(1-\frac{T_0}{T}\right)\right] \tag{9}$$

The well known Ozawa equation (10) is also capable of giving local Avrami exponent but as a function of temperature, $n(T)$ by simply taking the slope of Ln[-Ln(1-$X(T)$)] vs. Ln(1/β) at a given temperature for different β values.

$$\mathrm{Ln}\left[-\mathrm{Ln}\left[1-X\left(T\right)\right]\right]=Ln\left[Z\right]-Q_{\mathrm{a}}/RT-n\left(T\right)\mathrm{Ln}\left[\beta\right] \qquad (10)$$

Apart from local Avrami exponents, it is also possible to obtain reliable estimations of overall activation energy for phase transformations via non-isothermal measurements. Most of the non-isothermal approaches are based on the hypothesis that at some temperature (e.g. the peak temperature, T_{p}), transformation rate is maximum, i.e. $\left(\mathrm{d}^2X_{\mathrm{t}}/\mathrm{d}t^2\right)=0$. Based on this hypothesis, an overall activation energy $Q_{\mathrm{a,overall}}$ can be derived by selecting an appropriate temperature on each non-isothermal DSC curve. Among the non-isothermal methods are those proposed by Ozawa [97] given by Equation (11), Kissinger [98, 99] by Equation (12), Gao-Wang [100] by Equation (13), and Augis Bennett [101] by Equation (14).

$$\frac{d\left(Ln\left[\beta\right]\right)}{d\left(1/T_{\mathrm{P}}\right)}=-\frac{Q_{\mathrm{a,overall}}}{R} \qquad (11)$$

$$\frac{d\left(Ln\left[\beta/T_{\mathrm{P}}^{2}\right]\right)}{d\left(1/T_{\mathrm{P}}\right)}=-\frac{Q_{\mathrm{a,overall}}}{R} \qquad (12)$$

$$\frac{d\left(Ln\left[\left(dX/d_{\mathrm{t}}\right)_{\mathrm{P}}\right]\right)}{d\left(1/T_{\mathrm{P}}\right)} = -\frac{Q_{\mathrm{a,overall}}}{R} \tag{13}$$

$$\frac{d\left(Ln\left[\beta/\left(T_{\mathrm{P}} - T_0\right)\right]\right)}{d\left(1/T_{\mathrm{P}}\right)} = -\frac{Q_{\mathrm{a,overall}}}{R} \tag{14}$$

CHAPTER 5

INTERMETALLIC COMPOUNDS

The important phenomenon of α-phase precipitation responsible for strengthening of Ni–Al–Fe alloys in particular at high temperatures requires a convenient annealing heat treatment in order to form desirable precipitates. Therefore, the main aim of this study is to reveal the temperature dependence and thermal stability of α-Fe phase precipitates in $Ni_{50}Fe_xAl_{50-x}$ alloys with varying Fe contents of x=20, 25 and 30 at.%. For this purpose, a non-conventional characterization tool was used which exploits the ferromagnetic character [102] of the precipitating phase. The precipitation of ferromagnetic α-Fe is monitored by examining the changes in magnetization during continuous heating experiments and room temperature magnetization measurements following annealing heat treatments at various temperatures.

Magnetic monitoring approach has rarely been used to address such precipitation reactions occurring at the nanoscale in intermetallics [102, 103].

In light of the above, this study discusses the ductile γ-phase formation and α-Fe precipitation with a major addition of Fe in NiAl intermetallic compounds. The microstructural evolution of $Ni_{50}Fe_xAl_{50-x}$ alloys with iron contents of x=20, 25, and 30 is investigated to define favorable annealing temperatures that promote γ-phase formation. Moreover, while α-Fe phase precipitation is revealed and discussed based on magnetic characterization, transmission electron microscopy is used for examining such nano-sized

precipitates. Lastly, hardening effect of α-Fe precipitates is quantified in conjunction with the microstructure of studied alloys.

Most improtantly, the long term performance of Ni–Al–Fe alloys at high temperatures is strongly dependent upon the mechanical property enhancement by such decomposition of ordered and disordered regions within the B2 phase. From a general point of view, while very fine precipitates provide the largest strengthening effect, a balance between strength and ductility can be attained with relatively coarser precipitates. However, for long-term applications, evolution of α precipitates at high temperatures should be clarified in order to determine an upper limit where the microstructure coarsens resulting in reduced strength. A convenient annealing heat treatment is also essential to form desirable precipitates. Therefore, in addition to its temperature dependence, kinetic aspects and mechanism of nanoscale α-phase precipitation in Ni–Fe–Al alloys have attracted considerable interest [104]. However, determination of time and temperature dependent changes in these nanoscale precipitates using high-resolution electron microscopy is quite laborious and requires extensive image analysis.

In a few studies, magnetic monitoring approach was implemented to replace conventional thermal analysis as a tool to successfully reveal crystallization kinetics in amorphous-matrix nanocrystalline alloys. For instance, Luborsky [105] attempted to model the time and temperature dependent changes in magnetic parameters such as coercivity and anisotropy with the Johnson–Mehl–Avrami equation. Later, this approach was used to understand crystallization in Ni–P precursor films from the amorphous state [106]. Recently, using similar magnetic monitoring approaches, the disproportionation reaction observed in cast rare-earth transition metal alloys [103, 107] and crystallization kinetics of Fe-based soft magnetic amorphous alloys were examined [108].

To the best of our knowledge, kinetics of such precipitation reactions occurring at the nanoscale has not been examined via magnetic measurements for intermetallic alloys. Therefore, this study will be the first to discuss the kinetic aspects of α-phase precipitation in $Ni_{50}Fe_xAl_{50-x}$ (x = 20, 25, and 30) alloys by utilizing a non-conventional characterization technique which exploits the ferromagnetic character of the precipitating phase. In the current work, precipitation was monitored by magnetization measurements encompassing both temperature-scan and isothermal experiments with a vibrating sample magnetometer. Transmission electron microscopy (TEM) and micro-hardness measurements were conducted to support the kinetic analysis.

5.1 Binary NiAl and Ni_3Al Intermetallic Compounds

Figure 5.1 contains SEM micrographs of as-cast binary $Ni_{50}Al_{50}$ and $Ni_{75}Al_{25}$ alloys. The $Ni_{50}Al_{50}$ alloy has a single-phase coarse-grained microstructure with no microstructural features along grain boundaries. The as-cast $Ni_{75}Al_{25}$ alloy displays a two-phase microstructure of randomly oriented dendrites and featureless interdendrite matrix.

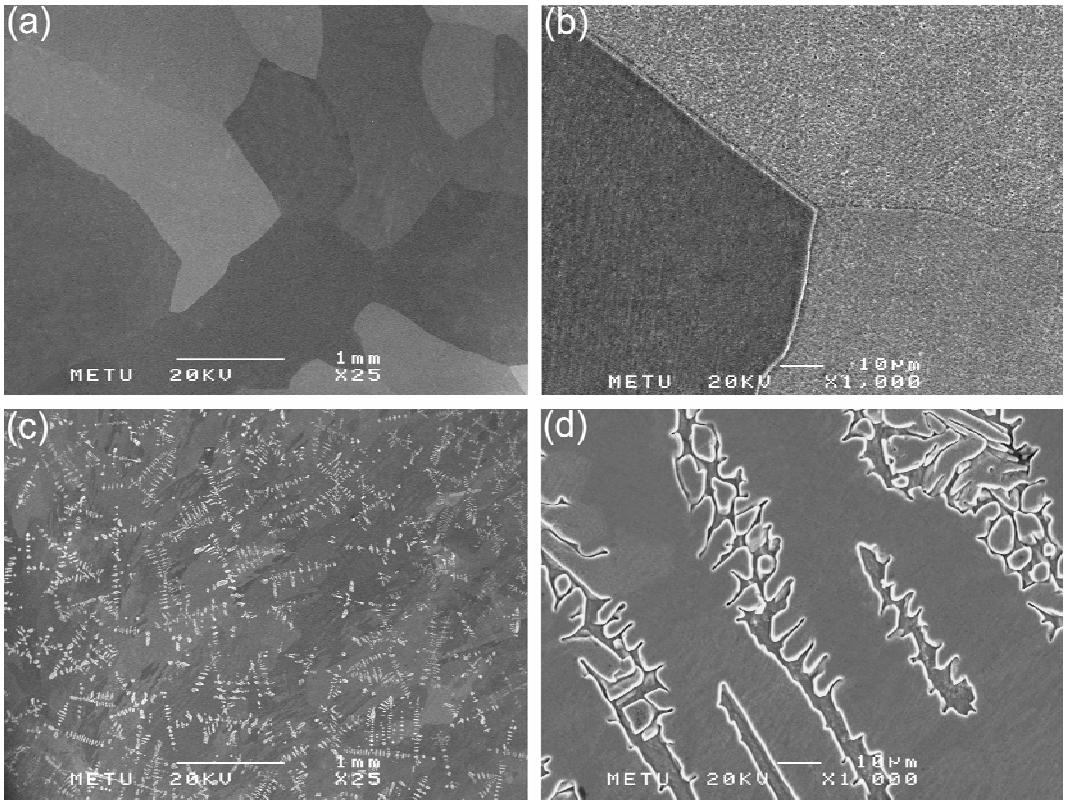

Figure 5.1 SEM micrographs of as–cast alloys; (a-b) $Ni_{50}Al_{50}$, and, (c-d) $Ni_{75}Al_{25}$.

Table 5.1 contains the results of compositional analysis of single-phase $Ni_{50}Al_{50}$ alloy and constituent phases in two-phase $Ni_{75}Al_{25}$ alloy. It is clear that nominal and exact compositions are almost the same and there exists no significant differences between dendritic and interdendritic regions in the two-phase $Ni_{75}Al_{25}$ alloy.

Table 5.1 Chemical compositions of $Ni_{50}Al_{50}$ and $Ni_{75}Al_{25}$ alloys.

Alloys	Phases and Chemical Compositions					
	β phase		γ phase in interdendrite		γ phase dendrite	
	Ni	Al	Ni	Al	Ni	Al
As-cast						
Ni-25Al			75	25	76	24
Ni-50Al	51	49				

It becomes clear by examining the XRD patterns of as-cast alloys (Figure 5.2) that the $Ni_{50}Al_{50}$ alloy is composed of a single phase with all reflections associated with an ordered bcc structure (B2) showing clear (100), (111) and (210) superlattice reflections. The $Ni_{75}Al_{25}$ alloy consists of a single apparent phase ascribed to an ordered fcc structure ($L1_2$) with apparent (100), (110), (210), (211), (221) and (310) superlattice reflections. In the latter alloy, the two-phase microstructure can be explained by the corresponding phase diagram given in Figure 2.6. During cooling from the molten state, a disordered fcc phase solidifies first in the form of dendrites which is followed by the formation of an ordered fcc phase as the interdendritic region.

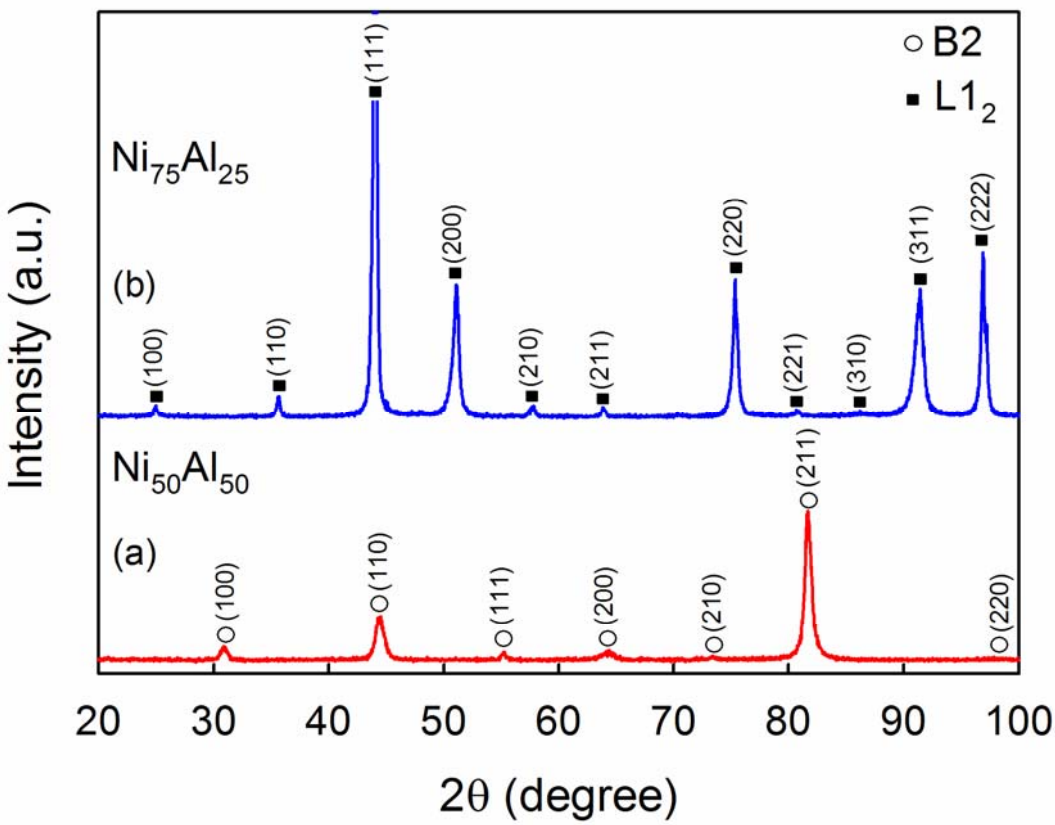

Figure 5.2 XRD patterns of as-cast (a) $Ni_{50}Al_{50}$, and, (b) $Ni_{75}Al_{25}$ alloys.

5.2 Macroalloying NiAl with Fe

5.2.1 Microstructure

Table 5.2 lists the nominal and actual compositions of as-cast $Ni_{50}Al_{50-x}Fe_x$ alloys with x=20, 25, and 30 at%. The microstructures of the as-cast alloys are shown in Figure 5.3 $Ni_{50}Fe_{20}Al_{30}$ alloy consists of course grains of a single phase (Figure 5.3(a)). $Ni_{50}Fe_{25}Al_{25}$ and $Ni_{50}Fe_{30}Al_{20}$ alloys exhibit a typical dendritic microstructure, in which a eutectic structure can be observed, as shown in Figure 5.3(b) and (c), respectively. Dendrites of the proeutectic phase initially arise due to its higher melting point. In the $Ni_{50}Fe_{30}Al_{20}$ alloy, the size of the eutectic region is larger than that of $Ni_{50}Fe_{25}Al_{25}$, indicating that the formation of the eutectic phase mixture will be favored with higher Fe content. Energy dispersive spectra of the $Ni_{50}Fe_{30}Al_{20}$ alloy taken from the dendritic region (Figure 5.3(d)) and interdendritic region (Figure 5.3(e)) show that the eutectic mixture has a higher Fe and a lower Al content compared to the dendritic region. Similar results were obtained for the $Ni_{50}Fe_{25}Al_{25}$ alloy in its as-cast state.

Table 5.2 Nominal and actual composition of samples in at.%

Nominal Composition	Ni	Fe	Al
$Ni_{50}Fe_{20}Al_{30}$	48	21	30
$Ni_{50}Fe_{25}Al_{25}$	49	26	25
$Ni_{50}Fe_{30}Al_{20}$	49	32	20

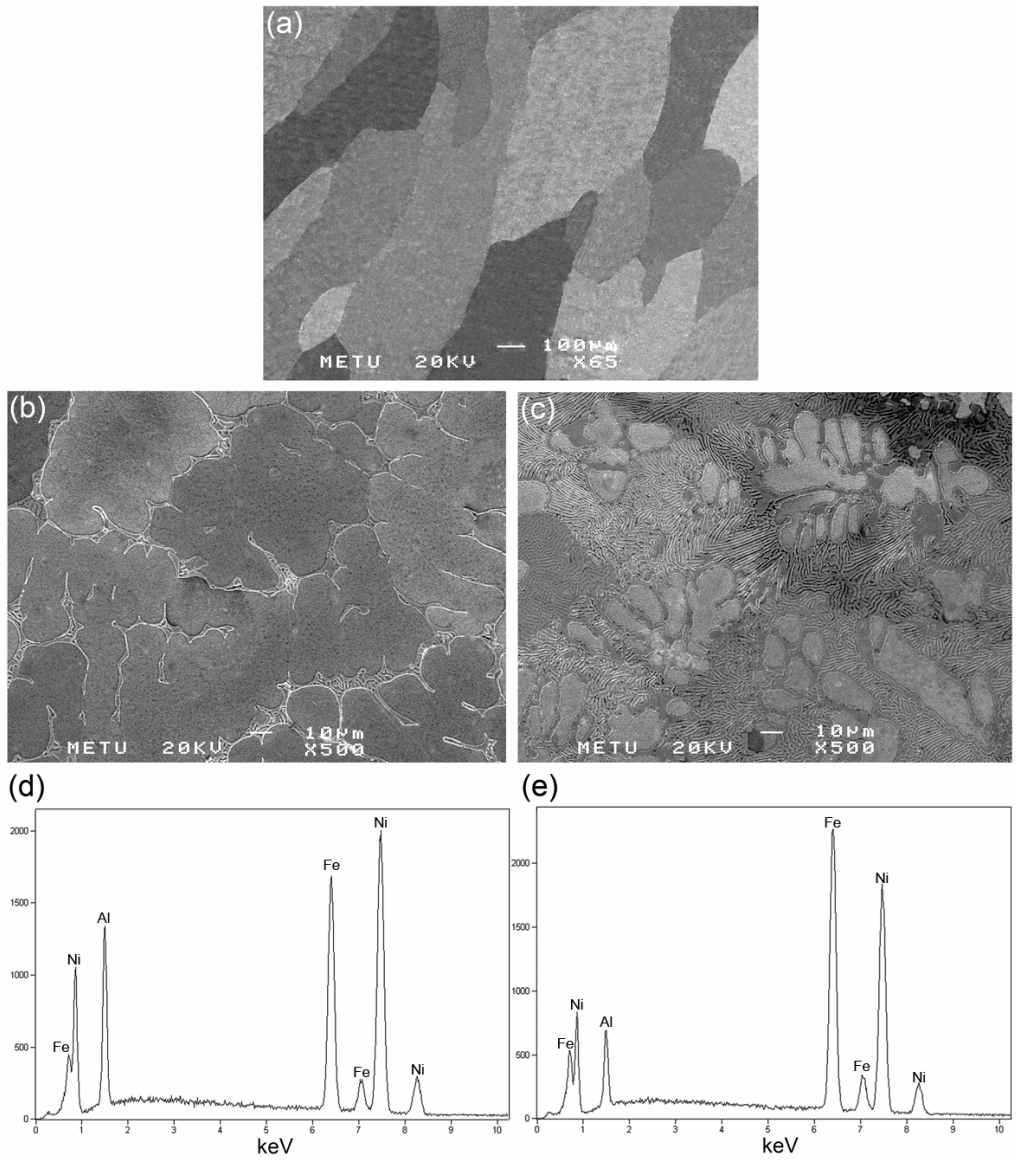

Figure 5.3 SEM micrographs of (a) $Ni_{50}Fe_{20}Al_{30}$, (b) $Ni_{50}Fe_{25}Al_{25}$ and (c) $Ni_{50}Fe_{30}Al_{20}$ as-cast alloys, and energy dispersive spectra of $Ni_{50}Fe_{30}Al_{20}$ alloy taken from (d) dendritic region and (e) among dendritic region.

Figure 5.4 shows the X-ray diffraction patterns of the as-cast $Ni_{50}Fe_{20}Al_{30}$, $Ni_{50}Fe_{25}Al_{25}$ and $Ni_{50}Fe_{30}Al_{20}$ alloys, over the diffraction angle, 2θ, range of 20°≤2θ≤100°. All diffraction peaks can be indexed to cubic structure. From the XRD patterns of the as-cast alloys, the (100), (110), (111), (200), (211), and (220) peaks indicate the presence of a B2 (β) structure; while the (111), (200), (220), (311), and (222) peaks indicate the presence of an FCC (γ) structure, respectively. While the $Ni_{50}Fe_{20}Al_{30}$ alloy has the single pattern of B2 structure, the $Ni_{50}Fe_{25}Al_{25}$ and $Ni_{50}Fe_{30}Al_{20}$ alloys show both B2 (β) and FCC (γ) structure peaks. From the equilibrium ternary phase diagram of the Ni–Fe–Al alloy [59, 109] and its compositions, by carrying out a phase identification it can be seen that there are several phases in the form of (Ni,Fe)(Al,Fe) with BCC structure and $(Ni,Fe)_3Al$ with FCC structure.

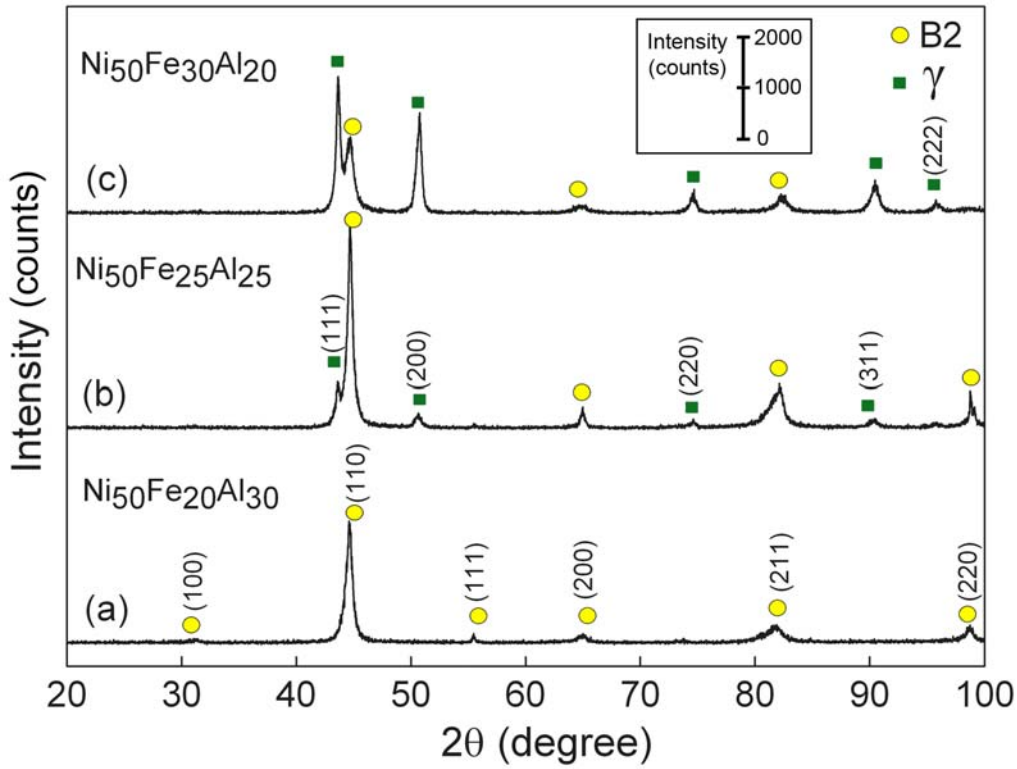

Figure 5.4 XRD patterns of (a) $Ni_{50}Fe_{20}Al_{30}$, (b) $Ni_{50}Fe_{25}Al_{25}$ and (c) $Ni_{50}Fe_{30}Al_{20}$ as-cast alloys.

The lattice parameters of the as-cast alloys have been calculated for the β-phase as a_{Fe20}=0.2872 nm, a_{Fe25}=0.2870 nm and a_{Fe30}=0.2866 nm; and for the γ-phase as a_{Fe25}=0.3599 nm and a_{Fe30}=0.3596 nm. Lattice parameters calculated for the β-phase are all smaller than that of binary NiAl (a_{NiAl}=0.2886 nm), whereas those calculated for the γ-phase are larger than Ni_3Al (a_{Ni3Al}=0.3561 nm). A major addition of Fe causes the Fe atoms to occupy both Ni- and Al-sites in the B2 (β) and FCC (γ) lattices [110-113], and so it can be said that increasing Fe content reduces the ordering of Ni atoms in the Ni-sites. This affects the intensities of the superlattice peaks in both the β- and γ-phases. The results of X-ray diffraction analysis confirm that only the as-cast $Ni_{50}Fe_{20}Al_{30}$ alloy exhibits the (100) superlattice peak of the B2 (β) structure, which indicates the ordering of the Ni-site, though with a very low intensity. None of the β- and γ-phase superlattice peaks were observed with the further addition of Fe, and annealing treatment.

Microstructural evolution and compositional changes of constituent phases by annealing of Ni-Fe-Al alloys are shown in Figures 5.5–5.7 and Table 5.3, respectively.

Figure 5.5 shows the microstructures of $Ni_{50}Fe_{20}Al_{30}$ alloy in the annealed state, which has the highest Al content and includes a single β-phase in its as-cast state. A second phase (γ-phase) nucleates on grain boundaries as a result of annealing at 673 K (Figure 5.5(a)). Moreover, the γ-phase grows both in the grains and along the grain boundaries with annealing at 1073 K (Figure 5.5(b)) together with change in γ-phase composition towards lower Al and higher Fe content (Table 5.3).

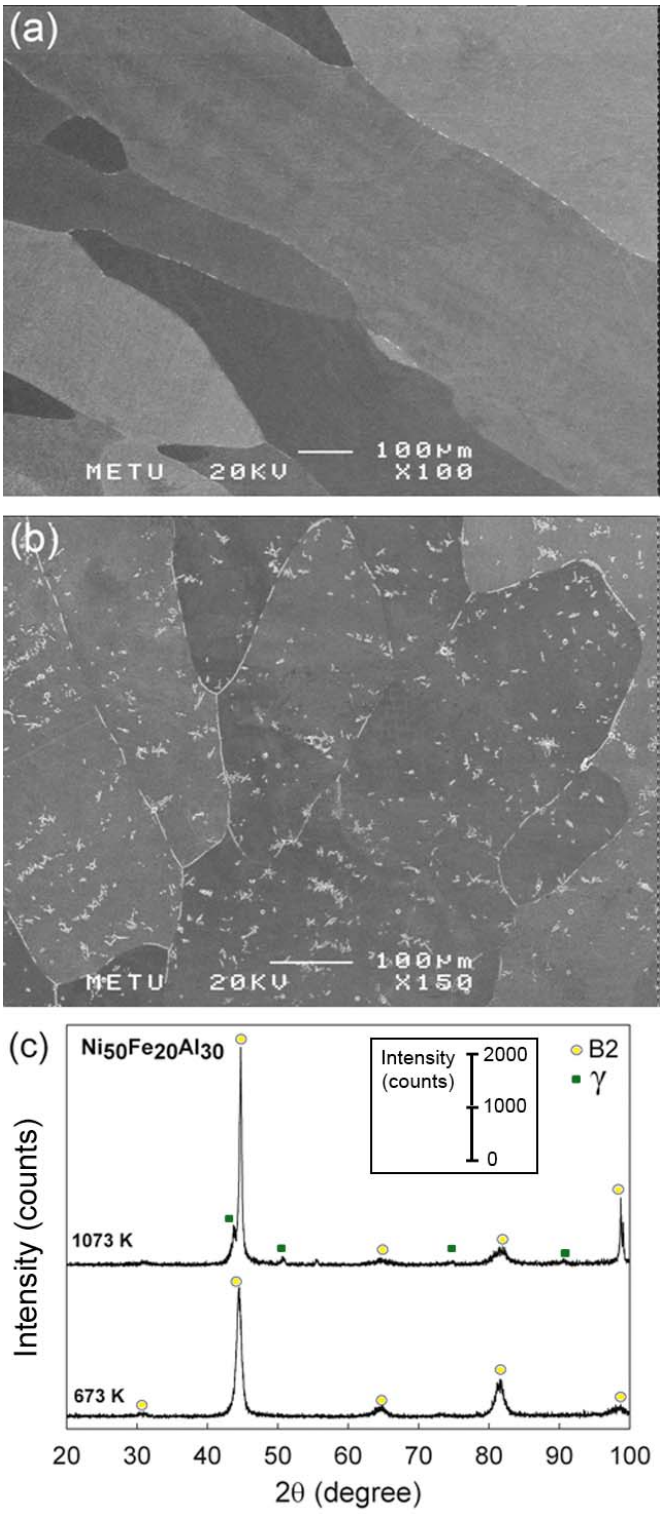

Figure 5.5 SEM micrographs of $Ni_{50}Fe_{20}Al_{30}$ alloy annealed for 168 h (a) at 673 K, and (b) at 1073 K, and (c) XRD patterns of annealed alloys.

Figure 5.6, Figure 5.7 and Table 5.3 contain the microstructures, XRD patterns and phase compositions of annealed $Ni_{50}Fe_{25}Al_{25}$ and $Ni_{50}Fe_{30}Al_{20}$ alloys. It is seen that no significant changes in the relative amounts of phases (β+γ) and compositions of the dendritic and eutectic regions are observed comparing the alloys annealed at 473 and 673 K. On the other hand, alloys annealed at 873 K and especially 1073 K possess larger volume fraction of the γ-phase as inferred from XRD line intensities and corresponding micrographs shown in Figure 5.6(b,c) and Figure 5.7(b,c). The eutectic structure of the alloys becomes thinner and a single phase region is formed upon annealing at 1073 K. This was accompanied by reductions of 4–8 at.% in Fe content of the proeutectic β-phase. Similar to that observed for Ni-30Al-20Fe alloy, interdendritic g-phase in alloys encounter changes in composition towards lower Al (by ~5 at.%) and higher Fe content (by ~9 at.%).

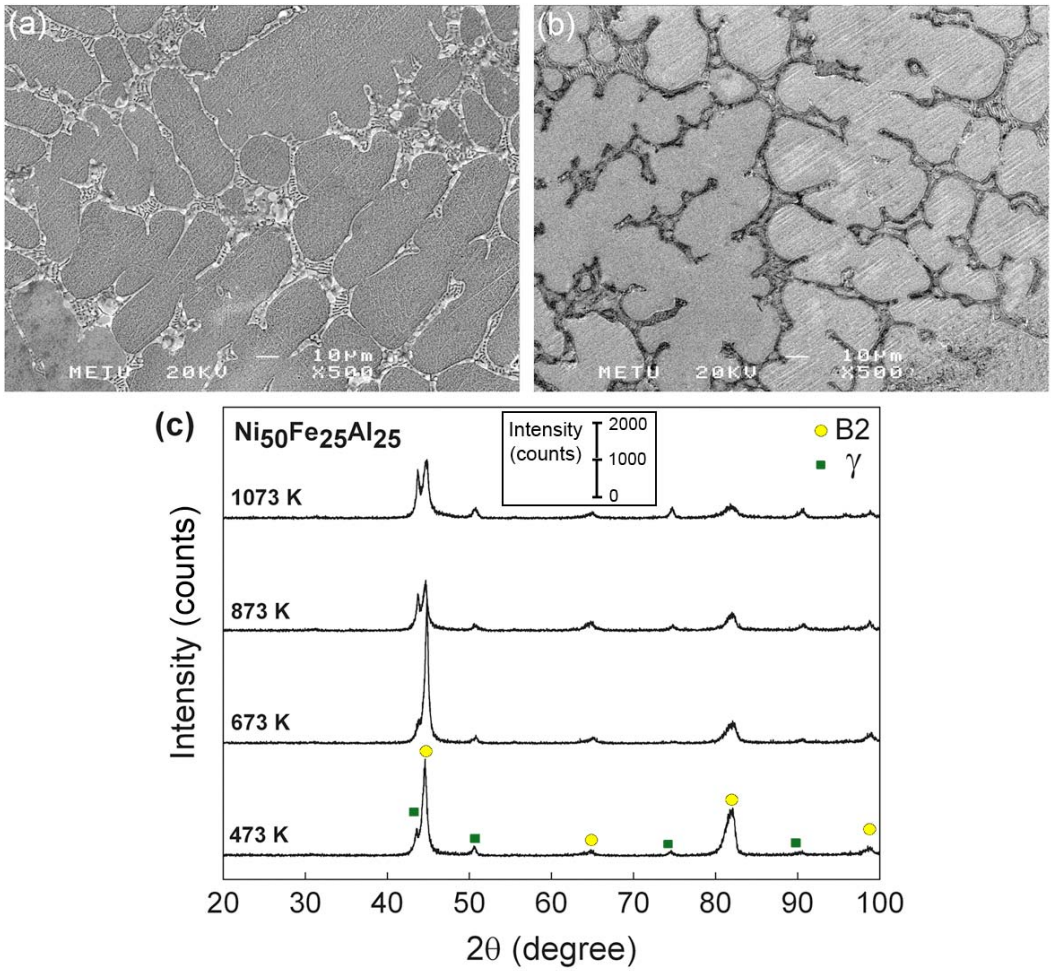

Figure 5.6 SEM micrographs of $Ni_{50}Fe_{25}Al_{25}$ alloy annealed at (a) 673 K and (b) 1073 K, (c) XRD patterns for annealed states.

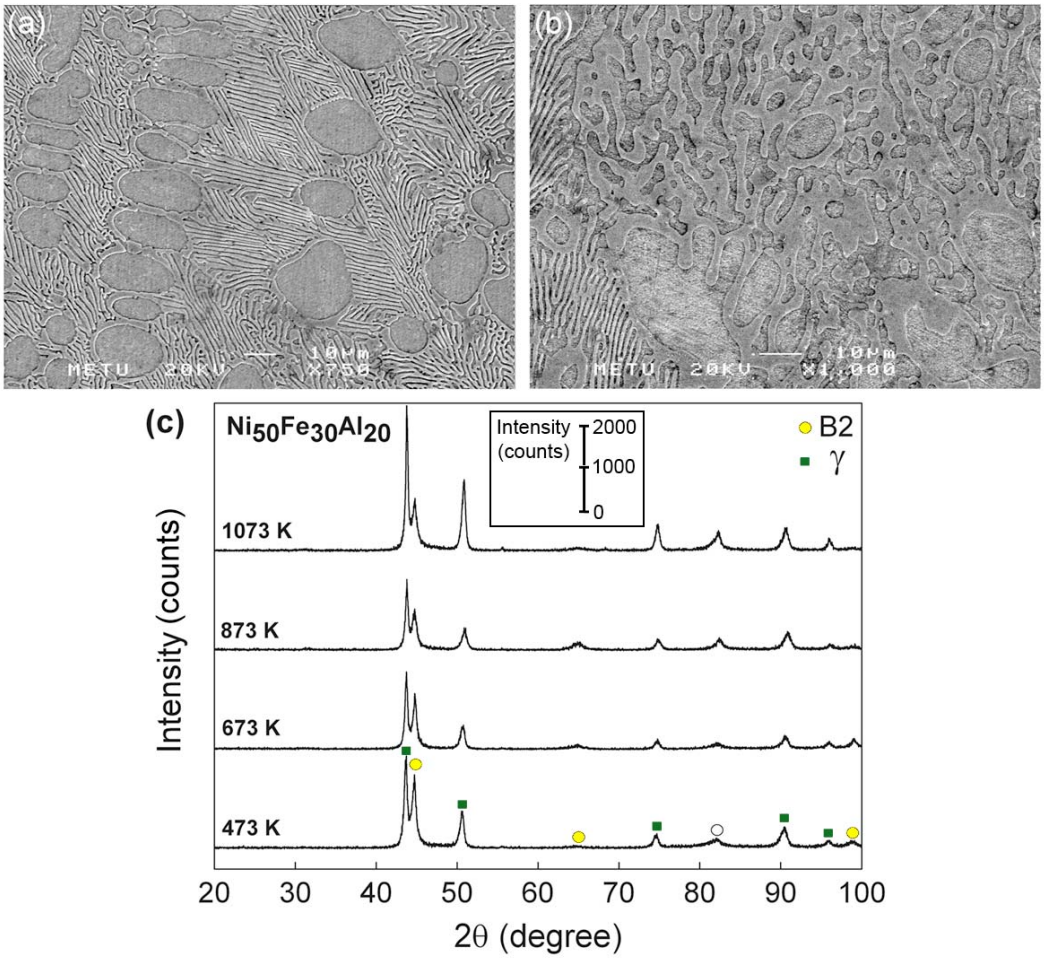

Figure 5.7 SEM micrographs of $Ni_{50}Fe_{30}Al_{20}$ alloy annealed at (a) 673 K and (b) 1073 K, (c) XRD patterns for annealed states.

Table 5.3 Compositional analysis of phases in as-cast and annealed Ni-Al-Fe alloys.

Alloys	Phases and Chemical Compositions								
	β phase in dendrite			β phase in interdendrite			γ phase in interdendrite		
	Ni	Al	Fe	Ni	Al	Fe	Ni	Al	Fe
As-cast									
Ni-30Al-20Fe	50	29	21						
Ni-25Al-25Fe	51	27	23	48	22	30	46	13	41
Ni-20Al-30Fe	50	23	27	48	19	33	48	13	39
673 K annealed									
Ni-30Al-20Fe	50	29	21				52	23	25
Ni-25Al-25Fe	51	26	23	47	25	28	47	12	41
Ni-20Al-30Fe	50	23	27	49	24	27	48	12	40
873 K annealed									
Ni-30Al-20Fe	50	29	21				50	23	27
Ni-25Al-25Fe	50	26	24	48	24	28	46	12	42
Ni-20Al-30Fe	49	24	27	49	25	26	49	13	38
1073 K annealed									
Ni-30Al-20Fe	51	30	19				36	6	58
Ni-25Al-25Fe	53	28	19	50	26	23	41	7	52
Ni-20Al-30Fe	53	29	18	52	27	21	44	8	48

5.2.2 Magnetic Properties

Figure 5.8 displays the magnetization curves of as-cast $Ni_{50}Fe_xAl_{50-x}$ alloys having x=0, 20, 25, and 30. NiAl is a B2-type alloy and is non-magnetic in the perfect atomic ordering state. However, $Ni_{50}Fe_xAl_{50-x}$ ternary alloys, consisting of single β-phase or β+γ two-phase microstructure exhibit ferromagnetism, and magnetization enhances with Fe content of the alloy.

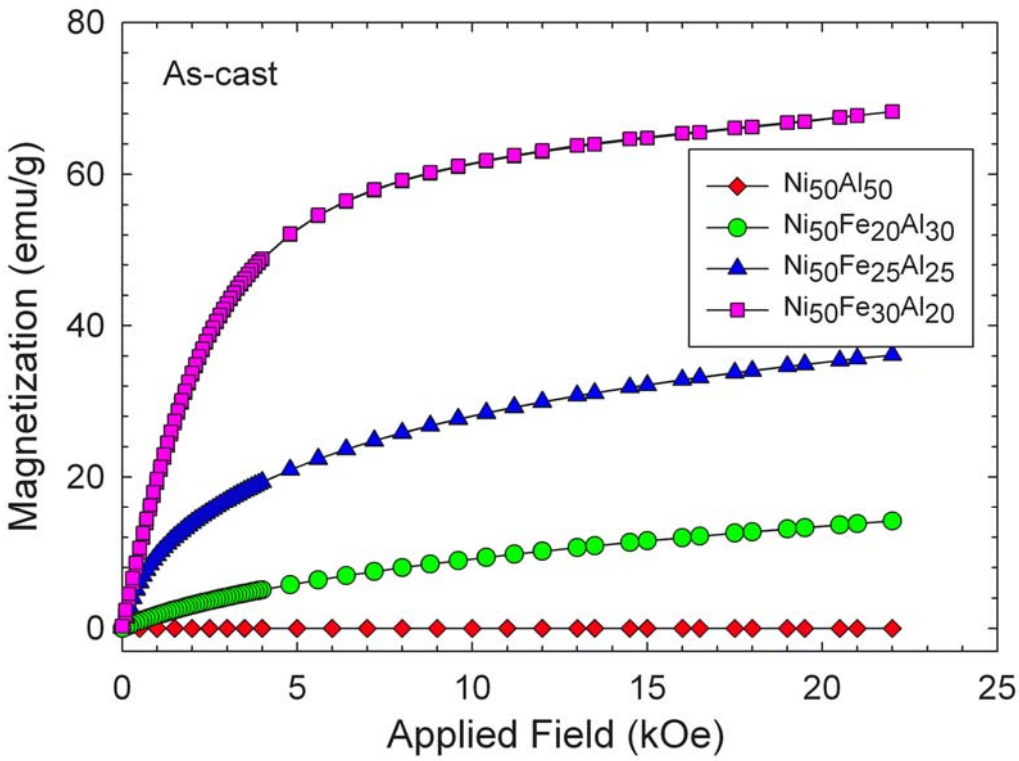

Figure 5.8 Magnetization versus applied field curves of $Ni_{50}Al_{50}$, $Ni_{50}Fe_{20}Al_{30}$, $Ni_{50}Fe_{25}Al_{25}$ and $Ni_{50}Fe_{30}Al_{20}$ alloys.

Thermomagnetization curves of alloys shown in Figure 5.9 compare the behavior of as-cast and annealed alloys. Magnetization of alloys in the as-cast and 1073 K annealed states decrease sharply to almost zero magnetization upon their Curie transition. On the other hand, alloys annealed at 673 K and 873 K still retain their magnetization at high temperatures which might be attributed to the presence of a new ferromagnetic phase of higher Curie temperature compared to the alloy matrix.

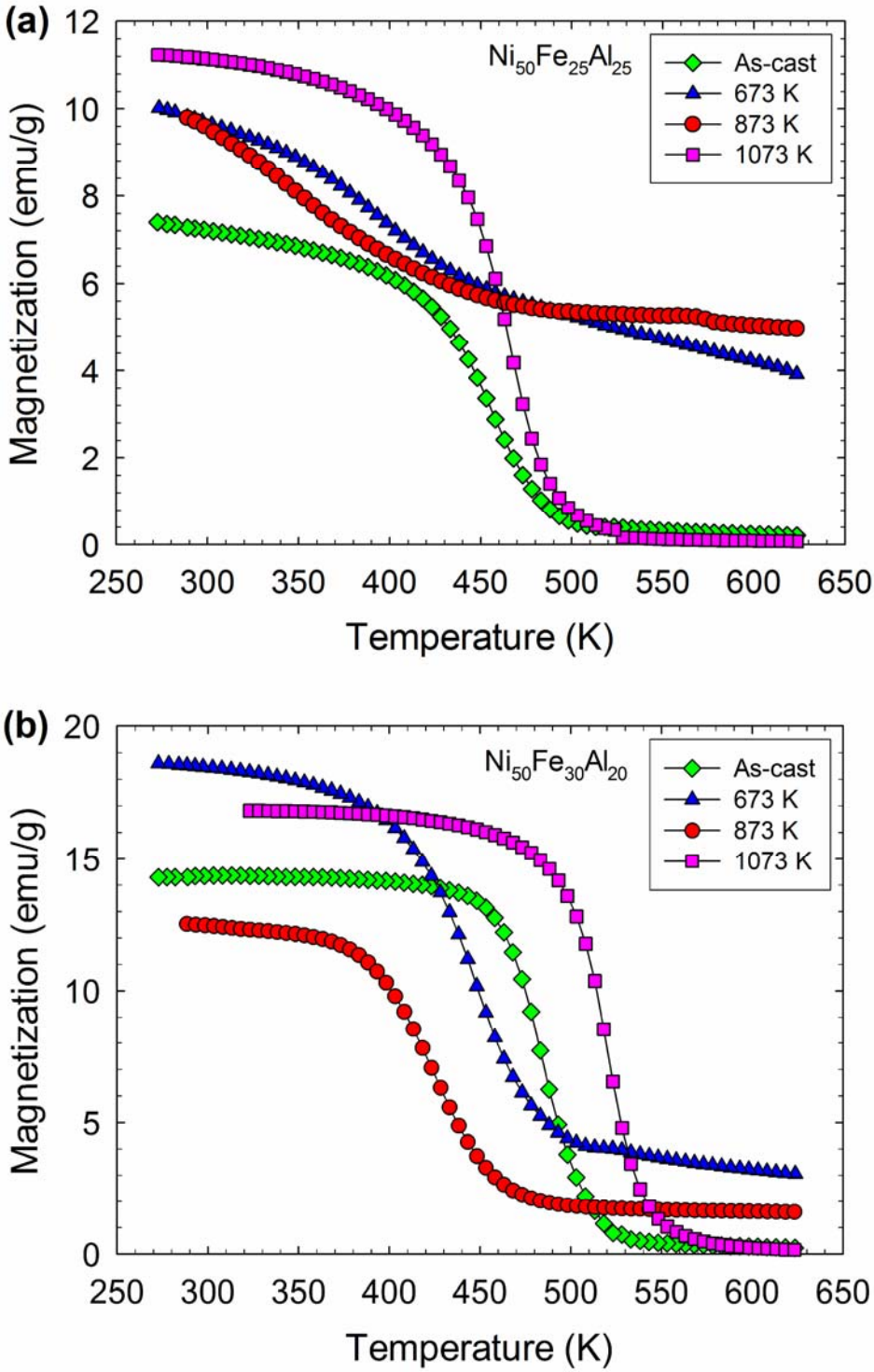

Figure 5.9 Thermomagnetization curves measured in a magnetic field of 500 Oe for (a) $Ni_{50}Fe_{25}Al_{25}$ and (b) $Ni_{50}Fe_{30}Al_{20}$ alloys in the as-cast and annealed states (673 K, 873 K and 1073 K).

Oikawa et al. [114] confirmed the precipitation of an Fe-rich BCC α-phase for $Ni_{57}Fe_{25}Al_{18}$ alloy annealed at 673 K. In addition to this, Guha et al. [54] also reported the formation of α-Fe precipitates in a B2 matrix for $Ni_{50}Fe_{20}Al_{30}$ alloy annealed at 773 K. Thus, in accord with previous studies, the increase in magnetization for alloys annealed at 673 K observed in the current study could be attributed to the formation of ferromagnetic Fe precipitates.

Considering the variations in saturation magnetization (at an applied field of 22 kOe) with annealing for $Ni_{50}Fe_{20}Al_{30}$, $Ni_{50}Fe_{25}Al_{25}$ and $Ni_{50}Fe_{30}Al_{20}$ alloys (Figure 5.10), a substantial increase can be observed for alloys annealed at 673 K compared both to the as-cast counterpart and alloys annealed above or below 673 K. Marked enhancements in saturation magnetization obtained through annealing at 673 K might as well be ascribed to the formation of ferromagnetic BCC α-phase.

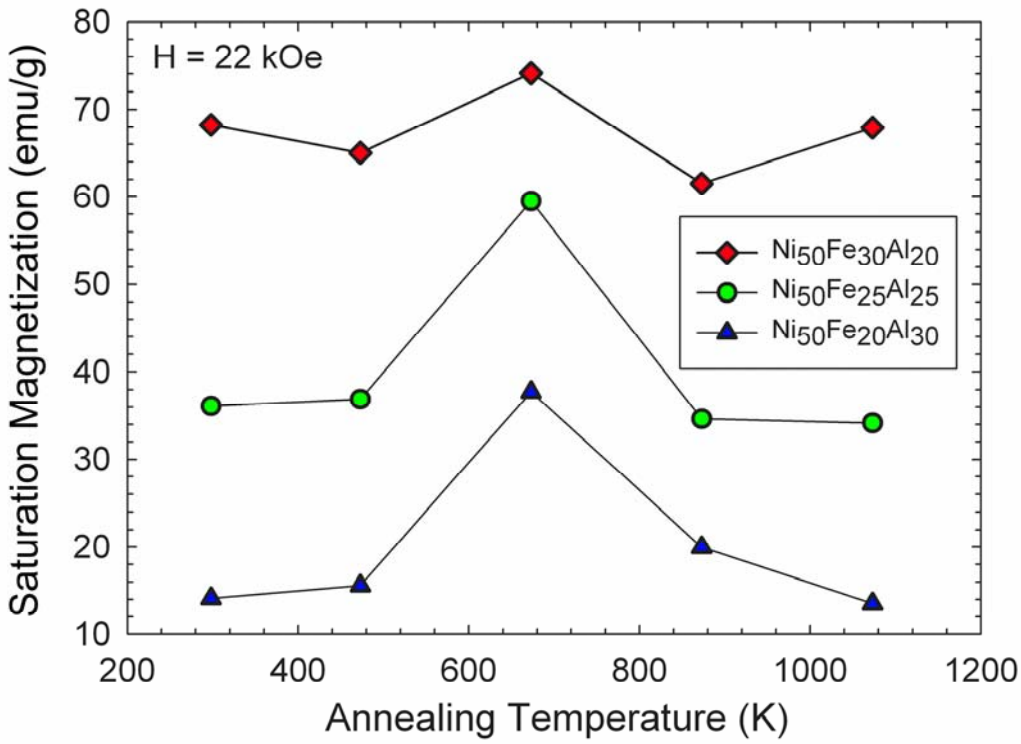

Figure 5.10 Room temperature saturation magnetization values of $Ni_{50}Fe_{20}Al_{30}$, $Ni_{50}Fe_{25}Al_{25}$ and $Ni_{50}Fe_{30}Al_{20}$ alloys as a function of annealing temperature.

In order to further examine the precipitation phenomenon, the magnetic properties of as-cast alloys have been measured by conducting temperature-scan magnetic measurements under an applied magnetic field of 500 Oe with a heating rate of 50 K/min. Accordingly, thermomagnetization heating curves (Figure 5.11) are obtained from as-cast $Ni_{50}Fe_{20}Al_{30}$, $Ni_{50}Fe_{25}Al_{25}$ and $Ni_{50}Fe_{30}Al_{20}$ alloys.

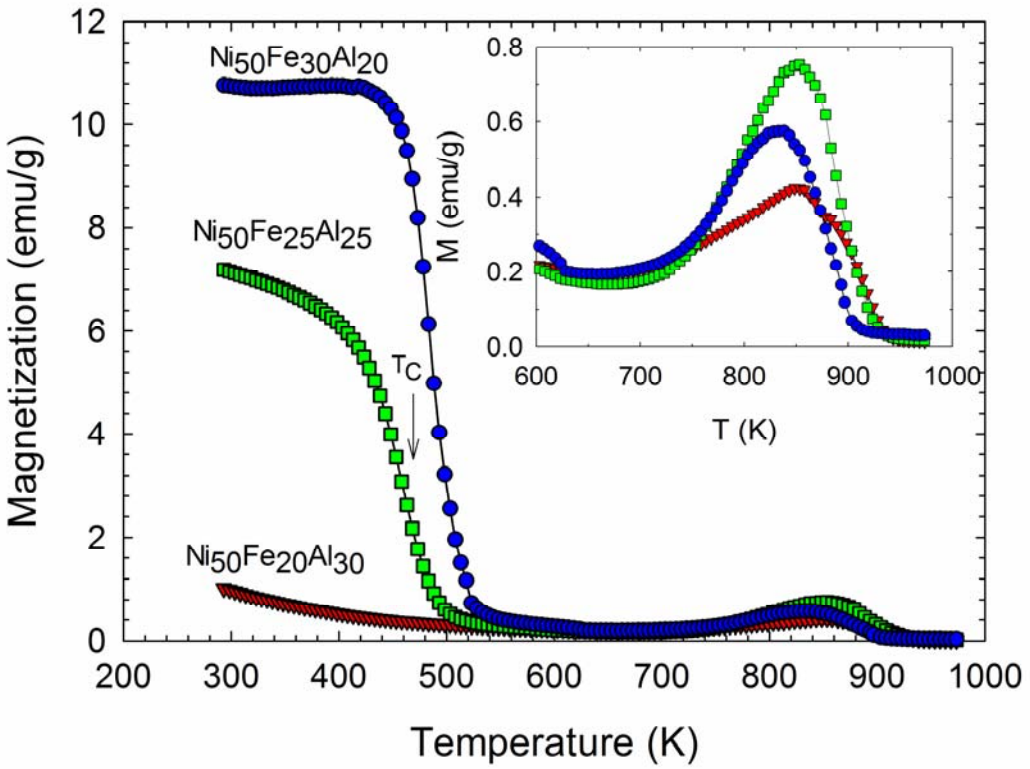

Figure 5.11 Thermomagnetization curves measured in a magnetic field of 500 Oe for as-cast $Ni_{50}Fe_{20}Al_{30}$, $Ni_{50}Fe_{25}Al_{25}$ and $Ni_{50}Fe_{30}Al_{20}$ alloys.

There is no Curie transition (T_C) observed for the $Ni_{50}Fe_{20}Al_{30}$ alloy above room temperature. With further increments of Fe content, T_C enhances in $Ni_{50}Fe_{25}Al_{25}$ and $Ni_{50}Fe_{30}Al_{20}$ alloys to 458 K and 483 K, respectively. It can be seen that magnetization falls with increasing temperature as a consequence of the transition from ferromagnetic to paramagnetic state. Considering the β+γ two phase $Ni_{50}Fe_{25}Al_{25}$ alloy of the current study, the Curie transition temperature is higher and magnetization values are lower compared to the single β-phase quenched $Ni_{50}Fe_{25}Al_{25}$ alloy reported as 202 K in a study by Oikawa et al. [115]. This could be attributed to the enhancement of Fe atoms in Ni-sites, which reduce T_C in quenched alloys.

Interestingly, during temperature scan measurements, magnetization begins to slowly rise above the T_C of the alloy matrix at around 700 K as

shown in the inset of Figure 5.11, indicating the formation of a new ferromagnetic phase. It can be inferred from the relevant phase diagrams [60, 61, 109] that this ferromagnetic phase is Fe-rich BCC formed within the miscibility gap between ordered (B2) and disordered (α-Fe) BCC phases. Magnetization rises to a maximum value at around 850 K, and then relatively sharply drops to reach zero magnetization at approximately 940 K. This behavior could be attributed to magnetic transition of the α-phase which takes place at a much lower temperature compared to the stable gap above which the α-phase does not eventually persist.

The $Ni_{50}Fe_{25}Al_{25}$ alloy annealed at 673 K was chosen for further examination of the proposed precipitation of Fe-rich BCC precipitates. It was stated above that the $Ni_{50}Fe_{25}Al_{25}$ alloy contained typical off-eutectic microstructure consisting of proeutectic B2 type β-dendrites and two-phase interdendritic regions (β and γ phases).. The dendritic region shown by the arrow in the low magnification TEM image in Figure 5.12(a) was observed in greater detail for the precipitates in Figure 5.12(b) where very fine (bright) particles are seen.

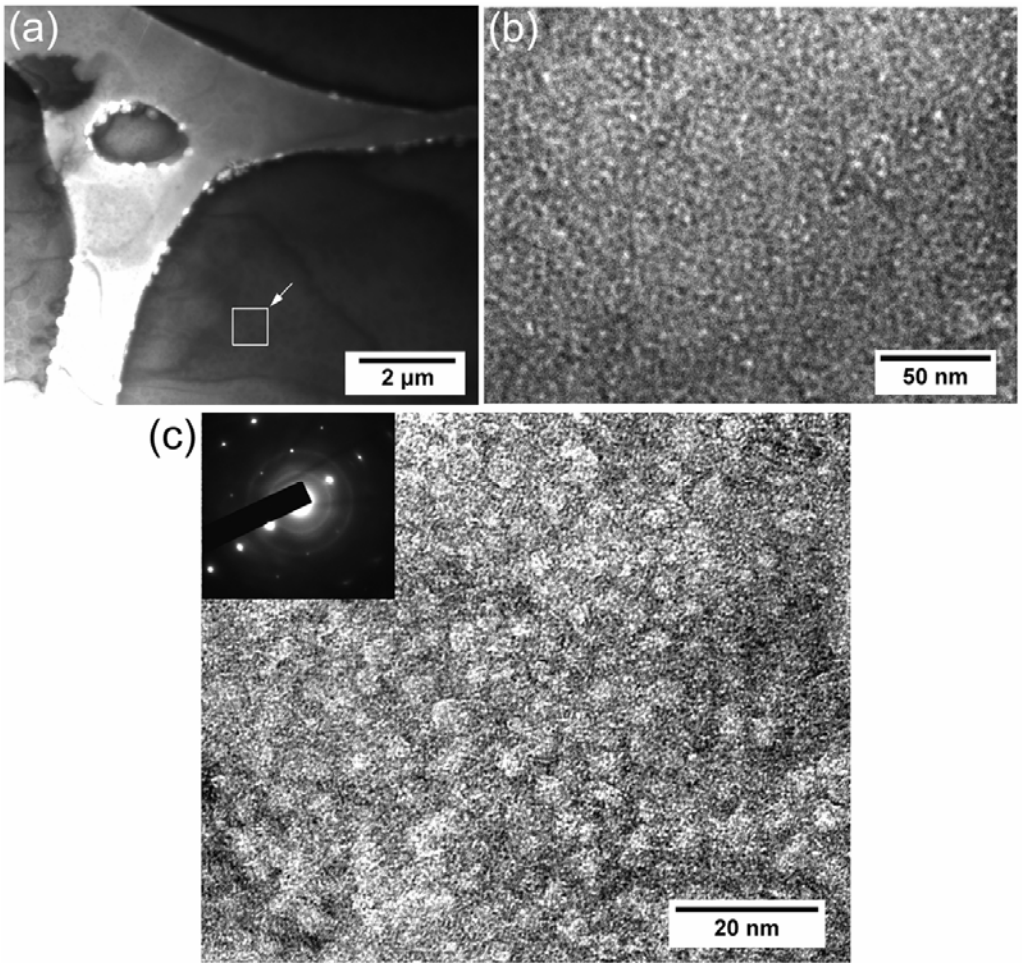

Figure 5.12 Bright-field TEM micrographs of the $Ni_{50}Fe_{25}Al_{25}$ alloy annealed at 673 K; (a) showing the eutectic and dendritic regions, (b) a larger magnification image of the dendritic region (matrix), (c) fine BCC precipitates and corresponding SAED pattern.

High magnification bright-field TEM micrograph and the corresponding selected area electron diffraction (SAED) pattern are shown in Figure 5.12(c). Transmission electron microscopy revealed fine precipitates that appear as bright regions in the size range of 3–5 nm which are distributed uniformly within the matrix. Spot reflections observed in the SAD pattern are completely attributed to a B2 structure since no extra reflections were observed. The weaker intensity extra ring pattern superimposed on the diffraction spots indicates the presence of BCC α-Fe precipitates in the nano-scale.

5.2.3 Microhardness

Figure 5.13 displays the micro-hardness values measured on the dendritic regions of as-cast and annealed alloys. Solid solution softening effects are observed in as-cast states with major addition of Fe in NiAl at 20, 25 and 30 at.% since hardness of the dendrites (β-phase) is reduced from 392 Hv to 341–361 Hv. This may be described by the major effect from disordering of the highly ordered B2 lattice and softening of strong directional Ni–Al bonds with Fe inclusion [116]. Considerable softening of the β-phase is a convincing evidence of increased ductility of as-cast single phase $Ni_{50}Fe_{20}Al_{30}$ alloy studied here. In two phase (β+γ) alloys, $Ni_{50}Fe_{25}Al_{25}$ and $Ni_{50}Fe_{30}Al_{20}$, further softening effects are induced with the formation of ductile γ-phase [55, 56].

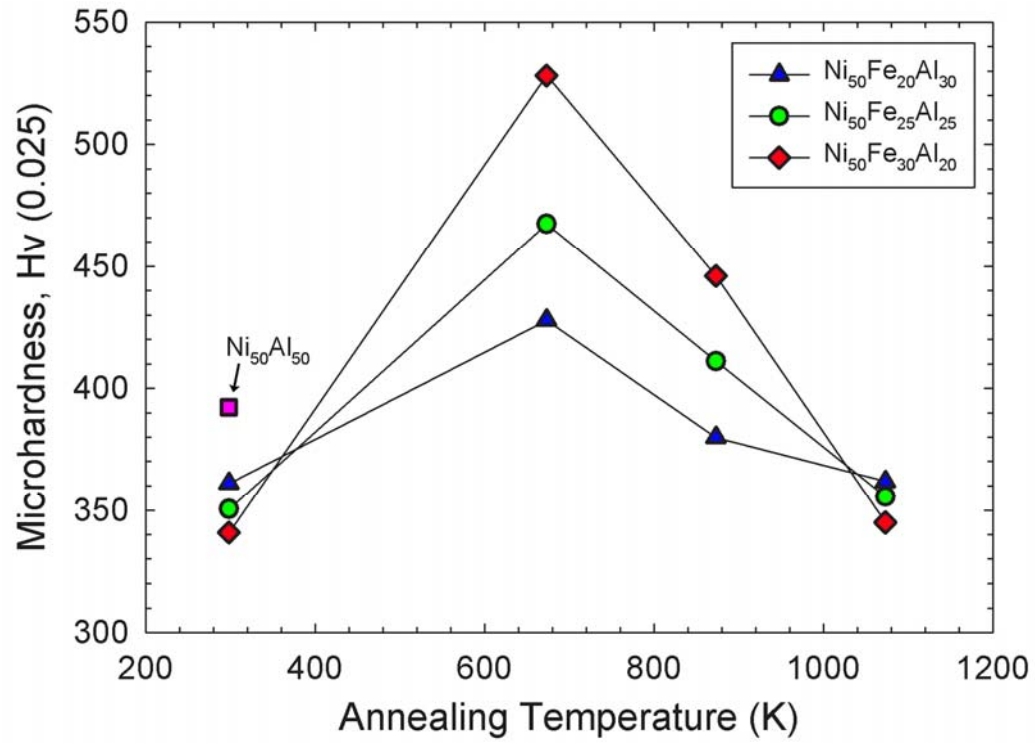

Figure 5.13 Microhardness of β-phase quantifying the precipitation hardening effect of nano-sized α-Fe precipitates.

Hardness values are marginally affected by increasing concentration of Fe which could be attributed to Fe atoms exclusively occupying Al anti-sites at Ni sublattice which is actually the case for $Ni_{50}Fe_xAl_{50-x}$ alloys with major Fe content [110]. In this way, exclusive site occupation of Ni sites by Fe results in limited size difference that would not cause significant negative lattice dilation by solute effect and thus should not induce marked changes in hardness of the β-phase.

Characterized by microstructural observations and modification in magnetic properties, fine α-Fe precipitates formed within the β-phase matrix impose significant hardening of the β-phase. It can be observed that in annealed alloys of the present study, hardness enhances with Fe content. With no exception, highest hardness values were measured for alloys annealed at 673 K. It could be thought that precipitates attain their optimum

size for precipitation hardening among the tested annealing conditions. Further increase in annealing temperature to 873 K causes remarkable losses in hardness related with coarsening of such fine precipitates at high temperatures [54]. In fact, β phase dendrites in alloys annealed at 1073 K soften to attain comparable hardness values to those of as-cast alloys indicative of diminished hardening effect of precipitates. This might be related to the dissolution of precipitates at such high temperatures where stable gap above which the α-phase does not eventually persist [60, 61, 109].

It should be noted that precipitation hardening effect is maximized at an annealing temperature of 673 K where, in a similar manner, substantial increases in room temperature saturation magnetization were seen. Comparing room temperature saturation magnetization values (Figure 5.10) and hardness of the β-phase (Figure 5.13) as a function of annealing temperature, a strong correlation is observed since both are exceedingly affected by the same precipitation reaction.

5.2.4 Mechanical Properties

Ni-Al-Fe alloys prepared by arc melting with nominal and actual compositions listed previously in Table 5.2 were used for the fabrication of 2 mm diameter compression test specimens by suction casting. Figure 5.14 displays the suction-cast microstructures with varying Fe content showing significant similarities with as-cast microstructures prior to suction-casting (Figure 5.1 and Figure 5.3).

The Fe_{20} alloy possesses a single phase microstructure with coarse β-grains where no apparent grain refinement is provided by suction-casting. The Fe_{25} alloy shows a dendritic microstructure where dendrites are a single β-phase (Ni: 50 at.%, Al: 24 at.%; Fe: 26 at.%) and interdendritic regions consist mainly of γ-phase (Ni: 50 at.%, Al: 14 at.%; Fe: 36 at.%) with some

embedded β-phase particles having the same composition to that of β-phase dendrites. With a further increase in the Fe content (Fe_{30} alloy), the volume fraction of interdendritic region increases to a great extent at the expense of the dendritic β-phase. A fine lamellar eutectic morphology is dominant in the solidification microstructure in addition to dendritic β-phase becoming refined compared to the Fe_{25} alloy.

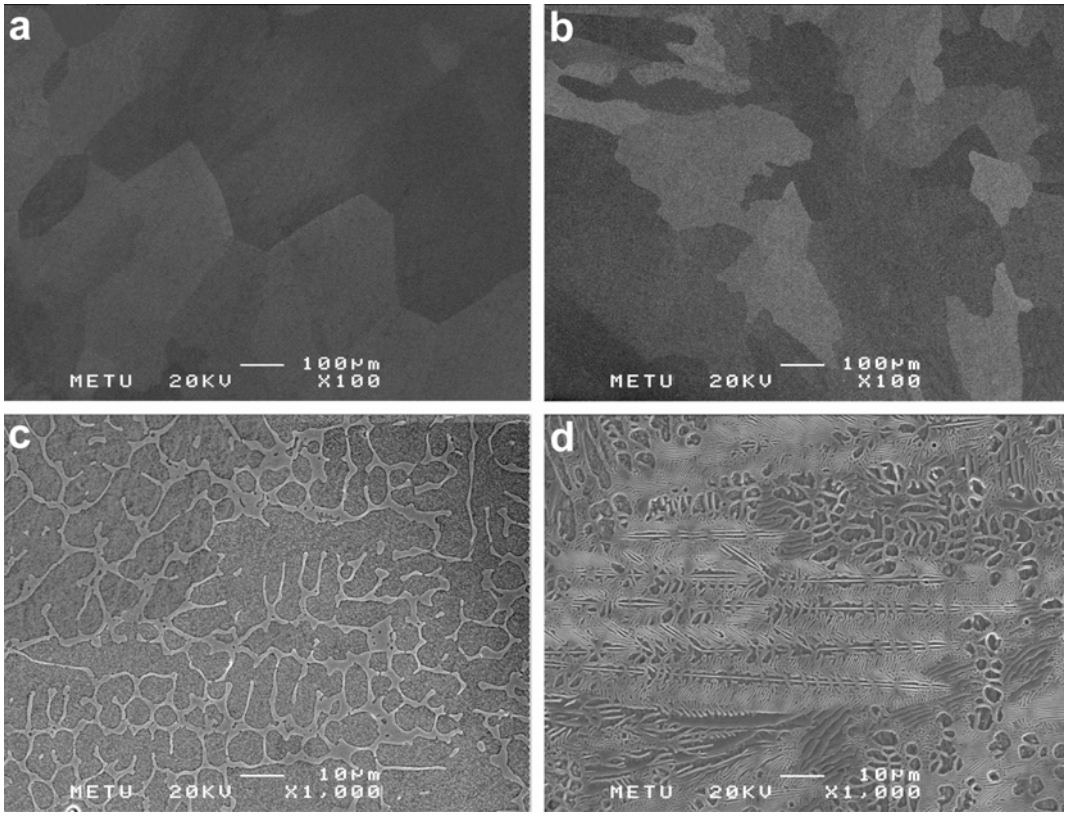

Figure 5.14 Suction-cast solidification microstructure of (a) binary NiAl, and, Ni-Al50-x-Fex alloys with (b) x=20 at.%, (c) x=25 at.% and (d) x=30 at.%.

Mechanical properties of Ni-Al-Fe alloys with varying Fe contents (20, 25 and 30 at.%) were investigated by compression tests, and, compressive properties such as compressive yield strength (σ_y) and compressive fracture strength (σ_f) are obtained in addition to the stress-strain behaviors shown in

Figure 5.15 The Fe_{20} alloy with single β-phase structure has σ_y=890 MPa, σ_f=3770 MPa and appreciable ductility which suggest remarkable improvements relative to the binary NiAl compound with σ_f=450 MPa, σ_y=1075 MPa and limited ductility. Improved σ_y and σ_f of the Fe_{20} alloy could be attributed to increased grain boundary strength and increased work hardening amount due to larger ductility, respectively.

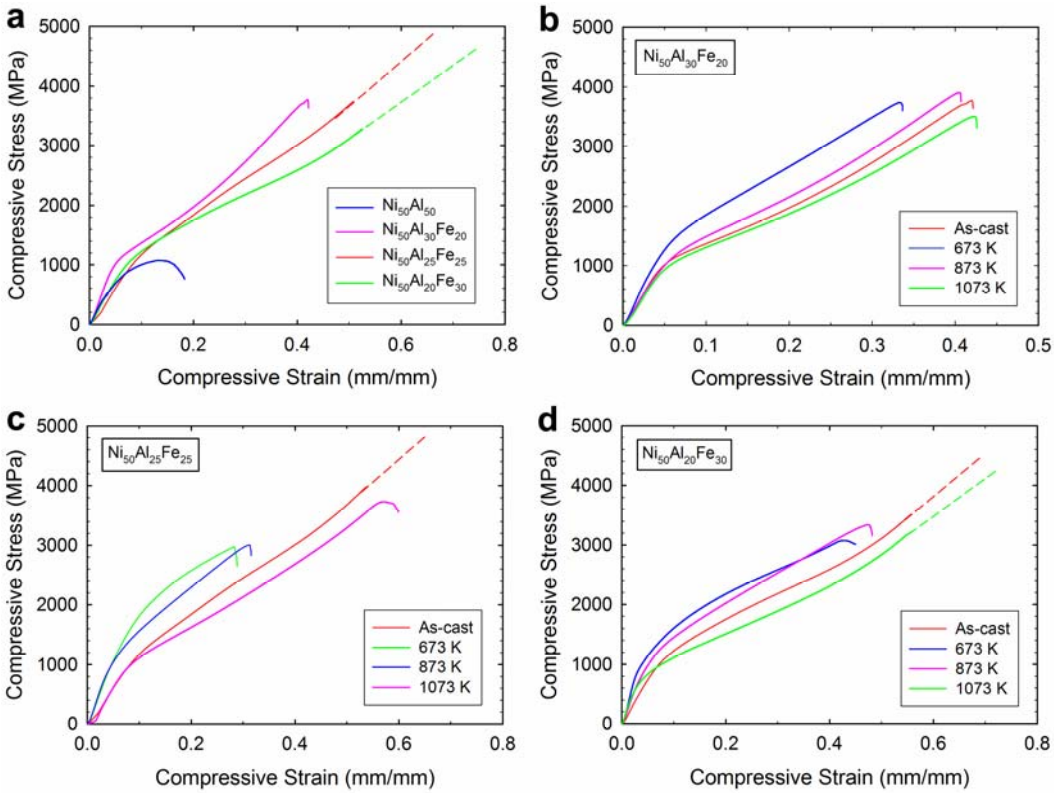

Figure 5.15 Compressive stress-strain behavior of alloys showing (a) the effect of Fe content in the as-cast state, and, the effect of annealing on (b) Fe_{20}, (c) Fe_{25} and (d) Fe_{30} alloys.

Figure 5.16 compares the fracture surface images around the crack tip region in binary NiAl and ternary Fe_{20} alloys. It can be stated that both alloys exhibit transgranular cleavage which is more significant for the binary alloy. Cleavage fracture occurs by crack initiation on grain boundaries and

propagation across the β-phase in NiAl and Fe_{20} alloys. In the previous section, annealing of the Fe_{20} alloy was shown to promote the formation of low volume fraction of γ-phase precipitates along β-grain boundaries. The influence of such a microstructural change by annealing on fracture morphology is clearly evidenced in Figure 5.16. In addition to predominant transgranular cleavage in the β-phase, the grain boundary γ-phase necks down to a chisel edge by plastic deformation. In this manner, slip is activated in the less ductile β-phase due to slip transfer from the more ductile γ-phase.

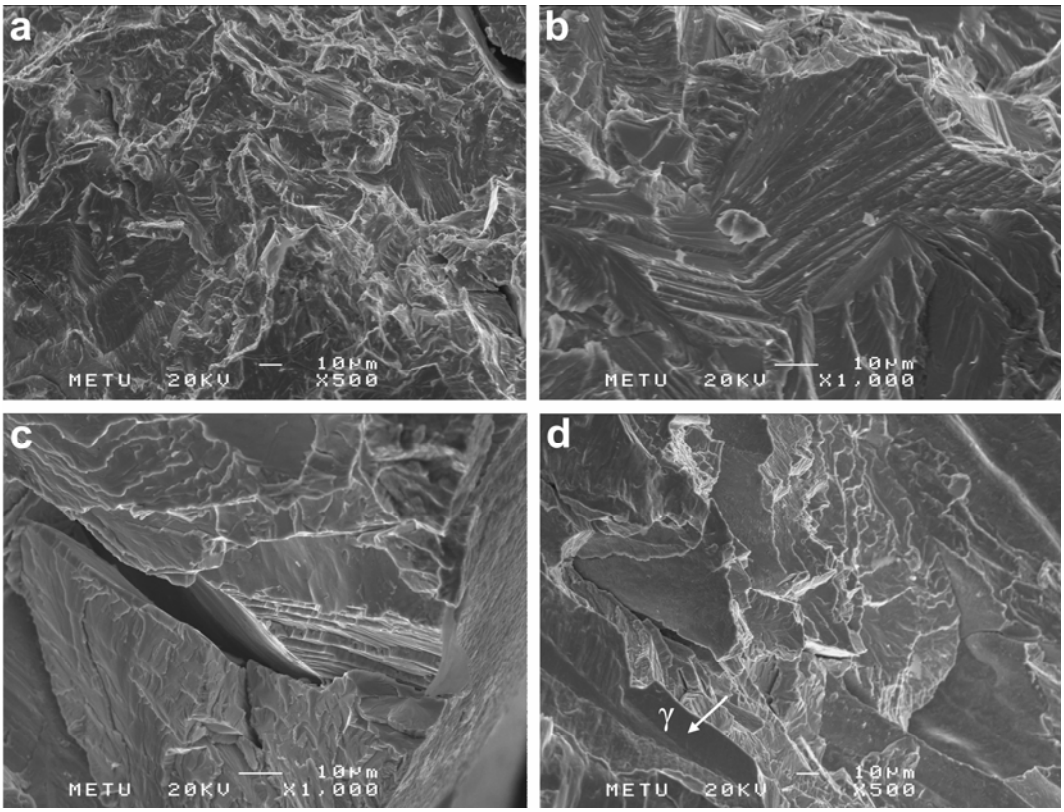

Figure 5.16 (a-b) as-cast binary NiAl at different magnifications, (c) as-cast Fe_{20} alloy, (d) Fe_{20} alloy annealed at 873 K.

The Fe_{25} alloy having a two-phase microstructure composed of hard β-phase dendrites and softer interdendritic γ-phase shows slightly lower σ_y of 850 MPa but increased ductility compared to the single β-phase Fe_{20} alloy. Improved ductility can be associated with blunting of cracks propagating in the β-phase reaching the softer γ-phase. An increase in the Fe content from 25 to 30 at.% leads to significant decrease in σ_y to 760 MPa due to larger volume fraction of interdendritic γ-phase at the expense of harder β-phase dendrites in the Fe_{30} alloy. Due to the appreciable amount of γ-phase in Fe_{25} and Fe_{30} alloys supporting plastic deformation to a large extent, specimens either did not fail under compressive loading or remained intact upon failure as shown in Figure 5.17 which did not allow for fractographic investigations to be done on the samples.

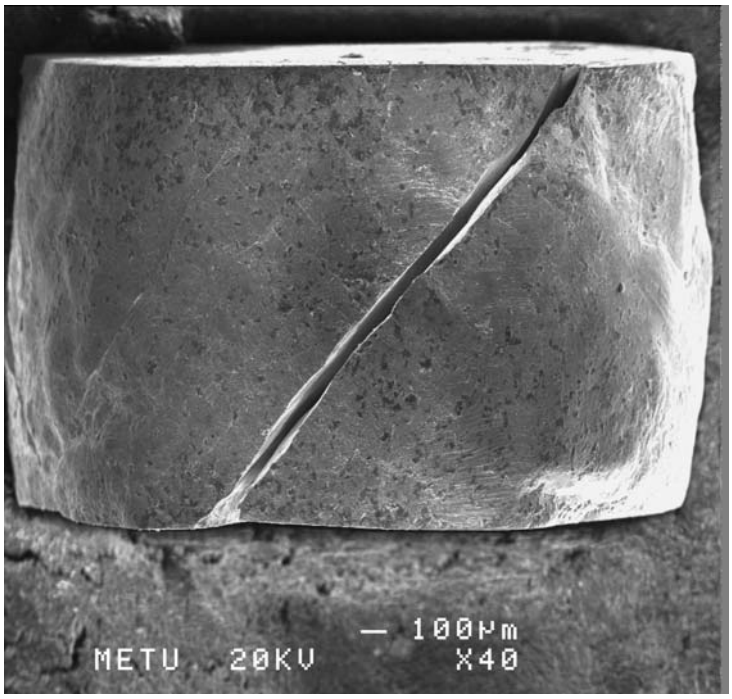

Figure 5.17 Compressive failure of Fe_{25} alloy showing critical resolved stress maximized on a plane inclined to an angle of around 45° to the loading direction.

In the preceding section, annealing was shown to have a profound influence on the microstructure of alloys with different Fe contents. In conjunction with altered microstructure, compressive properties are highly dependent on annealing temperature. The stress-strain behaviors of annealed alloys are shown in Figure 5.15 where it can be stated for all alloys that annealing promotes remarkable strengthening yet reduces ductility.

Figure 5.18 shows the variation of σ_y with annealing temperature suggesting significant strengthening of the alloy when an intermediate annealing temperature of 673 K is employed. Annealing at a temperature of 873 K causes significant reductions in σ_y but provides recovered ductility at least to some extent. With further increase in annealing temperature to 1073 K where marked changes in alloy microstructures were observed (Figures 5.5–5.7), strengthening effect by annealing is completely lost, and, in fact some softening of Fe_{25} and Fe_{30} alloys occur with respect to their as-cast state. This could be explained by the increased volume fraction of the interdendritic γ-phase by annealing at 1073 K, which at the same time allows for ductilization to a great extent.

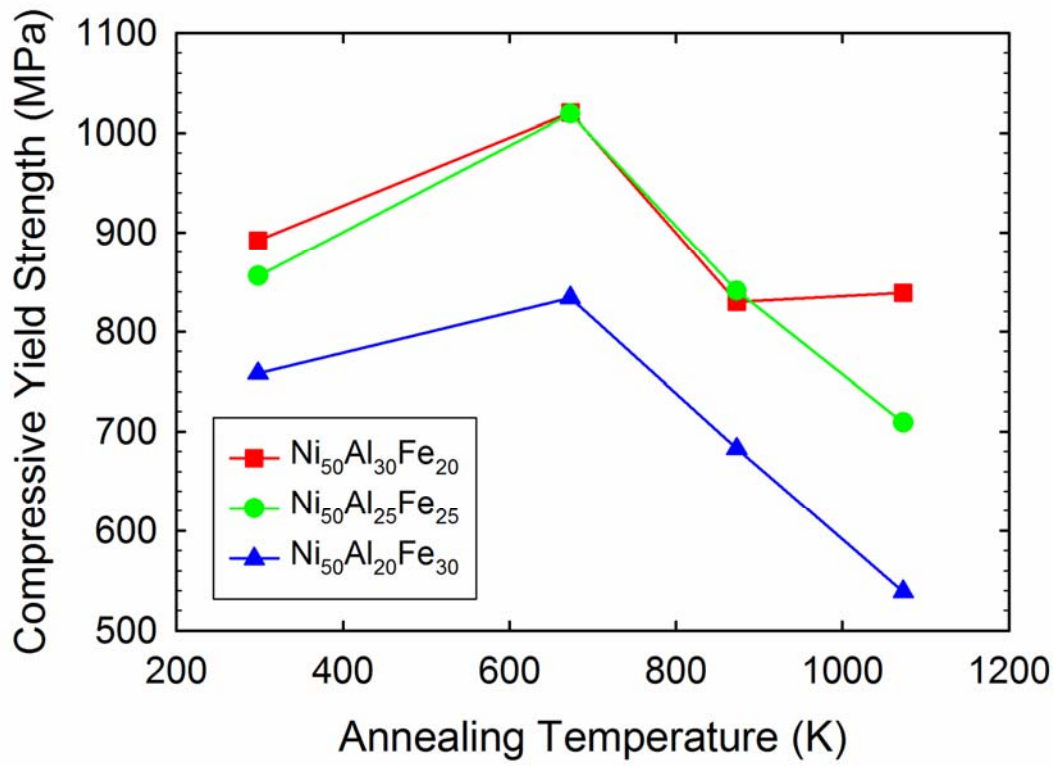

Figure 5.18 Variation of compressive yield strength with annealing of Ni-Al-Fe alloys.

The temperature dependence of σ_y shown in Figure 5.18 correlates well with the variation in β-phase microhardness by annealing as discussed in the preceding section (Figure 5.13). Therefore, the proposed mechanism for β-phase hardening, i.e. nanoscale precipitation of Fe-rich disordered phase inside the ordered β-phase dendrites, can also be thought to be the predominant mechanism of σ_y improvement by annealing. It has to be noted that although the extent of β-phase hardening by annealing is higher for larger Fe content, strengthening effect becomes significant towards lower Fe content. This can be explained by increased amount of γ-phase at the expense of β-phase as Fe content is increased since the γ-phase is not affected from such precipitation hardening.

5.2.5 Kinetics of Nanoscale Precipitation by Magnetic Monitoring

The $Ni_{50}Fe_xAl_{50-x}$ alloys (x = 20, 25 and 30) were chosen for the kinetic analysis of nanoscale α-phase precipitation via magnetic monitoring. The magnetization behavior of $Ni_{50}Fe_xAl_{50-x}$ alloys (x = 20, 25 and 30) was examined by continuous heating scans in VSM. Alloys undergo Curie transition below 500 K, and above these transition temperatures, magnetization values begin to rise again starting at around 700 K (Figure 5.19). This is associated with the precipitation of a secondary ferromagnetic phase with a higher Curie transition compared to the primary β-phase. Relevant phase diagrams [60, 61, 109] support that this ferromagnetic phase is an Fe-rich BCC phase formed within the miscibility gap between ordered (B2, β-phase) and disordered (α-Fe) BCC phases.

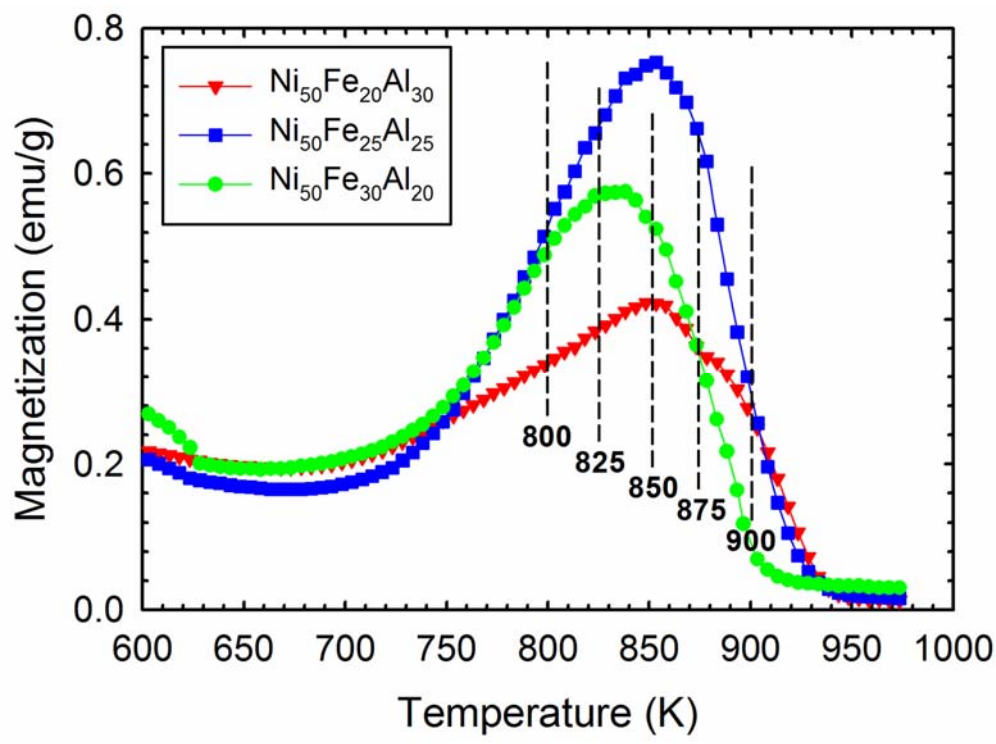

Figure 5.19 Thermomagnetization curves of alloys above 600 K where the temperatures for isothermal magnetization measurements are marked.

In order to study the temperature dependence and kinetics of precipitation of the mentioned ferromagnetic phase, isothermal magnetization measurements were carried out at several selected temperatures marked in Figure 5.19 over the temperature range where transient rises in magnetization are seen. Isothermal kinetics treatment of the magnetization data covers temperatures above 800K since lower temperatures do not provide practical rates of magnetization.

Figure 5.20 shows the time-dependent magnetization behavior of alloys measured over a temperature range of 800–900 K in 25 K intervals under an applied field of 500 Oe for 2 h periods. Magnetization increases gradually with a decreasing rate with time in all isothermal experiments. Since an increase in the isothermal temperature results in increased magnetization and rate of magnetization with respect to time, it is clear that precipitation of a new ferromagnetic phase is a thermally activated process favored at higher annealing temperatures.

It is also seen in Figure 5.20 that non-zero magnetization values are recorded for the very first measurements following the relatively fast heating stage (50 K/min) up to the isothermal temperature. Thus, it could be stated that precipitation as monitored by isothermal magnetization does not show an apparent incubation period. This behavior was previously encountered in studies utilizing a similar magnetic monitoring approach and was attributed to the fact that incubation takes place during the heat-up stage obscuring its observation [107].

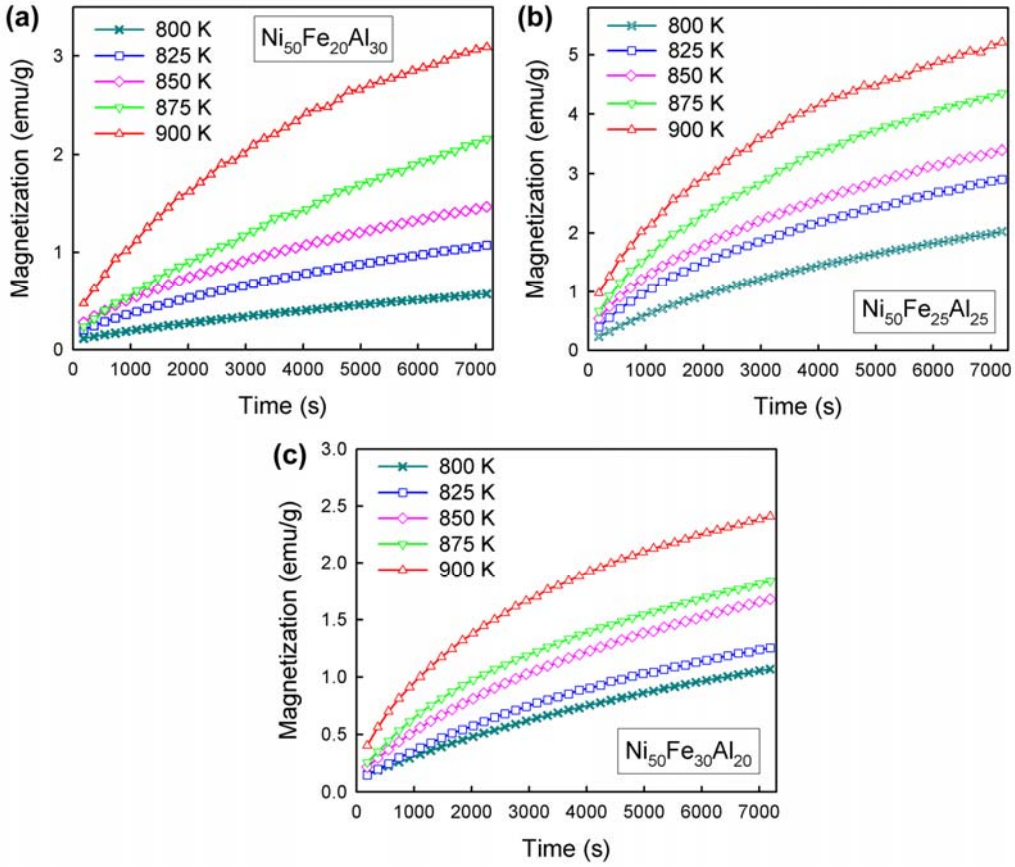

Figure 5.20 Time-dependent magnetization curves of (a) $Ni_{50}Fe_{20}Al_{30}$, (b) $Ni_{50}Fe_{25}Al_{25}$ and (c) $Ni_{50}Fe_{30}Al_{20}$ alloys between 800 K and 900 K.

Figure 5.21 shows the time and temperature dependence of magnetization rates during isothermal measurements in VSM. Increase in the isothermal temperature above 750 K results in sharp rises in magnetization rates, particularly for the early stages of precipitation (10 min curve), which is indicative of notable precipitate growth rates. However, below 750 K magnetization increments are marginal at all measurement times (10, 30 and 120 min curves). Therefore, by choosing an appropriate annealing temperature such as 673 K, one could form desirable fine precipitates that would impart an ultimate strengthening effect. On the other hand, following an annealing heat treatment where notable growth rates are encountered

(873 K in this case), significant losses in precipitation strengthening are foreseeable.

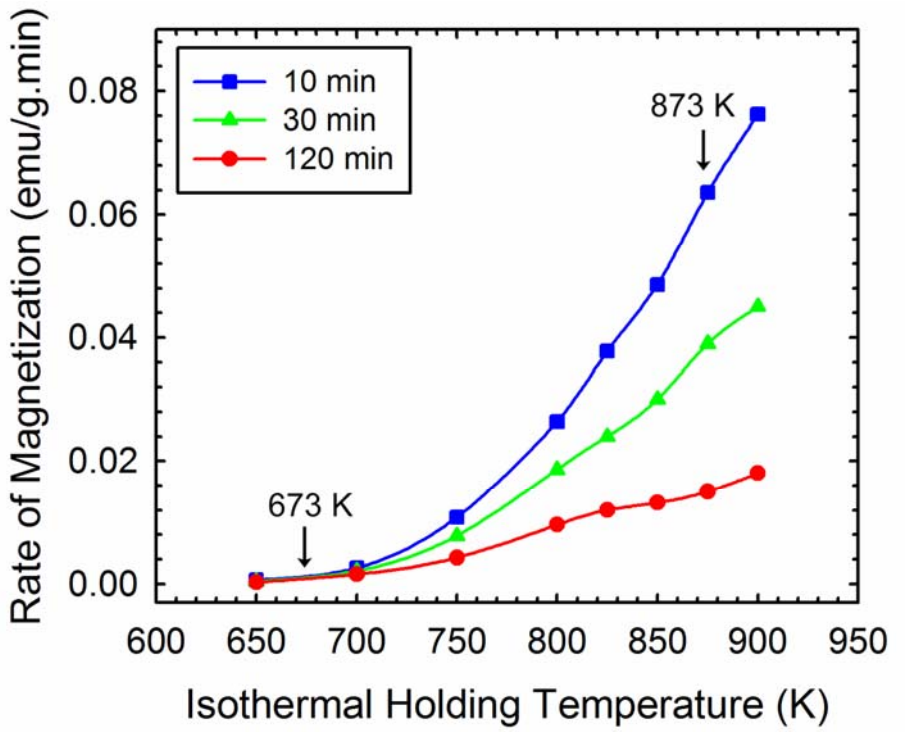

Figure 5.21 Rate of magnetization at different measurement times as a function of temperature in isothermal VSM experiments. The curves correspond to the $Ni_{50}Fe_{25}Al_{25}$ alloy.

It can be inferred from Figure 5.22 that comparable magnetization values are obtained at early stages during annealing when an annealing temperature above 900 K is employed. However, as the isothermal experiment proceeds, magnetization increments are considerably suppressed such that plateaus of lower magnetization are observed. The reason behind that the overall process becomes thermally de-activated above a certain temperature could be the competition between the diffusion controlled growth process and magnetic disordering encountered by the precipitating ferromagnetic α-phase at high temperatures. In fact, the magnetic transition of the α-phase

formed within the miscibility gap is located at a lower temperature compared to the stable gap above which the α-phase eventually dissolves.

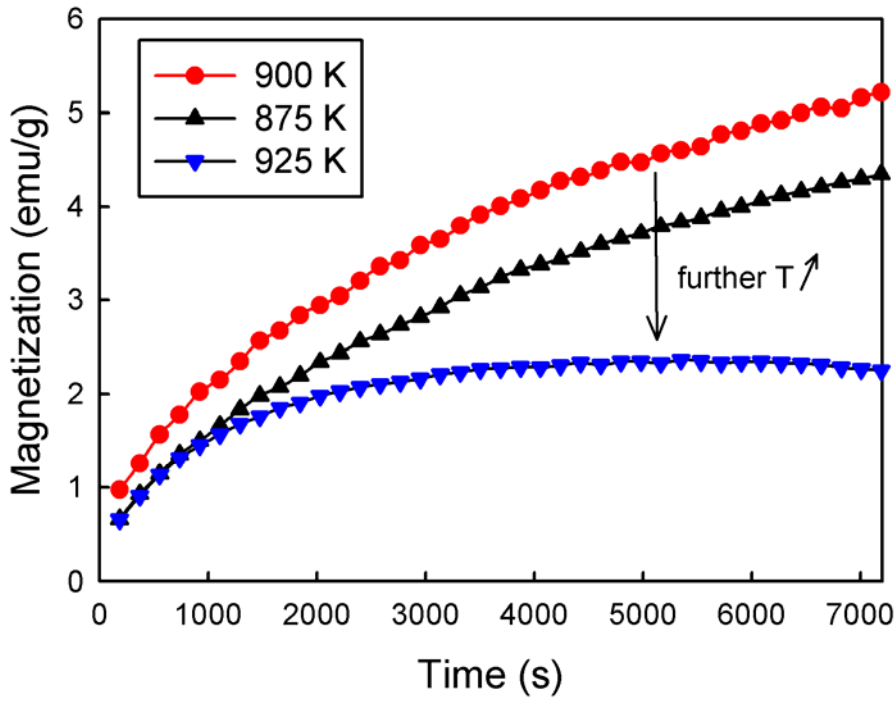

Figure 5.22 Representative example of time-dependent magnetization above the optimum isothermal temperature. The curves correspond to the $Ni_{50}Fe_{25}Al_{25}$ alloy.

Annealing at 673 K promotes the formation of fine α-Fe precipitates within the β-phase matrix that impose significant hardening (20–55% gain in hardness relative to as-cast samples) via dislocation pinning. It can be stated that these precipitates attained their optimum size because an increase in the annealing temperature to 873 K caused drops in hardness by ~10–15%. This could be related with the coarser microstructure formed at high temperatures [54] in accordance with the significant increases in rates of magnetization during isothermal scans at such high temperatures in VSM. In this respect, it is clear from Figure 5.23 that an increase in the average rate of

magnetization causes decreased micro-hardness of the primary β-phase within which ferromagnetic precipitates are formed.

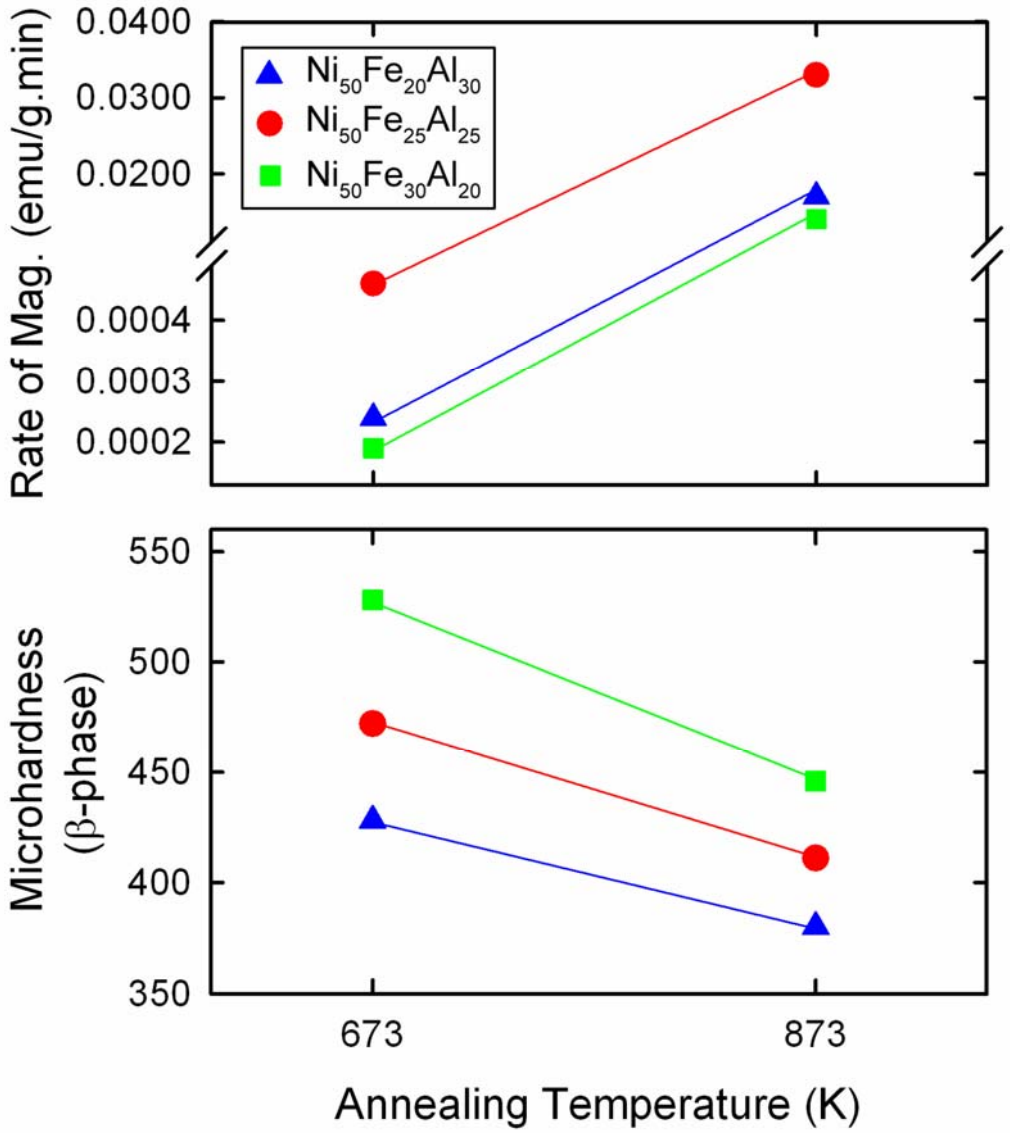

Figure 5.23 Correlation between average rates of magnetization and micro-hardness of the primary β-phase.

Figure 5.24 shows the TEM microstructures and selected area diffraction patterns of the dendritic regions in $Ni_{50}Fe_{25}Al_{25}$ alloy. The high-density fine BCC α-phase precipitates appear as bright regions in the size range of 3–5 nm distributed uniformly within the matrix of the alloy annealed at 673 K (Figure 5.24a). In conformity with reduced hardness and remarkable growth rates deduced from large average rate of magnetization at 873 K isotherm (Figure 5.23), the microstructure of the alloy annealed at this temperature is coarser and precipitate sizes lie in the range of 8–15 nm (Figure 5.24b).

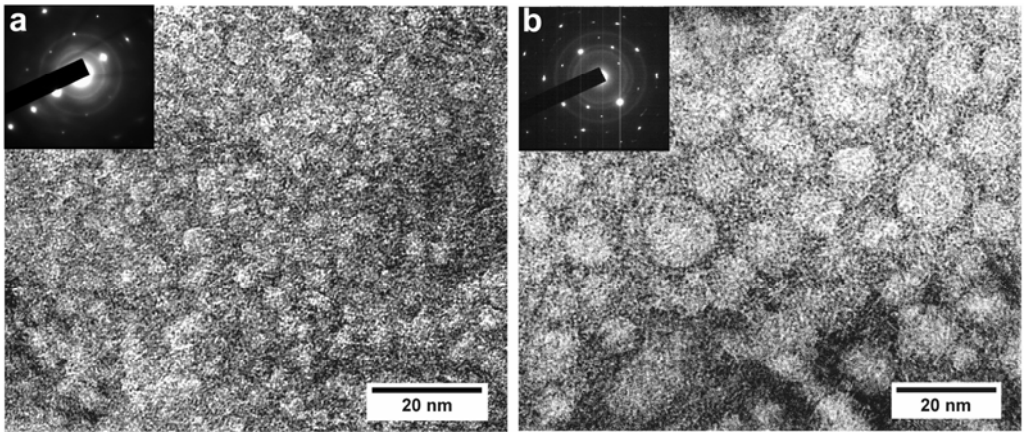

Figure 5.24 Bright field TEM micrographs and corresponding selected area diffraction patterns of $Ni_{50}Fe_{25}Al_{25}$ alloy at annealed (a) 673 K, and (b) 873 K.

Figure 5.25 shows the Avrami plots drawn for various annealing temperatures. The Avrami time exponent for the entire range of alloys are close to n = 1, indicating that the precipitation reaction follows a first order kinetics. Therefore, it can be stated that the investigated process is predominated by diffusion controlled growth [117]. The straight line fits do not significantly deviate for the whole timescale of the measurements which means that precipitation occurs without a change in its mechanism throughout the entire process.

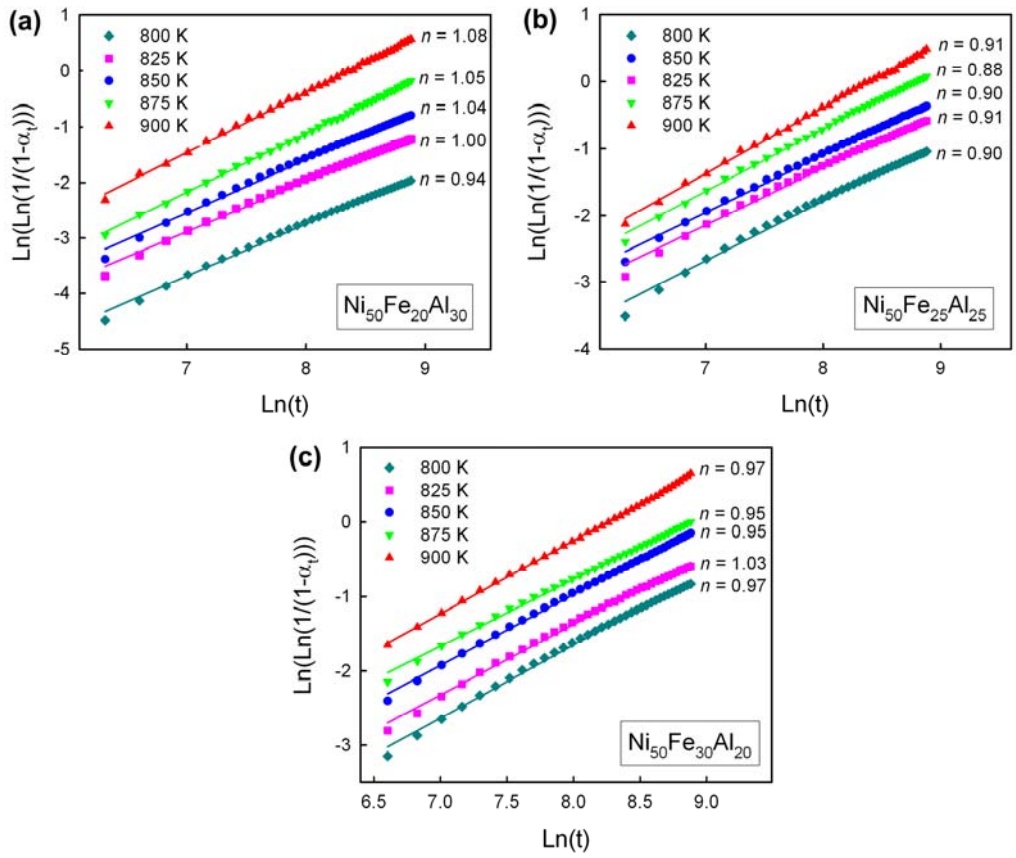

Figure 5.25 Avrami plots for (a) $Ni_{50}Fe_{20}Al_{30}$, (b) $Ni_{50}Fe_{25}Al_{25}$ and (c) $Ni_{50}Fe_{30}Al_{20}$ alloys.

Activation energies (E_a) for the growth process were determined in Figure 5.26 employing isothermal magnetization measurements at several temperatures where the ferromagnetic phase precipitates. The activation energies were found to range between 74.6 kJ/mol and 82.6 kJ/mol with a maximal deviation of ±3.5 kJ/mol. The slight differences in calculated activation energies for studied alloys might be related to variation in the composition of the primary β-phase where α crystallites precipitate.

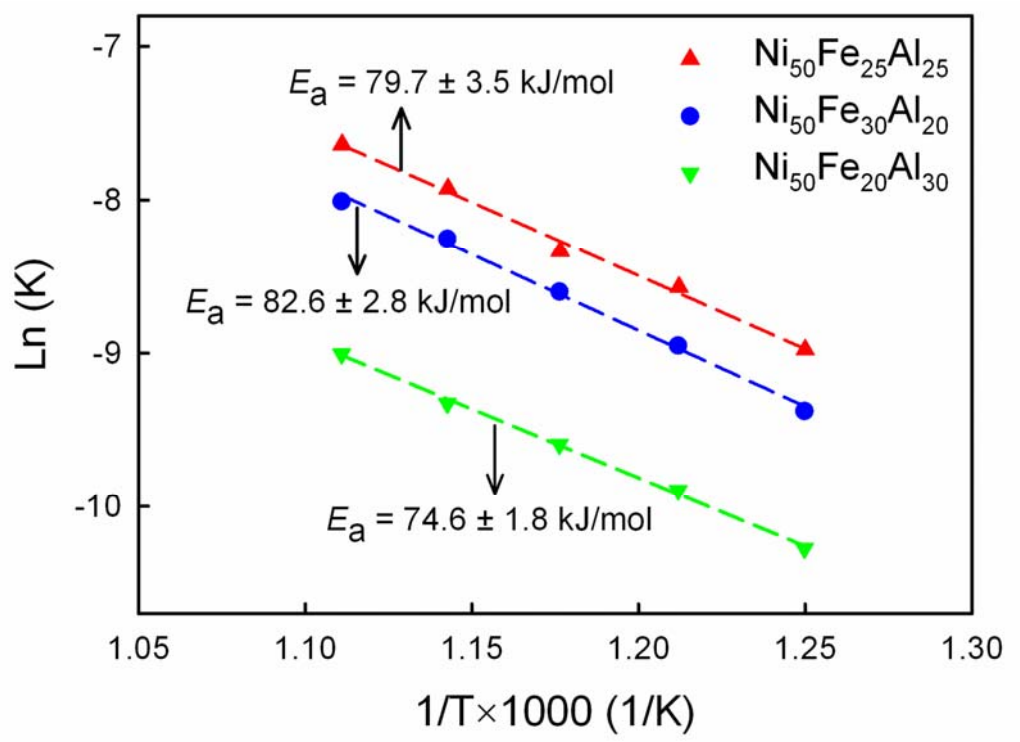

Figure 5.26 Activation energies of precipitation as monitored by magnetization measurements.

The low activation energies together with non-zero magnetizations at the beginning of isothermal measurements (no detectable incubation time) can indicate a process dominated by the growth of already existing nuclei. Considering diffusivities in ternary Ni–Al–Fe alloys, the relatively lower activation energies deduced here might also be related to compositional effects on diffusivity and influence of thermal vacancies [118].

Having found the magnetically assessed kinetic parameters (E_a, n and K), the general precipitation behavior of nano-sized BCC α-phase can be followed by plotting the isothermal transformation diagram provided in Figure 5.27 The magnetic monitoring approach is limited by the magnetic disordering temperature above which the magnetization of alloys cease and the growth process cannot be magnetically tracked. These upper limits were taken as the maxima of the derivative of temperature-scan magnetization curves (Figure

5.19). Actually, during isothermal experiments, temperatures above magnetic disordering yielded lower rates of magnetization and suppressed magnetization values. The reason why the overall process cannot be magnetically monitored above a certain temperature could be the competition between the diffusion controlled precipitation process and the magnetic disordering induced in the ferromagnetic α-phase at high temperatures.

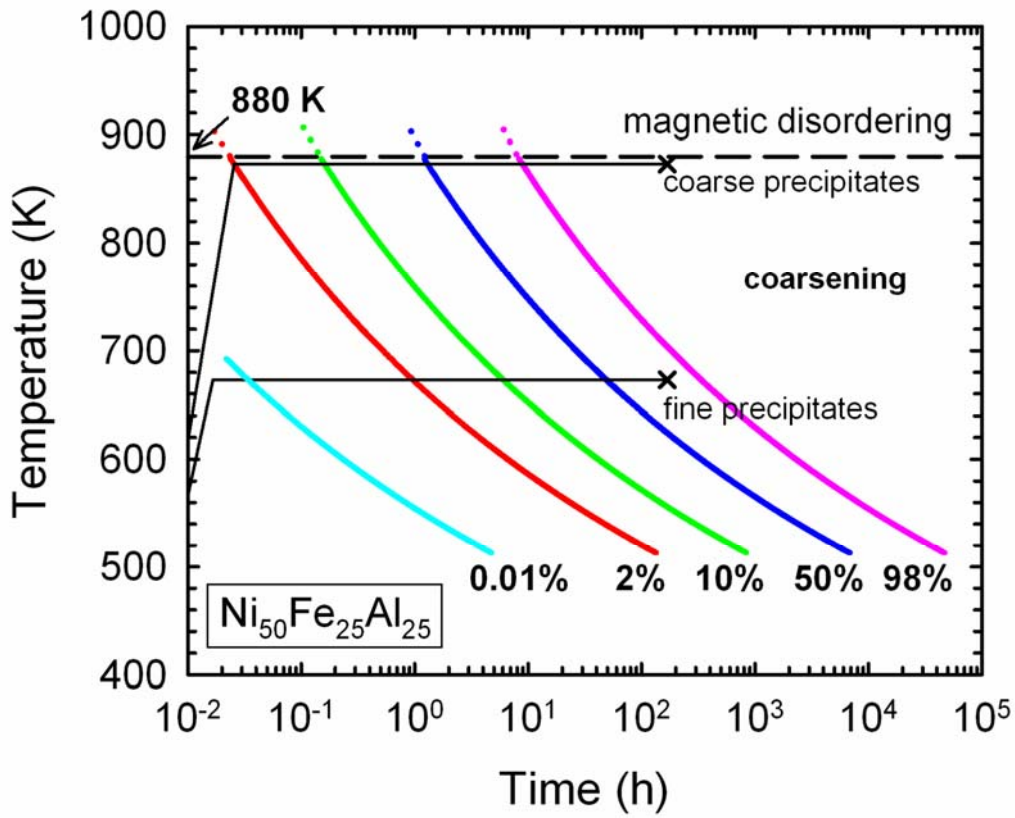

Figure 5.27 Magnetically assessed time–temperature dependence of α-phase precipitation in the $Ni_{50}Fe_{25}Al_{25}$ alloy.

The diffusion controlled growth of precipitates is highly dependent on annealing temperature and proceeds faster at a higher temperature. The completion of transformation, i.e. α~1, is referred as the state where the equilibrium fraction of α-phase precipitates is reached. For instance,

transformation will be completed at 873 K within 10 h for $Ni_{50}Fe_{20}Al_{30}$ and $Ni_{50}Fe_{25}Al_{25}$ alloys, and 6 h for the $Ni_{50}Fe_{30}Al_{20}$ alloy, and further annealing will cause the microstructure to become unstable and coarsen to a lower density of larger particles. On the other hand, at a lower annealing temperature (e.g. 673 K), transformation is almost complete in 168 h ($\alpha \approx 0.97$, 0.90, and 0.97 for $Ni_{50}Fe_{20}Al_{30}$, $Ni_{50}Fe_{25}Al_{25}$ and $Ni_{50}Fe_{30}Al_{20}$, respectively) yielding finer precipitates without further coarsening.

5.3 Microalloying Effects in Ni-Al-Fe Alloys

It is known that a major addition of Fe into the NiAl system imparts remarkable strengthening through precipitation of a fine bcc α-phase in B2 matrix [54-57, 60, 62]. It is generally accepted that fine precipitates provide the highest strengthening effect whereas balanced strength and ductility properties could be attained with a relatively coarser microstructure [104]. Therefore, the long-term performance of finely precipitated Ni-Fe-Al alloys is strongly dependent on precipitate coarsening. Apparently, it might be interesting to make slight modifications in alloy composition which would slow down coarsening by changing the precipitation kinetics, stabilizing the fine microstructure and providing retained mechanical properties at high service temperatures.

The present study concentrates on microalloying effects of Co, Mn and V as substitutes for 1 at.% Fe in Ni-25Al-25Fe alloy covering the microstructural evolution, magnetic properties and kinetics of bcc α-phase precipitation. One novelty in this study is that it employs a novel magnetic characterization technique for the determination of time and temperature dependence of nanoscale α-phase precipitates having ferromagnetic character, otherwise requiring laborious image analysis.

5.3.1 Microstructure

The representative solidification microstructures of as-cast NiAlFe-*X* alloys with substitution of Co, Mn or V for 1 at.% Fe are shown in Figure 5.28 and nominal and actual compositions are listed in Table 5.4.

The as-cast Ni-25Al-25Fe alloy possesses a typical dendritic microstructure, where dendrites are a single phase and the interdendritic regions are a eutectic phase mixture. The dendritic microstructure is retained in the presence of quaternary additions as substitutes for Fe. After analyzing the microstructures according to the systematic manual point count procedure described in ASTM E562 standards, volume fraction of the interdendritic region is found as 12 vol.%, 19 vol.% and 10 vol.% for Co, Mn and V additions, respectively. Compared to Ni-25Al-25Fe alloy with 14 vol.% interdendritic region, it becomes clear that addition of Mn increases the amount of interdendritic region while Co and V has an opposite effect.

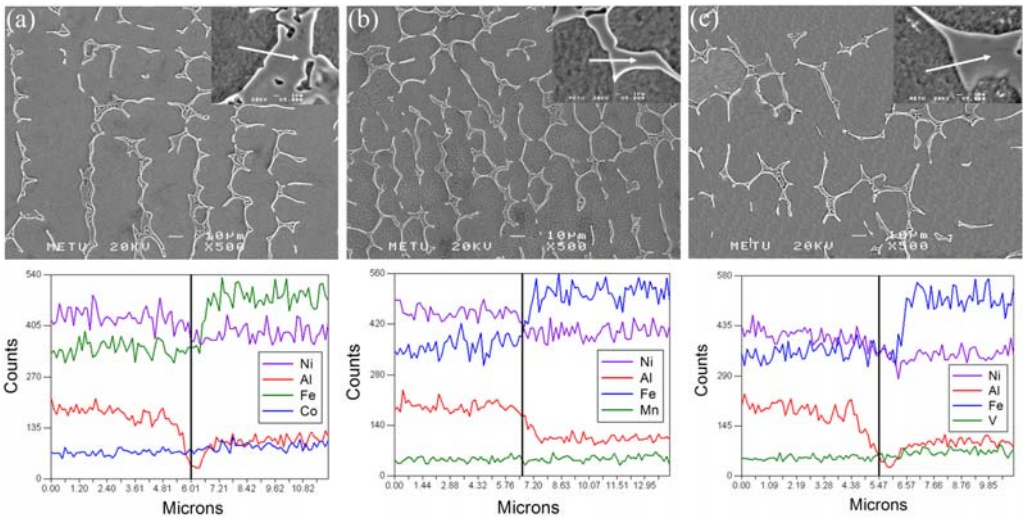

Figure 5.28 SEM micrographs and EDS line scan analyses of as-cast NiAlFe-*X* alloys where (a) *X* = Co, (b) *X* = Mn, and (c) *X* = V. Insets to SEM images show line scan positions.

Table 5.4 Nominal and actual composition of Ni-Al-Fe-X samples in at.%

Nominal Composition	Ni	Al	Fe	Co	Mn	V
$Ni_{50}Al_{25}Fe_{24}Co_1$	51	25	23	1	-	-
$Ni_{50}Al_{25}Fe_{24}Mn_1$	51	25	23	-	1	-
$Ni_{50}Al_{25}Fe_{24}V_1$	50	25	24	-	-	1

Considering the SEM-EDS line scans given in Figure 5.28, the quaternary alloying elements are dissociated both within the dendrites and in the interdendritic region. In all studied alloys, dendrites are richer in Al and poor in Fe compared to the interdendritic region due to the higher melting point phase solidifying first in the form of dendrites. During solidification, Fe atoms act as solute, and liquid surrounding the dendrite arms, which solidifies to form the interdendritic region, gets enriched in Fe. Quaternary additions also act as solute, and during solidification, melt surrounding the dendrite arms becomes enriched in Co, Mn or V. Therefore, dendrites have lower microalloying element content compared to interdendrites.

Bright field TEM image of Ni-25Al-25Fe alloy displays dendritic and interdendritic regions in its as-cast state (Figure 5.29a). The dendritic region consists of a single β-phase with B2 structure while the interdendritic region contains embedded coarse β-phase particles. The selected area electron diffraction (SAED) pattern (Figure 5.29b) taken from the matrix of the interdendritic region along [011] beam direction contains 100 and 110 superlattice reflections arising from $L1_2$ structure as well as fundamental spots from fcc lattice. Dark field image (Figure 5.29c) taken from 100 superlattice reflection reveals fine ordered γ' precipitates appearing as bright regions uniformly distributed within the disordered γ-phase matrix. The SAED pattern also indicates that ordered γ' precipitates are coherent with the disordered γ matrix.

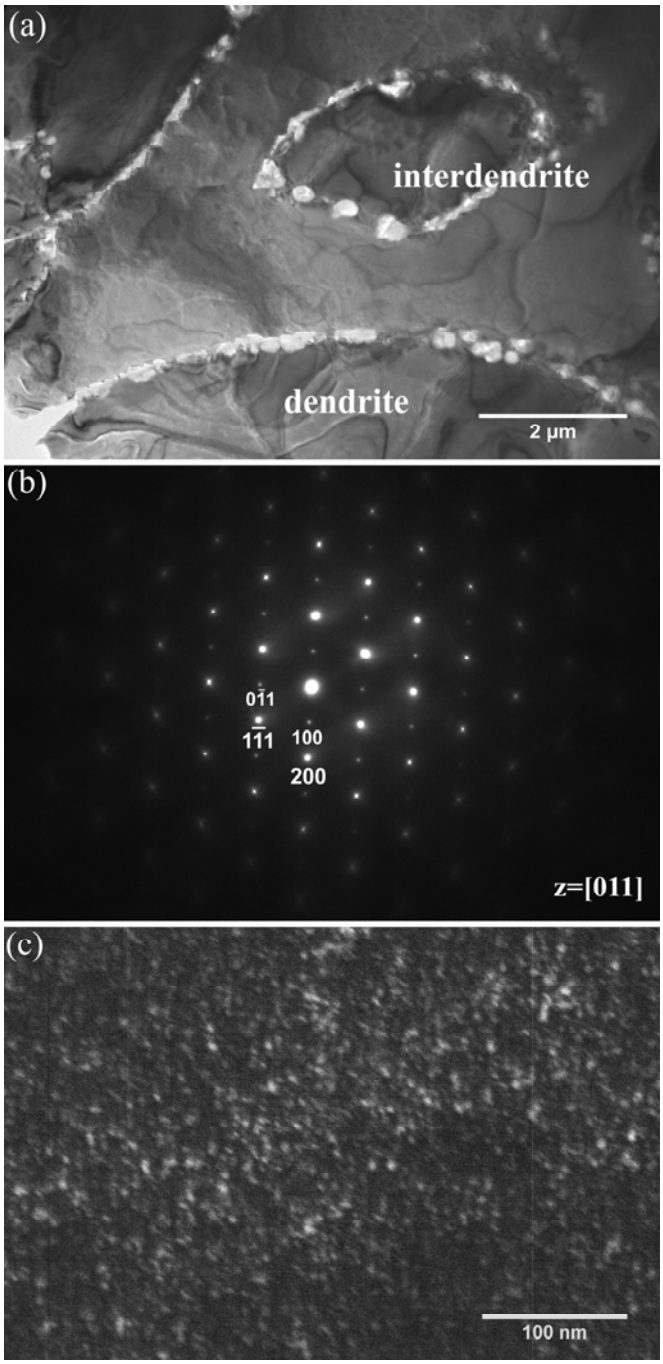

Figure 5.29 (a) Bright field TEM image of as-cast Ni-25Al-25Fe alloy showing dendritic and interdendritic regions, (b) SAED pattern taken along [011] direction of interdendrite matrix, (c) Dark field image formed using 100 superlattice reflection showing fine ordered γ' precipitates (brighter regions) inside γ-phase matrix.

Figure 5.30 contains the XRD patterns of as-cast alloys showing reflections from two apparent phases, β-phase with B2 structure in the form (Ni, Fe)(Al, Fe) and disordered γ (Ni,Fe) solid solution phase with fcc structure. However, TEM investigations reveal triple phased microstructures consisting of β, γ and ordered fcc γ' in the form $(Ni, Fe)_3(Al, Fe)$. Due to the small volume fraction of the γ'-phase and also site occupation of Fe atoms reducing the structure factor, superlattice reflections from ordered γ'-phase could not be detected by XRD.

Using XRD data, lattice parameters for the β-phase are calculated as $a_{NiAlFe\text{-}Co}$ = 0.2869 nm, $a_{NiAlFe\text{-}Mn}$ = 0.2876 nm and $a_{NiAlFe\text{-}V}$ = 0.2875 nm. The Ni-25Al-25Fe alloy without quaternary addition has a lattice parameter of a=0.2870 nm. In previous studies [119-123], Mn and Co was found to occupy the Ni sublattice whereas V extensively prefers Al sublattice sites. Since atomic radius of Co (r_{Co}=0.125 nm) almost matches those of Ni (r_{Ni}=0.125 nm) and Fe (r_{Fe}=0.126 nm), the lattice parameter of β-phase is not changed with Co incorporation into the lattice. Expansion of the β-phase lattice with V addition (r_V=0.134 nm) can be explained by the replacement of Fe^{Al} with V^{Al} anti-site defects (r_{Al}=0.143 nm). The increase in lattice parameter of β-phase with Mn addition might be explained by the replacement of Ni atoms in Ni sublattice or Fe^{Ni} anti-site defects with larger Mn atoms (r_{Mn}=0.131 nm).

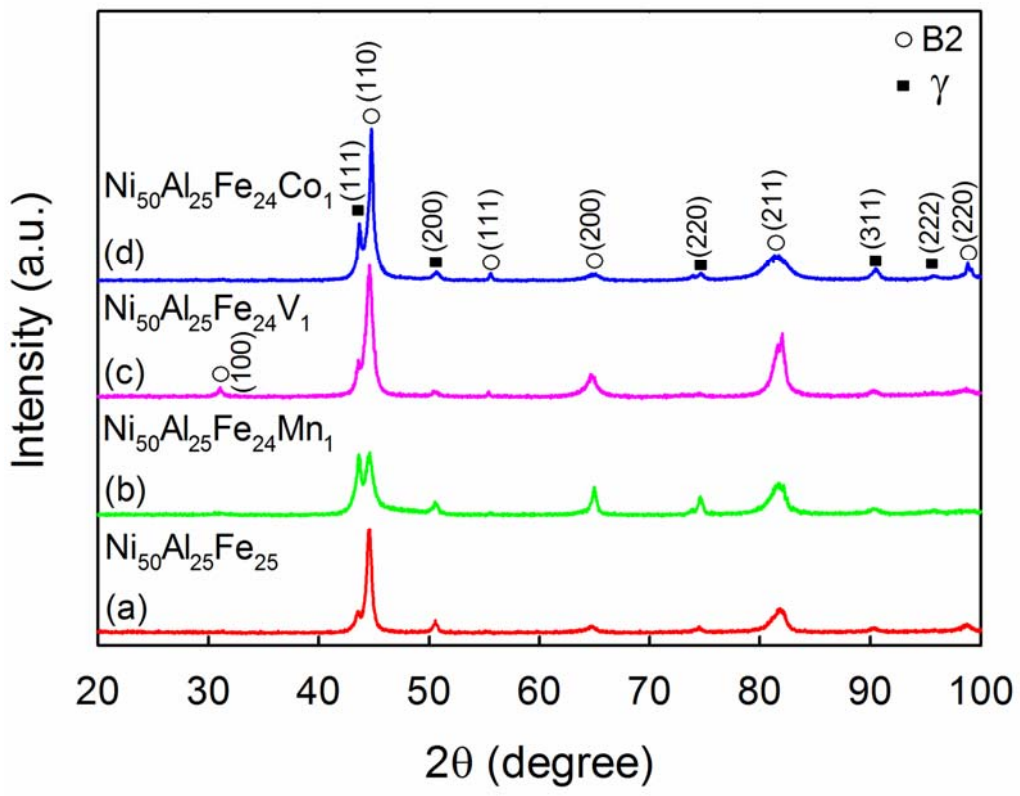

Figure 5.30 XRD patterns of as-cast (a) Ni-25Al-25Fe alloy, and, NiAlFe-*X* alloys where (b) *X* = Mn, (c) *X* = V, and (d) *X* = Co.

Additionally, due to site preference, it might also be postulated that Mn and Co addition reduces ordering of Ni atoms in the Ni sublattice, thereby affecting (100) superlattice reflections arising from the β-phase. Contrarily, the superlattice reflection is clearly seen for the V-modified alloy (Figure 5.30(c)) as an indication of ordering of Ni site and extensive V occupation of Al site. Lattice parameters of the γ-phase does not significantly varying with microalloying, a_{Co}=0.3600 nm, a_{Mn}= 0.3601 nm and a_{V}=0.3602 nm, when compared to Ni-25Al-25Fe alloy having a=0.3599 nm.

Microstructural evolution and compositional changes of constituent phases by annealing of Ni-Fe-Al-X alloys are shown in Figures 5.31–5.33 and Table 5.5, respectively.

Figure 5.31 and Figure 5.32 shows the annealed microstructures and corresponding XRD patterns of NiAlFe-Mn and NiAlFe-Co alloys, respectively. The dendritic microstructure of alloys in the as-cast state is retained with annealing. Microstructures of alloys annealed at 673 K and 873 K have many similar features, i.e. interdendritic region exhibits few β-phase particles with the same chemical composition to that of dendrites. Upon annealing at 1073 K, needle-like γ-phase precipitates are formed at a low volume fraction inside β-phase dendrites having almost the same chemical composition with γ-phase in the interdendritic region (Table 5.5). In the Co-modified alloy, growth of β-phase particles in the interdendritic region takes place so that particles attain needle-like or nearly spherical shapes upon annealing at 1073 K indicating a duplex dendrite-interdendrite microstructure.

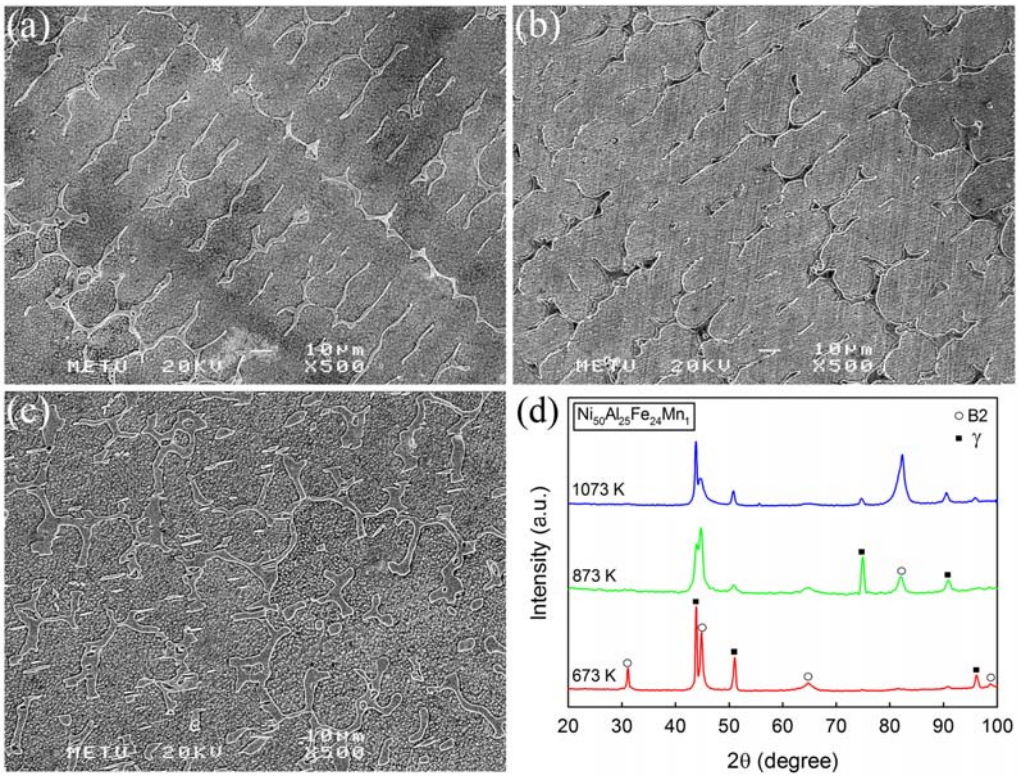

Figure 5.31 SEM micrographs of annealed NiAlFe-Mn alloy at (a) 673 K, (b) 873 K, and (c) 1073 K, and, (d) corresponding XRD patterns.

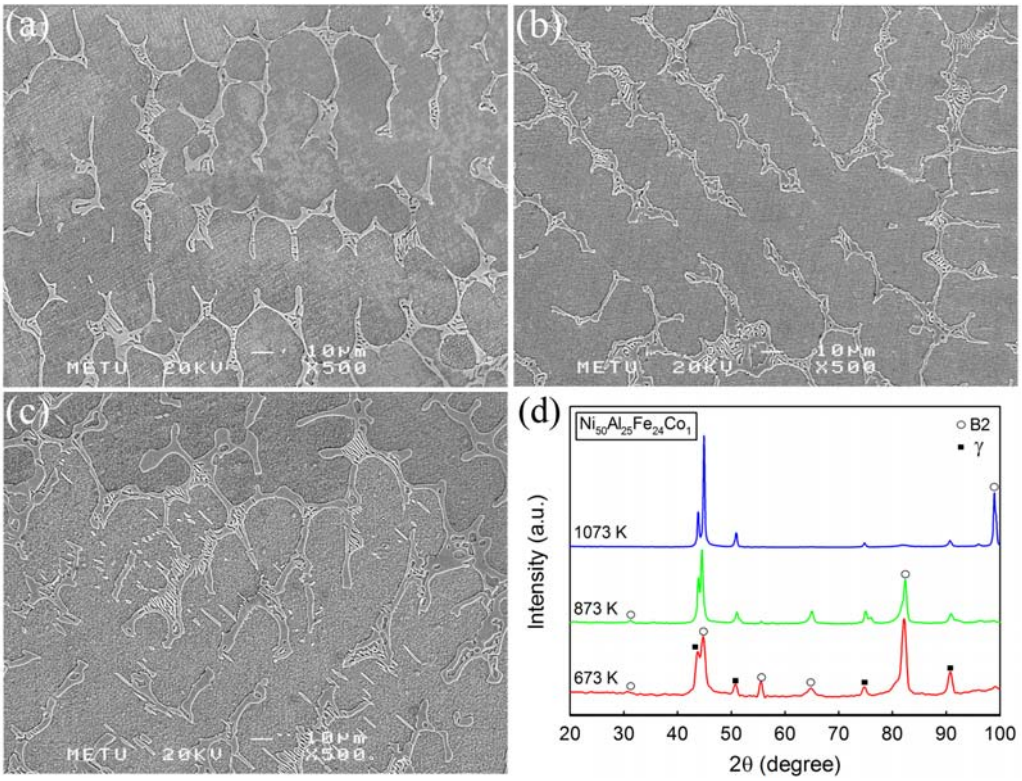

Figure 5.32 SEM micrographs of annealed NiAlFe-Co alloy at (a) 673 K, (b) 873 K, and (c) 1073 K, and, (d) corresponding XRD patterns.

Figure 5.33 displays the annealed microstructures and corresponding XRD patterns of NiAlFe-V alloy. Upon annealing at 1073 K, the dendritic microstructure vanishes and both needle-like and particle-like precipitates are seen at large volume fraction inside the β-matrix with a clear increase in XRD line intensities arising from γ-phase. The precipitation of coarse needle-like γ-phase with a large volume fraction inside brittle β-phase regions was previously shown to impart significant ductility through crack blunting mechanism [124].

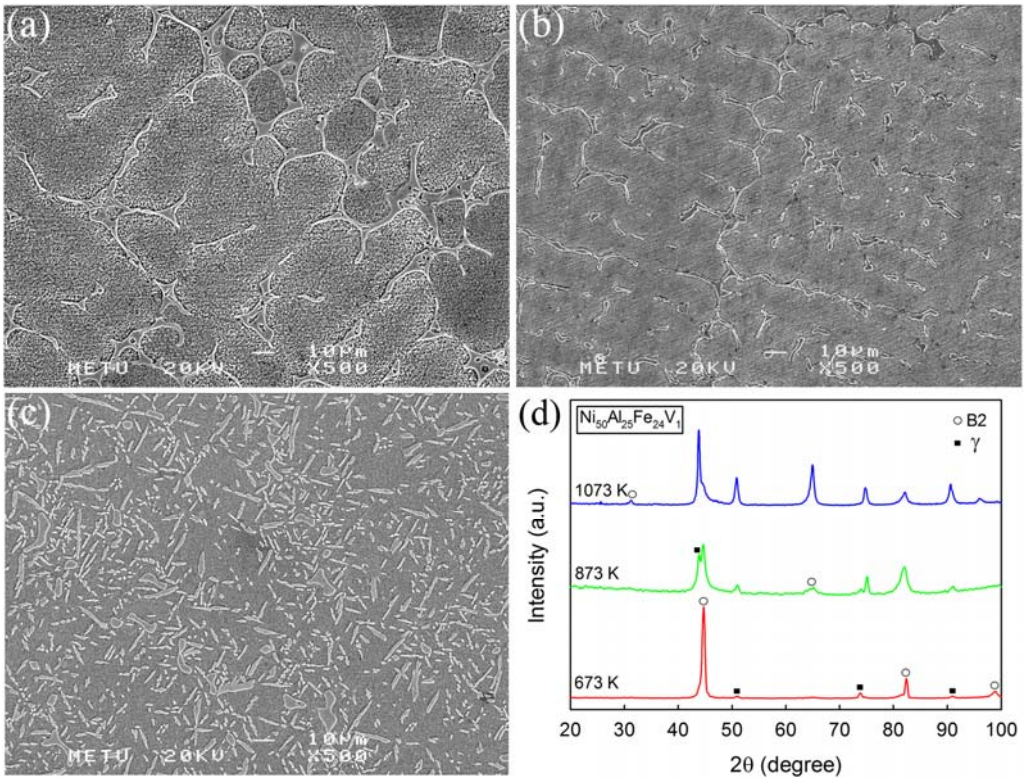

Figure 5.33 SEM micrographs of annealed NiAlFe-V alloy at (a) 673 K, (b) 873 K, and (c) 1073 K, and, (d) corresponding XRD patterns.

Table 5.5 Compositional analysis of phases in as-cast and annealed Ni-Al-Fe-X alloys.

Alloys	Phases and Chemical Compositions							
	β phase in dendrite				β phase in interdendrite			
	Ni	Al	Fe	*X*	Ni	Al	Fe	*X*
As-cast								
Ni-25Al-24Fe-1Mn	50	26	23	1	49	23	27	1
Ni-25Al-24Fe-1Co	50	26	23	1	50	23	26	1
Ni-25Al-24Fe-1V	48	29	22	1	46	24	28	1
673 K annealed								
Ni-25Al-24Fe-1Mn	50	26	23	1	50	23	26	1
Ni-25Al-24Fe-1Co	50	25	24	1	49	24	26	1
Ni-25Al-24Fe-1V	48	27	24	1	47	22	30	1
873 K annealed								
Ni-25Al-24Fe-1Mn	50	26	23	1	48	25	26	1
Ni-25Al-24Fe-1Co	49	25	25	1	48	25	26	1
Ni-25Al-24Fe-1V	49	28	22	1	46	26	27	1
1073 K annealed								
Ni-25Al-24Fe-1Mn	51	29	19	1	51	29	19	1
Ni-25Al-24Fe-1Co	52	28	19	1	52	28	19	1
Ni-25Al-24Fe-1V	49	30	20	1				

Table 5.5 Compositional analysis of phases in as-cast and annealed Ni-Al-Fe-X alloys. (continued)

Alloys	Phases and Chemical Compositions							
	γ phase in interdendrite				γ precipitate in dendrite			
	Ni	Al	Fe	*X*	Ni	Al	Fe	*X*
As-cast								
Ni-25Al-24Fe-1Mn	46	12	41	1				
Ni-25Al-24Fe-1Co	46	13	40	1				
Ni-25Al-24Fe-1V	41	12	44	3				
673 K annealed								
Ni-25Al-24Fe-1Mn	46	13	40	1				
Ni-25Al-24Fe-1Co	47	13	39	1				
Ni-25Al-24Fe-1V	43	12	42	3				
873 K annealed								
Ni-25Al-24Fe-1Mn	46	13	40	1				
Ni-25Al-24Fe-1Co	47	13	39	1				
Ni-25Al-24Fe-1V	42	12	43	2				
1073 K annealed								
Ni-25Al-24Fe-1Mn	41	7	51	1	40	7	52	1
Ni-25Al-24Fe-1Co	42	8	49	1	41	7	50	2
Ni-25Al-24Fe-1V					36	7	54	3

Further TEM investigations on annealed alloys at 673 K and 873 K show no significant change in phases where dendritic regions maintain single β-phase with B2 structure and the γ-phase matrix of interdendritic regions still contains ordered γ' precipitates in addition to a few embedded β-phase particles. Figure 5.34 displays bright field TEM images of alloys annealed at 873 K where SAED patterns taken from the matrix of the interdendritic regions involve superlattice reflections of ordered γ' precipitates in addition to fundamental spots arising from fcc lattice.

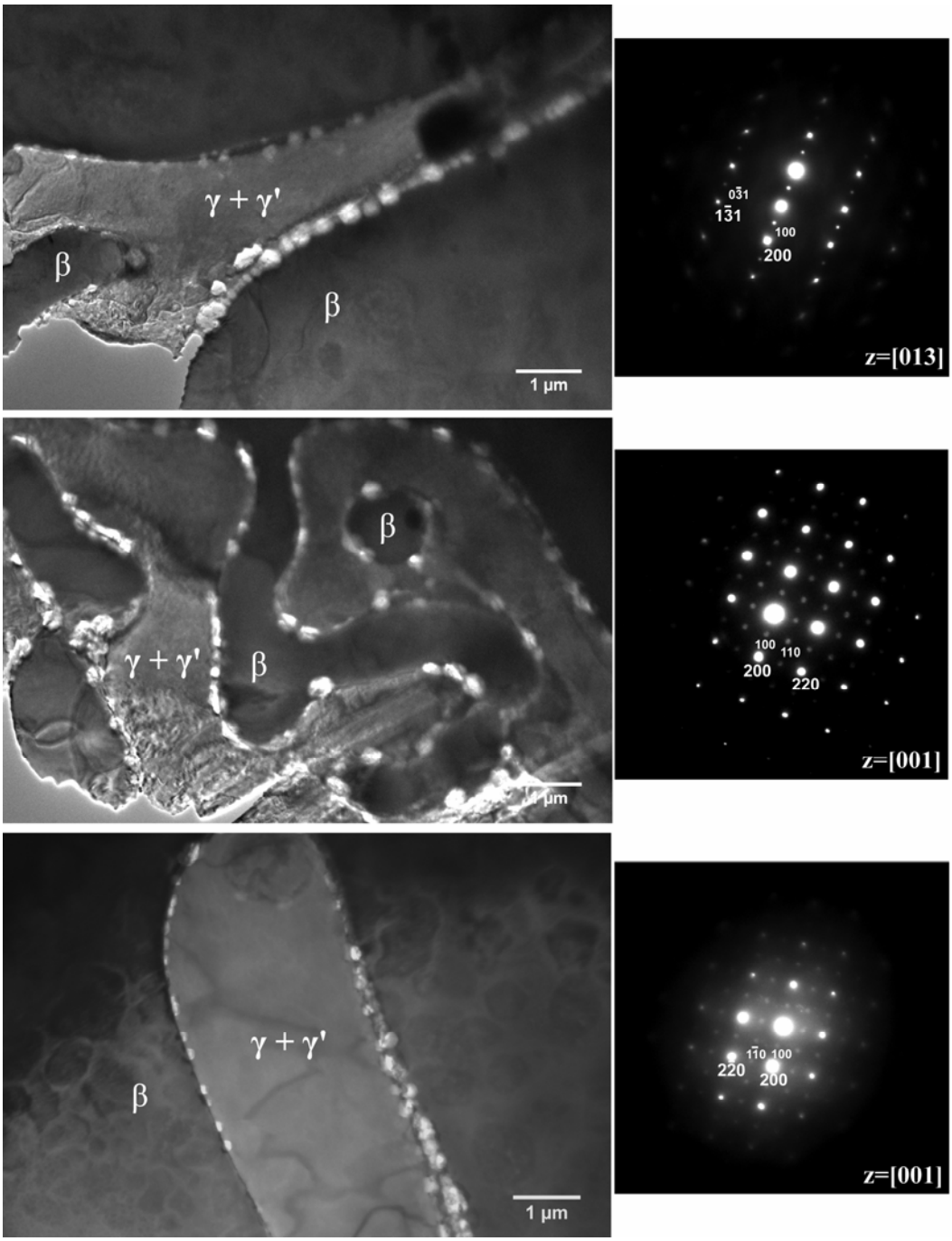

Figure 5.34 Bright field TEM images and SAED patterns of interdendrite matrix in 873 K annealed NiAlFe-*X* alloys where (a) *X* = Mn, (b) *X* = Co, and (c) *X* = V.

Figure 5.35 shows TEM images of 1073 K annealed alloys with quaternary additions where SAED patterns of the interdendrite matrix lack 100 and/or 110 superlattice reflections. Therefore, it can be stated that ordered γ' (Ni, Fe)$_3$Al phase dissolves into the disordered γ matrix which conforms to the ternary phase diagram where equilibrium phases at 1073 K are ordered β and disordered γ [55, 61]. The disordering transition takes place by the diffusion of Al to the β-phase particles in the interdendritic region promoting their growth. In fact, composition of γ-phase in the interdendritic region changed with annealing at 1073 K so that Al content is reduced around 12–13 at.% in as-cast or 673 K / 873 K annealed states to 7–8 at.% in 1073 K annealed state (Table 5.5). In addition to phase transformations within the interdendritic region of Mn- and Co-modified alloys, needle-like disordered γ-phase precipitates start to form within dendrites upon annealing at 1073 K. For the V-modified alloy, the dendritic microstructure is lost and the alloy consists of needle-like disordered γ-phase inside β-phase matrix (Figure 5.35(c)).

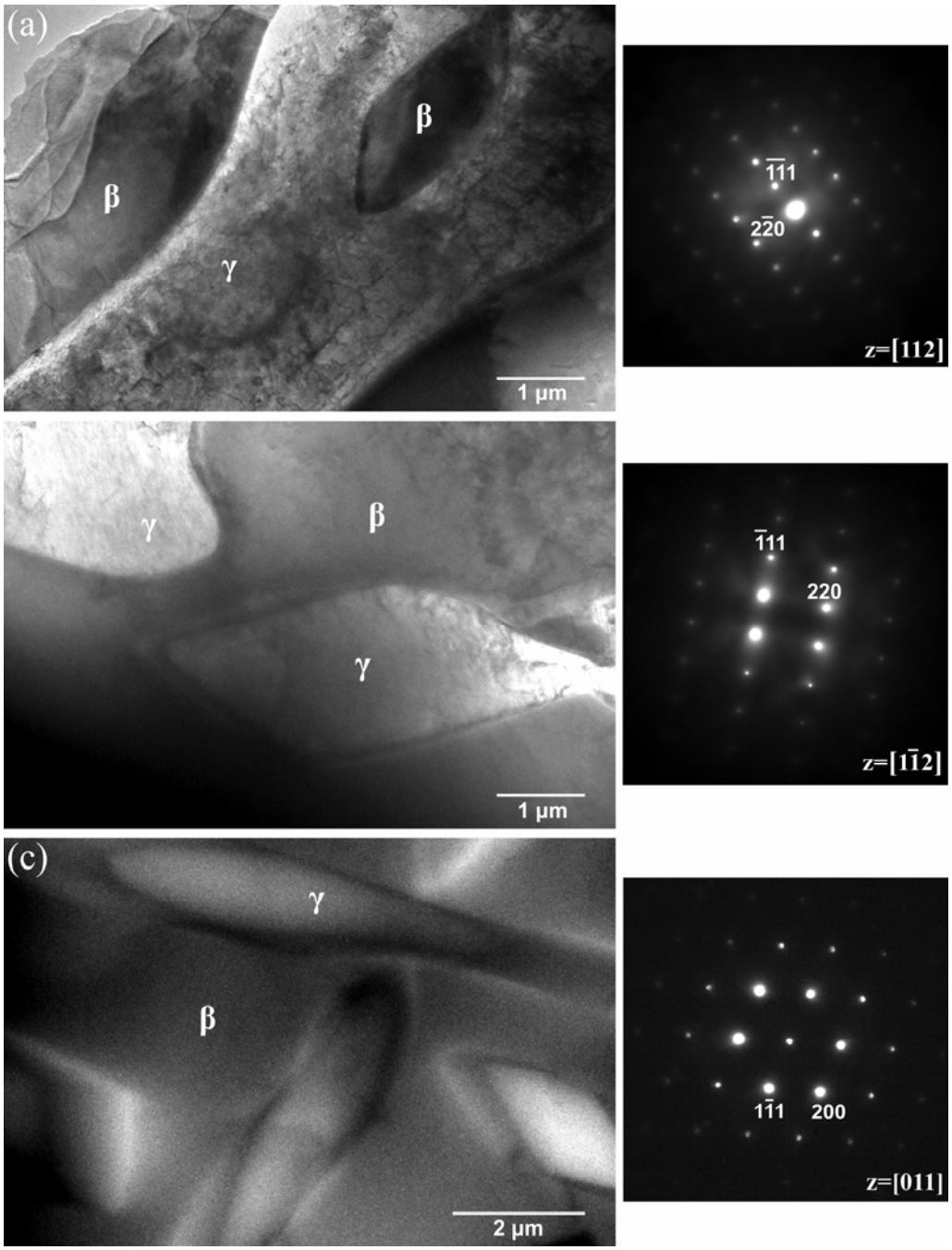

Figure 5.35 Bright field TEM images and SAED patterns of γ-phase in 1073 K annealed NiAlFe-*X* alloys where (a) *X* = Mn, (b) *X* = Co, and (c) *X* = V.

5.3.2 Microhardness and Magnetic Properties

Figure 5.36(a) shows the microhardness of the β-phase in as-cast and annealed alloys containing quaternary additions. Quaternary additions behave differently such that V induces remarkable hardening of the β-phase while Co and Mn impart an opposite effect. This can be ascribed to different site occupancy and solid solution hardening effects of the quaternary elements in the β-phase. Due to site preference of Mn and Co atoms, ordering of Ni atoms in the Ni sublattice is reduced which might be causing solid solution softening of the β-phase in the as-cast state. Through the replacement of Fe^{Al} with V^{Al} anti-site defects with V addition, hardening of the β-phase is promoted since V is a more potent strengthener at Fe^{Al} sites causing lattice dilation.

Annealing of alloys causes remarkable changes in the microhardness of the β-phase where similar trends are observed for different quaternary additions. Highest hardening effect is seen when an intermediate annealing temperature (673 K) is utilized. It is interesting to note that the exact optimum temperature also persists (i.e. 673 K) for saturation magnetization of annealed alloys (Figure 5.36(b)). This could be attributed to the precipitation of second phase particles possessing ferromagnetism. The precipitating ferromagnetic phase is an Fe-rich bcc formed within the miscibility gap between ordered (B2) and disordered bcc α-Fe phases [60, 61, 109] which strengthens the alloy via precipitation hardening through dislocation pinning effect [54, 58, 62]. Annealing at 873 K causes softening of the β-phase by coarsening of α-phase precipitates, and, annealing at 1073 K decreases the microhardness to values similar to those in the as-cast state which can be explained by the dissolution of precipitates above the miscibility gap. Saturation magnetization decreased when an annealing temperature above 673 K is used which can be explained by changes in the chemical composition of ferromagnetic α-phase precipitates with 873 K

annealing, and dissolution of ferromagnetic precipitates with 1073 K annealing. Saturation magnetization of NiAlFe-V alloy annealed at 1073 K is below that of the as-cast NiAlFe-V which could be related to the substantial increase in the volume fraction of γ-phase in expense of the β-phase as can be inferred from SEM micrographs in Figure 5.33.

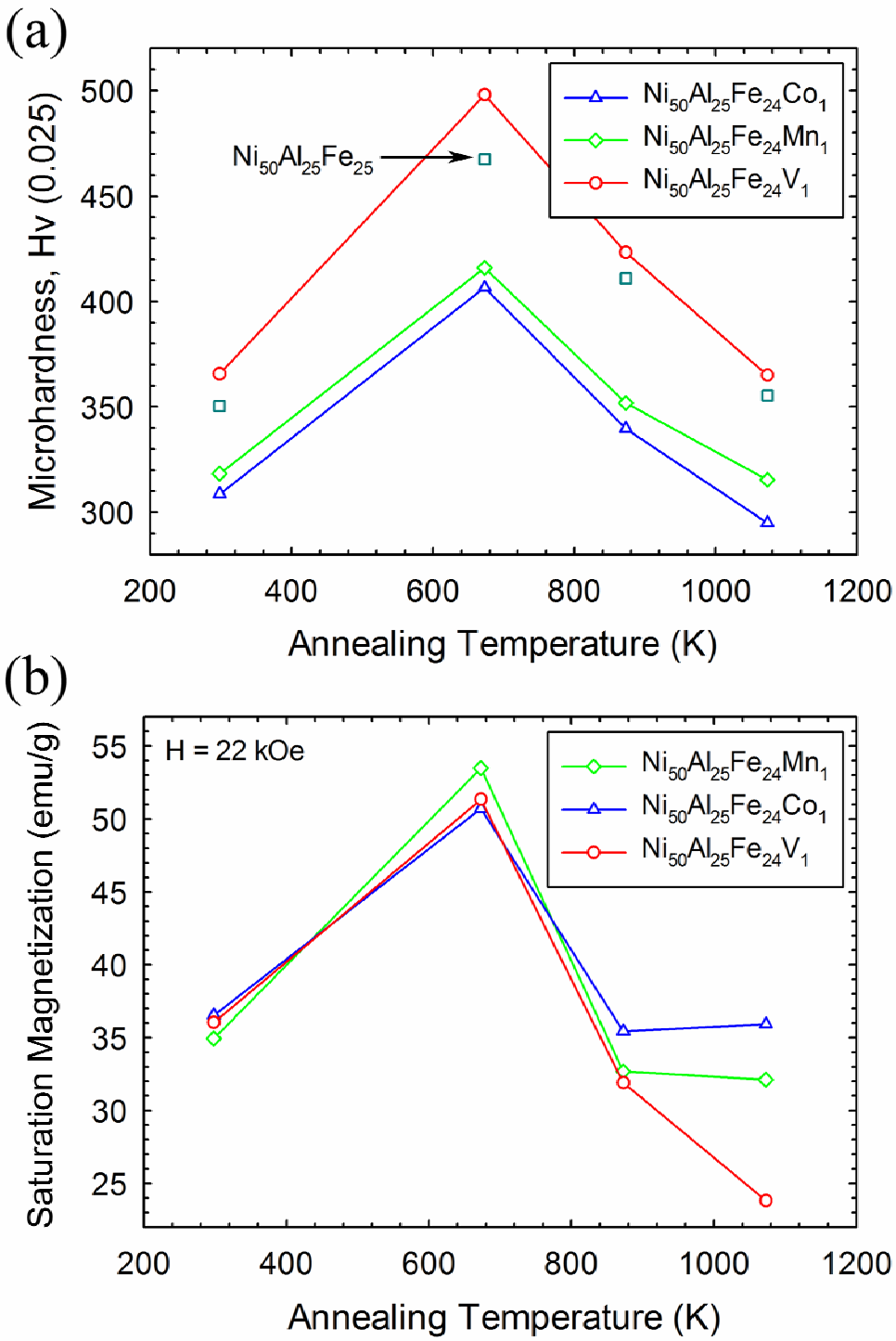

Figure 5.36 Correlation of (a) microhardness of β-phase, and (b) room temperature saturation magnetization in annealed alloys.

The bright field TEM micrograph given in Figure 5.37 for the NiAlFe-V alloy annealed at 873 K for 168 h contains fine spherical precipitates in β-phase matrix. In addition to the fundamental spots from bcc lattice, small 100 superlattice spots are evident in the SAED pattern recorded along [001] direction (Figure 5.37(b)). No extra reflections could be observed in the SAED pattern that could arise from precipitates with different crystal structure. This confirms that fine precipitates appearing as bright regions in the TEM image (Figure 5.37(a)) are coherent disordered bcc α-Fe precipitates inside an ordered matrix [54, 62, 102].

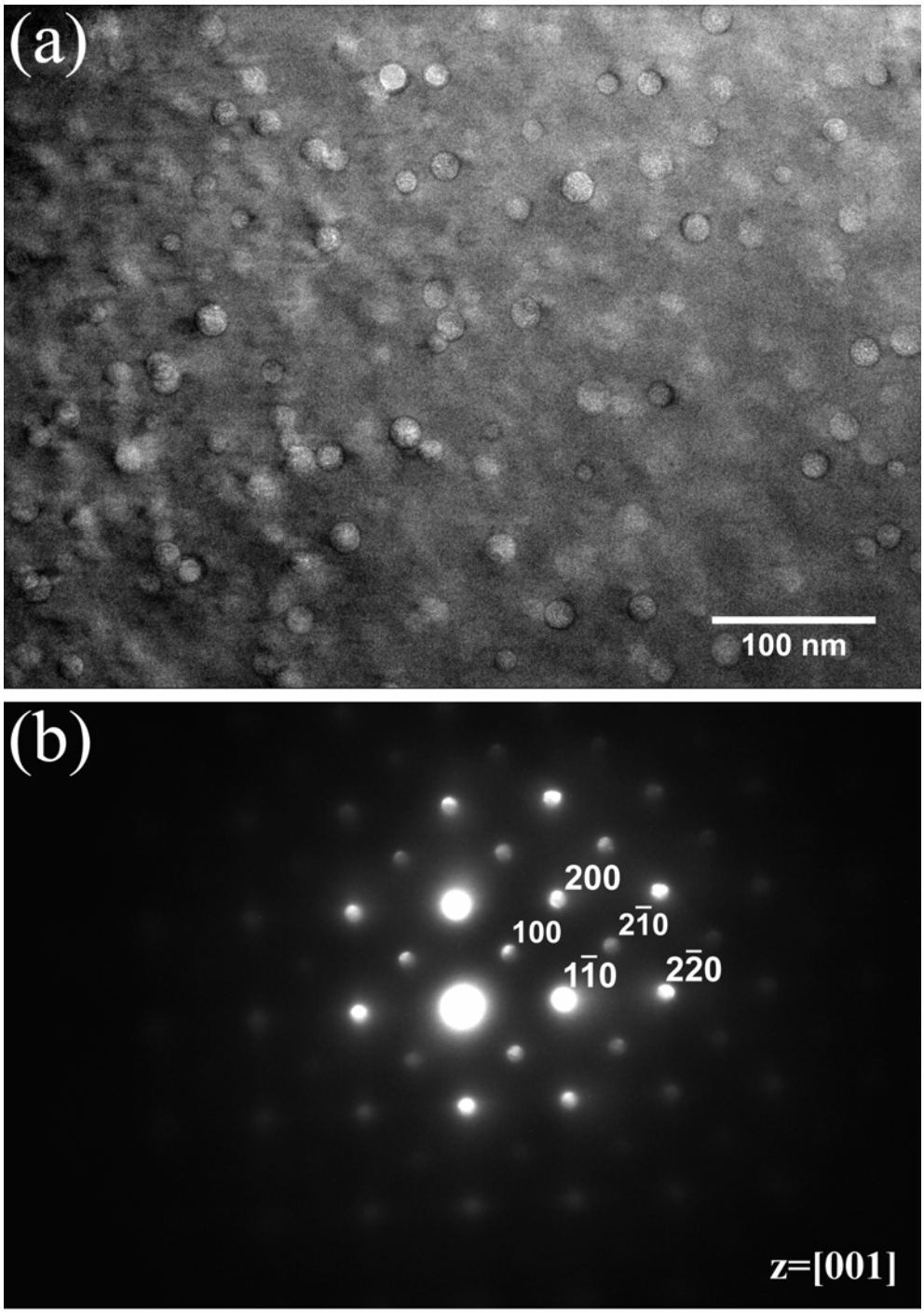

Figure 5.37 (a) Bright field TEM image of β-phase NiAlFe-V alloy following annealing at 873 K for 168 h, and (b) corresponding SAED pattern taken along [001] direction of β-phase.

It can be seen from Figure 5.29 and 5.34 that the interdendritic regions of as-cast and 673/873 K annealed NiAlFe-V alloy are surrounded by bright regions at the γ/β interface boundary which were not evident in the 1073 K annealed alloy. Representative interface boundaries for 673 K annealed alloy where the mentioned regions are clearly observed in the bright-field TEM micrographs in Figure 5.38 (a-b). The SAED pattern in Figure 5.38(c) taken from the interface boundary contains diffraction spots both from the β dendrite and interdendritic γ/γ' phases. The dark-field micrograph (Figure 5.38d) recorded from superlattice reflection of the β phase reveals that disordered α-Fe precipitates with dark contrast are uniformly distributed in the β-grain interior while ordered regions with brighter contrast are concentrated in the vicinity of β/γ interface boundary. Energy dispersive spectra recorded from β- and γ/γ' grain interiors, and β/γ interface boundary are shown in Figure 5.38(e). It can be stated that the boundary layer demonstrates lower Fe and higher Al content compared to β- and γ/γ' grain interiors. Therefore, further examination of the interface by detailed TEM studies revealed that those bright regions might correspond to a transition region which undergoes selective etching during electropolishing.

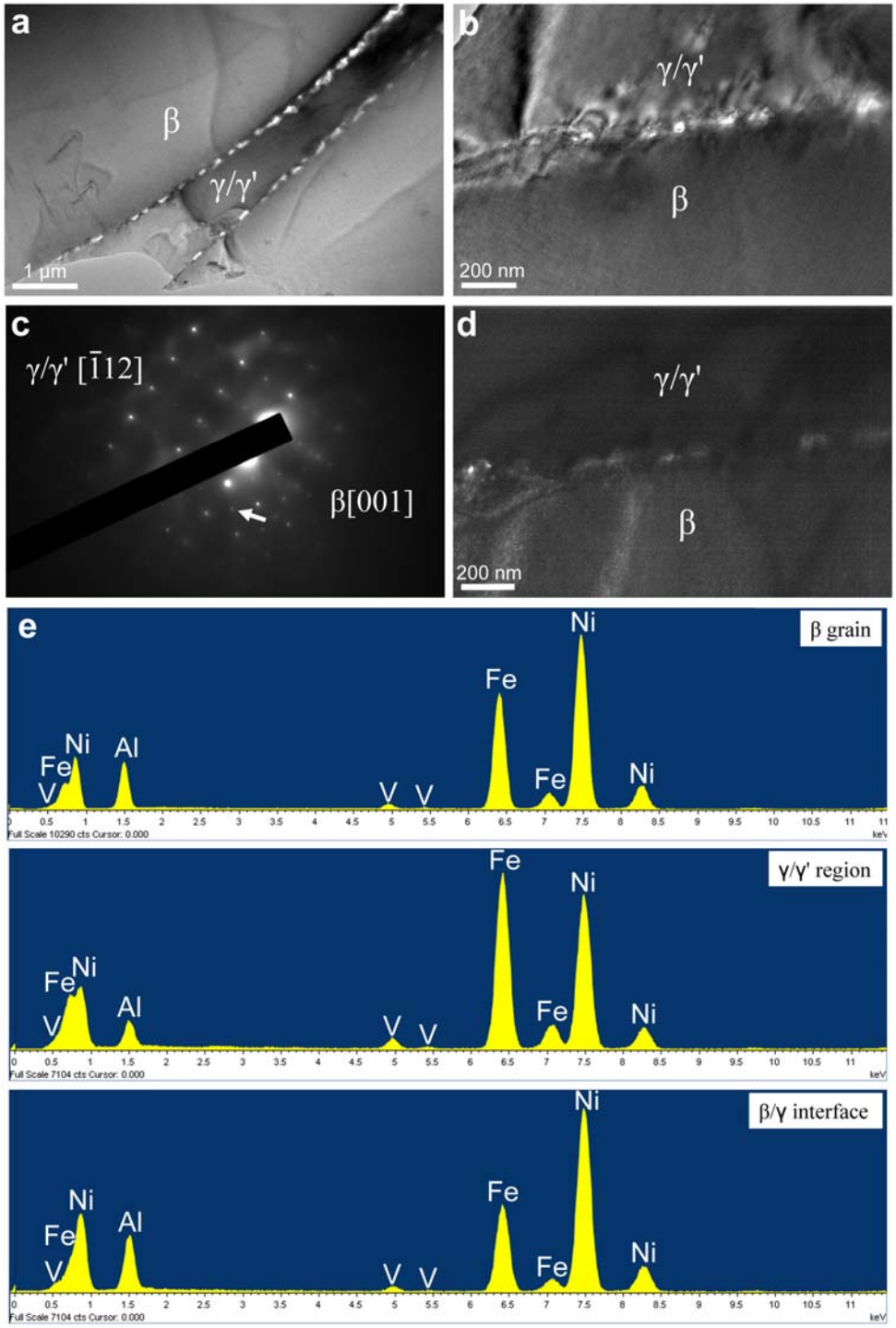

Figure 5.38 TEM images of NiAlFe-V alloy annealed at 673 K; (a-b) bright-field micrographs, (c) SAED pattern taken from the interface boundary, (d) dark-field micrograph taken from superlattice reflection of the β-phase, and (e) EDS analyses of grain interiors and interface boundary.

5.3.3 Mechanical Properties

The suction-cast solidification microstructures of Co, Mn and V microalloyed $Ni_{50}Al_{25}Fe_{25}$ alloys are shown in Figure 5.39. In all three alloys, no significant changes in the morphology and volume fraction of dendritic and interdendritic regions can be seen when compared with the as-cast microstructures prior to suction casting shown in Figure 5.28. Considering Co- and V- modified alloys, the interdendritic region is almost completely composed of the γ-phase with minor β-phase particles embedded inside the γ-phase. Similar to as-cast microstructures prior to suction casting, the volume fraction of the interdendritic region and the amount of embedded β-phase particles are slightly higher in the suction-cast Mn-modified alloy.

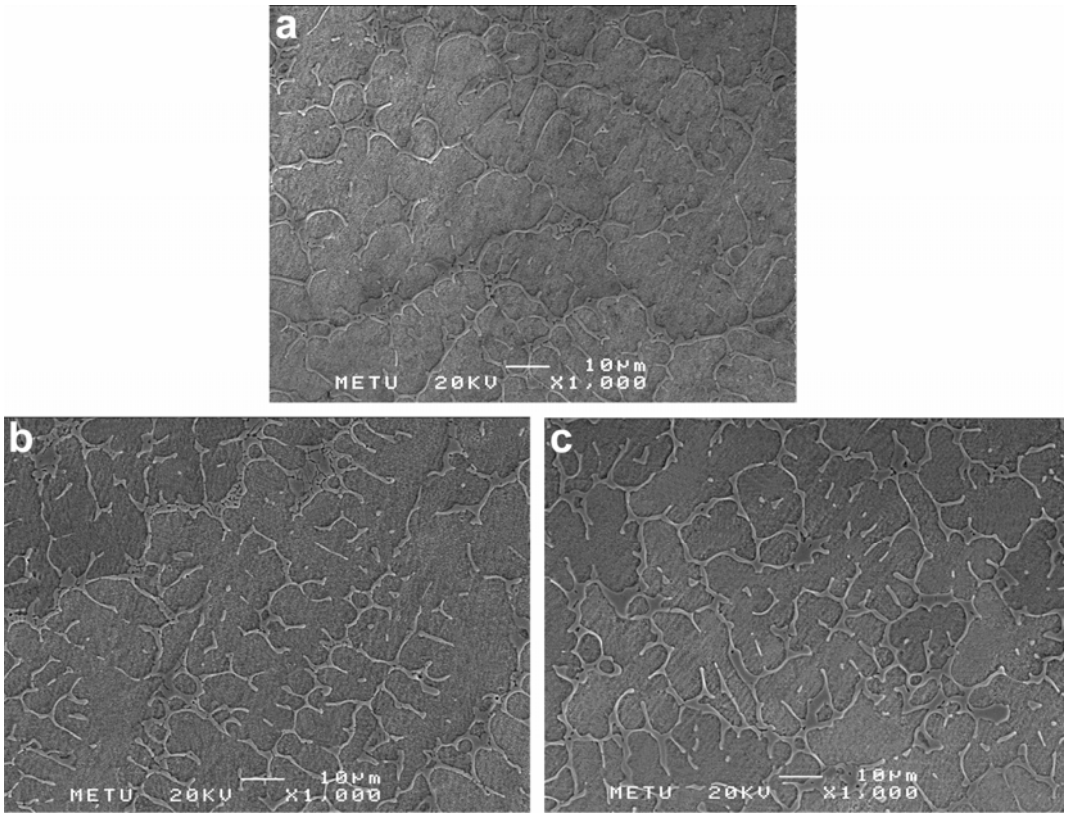

Figure 5.39 Suction-cast solidification microstructure of NiAlFe-X alloys where X= (a) Co, (b) Mn and (c) V.

Ni-Al-Fe alloys with Co, Mn and V microalloying possess two-phase microstructures composed of hard β-phase dendrites and softer interdendritic γ-phase. The compressive yield strength of Fe_{25} (850 MPa) is improved by V to 1050 MPa and deteriorated by Co and Mn to 850 MPa and 780 MPa, respectively. The changes in σ_y are in good agreement with those observed for the β-phase microhardness which was explained in the preceding section by long-range order and solid solution hardening mechanisms. It can be inferred from stress-strain behaviors given in Figure 5.40 that ductility of Fe_{25} alloy is slightly impaired by microalloying, especially by V modification. The stress-strain behavior of modified alloys annealed at 673 K, i.e. the optimum temperature where nanoscale precipitation occurs inside β-phase dendrites, are shown in Figure 5.40(b). It

is clear that there exist slight σ_y and ductility differences among different modifications, V providing the highest σ_y but the lowest ductility. Figure 5.41 shows the influence of annealing on the stress-strain behavior of V-modified Ni-Al-Fe alloy. It becomes clear that ductility and thus σ_f are reduced with annealing at 673/873 K and recovered by annealing at 1073 K.

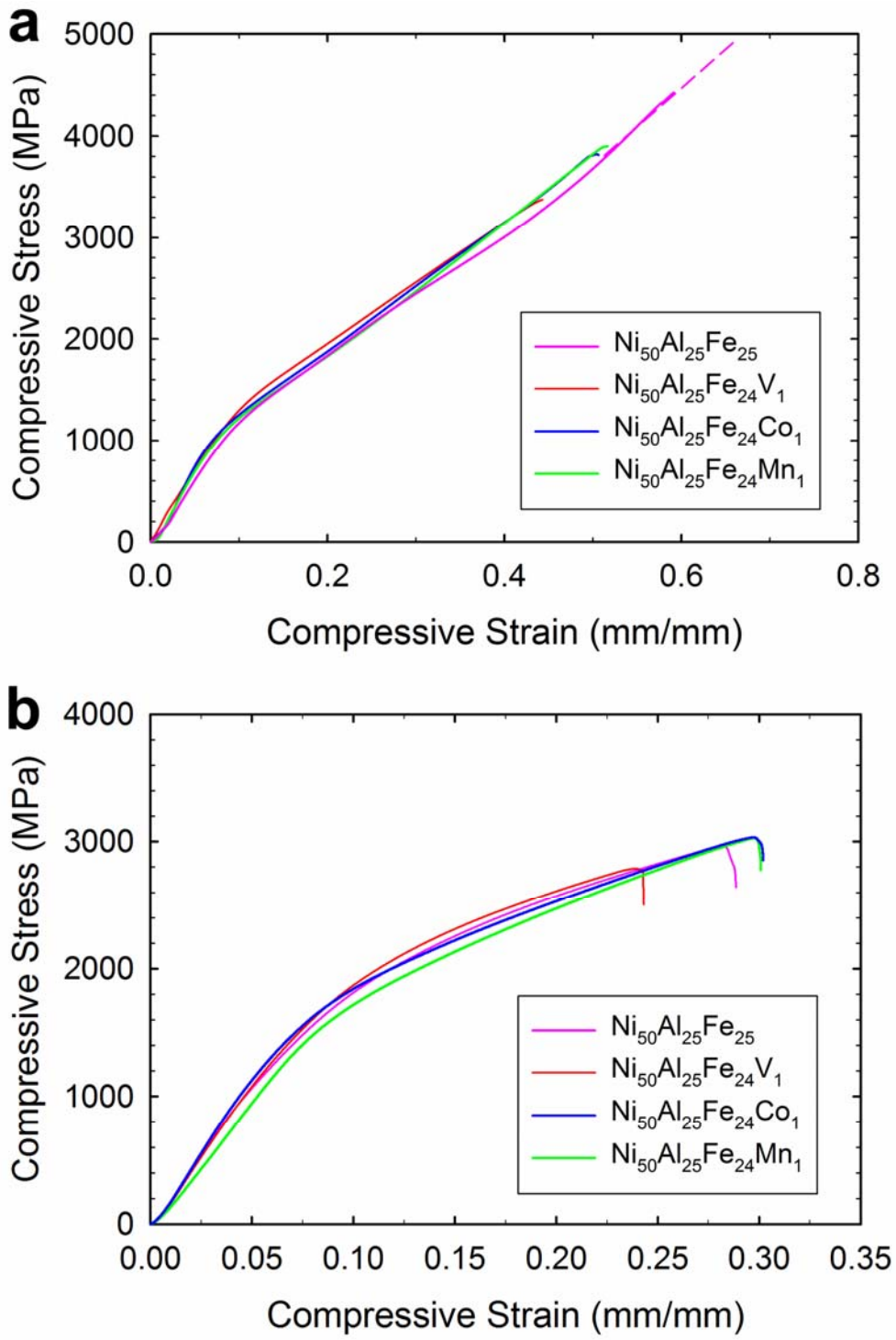

Figure 5.40 Compressive stress-strain behavior of alloys showing the influence of microalloying on (a) as-cast alloys and (b) alloys annealed at 673 K.

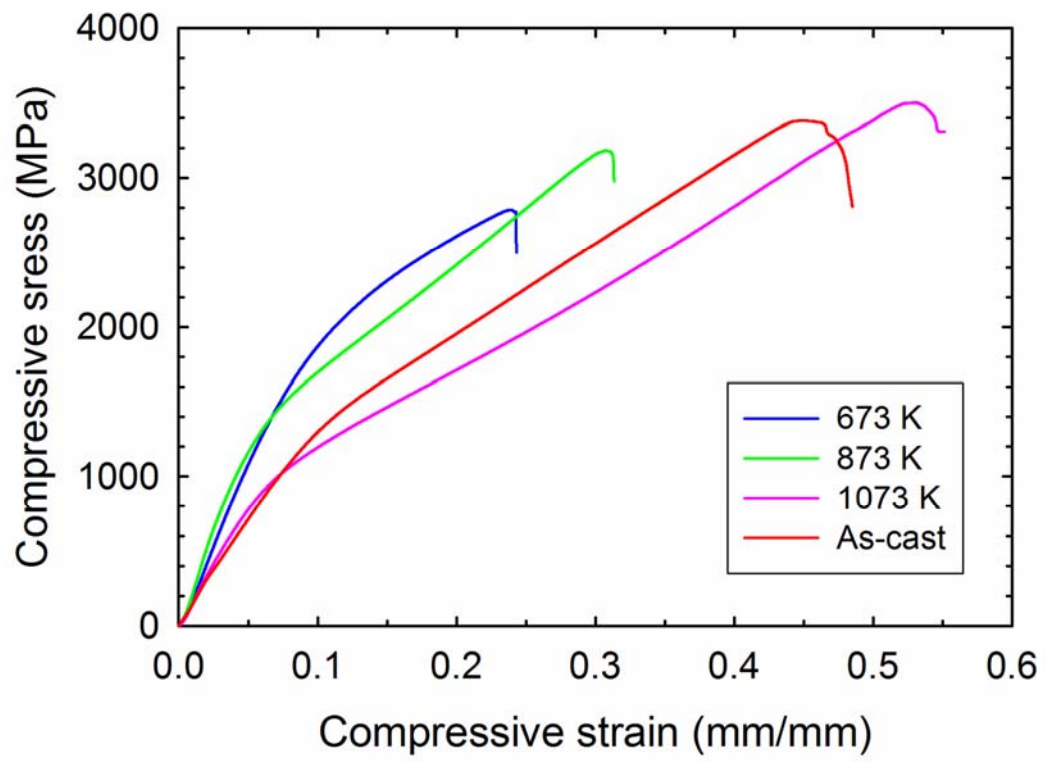

Figure 5.41 Compressive stress-strain behavior of annealed V-modified Ni-Al-Fe alloy.

The temperature dependence of σ_y shown in Figure 5.42 correlates well with the variation in β-phase microhardness by annealing as discussed in the preceding section (Figure 5.36). It can be summarized that there exists an optimum temperature where the fine-sized disordered a-phase precipitates are formed inside β-phase dendrites providing remarkable precipitation strengthening. Above that optimum annealing temperature, the α-phase either dissolves within the β-phase or coarsens not to provide significant strengthening effect.

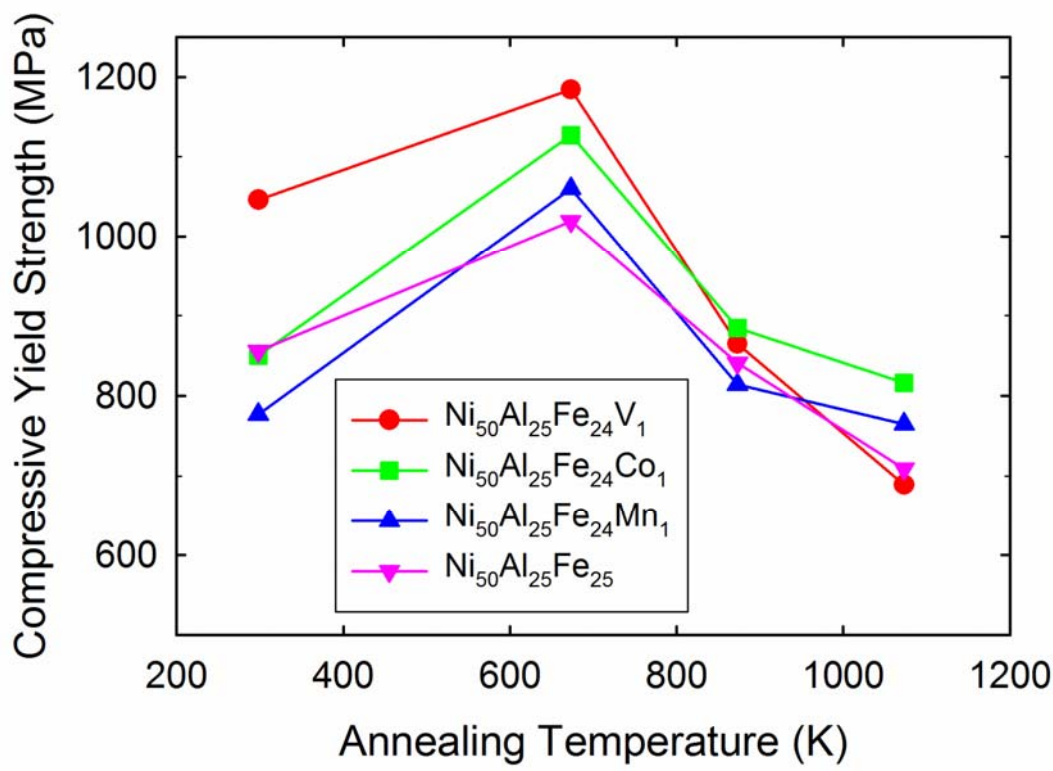

Figure 5.42 Variation of compressive yield strength with annealing of Co, Mn and V microalloyed Ni-Al-Fe alloys.

Figure 5.43 shows the fracture surface images around the crack tip region in V-modified Ni-Al-Fe alloy annealed at the optimum annealing temperature of 673 K. It can be said that the alloy exhibit a predominant dimple rupture mode. The dimples might have been formed due to the weak β / γ interface prone to initiation of cracks which may then propagate along the interdendrite and the interface between β and γ.

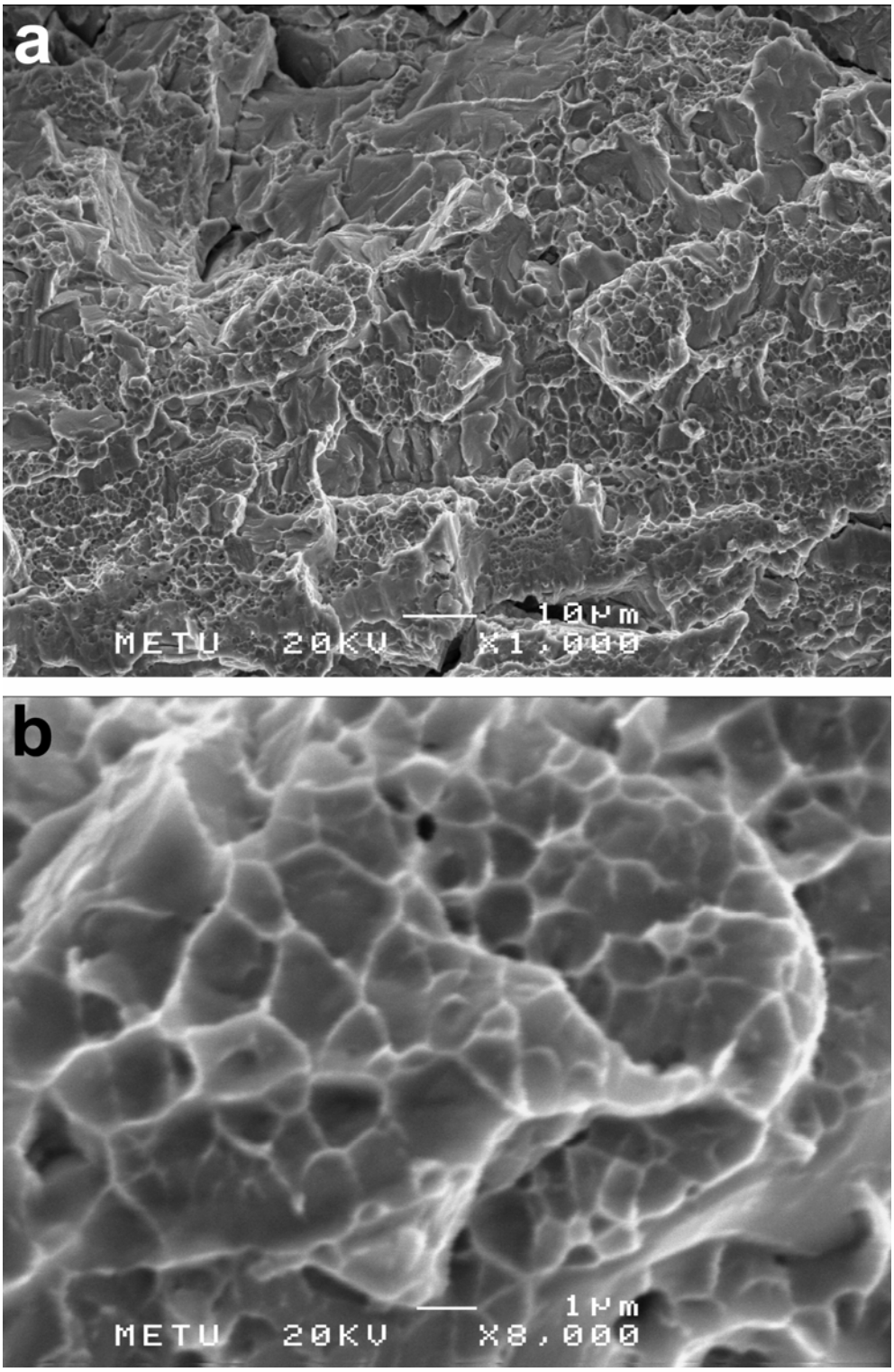

Figure 5.43 Fracture surface images of NiAlFe-V alloy annealed at 673 K.

5.2.6 Kinetics of Nanoscale Precipitation by Magnetic Monitoring

A magnetic monitoring approach is utilized in order to further elaborate on the ferromagnetic bcc α-phase precipitation phenomenon which provides matching of room temperature saturation magnetization and microhardness of the β-phase in annealed alloys. Thermomagnetization curves (Figure 5.44) obtained between 293 K and 973 K with 5 K intervals under an applied field of 500 Oe disclose the influence of quaternary microalloying. The low temperature curve (Figure 5.44(a)) reveals the Curie transition behavior of alloys where 45 K and 125 K shifts in transition temperature (T_C) to lower temperatures are caused by Mn and V additions, respectively, when compared to Ni-25Al-25Fe alloy without quaternary addition. Decrease in T_C with substitution of Mn for Fe is due to the smaller 3d-3d exchange interaction of Mn-Fe compared to Fe-Fe. The larger decrease of T_C with V substitution is related with antiparallel alignment of magnetic moment of V atom to that of Fe [125]. Substitution of Co for Fe slightly increases T_C of the alloy by 15 K which might be due to stronger exchange interaction between Fe-Co (Co-Co) compared to Fe-Fe.

High temperature region of the thermomagnetization curves (Figure 5.44(b)) contains transient rises in magnetization where the behavior of Ni-25Al-25Fe alloy is not significantly affected by Co and Mn additions. However, it is clear that with V microalloying, together with enhanced magnetization values, a shift of around 50 K to higher temperatures is seen in contrast with Co and Mn additions. This might be related to the slowing down of ferromagnetic α-phase precipitation due to the interaction of V atoms in the β-matrix during growth of α-precipitates. It is also clear that higher transient magnetization is reached with V addition that might indicate a larger volume fraction of the precipitated α-phase.

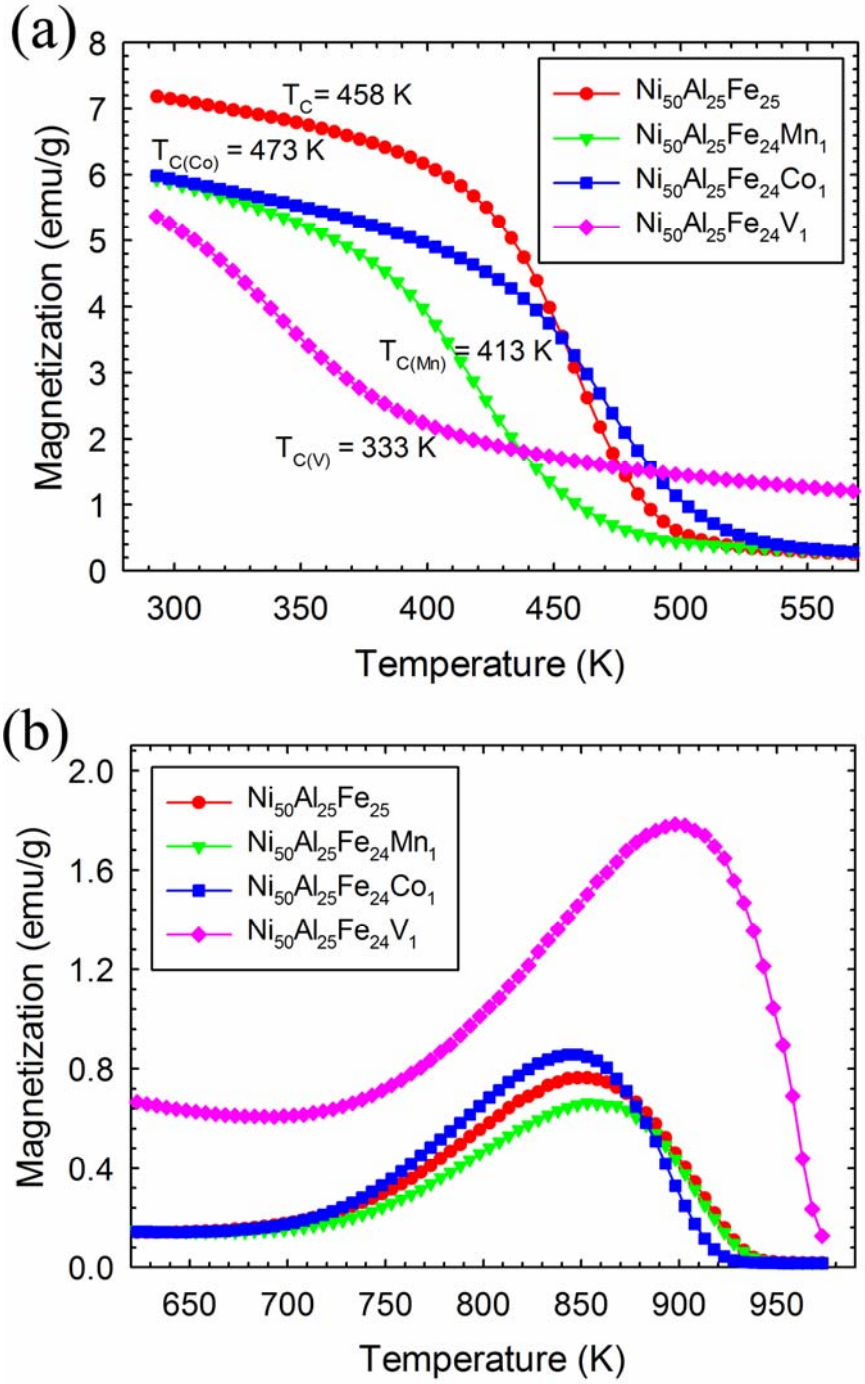

Figure 5.44 Temperature scan magnetization curves of as-cast alloys under an applied magnetic field of 500 Oe from (a) room temperature to 600 K, and (b) above 600 K.

The influence of quaternary additions on the precipitation of α-phase in β-matrix at high temperatures is studied using isothermal kinetic analysis. Figure 5.45 shows the isothermal magnetization curves of alloys in the temperature range 800 K – 925 K during 2 h annealing. The growth of ferromagnetic α-phase is tracked using magnetic monitoring which reveals that magnetization increase is a thermally activated process favored at higher annealing temperatures.

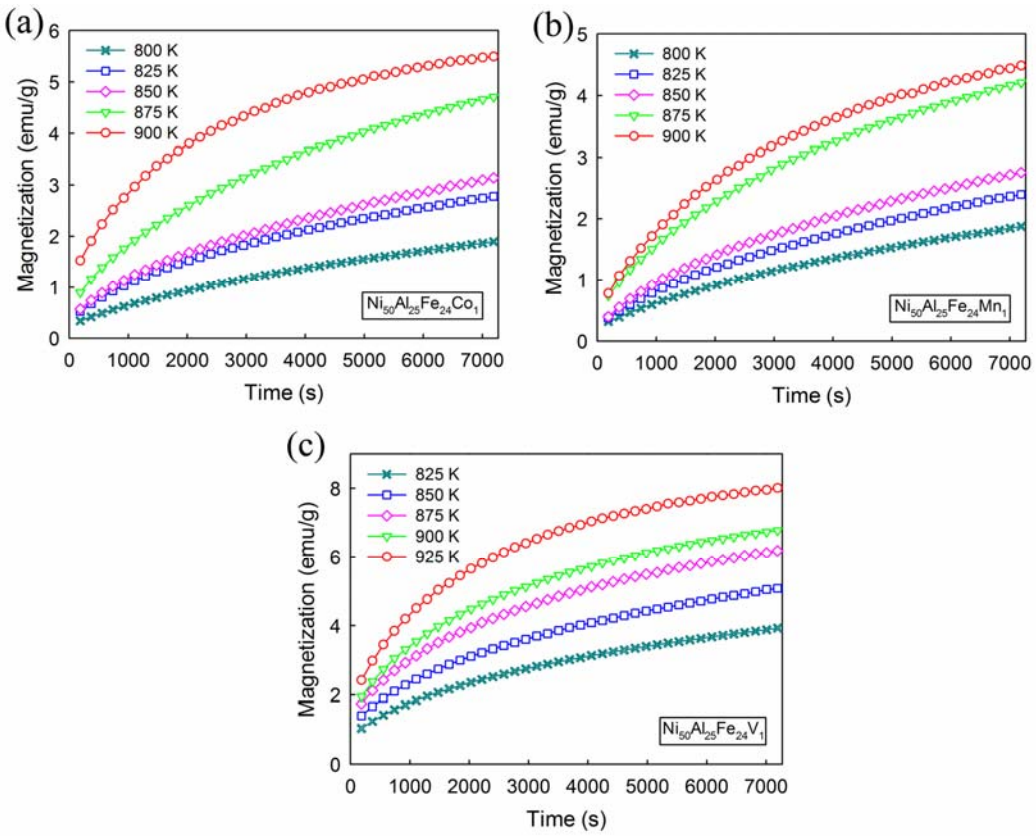

Figure 5.45 Isothermal magnetization curves of as-cast NiAlFe-*X* alloys where (a) *X* = Co, (b) *X* = Mn, and (c) *X* = V.

Time dependent magnetization can be implemented in the Johnson-Mehl-Avrami model by relating the fraction transformed (α_t) to magnetization at time t (M_t), initial magnetization (M_i) and final magnetization (M_f) by $\alpha_t = (M_t - M_i)/(M_f - M_i)$. Avrami plots are given in Figure 5.46 constructed using the isothermal magnetization data. The calculated Avrami time exponents range between n = 0.8 – 1, showing no clear discrepancy with the type of quaternary addition. It can be stated that the precipitation of α-phase in the β-matrix is predominated by diffusion controlled growth without a change in mechanism throughout the entire measurement time.

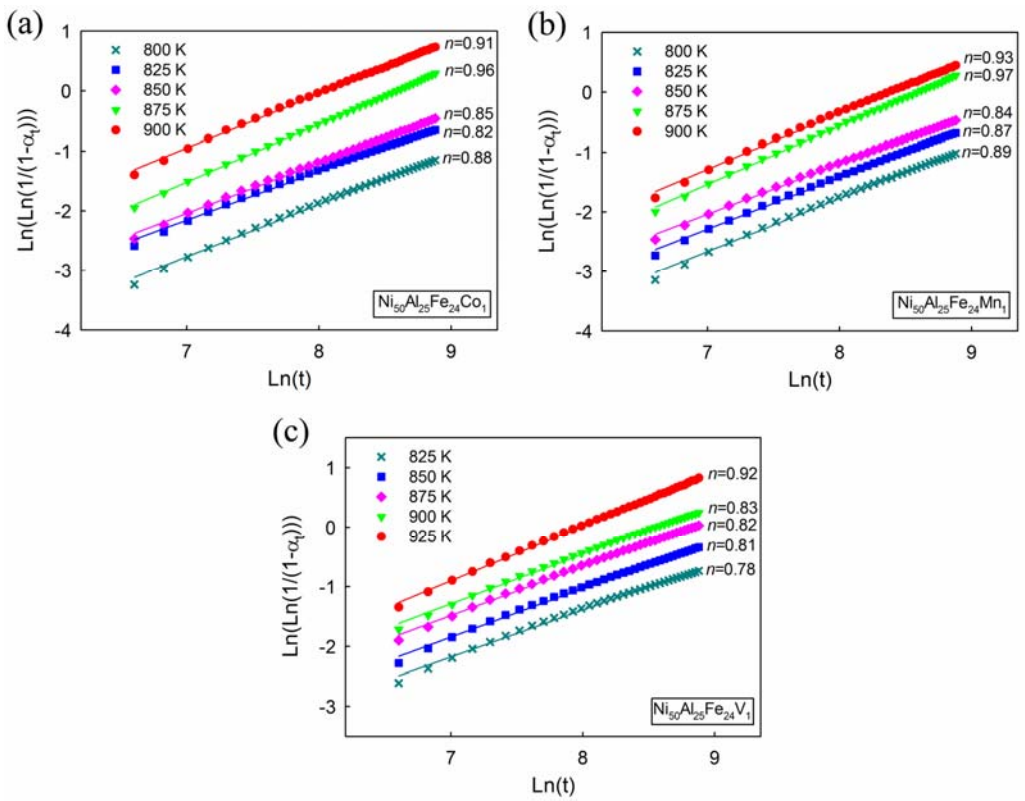

Figure 5.46 Avrami plots for as-cast NiAlFe-*X* alloys where (a) *X* = Co, (b) *X* = Mn, and (c) *X* = V.

Figure 5.47 discloses the influence of quaternary alloying additions on the activation energy (E_a) for α-phase precipitation. Considerably low E_a deduced from the kinetic analysis could be due to a process where growth of already nucleated phase occurs. While Co and Mn do not significantly alter the energy barrier, V remarkably lowers E_a for precipitate growth which could be explained by ordering of Ni site due to extensive V occupation of Al site and compositional effects on diffusivity in the β-phase matrix. Though, the presence of V in the β-phase shifts the temperatures required for precipitate growth as can be deduced from corresponding thermomagnetization curve in Figure 5.44(b).

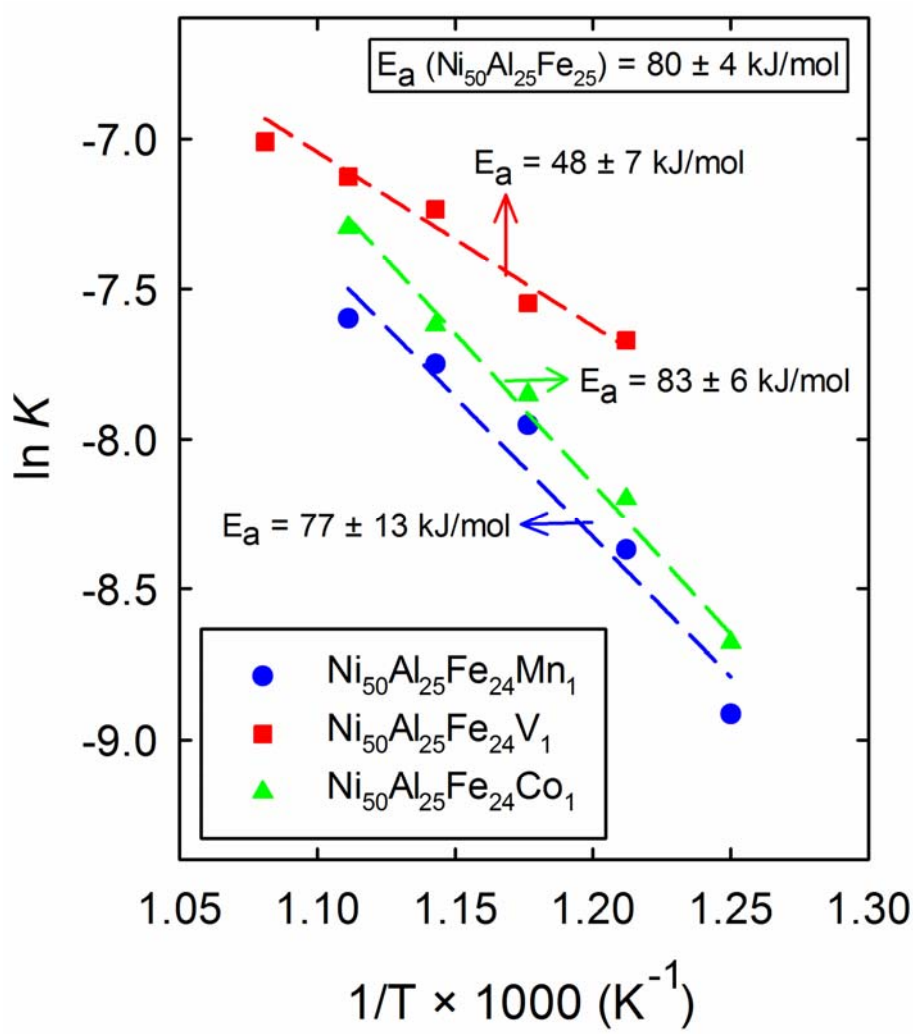

Figure 5.47 Activation energies for nanoscale α-phase precipitation.

Figure 5.48 contains magnetically assessed time-temperature-transformation (TTT) curves for α-phase precipitation. The magnetic monitoring approach has a certain temperature limit above which the process can not be followed by the ferromagnetic character of the precipitating phase due to the fact that the growing precipitates encounter magnetic disordering. Therefore, the growth process could only be tracked below those temperatures, indicated by dashed horizontal lines in Figure 5.48. When constructing the TTT curves, it is presumed that transformed fraction approaches $\alpha_t \sim 1$ when an equilibrium volume fraction of α-phase in the β-matrix is attained. Figure 5.48(a) shows that Co and Mn behave similar in terms of precipitation kinetics whereas V considerably slows down the growth rate and shifts the magnetically assessable temperature limit to a higher value. It is clear from Figure 5.48(b) that growth of α-precipitates is slower with V addition compared to Ni-25Al-25Fe alloy, particularly at high temperatures (e.g. above 750 K) and towards large transformed fractions. This indicates that V microalloying is effective in improving the high temperature long-term stability of finely precipitated microstructure in Ni-Al-Fe alloys.

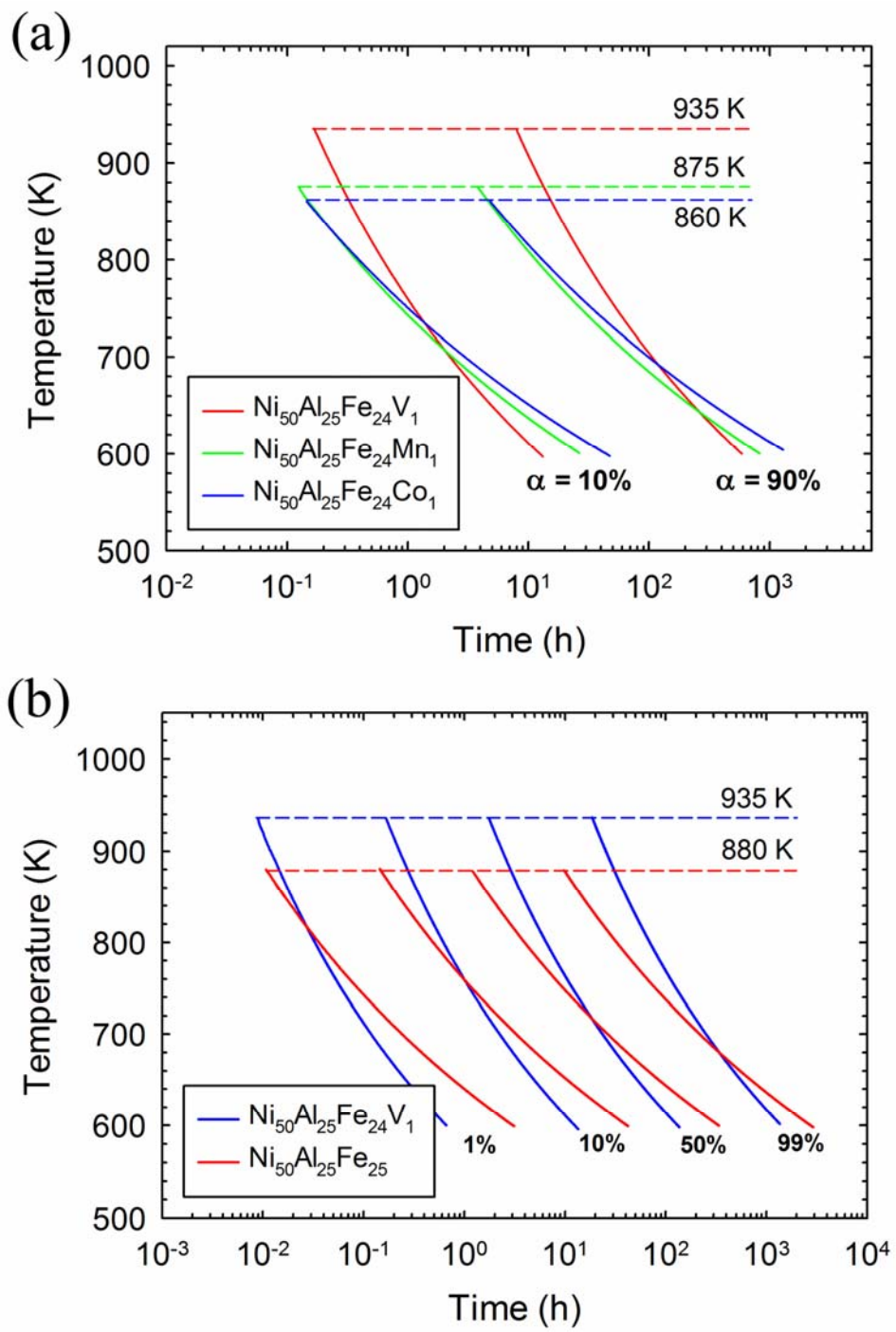

Figure 5.48 (a) Magnetically assessed TTT diagrams for α-phase precipitation in NiAlFe-*X* alloys, (b) TTT diagrams for Ni-25Al-25Fe and NiAlFe-V alloys showing the influence of V addition on the kinetics of α-phase precipitation.

CHAPTER 6

AMORPHOUS ALLOYS

Evolution of the metastable glassy state to new metastable or stable partially-crystalline structures has raised interest due to the modification of various physical properties [126]. Therefore, it is of great importance both from fundamental and applicability aspects to have better understanding of crystallization mechanisms and its kinetics which would eventually provide good control over the thermal dependence of nanocrystals that are formed from amorphous precursors. Kinetic considerations on the nanocrystallization phenomenon should involve methodologies to reveal the primary crystallization behavior and local transformation mechanisms throughout the course of microstructure development during annealing. The present study deals with the nanocrystallization kinetics in Cu-modified Fe-Co-Ni-B-Si-Nb bulk amorphous alloy under isothermal and non-isothermal conditions. For this purpose, an isothermal magnetic monitoring approach was implemented to classical Johnson-Mehl-Avrami-Kolmogorov (JMAK) theory and compared with the kinetic parameters obtained from conventional thermal analysis employing a direct extension of the JMAK theory to non-isothermal regimes.

6.1 Solidification Behavior

Suction-cast rods from 1 at.% Cu modified $Fe_{43}Co_{28-x}Ni_xB_{19}Si_5Nb_4$ alloys with different Co/Ni ratios and thicknesses were analyzed by means of XRD in

order to identify the amorphous structure and the best glass forming composition (Figure 6.1). It can be stated that the alloy with the highest Ni content (19 at.% Ni, 9 at.% Co) does not favor glass formation at both 1 mm and 2 mm diameters while the alloy with Co/Ni ratio of 1/1 (14 at.% each) can solidify without apparent crystallization at 1 mm diameter but retains crystalline phases at 2 mm diameter corresponding to a lower cooling rate. The alloy with the highest Co content (9 at.% Ni, 19 at.%Co) displays an X-ray amorphous structure with no detectable diffraction lines at both 1 mm and 2 mm rod diameters. Owing to the fully amorphous structure up to 2 mm diameter, the Cu-modified $Fe_{43}Co_{19}Ni_9B_{19}Si_5Nb_4$ alloy was chosen for a detailed analysis of the microstructural evolution and kinetics of nanocrystallization.

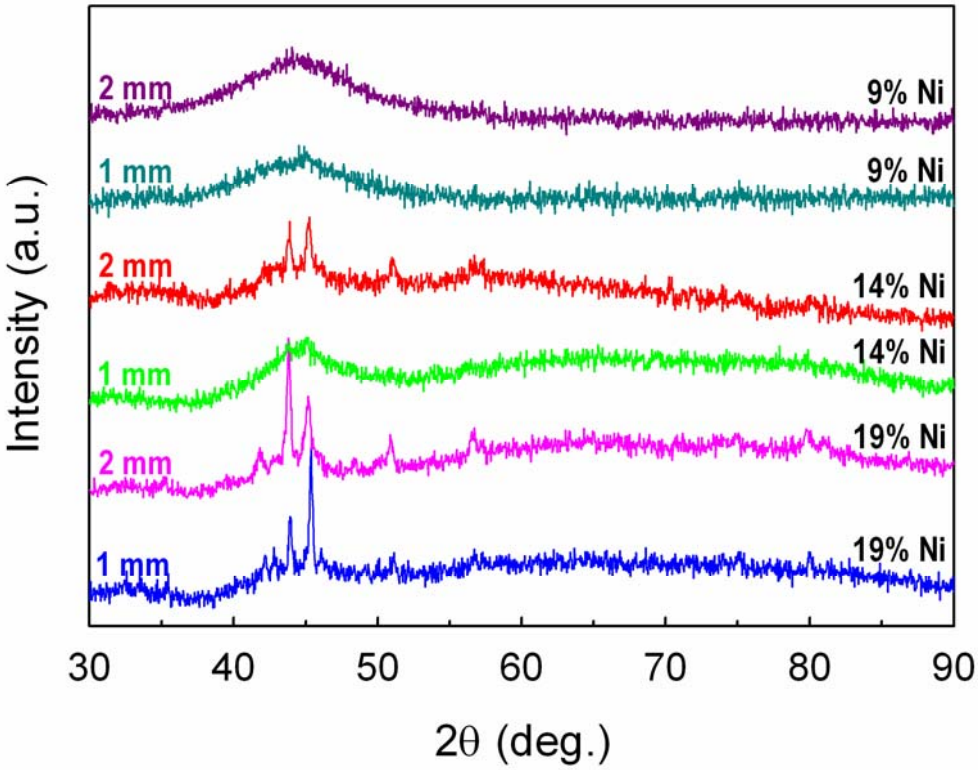

Figure 6.1 XRD patterns of Cu-modified $Fe_{43}Co_{28-x}Ni_xB_{19}Si_5Nb_4$ alloys with different Co/Ni ratios.

Figure 6.2 shows SEM secondary electron and back-scattered electron images of suction-cast Cu-modified $Fe_{43}Co_{19}Ni_9B_{19}Si_5Nb_4$ alloy possessing featureless microstructure upon nital etching for an appreciable duration. On the other hand, complex solidification microstructures shown in Figure 6.3 are formed when a lower cooling rate is employed. The solidification microstructure consists of three distinguishable regions. Energy dispersive maps, line scan and point analyses (Figure 6.4–6.6) on these distinguishable regions revealed that the region denoted as "A" is enriched in Fe, while region "B" is rich in Nb and poor in Fe. It becomes also clear that Si and Ni atoms are predominantly located in the region denoted by "C". Figure 6.7 contains the XRD pattern of relatively slow-cooled Cu-modified $Fe_{43}Co_{19}Ni_9B_{19}Si_5Nb_4$ alloy. The crystalline reflections were identified to three phases, i.e. α–(Fe,Co), (Fe,Co)NbB and $(Fe,Co)_2B$, which corresponds respectively to A, B and C regions labeled in the solidification microstructure.

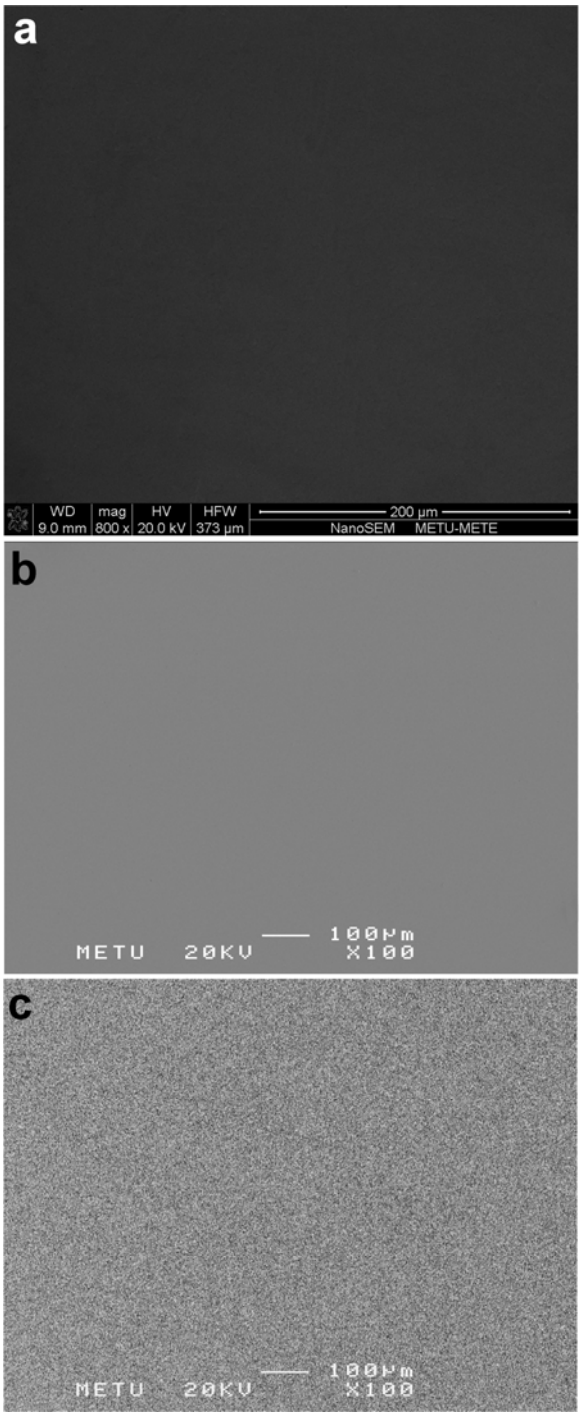

Figure 6.2 Solidification microstructures of rapidly solidified Cu-modified $Fe_{43}Co_{19}Ni_9B_{19}Si_5Nb_4$ alloy; (a) field-emission SEM secondary electron image, (b) conventional SEM secondary electron image and (c) back-scattered electron image.

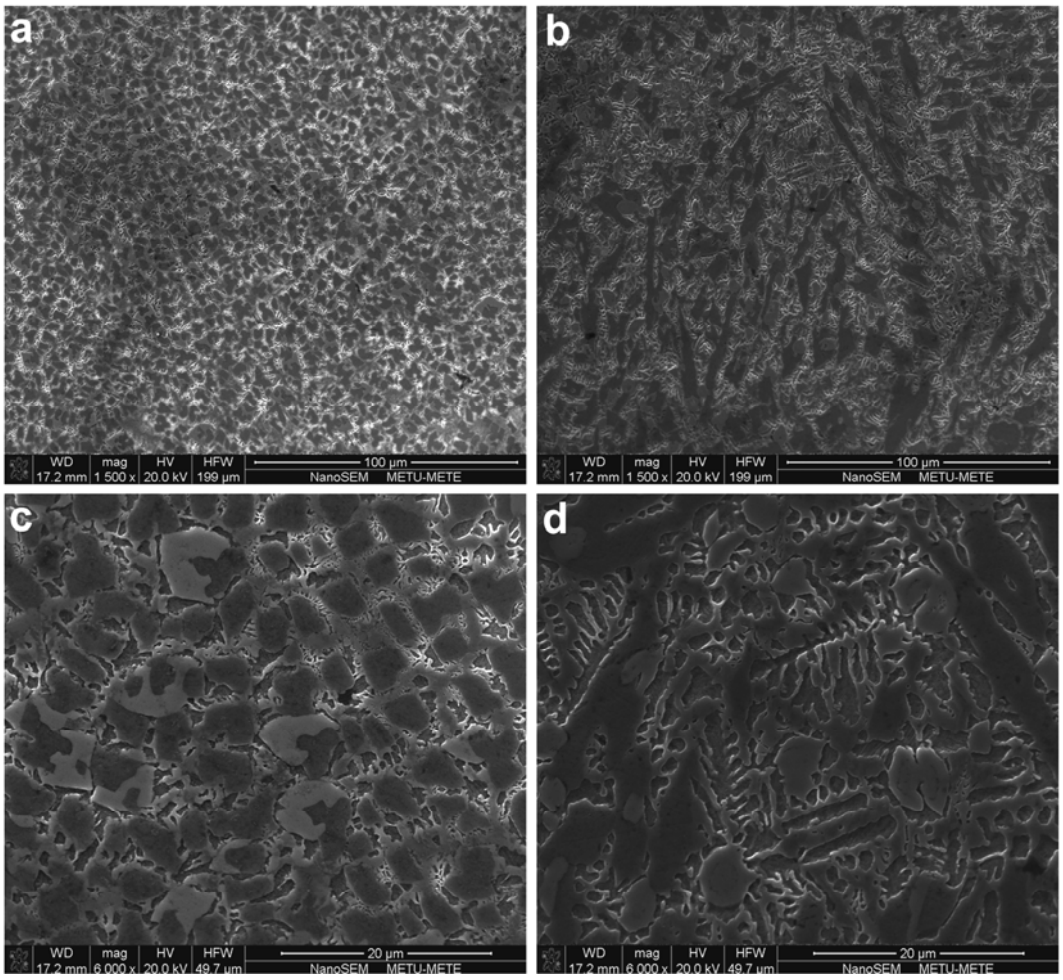

Figure 6.3 Solidification microstructure of relatively slow-cooled Cu-modified $Fe_{43}Co_{19}Ni_9B_{19}Si_5Nb_4$ alloy.

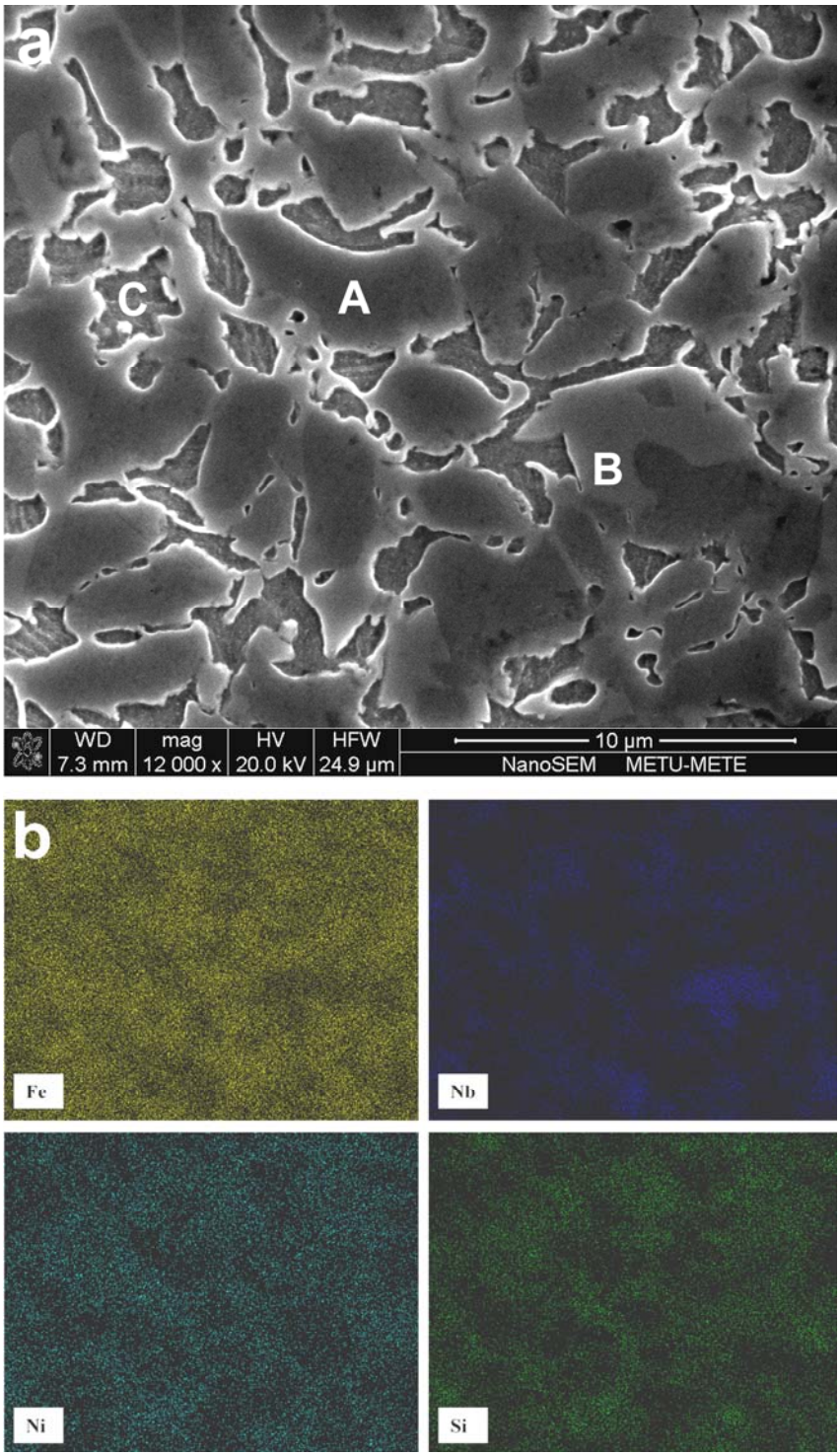

Figure 6.4 Energy dispersive maps (field-emission SEM) of relatively slow-cooled Cu-modified $Fe_{43}Co_{19}Ni_9B_{19}Si_5Nb_4$ alloy.

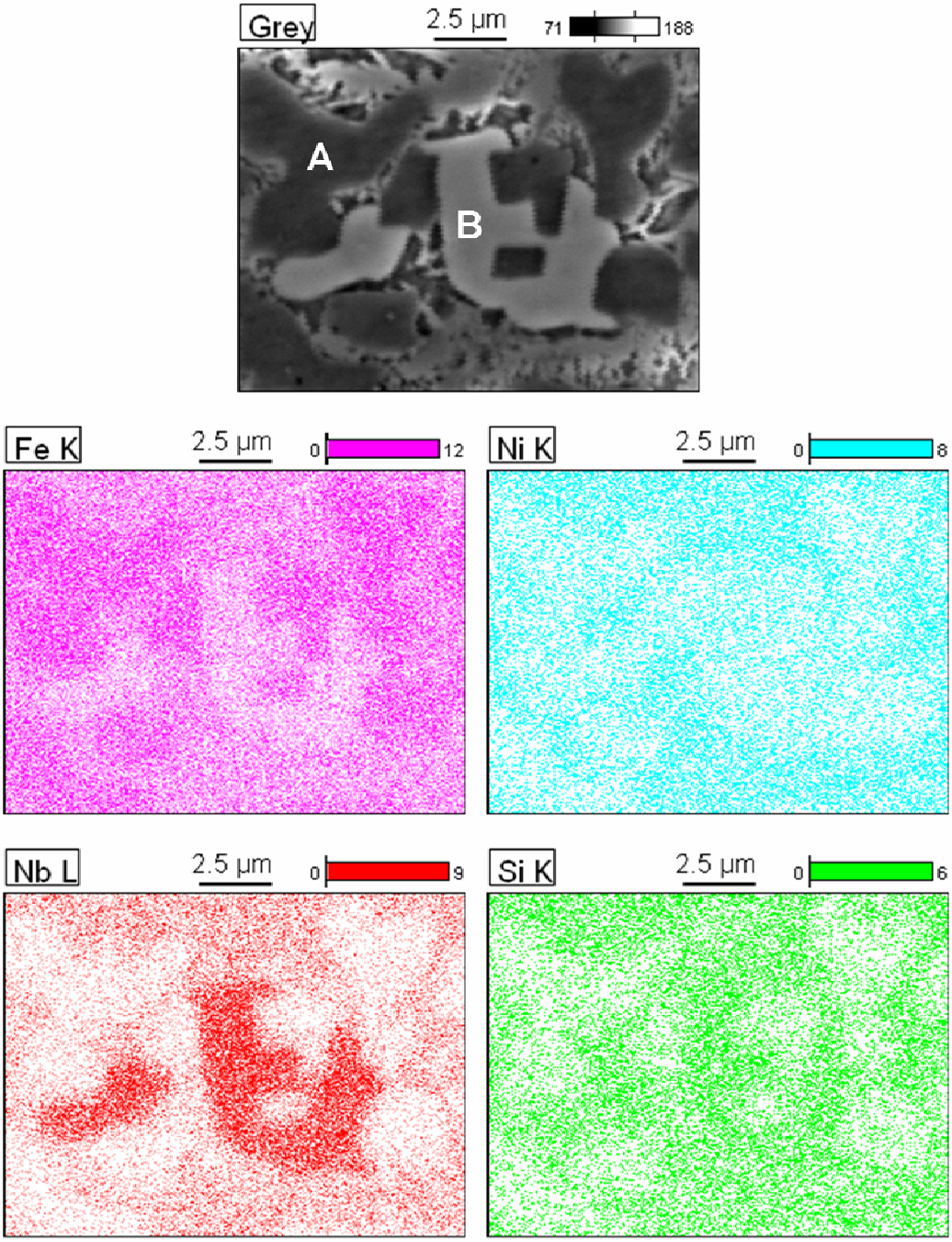

Figure 6.5 Energy dispersive maps (conventional SEM) of relatively slow-cooled Cu-modified $Fe_{43}Co_{19}Ni_9B_{19}Si_5Nb_4$ alloy.

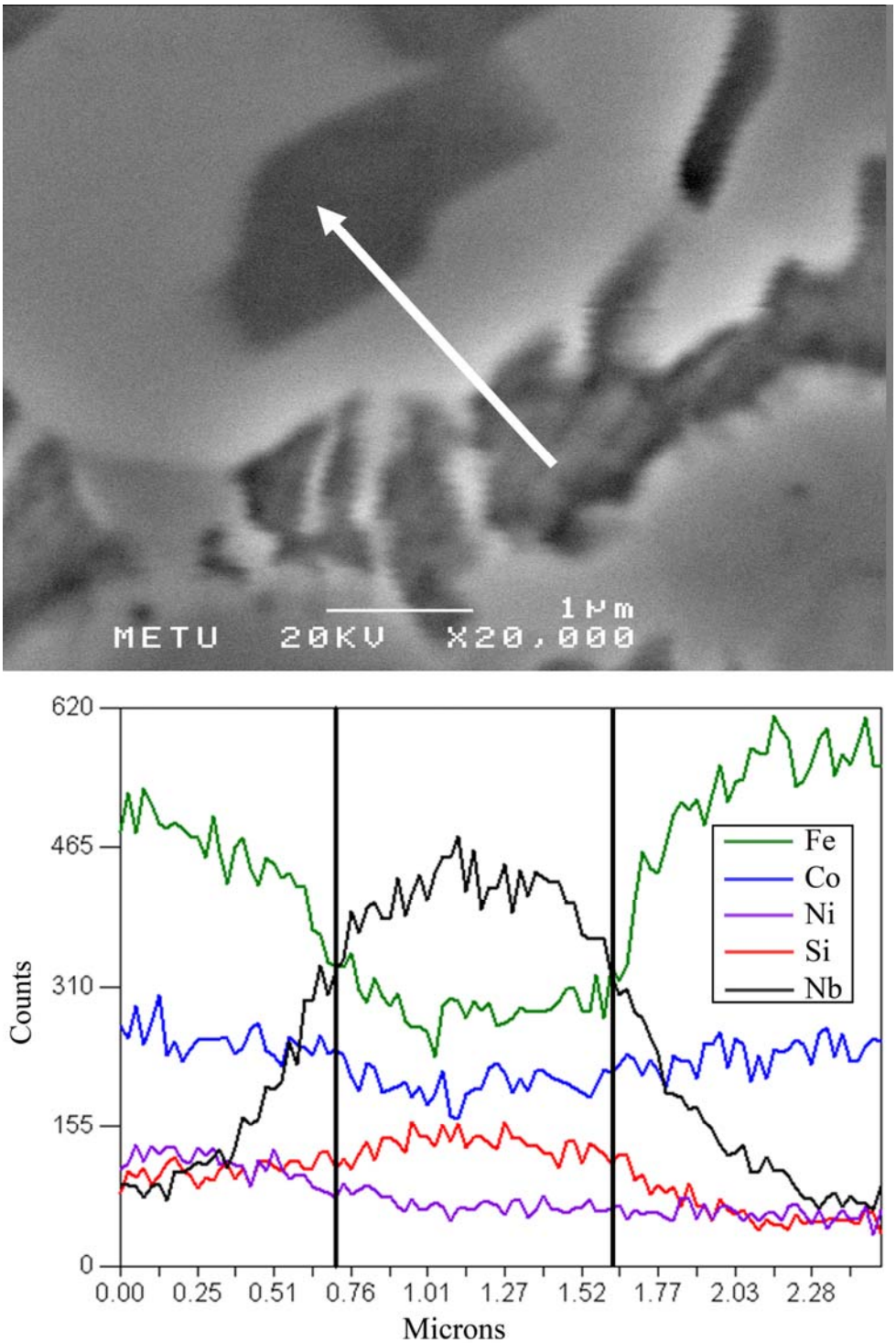

Figure 6.6 Energy dispersive line scan from distinguishable regions in relatively slow-cooled Cu-modified $Fe_{43}Co_{19}Ni_9B_{19}Si_5Nb_4$ alloy.

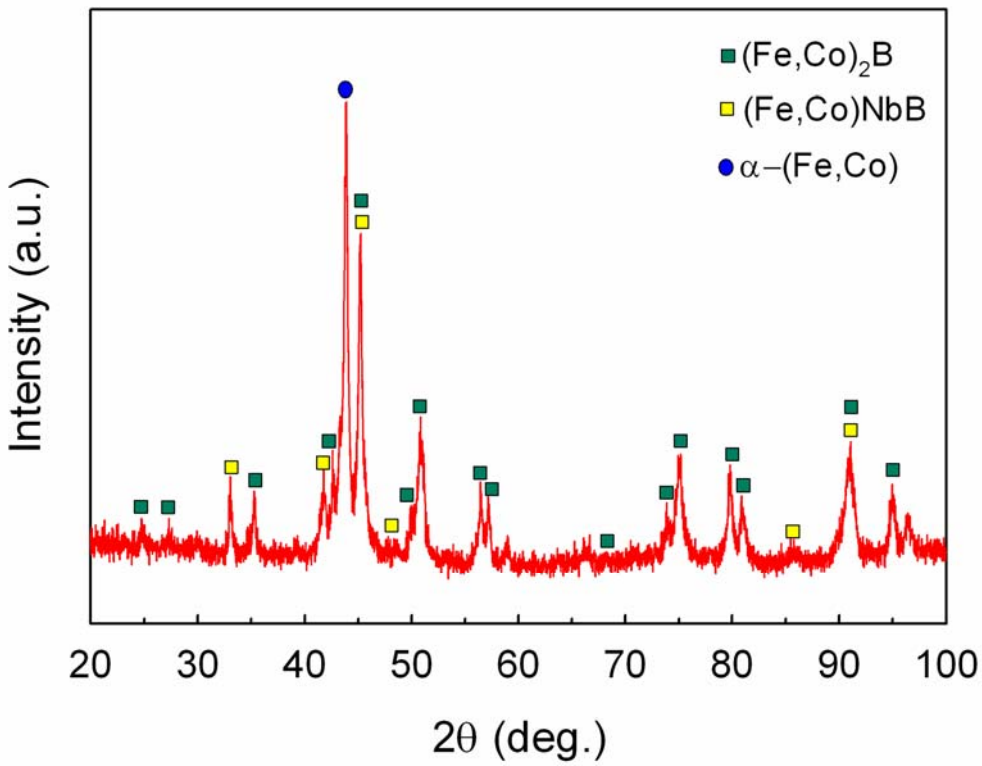

Figure 6.7 XRD patterns of relatively slow-cooled Cu-modified $Fe_{43}Co_{28-x}Ni_xB_{19}Si_5Nb_4$ alloy.

6.2 Crystallization Behavior

Figure 6.8 contains representative bright-field TEM image and corresponding selected area electron diffraction (SAED) pattern of the as-cast 1 at.% Cu-modified $Fe_{43}Co_{19}Ni_9B_{19}Si_5Nb_4$ bulk amorphous alloy. The uniform image contrast and full halo rings without detectible diffraction spots in the SAED pattern are typical for amorphous alloys.

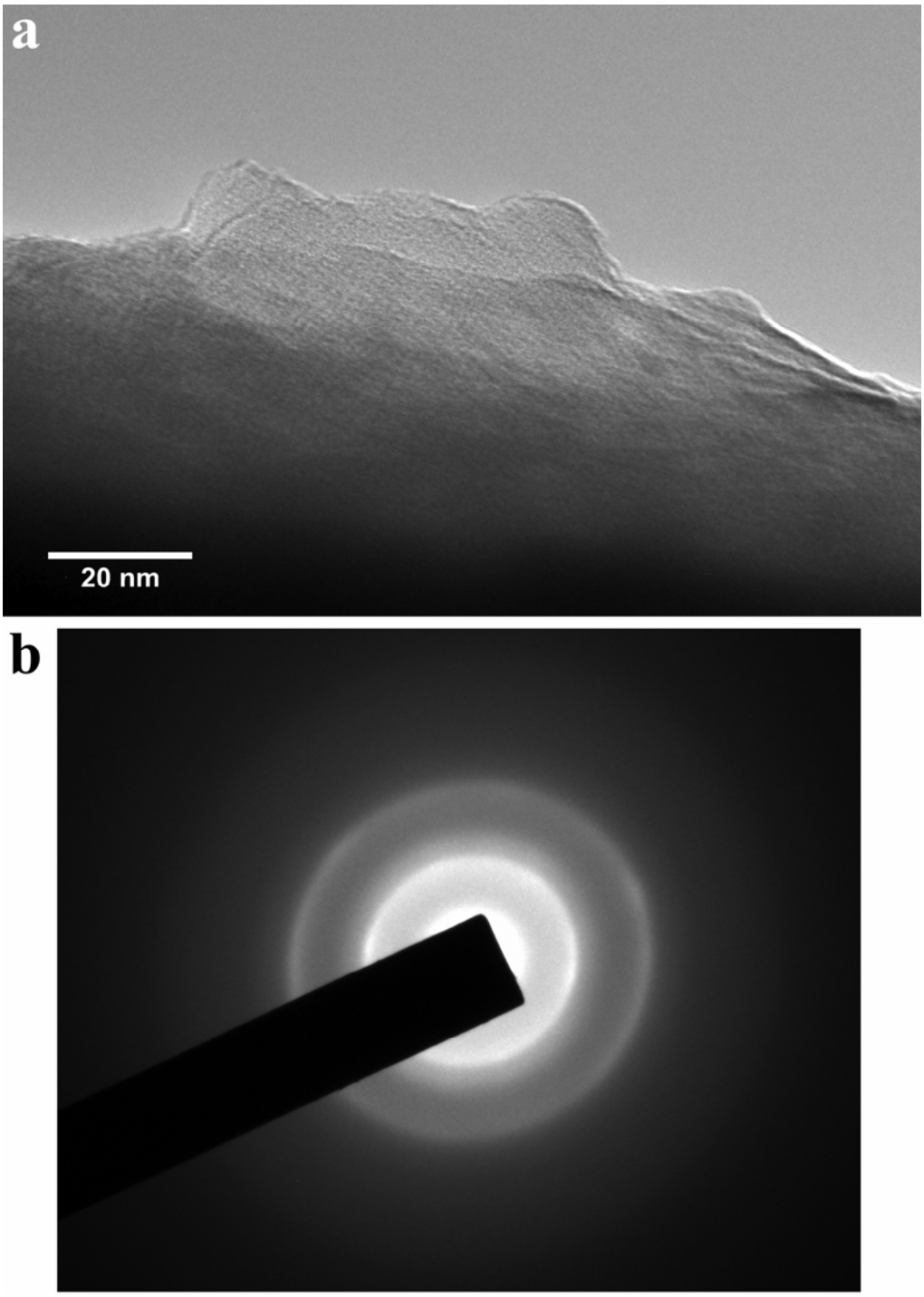

Figure 6.8 (a) Bright-field TEM image showing the amorphous structure of suction-cast Cu-modified $Fe_{43}Co_{19}Ni_9B_{19}Si_5Nb_4$ alloy, and (b) corresponding SAED pattern.

Figure 6.9 contains DSC heat flow curves obtained at 40 K/min heating rate (β) where the amorphous alloy undergoes glass transition upon heating to around T_g = 802 K followed by three crystallization steps denoted as T_{p1}, T_{p2} and T_{p3} at temperatures 881 K, 948 K and 974 K, respectively. Heating an amorphous alloy to a temperature in the glass transition region will change the structure of the glass to the metastable equilibrium structure. The onset of first crystallization exotherm, marked as T_x = 851 K, is the point where the supercooled liquid phase starts to crystallize. The crystallization products are usually thought to be metastable and can evolve to different stable or still metastable structures through annealing. The temperature range between T_g and T_x, which is a measure of the resistance of the supercooled liquid to nucleation and growth of crystalline phases, is calculated as 49 K.

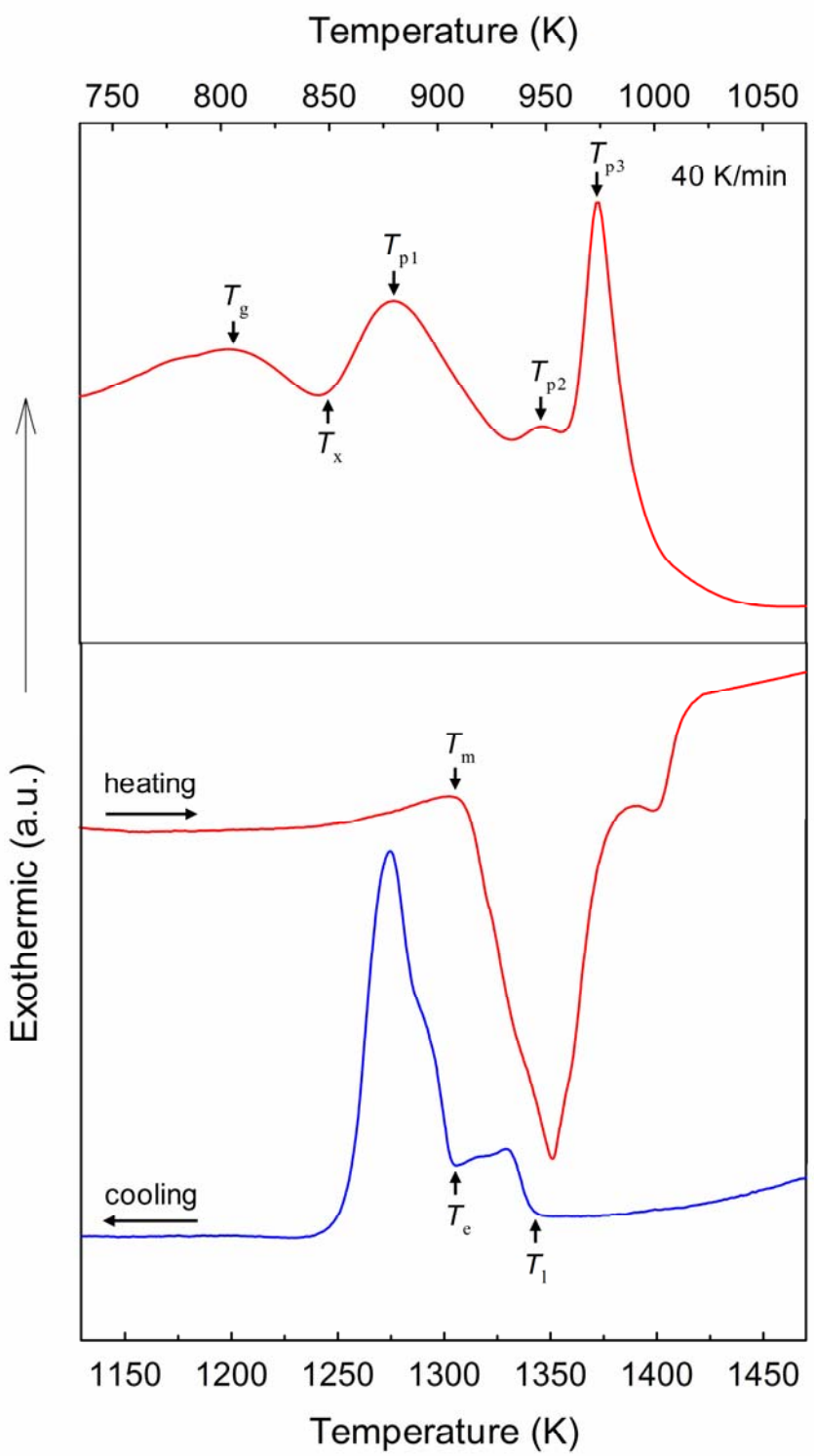

Figure 6.9 DSC heat flow curves of the bulk amorphous Cu-modified $Fe_{43}Co_{19}Ni_9B_{19}Si_5Nb_4$ alloy.

XRD patterns displayed in Figure 6.10 show that α–(Fe,Co) nanocrystals are formed by annealing the amorphous alloy at 873 K, i.e. slightly below T_{p1} = 880 K, where no other crystalline phases are seen. It thus becomes clear that an amorphous matrix nanocrystalline alloy can be obtained employing an appropriate annealing procedure. The lattice parameter of α–(Fe,Co) nanocrystalline phase is calculated as $a_{\alpha\text{-(Fe,Co)}}$ = 0.2856 nm, smaller than that of pure α–Fe (0.2866 nm) due to the presence of smaller atomic radius Co atoms as the solute in the bcc lattice (Appendix C).

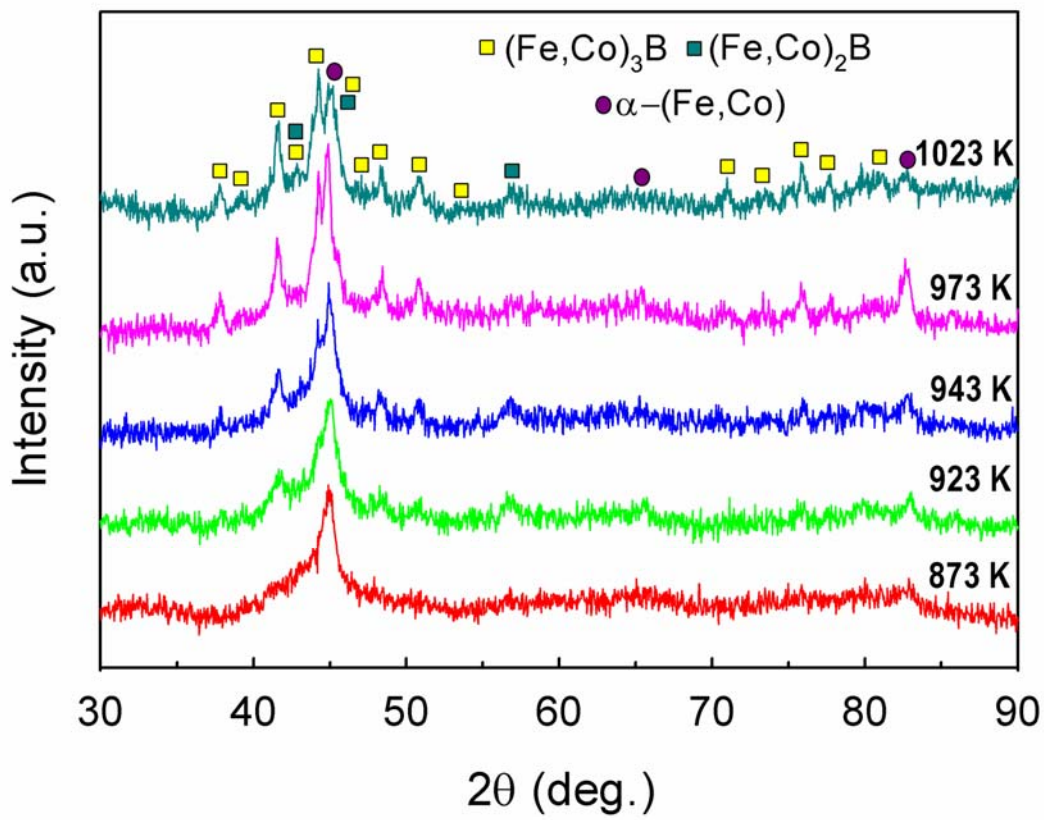

Figure 6.10 XRD patterns elucidating the crystallization behavior of the Cu-modified $Fe_{43}Co_{19}Ni_9B_{19}Si_5Nb_4$ amorphous alloy.

The two-phase metastable microstructure consisting of α–(Fe,Co) nanocrystals embedded in an amorphous matrix is known to provide very good soft magnetic properties, i.e. high saturation magnetization as well as low coercive force [127, 128]. It can be generalized that Cu modification provides lower T_x value when compared to Cu-free alloys indicating lower supercooling necessary for primary crystallization of the amorphous phase. This is attributed to the heterogeneous nucleation effect of Cu clusters formed by structural relaxation of the as-quenched glass during annealing. The large difference between primary crystallization temperature (T_{p1}) and those of subsequent crystallization steps (T_{p2} and T_{p3}) in the studied alloy is due to α–(Fe,Co) crystallization being thermodynamically favored at lower temperatures within the supercooled region.

Crystallization exotherms following that of primary crystallization in the DSC curve (Figure 6.9) are usually attributed to secondary or higher order crystallization of stable or metastable metal-metalloid intermetallic compounds such as $Fe_{23}B_6$, Fe_3B, Fe_2B, FeB and FeSi [129-131]. It can be inferred from Figure 6.10 that annealing at temperatures well above T_{p1} results in the formation of orthorhombic metastable Fe_3B phase together with minor tetragonal stable Fe_2B phase. The Fe_3B phase displayed markedly increased XRD line intensity with increasing annealing temperature. The crystallization of iron borides is thought to be controlled by nucleation and growth from the amorphous matrix and in some cases partial transformation of already formed primary crystals.

6.3 Non-Isothermal Kinetics of Nanocrystallization by DSC

Figure 6.11 displays the DSC traces obtained at different heating rates (β) where crystallization exotherms shift progressively to higher temperatures as expected for a thermally activated process. The relative amounts of crystallization for the second and third steps are strongly influenced by heating rate due to competitive crystallization of metal-metalloid intermetallics during heating. It is also apparent that the second crystallization step is kinetically favored against the third step when lower heating rates are utilized.

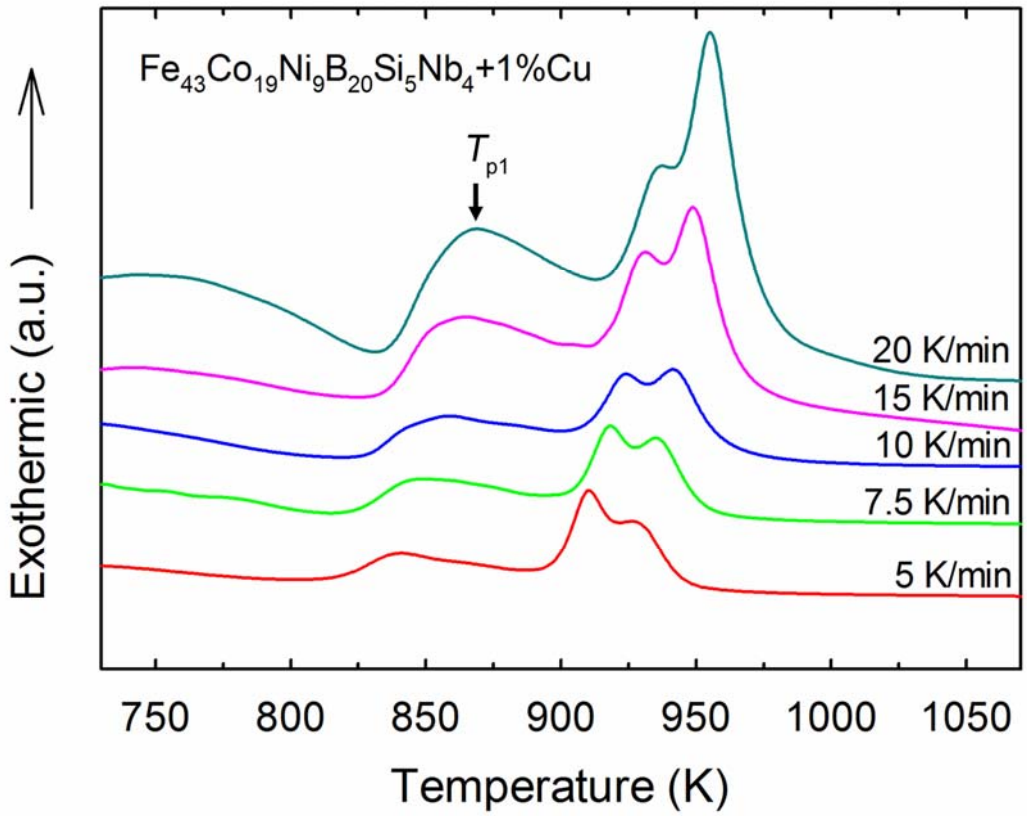

Figure 6.11 DSC heat flow curves showing crystallization exotherms obtained at different heating rates.

The transformation kinetics from amorphous to crystalline phases under non-isothermal conditions has so far been successfully interpreted by Kissinger analysis [98, 99]. Using DSC traces for different heating rates, activation energy (Q_a) for the three crystallization steps are calculated by taking the slopes of $\mathrm{Ln}(\beta/T_p^2)$ vs. $1/T_p$ curves equal to $-Q_a/R$. Figure 6.12 shows Kissinger plots where it is seen that overall Q_a for the three crystallization steps can be extracted with reasonably small standard deviation. It has to be noted that Q_a is an overall energy barrier which is assumed to be independent of β and constant throughout crystallization. Overall activation energies for the second and third steps corresponding to crystallization of metal-metalloid compounds are very close to each other, i.e. around 350 kJ/mol, which is in good agreement with secondary crystallization of similar Fe-based amorphous systems [132, 133].

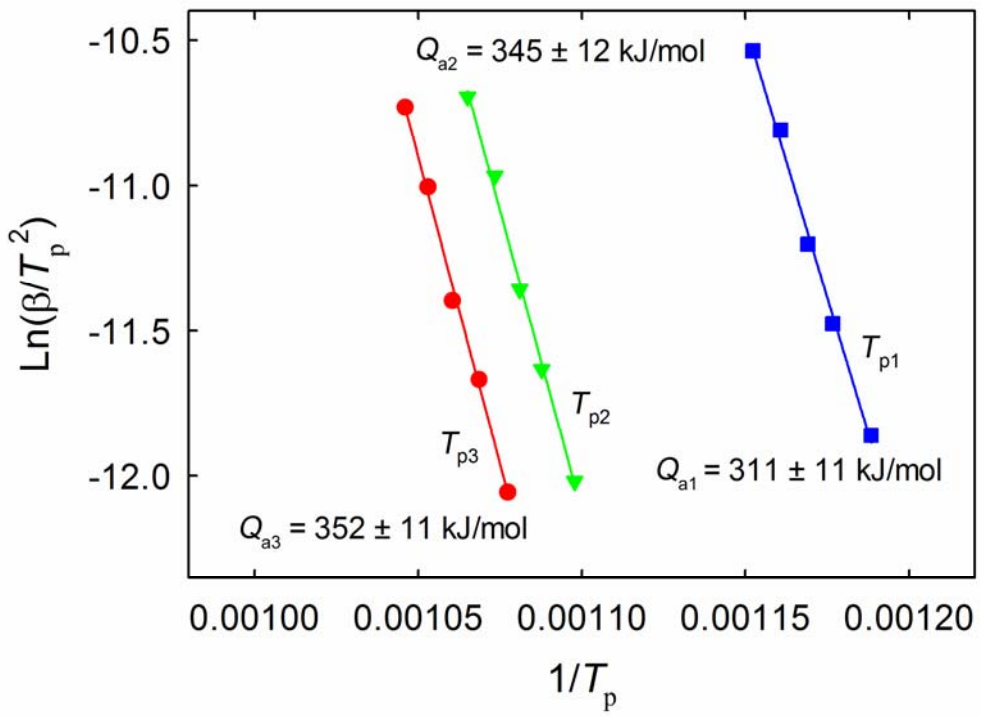

Figure 6.12 Kissinger plots and activation energies for different steps of crystallization.

The energy barrier for α–(Fe,Co) nanocrystallization (T_{p1}) is calculated to lie in the range Q_a = 272 – 325 kJ/mol where good agreement is seen between different non-isothermal models as shown in Figure 6.13. It has to be noted that Q_a for primary crystallization found in this study is slightly lower than those reported earlier using Kissinger method (347–367 kJ/mol) for Cu-modified Fe-based systems [134, 135] indicating reduced nucleation barrier.

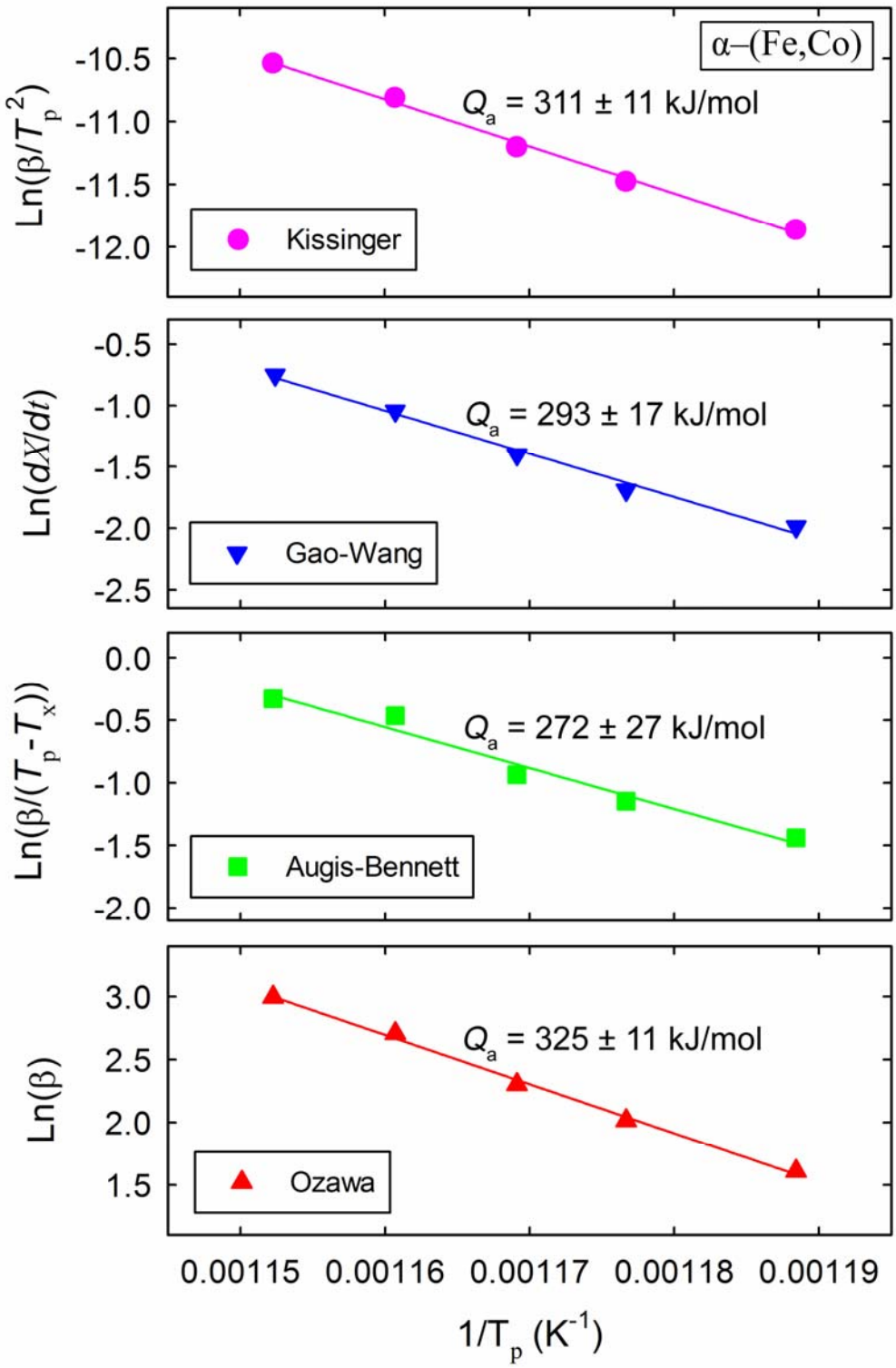

Figure 6.13 Plots obtained from different non-isothermal models for the calculation of overall activation energy for α–(Fe,Co) crystallization.

Figure 6.14 shows the transformation rate and transformed fraction curves for α–(Fe,Co) crystallization which were calculated using non-isothermal heat flow curves through Equation (8). It should be noted that the first crystallization exotherm occurs at a considerably lower temperature compared to those for subsequent crystallizations meaning that there is no overlap of exotherms which is essential for the kinetic analysis without the need for a deconvolution procedure [134].

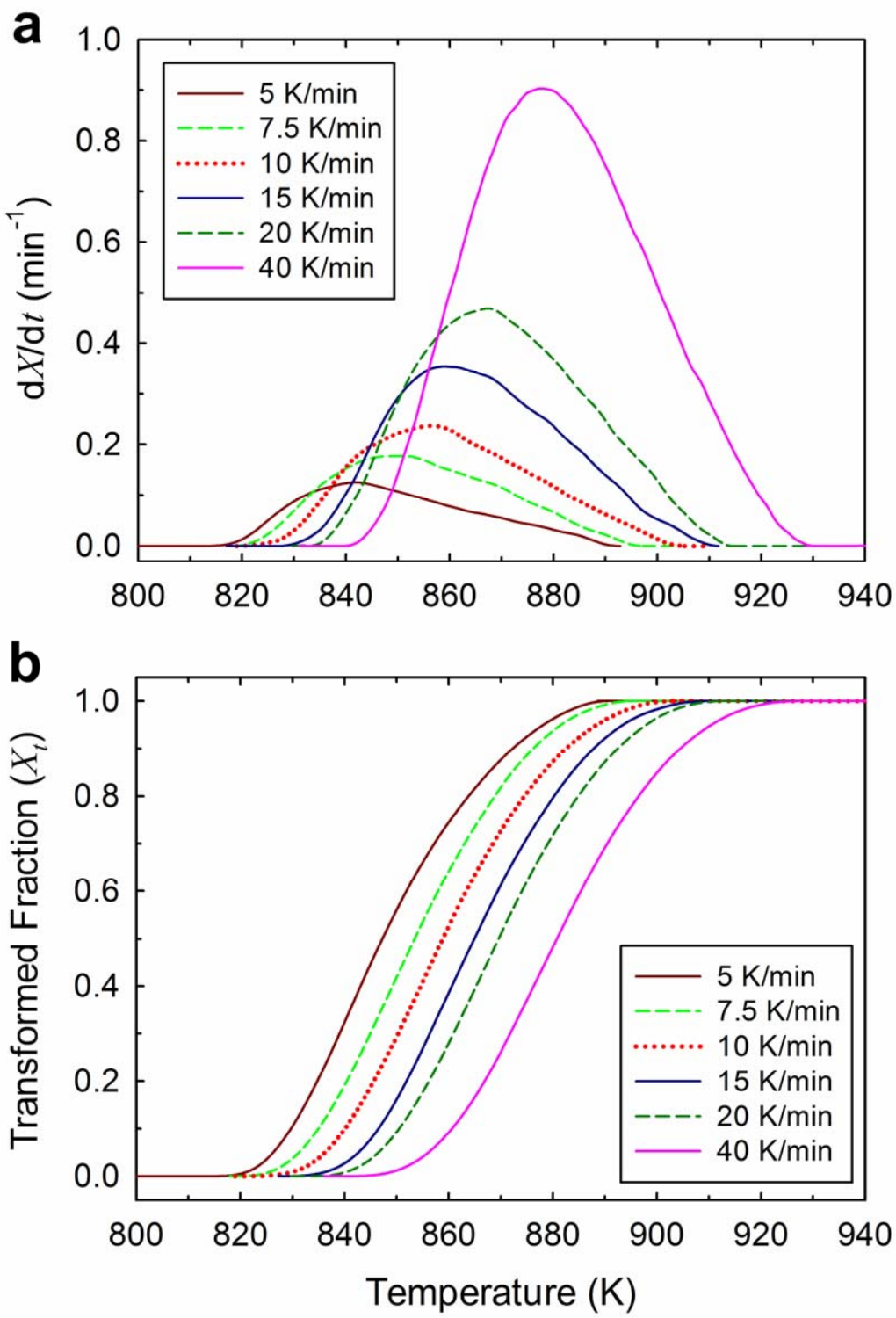

Figure 6.14 (a) Transformation rate and (b) transformed fraction curves obtained for different heating rates in DSC.

Johnson-Mehl-Avrami-Kolmogorov (JMAK) theory [35-38] is considered as a universally applicable model for studying the kinetics of solid state processes aiming to interpret the crystallization mechanisms. Provided that transformation mechanism does not vary throughout the process, slopes of Ln(-Ln(1-X_t)) vs. Ln(t-t_0) plots are taken as an overall value for Avrami exponent (n), where t_0 is the incubation time. However, this is not essentially observed for some real cases of crystallization where significant alterations of the linearity of Avrami plots were observed along the course of crystallization [134, 136-138]. Therefore, determination of local Avrami exponent, $n(X)$, is essential to track the evolution of nanocrystallization mechanism throughout the entire process.

The direct extension of JMAK to non-isothermal kinetics under the isokinetic assumption is capable of extracting $n(X)$ from a single non-isothermal DSC curve, provided that an overall activation energy is estimated for the process. Figure 6.15 shows that the local Avrami exponent, $n(X)$, is found to show similar trends for different heating rates, yielding maximum values in the range n = 1–1.2 in the very early stages of crystallization, i.e. when X_t < 0.1. The initial values of $n(X)$ are followed by gradual decreases throughout crystallization and yielding minimum values in the range n=0.6-0.7 when the transformed fraction reaches X_t~0.8. The trends obtained in $n(X)$ for the Cu-modified $Fe_{43}Co_{19}Ni_9B_{19}Si_5Nb_4$ alloy show very good agreement with those reported earlier [139-141] for other bulk amorphous alloy systems that exhibit nanocrystallization via annealing. The isokinetic assumption can be thought to be fulfilled since trends in $n(X)$ are not remarkably affected by heating rate (thermal history). Considering the concept of additivity by Cahn [13], the isokinetic assumption is also satisfied when saturation of nucleation sites occurs at early stages during transformation and the growth rate depends only on temperature, which is realized by instantaneous nucleation through Cu clusters acting as heterogeneous nucleation sites in the studied alloy.

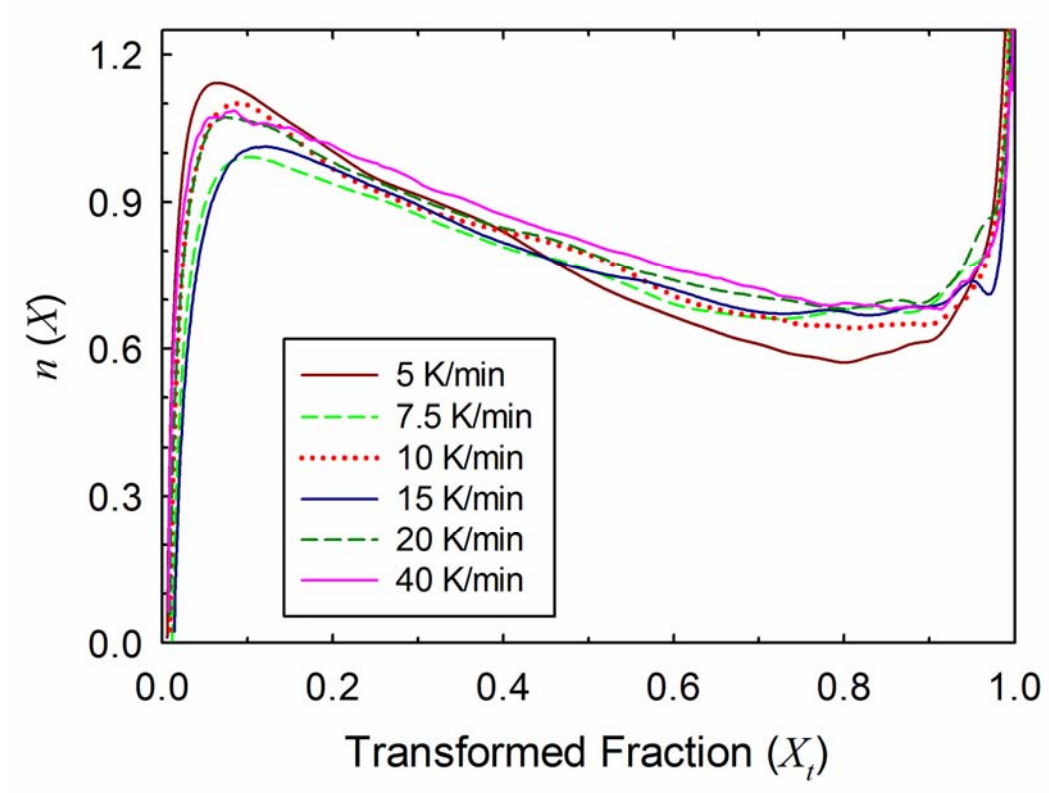

Figure 6.15 Local Avrami exponent, $n(X)$, obtained by non-isothermal DSC analysis at different heating rates.

The well known Ozawa approach [97] can also yield the local Avrami exponent but as a function of temperature, $n(T)$ by simply taking the slope of Ln[-Ln(1-$X(T)$)] vs. Ln(1/β) at a given temperature for different β values. Similar trends in $n(T)$ were obtained by the Ozawa method and the direct extension of JMAK theory to non-isothermal regimes as shown in Figure 6.16. The gradual decrease of $n(T)$ from the direct extension to JMAK theory is also observed for $n(T)$ derived from Ozawa analysis, especially towards high temperatures (or crystallized fractions) characterized by slow growth kinetics with zero nucleation rate. At high temperatures, the process better satisfies the isokinetic assumption and becomes less dependent on the heating rate since crystallized fraction evolves slow enough so that the restriction of Ozawa analysis, i.e. X_t independent n, is better satisfied.

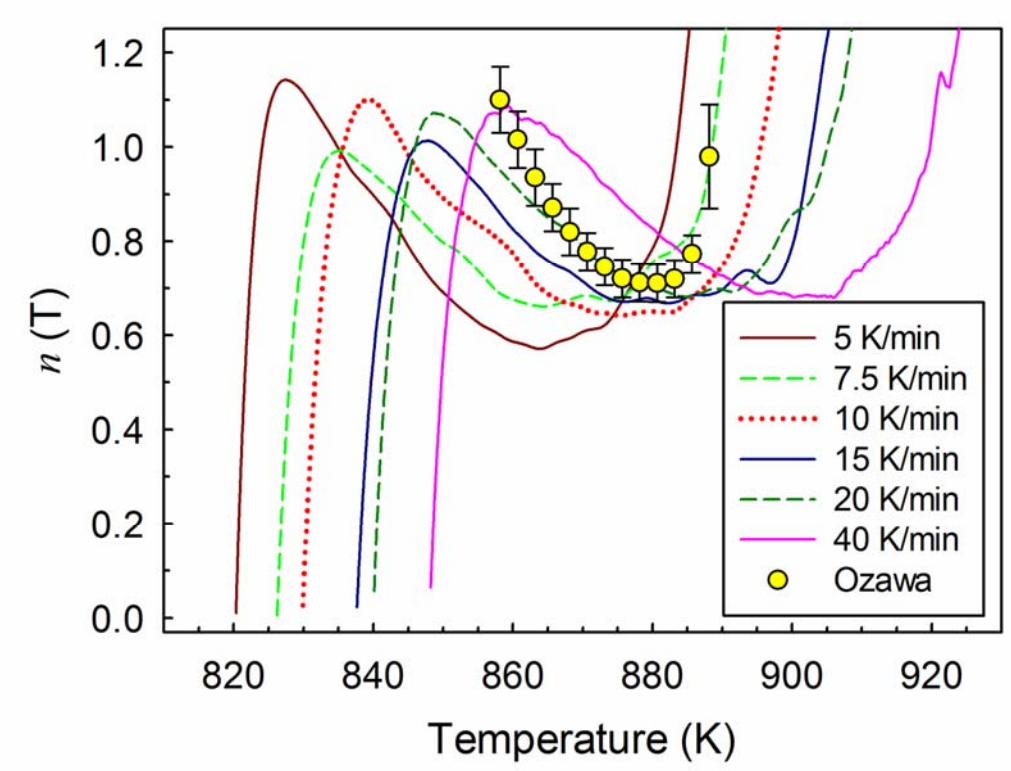

Figure 6.16 Local Avrami exponent, $n(T)$, obtained by non-isothermal DSC analysis at different heating rates compared with Ozawa analysis.

6.4 Isothermal Kinetics of Nanocrystallization by Magnetic Monitoring

Figure 6.17 shows the thermomagnetization behavior of the Cu-modified $Fe_{43}Co_{19}Ni_9B_{19}Si_5Nb_4$ alloy obtained under 500 Oe applied magnetic field with a heating rate of 5 K/min. The low temperature region corresponds to the glassy state and displays a linear behavior with temperature, however, the alloy possess a ferro-paramagnetic transition with an abrupt drop in magnetization to fairly low values above Curie temperature T_C = 631 K, where again a linear M-T dependence is observed up to the onset of primary crystallization around 850 K. The inset corresponds to the high temperature region (above glass transition, T_g ~ 802 K) of the magnetization behavior

where the amorphous phase is paramagnetic. The first transient increase in magnetization can be said to correspond to the primary crystallization of ferromagnetic α–(Fe,Co) phase with higher T_C than the amorphous matrix. The Curie transition-type fall in magnetization around 943 K occurs well below the expected T_C for α–(Fe,Co) nanocrystals (1040 – 1250 K) which was previously ascribed to a non-reversible process of crystallization of boride phases lowering the volume fraction of α–(Fe,Co) phase [142]. The first increase in magnetization in the form of a peak is followed by a second transient increase associated with increase in the volume fraction of Fe-boride phases.

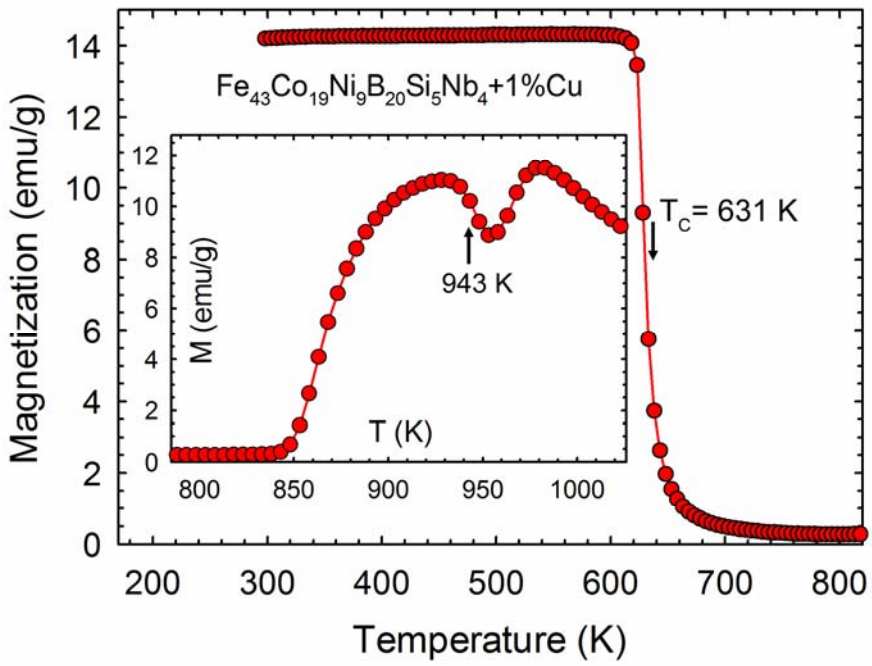

Figure 6.17 Temperature scan magnetization curve showing successive crystallization of ferromagnetic phases above T_C of amorphous alloy.

Owing to the ferromagnetic character of the primary crystallization product, it will be interesting to monitor the evolution of α–(Fe,Co) crystals above T_C of the amorphous alloy matrix where the contribution of the amorphous phase to magnetization is negligible. For this purpose, a number of isothermal magnetization traces were recorded (Figure 6.18) at various temperatures above T_g, and, transformed fraction, X_t, was calculated by Equation (7).

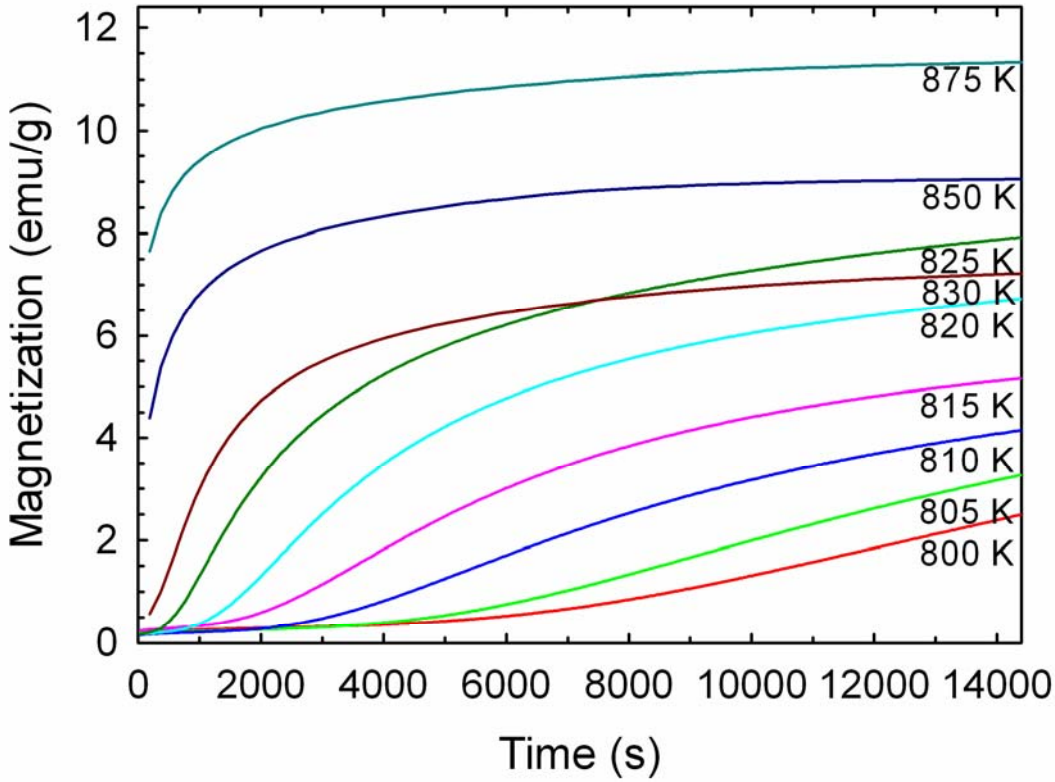

Figure 6.18 Isothermal magnetization behavior of Cu-modified $Fe_{43}Co_{19}Ni_9B_{19}Si_5Nb_4$ alloy under 500 Oe applied magnetic field.

Transformed fraction curves given in Figure 6.19 disclose that isotheral magnetization of alloys follow sigmoidal shapes at intermediate temperatures 810–825 K with clearly identifiable incubation times which were not observed at higher temperatures (T > 830 K) due to the fact that incubation took place during heating to the prescribed annealing temperature. As expected, due to the very slow crystallization kinetics at temperatures slightly above T_g, isotherms below 810 K provided only small increments in magnetization within the utilized measurement time.

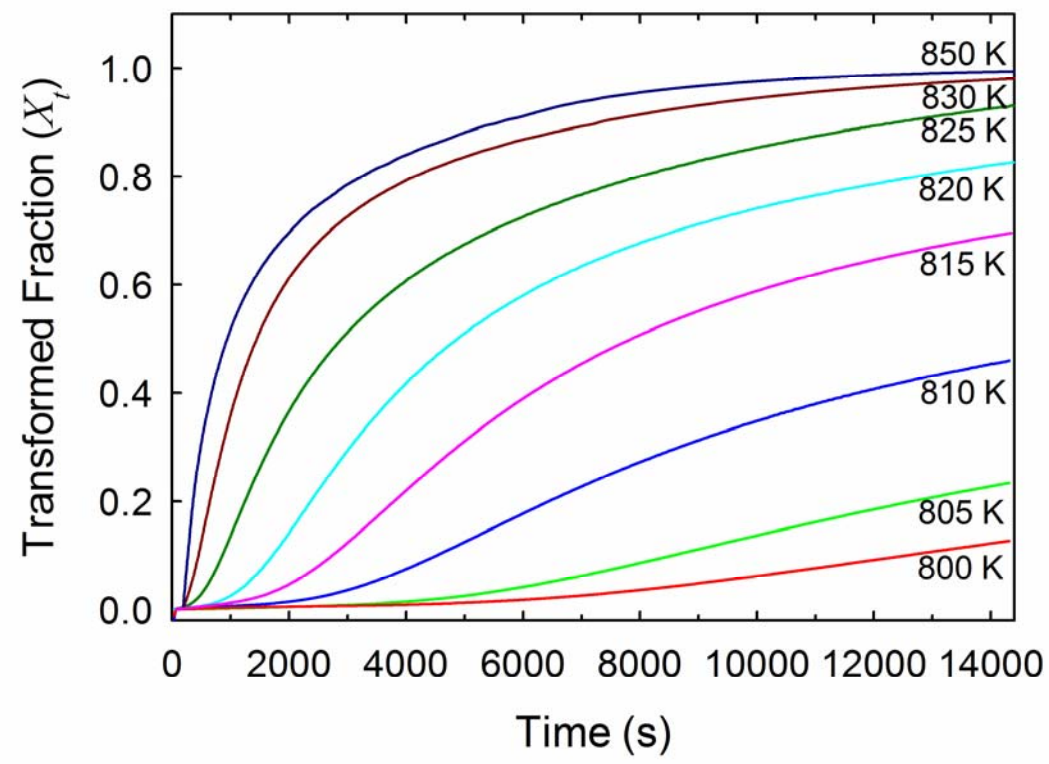

Figure 6.19 Transformed fraction curves for α–(Fe,Co) phase calculated by isothermal magnetization measurements.

Avrami plots extracted from three isotherms (Figure 6.20) show significant non-linearity along crystallization path which might be qualitatively described by three crystallization regimes; (I) an initial regime with low and increasing $n(X)$ with t, (II) an intermediate regime where highest values of $n(X)$ are obtained, and, (III) a later regime with decreasing $n(X)$ with t. Each transformation regime along the course of crystallization can be understood by examining local Avrami exponent, $n(X)$, calculated using Equation (4).

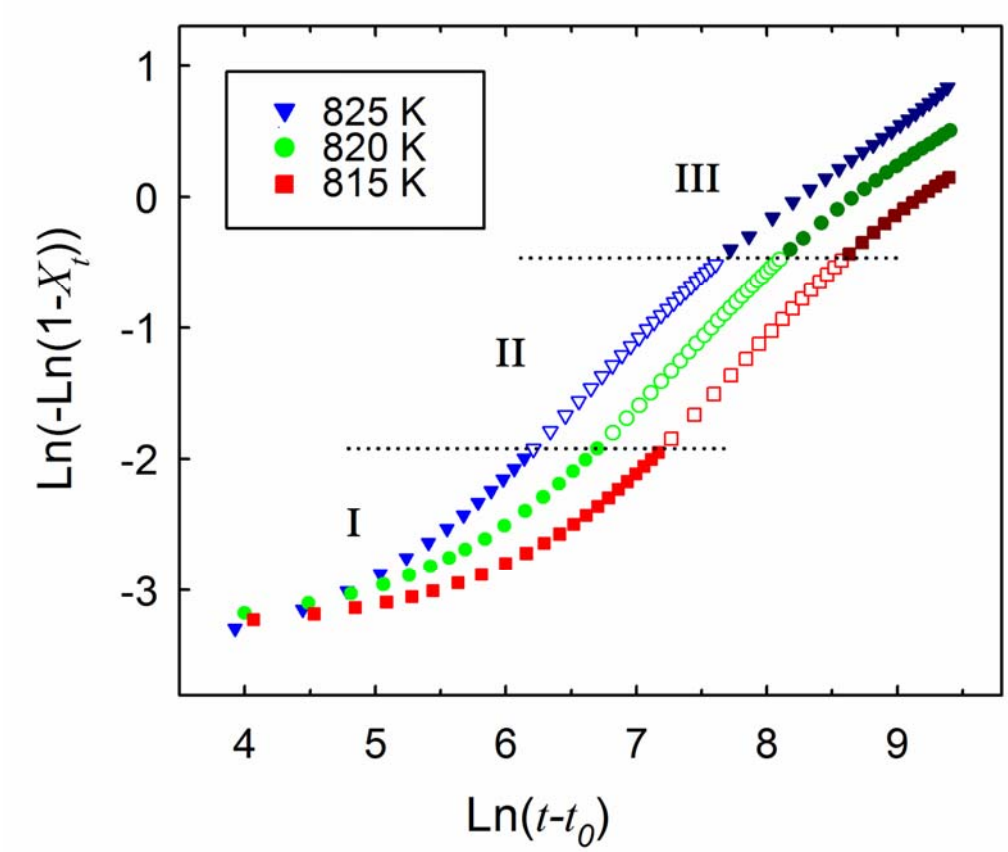

Figure 6.20 Avrami plots for different isotherms revealing three qualitative regions.

Figure 6.21 compares local Avrami exponent, $n(X)$, curves obtained from the direct extension of JMAK theory to non-isothermal DSC analysis (at different β) and that from classical JMAK theory as applied to isothermal magnetic monitoring. It is clear that excellent agreement exists between non-isothermal DSC and isothermal magnetic monitoring approaches throughout almost the whole crystallization process.

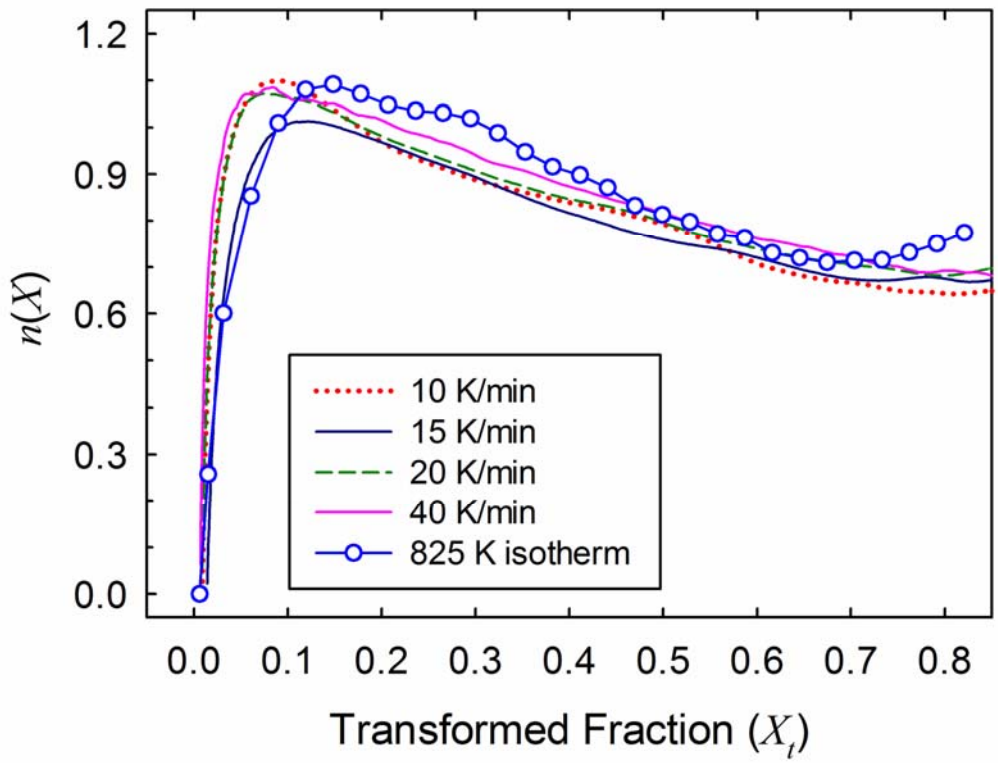

Figure 6.21 Local Avrami exponents comparing non-isothermal DSC analysis and isothermal magnetization measurements.

Mechanisms underlying nanocrystallization by primary crystallization of the amorphous precursor can be interpreted by examining the three qualitatively distinct transformation regimes (I, II and III) observed in the Avrami plots. Figure 6.22 contains $n(X)$ curves which reveal local transformation kinetics along the crystallization process.

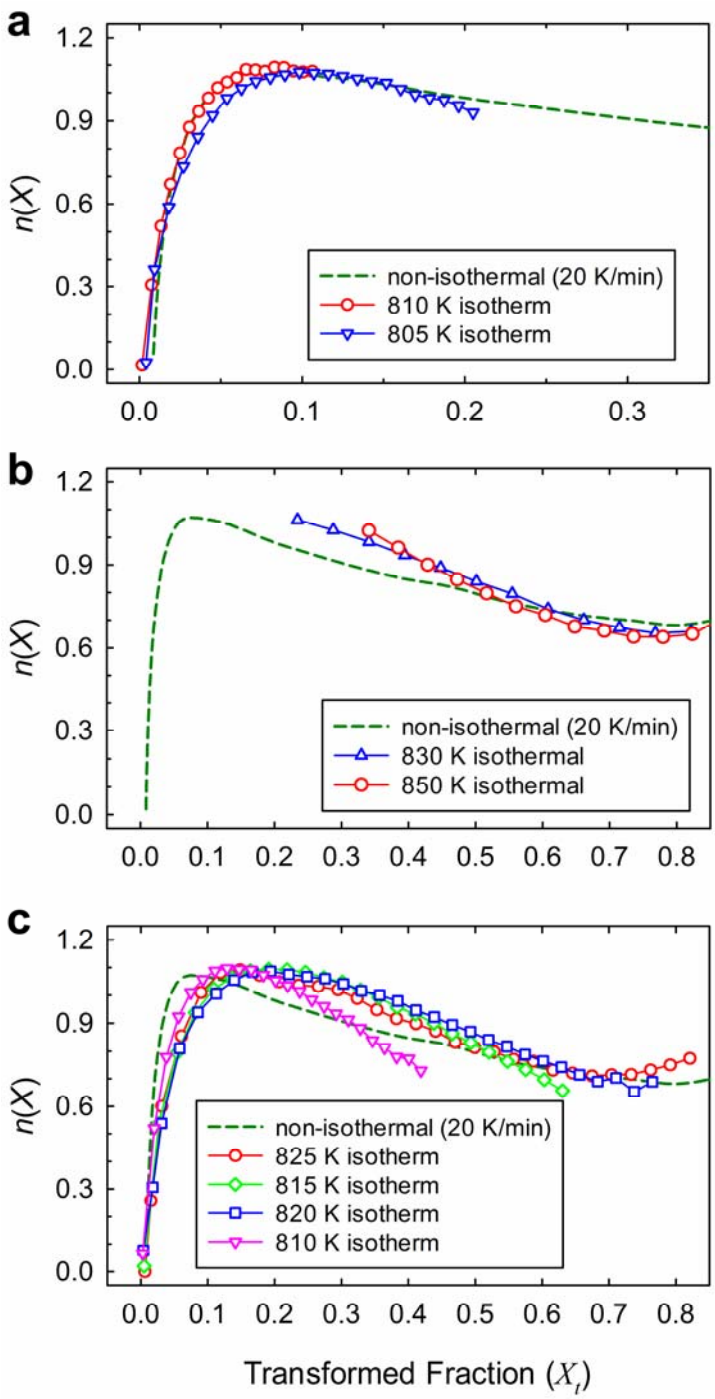

Figure 6.22 Local Avrami exponent, $n(X)$, calculated at different isotherms compared with non-isothermal JMAK direct extension; (a) initial crystallization regime (b) late crystallization regime, (c) overall crystallization process.

The initial transformation regime (I) in Figure 6.22(a) roughly corresponding to transformed fractions less than $X_t < 0.1$, evolves through abnormally low and increasing local Avrami exponent below unity. Due to the extremely fine size of nucleating α–(Fe,Co) crystals, the stage of establishment of steady state diffusion field can not be neglected. In addition, the transient nucleation effect, which causes deviation from the JMAK theory, was shown to be significant at small crystallized fractions for processes with moderate nucleating barrier [143]. These should provide an explanation for abnormally low and increasing $n(X)$ in the early transformation regime.

The second transformation regime (II) outlined in Figure 6.22(b) corresponds roughly to $0.1 < X_t < 0.4$ and contains the highest $n(X)$ values over the whole primary crystallization process. Local Avrami exponent reaching maxima in the range n=1–1.2 for different isotherms might correspond to diffusion controlled growth of nuclei formed by instantaneous nucleation and site saturation (zero nucleation rate) with negligible initial dimensions [93]. It can be presumed that crystallization is dominated by the growth process provided that instantaneous nucleation occurs. The local Avrami exponent derived from JMAK can be considered valid since the requirement of JMAK theory is fulfilled in respect of uniformly distributed and random nucleation sites. These explanations should make sense for the particular Cu-modified $Fe_{43}Co_{19}Ni_9B_{19}Si_5Nb_4$ alloy since transient or initial nucleation effects are imposed in nanocrystalline systems by Cu clusters formed through structural relaxation of the glass prior to its crystallization which act as random heterogeneous nucleation sites.

The third transformation regime (III) shown by Figure 6.22(c) representing crystallized fractions $X_t > 0.4$ show gradual decrease of $n(X)$ from around unity to n=0.6-0.7 which indicates significant slowing down of crystallization reaction as transformation proceeds. Decrease in the nucleation rate was shown to be insufficient in explaining the observed experimental $n(X)$ values going below unity in the late stages of

transformation [144]. In the studied Cu-modified $Fe_{43}Co_{19}Ni_9B_{19}Si_5Nb_4$ amorphous alloy, Nb plays a significant role on growth suppression due to its low solubility in the α–(Fe,Co) phase (Appendix C) and slow diffusivity in the amorphous phase. This causes Nb atoms to be rejected from nanocrystals to the residual amorphous matrix and piling up of Nb atoms at nanocrystal edges acting as a diffusion barrier against growth.

In addition to the nanocrystal pinning effect of Nb, decrease in the local Avrami exponent with X_t can be alternatively explained by a soft-impinged growth mechanism [145, 146]. It was mentioned above that growth of the nanocrystalline phase in the amorphous matrix occurs by a diffusion controlled mechanism. The redistribution of alloy components among the nanocrystalline phase and the residual amorphous phase creates a concentration gradient of solute atoms in the residual amorphous phase. Due to small interparticle spacing of α–(Fe,Co) nanocrystals, diffusion profiles of neighboring grains interfere with each other yielding lower concentration gradient at the interface. Therefore, suppressed growth of nanocrystalline phase takes place under the influence of soft-impingement diffusion mechanism after a crystallized fraction of around X_t=0.4 is attained.

Additionally, it is shown in Figure 6.23 that $n(X)$ becomes nearly constant when the crystallized volume fraction reaches $X_t > 0.25$ when a relation which accounts for soft-impingement was employed as a modified JMAK isothermal kinetic model [147]. This confirms the proposed soft-impinged growth mechanism for the gradual decrease of $n(X)$ in the late transformation regime.

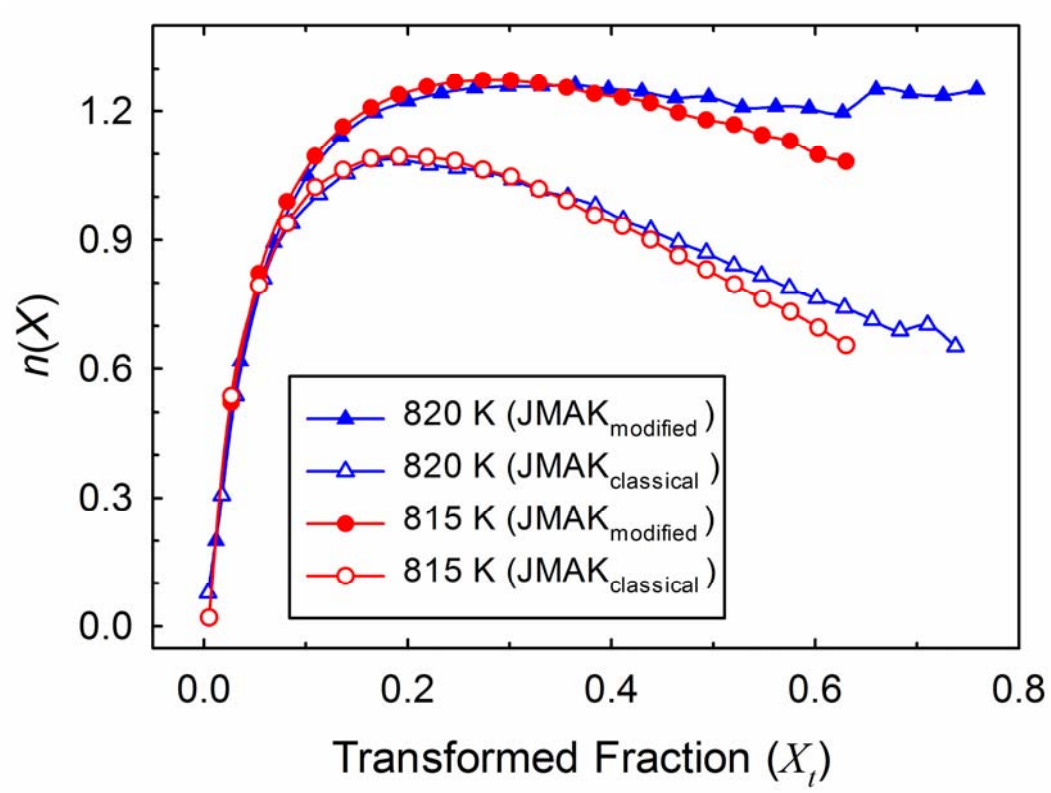

Figure 6.23 The classical JMAK treatment as applied to isothermal magnetization compared to a soft-impingement diffusion mechanism represented by a modified JMAK relation.

Lastly, the influence of varying activation energy during crystallization is also taken into account in the direct extension of JMAK theory and $n(X)$ values are recalculated using non-isothermal DSC analysis implementing local activation energy, $Q_a(X)$, estimations from classical JMAK theory as applied to isothermal magnetization (Figure 6.24). Energy barrier for crystallization has a moderate dependence on the extent of transformation and gradually decreases when $X_t > 0.4$. The variation of Q_a during crystallization was ascribed to change in the nucleation and growth behavior during crystallization. However, consistent with an earlier study [96], the local Avrami exponent is only slightly sensitive to Q_a.

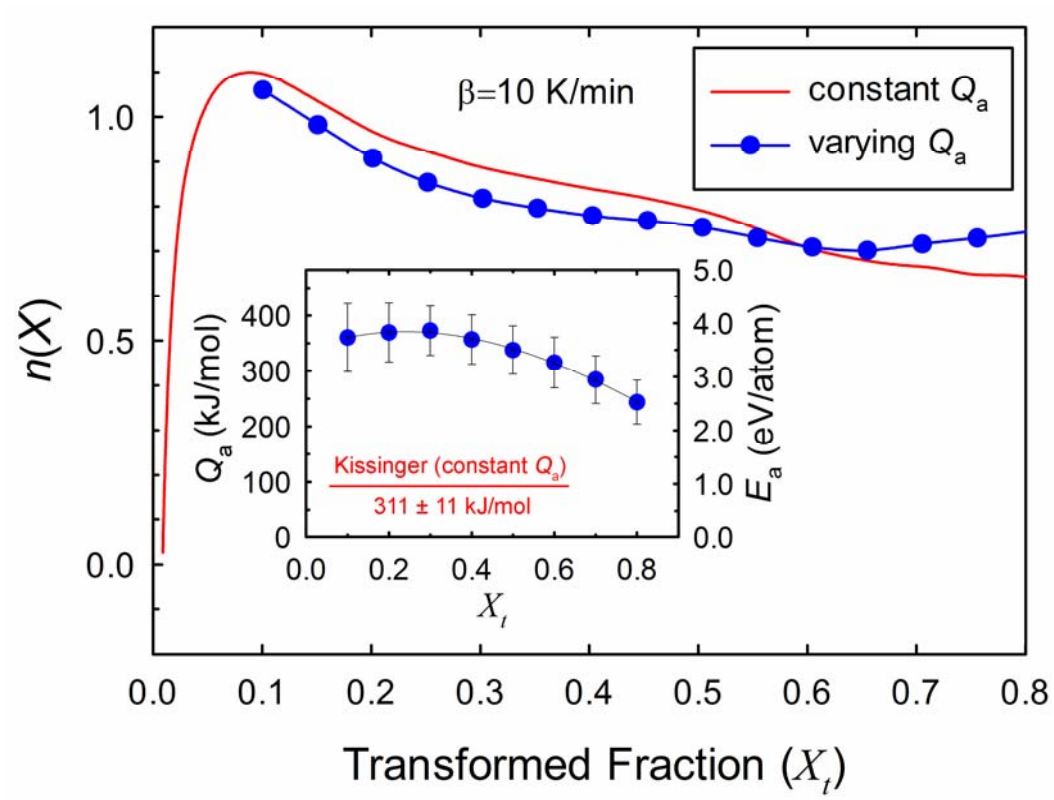

Figure 6.24 Local Avrami exponents calculated by non-isothermal DSC analysis utilizing constant and varying Q_a values. Inset shows the variation of Q_a calculated by classical JMAK as applied to isothermal magnetization compared to constant Q_a derived from Kissinger analysis.

The course of α–(Fe,Co) nanocrystallization was microscopically investigated by annealing the suction-cast Cu-modified $Fe_{43}Co_{19}Ni_9B_{19}Si_5Nb_4$ alloy in the supercooled liquid region (~30 K below the onset of first crystallization exotherm) for different durations in Figure 6.25. Three annealing periods (i.e. 15 min, 40 min, 3 h) were determined from the 820 K isothermal transformation curve obtained by magnetic monitoring so as to correspond to transformed fractions within the mentioned three qualitatively distinct transformation regimes; (i) initial regime (Xt ~ 0.05), (ii) the intermediate regime (Xt ~ 0.3) and (iii) the later regime (Xt ~ 0.8).

Figure 6.25 contains bright-field TEM images, corresponding SAED patterns and high-resolution TEM images of annealed Cu-modified $Fe_{43}Co_{19}Ni_9B_{19}Si_5Nb_4$ alloy. The bright field TEM image of the alloy crystallized in the initial transformation regime indicates the formation of extremely fine (3–4 nm) crystalline regions in the amorphous matrix.

In the intermediate regime (Figure 6.25b), a two-phase microstructure consisting of fine α–(Fe,Co) nanocrystals and residual amorphous matrix is obtained via high number density Cu-enriched clusters being formed prior to crystallization acting as nucleation sites. In this regime, the nucleated nanocrystals grow with the highest rate over the whole primary crystallization process course to attain an average apparent size around 4–7 nm with 2400 s annealing. The SAED pattern taken from a representative region showing polycrystalline rings completely indexed to a bcc structure (Figure 6.25c). It becomes clear that appropriate annealing leads to high number density, fine-sized and randomly oriented α–(Fe,Co) nanocrystals inside an amorphous matrix. Figure 6.25(d) contains the high-resolution TEM image showing (110) lattice fringes of an α–(Fe,Co) nanocrystal covered by the amorphous matrix. Approximate compositional analysis by TEM-EDS reveal that α–(Fe,Co) nanocrystals possess an average Fe/Co ratio of ~1.8 which is lower than the overall Fe/Co~2.3 in the amorphous state prior to crystallization which suggests Co partitioning at least to some extent. Nanocrystallization is also found to proceed through partitioning of Si being almost equally distributed in nanocrystals and the residual amorphous phase.

Throughout the late transformation regime, the growth rate of α–(Fe,Co) nanocrystals is reduced and nanocrystals attain sizes in the range 6–9 nm upon 3 h annealing. The suppressed growth of nanocrystals is due to small interparticle spacing and increased crystallized fraction causing soft-impingement, i.e. overlapping of solute diffusion fields. In particular, the diffusion-controlled growth of nanocrystals is rather sluggish since it

requires long-range diffusion of Nb atoms in the amorphous phase. Examining TEM micrographs for intermediate and late transformation regimes (Figure 6.25), the areal nucleation density of nanocrystals in the amorphous matrix does not significantly change which confirms heterogeneous nucleation on Cu-clusters and subsequent site saturation during annealing.

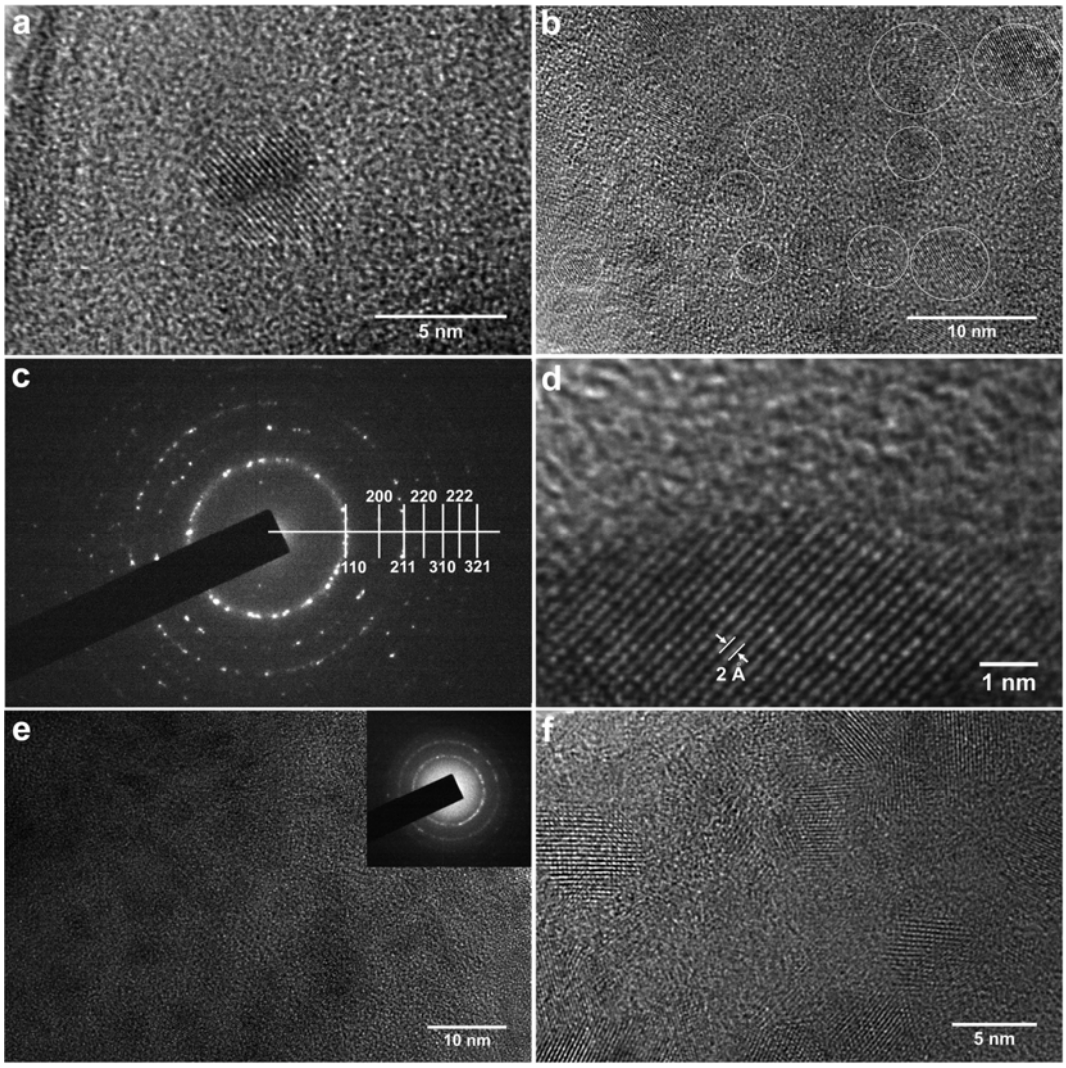

Figure 6.25 TEM images and SAED patterns of Cu-modified $Fe_{43}Co_{19}Ni_9B_{19}Si_5Nb_4$ alloy annealed at 823 K; (a) 900 s annealing, (b) 2400 s annealing, (c-d) SAED pattern and high-resolution micrograph corresponding to 2400 s annealing, (e-f) 10800 s annealing.

Figure 6.26 contains the XRD patterns which reveal the evolution of α–(Fe,Co) nanocrystals during annealing. Average thicknesses of nanocrystals were calculated using X-ray line broadening of deconvoluted (110) reflection of the α–(Fe,Co) phase by taking linear background, and mixed Gaussian-Lorentzian and Gaussian line shapes for the crystalline and the amorphous phases, respectively as shown in Figure 6.27. Detectable α–(Fe,Co) (110) reflection occurs only when t > 20 min at an annealing temperature of 823 K where the crystallite thickness and volume fraction of the crystalline phase was calculated as ~6 nm and 0.07, respectively. Longer annealing times lead to increases in volume fraction of crystals to ~ 0.19–0.23 while the nanocrystals grow asymptotically to attain average sizes slightly lower than 10 nm.

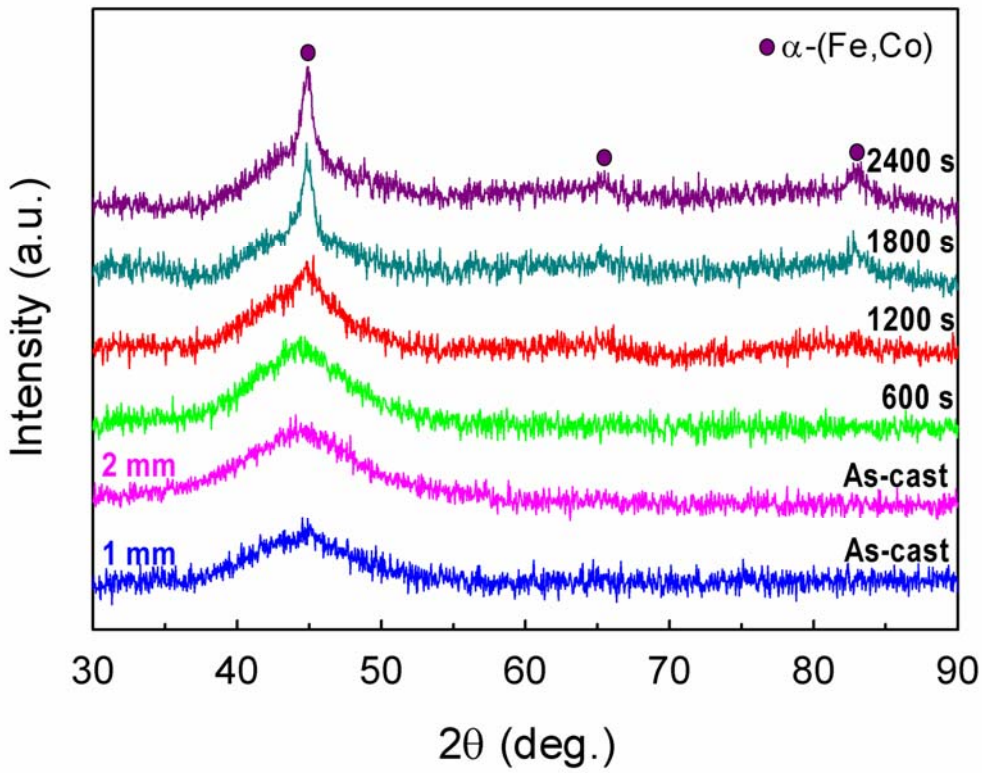

Figure 6.26 XRD patterns showing the evolution of α–(Fe,Co) nanocrystals during 823 K annealing for different durations.

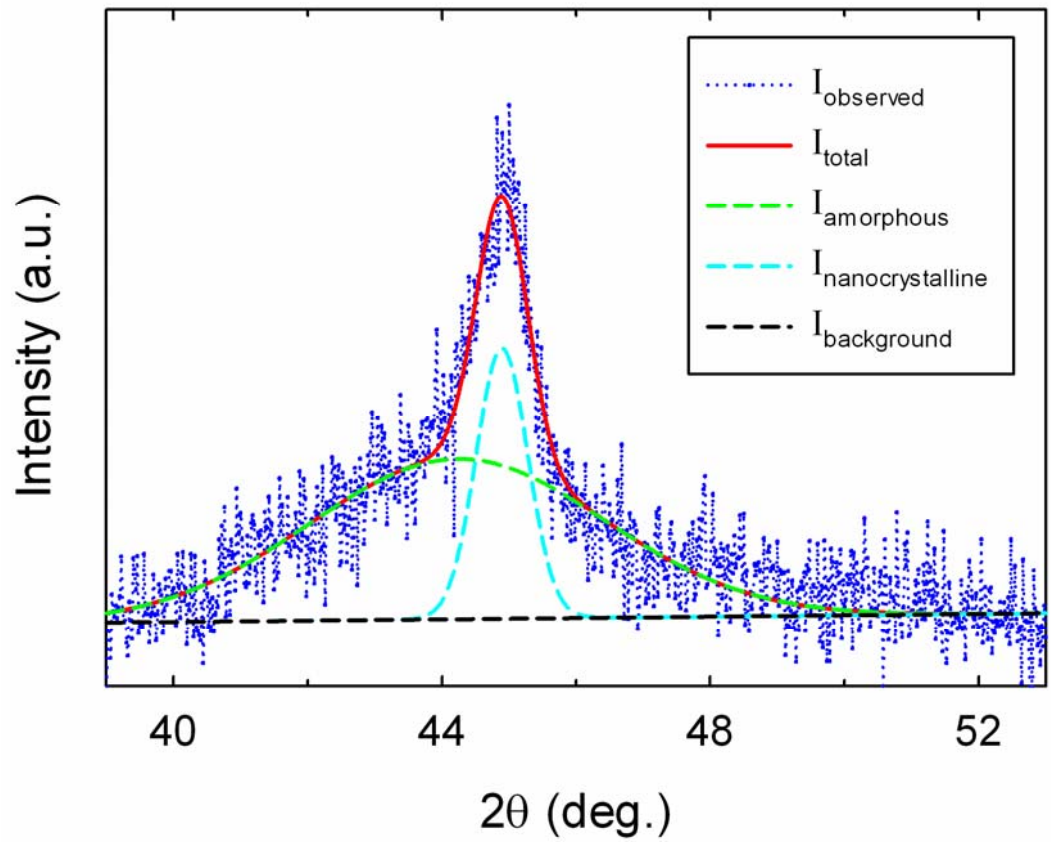

Figure 6.27 Deconvoluted XRD pattern of 873 K annealed alloy showing reflections from amorphous matrix and α–(Fe,Co) nanocrystals.

Figure 6.28 shows the magnetic behavior of the Cu-modified $Fe_{43}Co_{19}Ni_9B_{19}Si_5Nb_4$ alloy in the suction-cast and annealed states. Annealing at the peak temperature of first crystallization exotherm corresponding to α–(Fe,Co) nanocrystallization imparts enhanced saturation magnetization accompanied by a slight increase in coercivity. On the other hand, annealing at peak temperatures of iron-boride crystallization exotherms leads to increased saturation magnetization along with significantly larger coercive force indicating deteriorated soft magnetic properties.

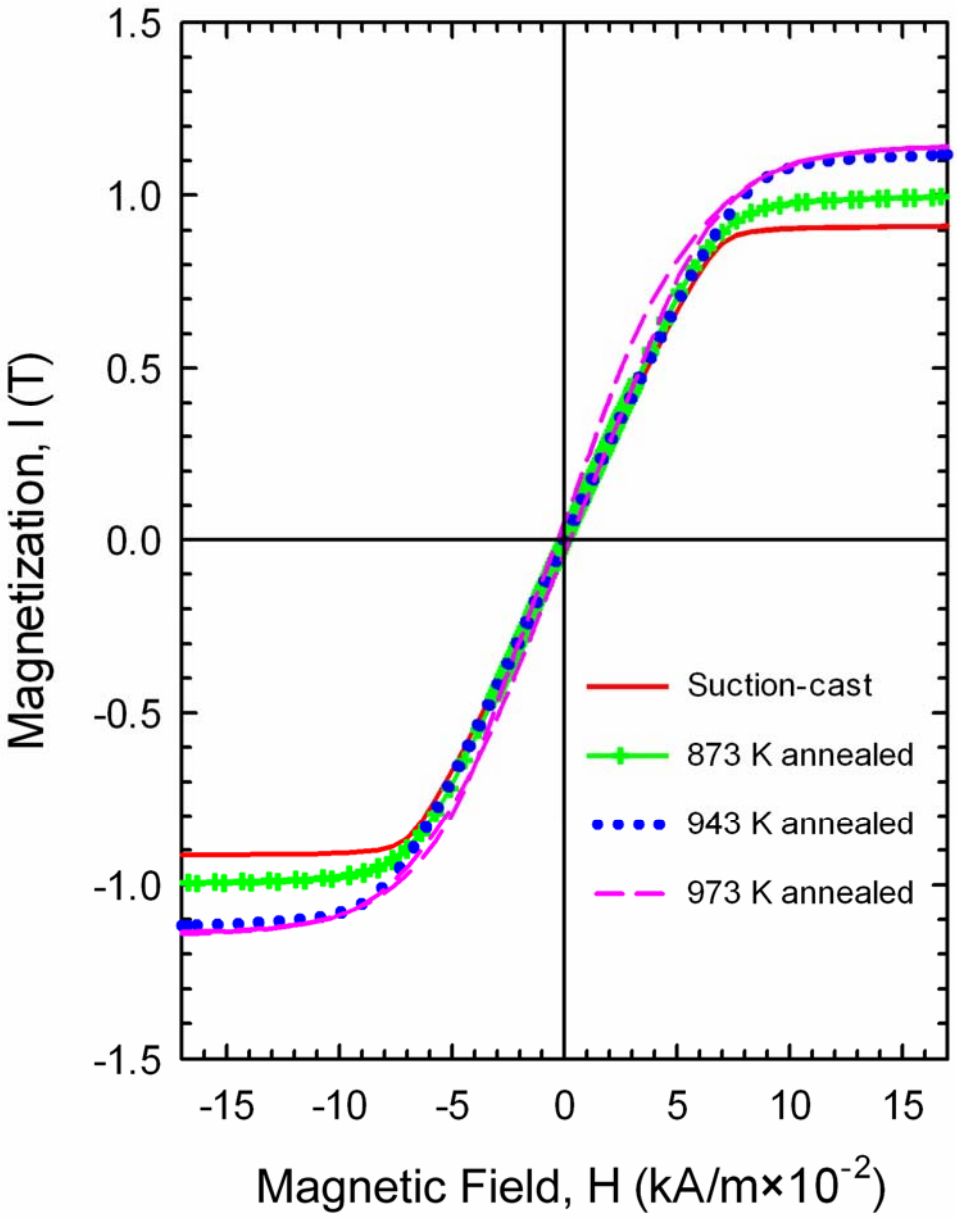

Figure 6.28 Room temperature hysteresis loops of suction-cast and annealed Cu-modified $Fe_{43}Co_{19}Ni_9B_{19}Si_5Nb_4$ alloy.

CHAPTER 7

CONCLUSIONS

Macroalloying NiAl with Fe

The microstructure and properties of $Ni_{50}Fe_xAl_{50-x}$ alloys where x=20, 25, and 30 were investigated at various annealing temperatures. Annealing carried out at 1073 K promoted the formation of an FCC γ-phase within the grains and along grain boundaries of $Ni_{50}Fe_{20}Al_{30}$ single β-phase alloy. The $Ni_{50}Fe_{25}Al_{25}$ and $Ni_{50}Fe_{30}Al_{20}$ alloys showed a dendritic microstructure, and the amounts of γ-phase increased together with that the eutectic regions transformed into single γ-phase in alloys annealed at 1073 K.

Transient rises in magnetization of alloys observed at temperatures higher than the T_C of alloy matrices during temperature-scan measurements were attributed to the formation of a new ferromagnetic phase. Retained magnetization upon the Curie transition of the alloy matrix seen in alloys annealed at 673 K and 873 K supported the presence of ferromagnetic precipitates of higher Curie transition temperature. An annealing temperature of 673 K induced significant enhancements in room temperature saturation magnetization of $Ni_{50}Fe_xAl_{50-x}$ alloys owing to favored ferromagnetic phase precipitation.

Significant improvements were obtained in compressive yield strength and ductility of binary NiAl with the incorporation of Fe as a macro-alloying element. The $Ni_{50}Fe_{25}Al_{25}$ alloy shows slightly lower yield strength but increased ductility compared to $Ni_{50}Fe_{20}Al_{30}$ alloy due to the presence of a softer γ-phase in the interdendritic region in addition to hard β-phase

dendrites. Further decreases were observed in compressive yield strength for the $Ni_{50}Fe_{30}Al_{20}$ alloy since the volume fraction of the softer γ-phase was increased at the expense of hard β-phase. Due to increased volume fraction of the soft γ-phase, significant improvement in ductility can be obtained in alloys by annealing at 1073 K. Annealing of alloys at 673 K provided significant enhancements in yield strength through precipitation strengthening by nano-scale BCC α-Fe second phase particles. Micro-hardness of the β-phase, within which the nano-sized precipitates were observed, well correlates with room temperature saturation magnetization values of alloys as a function of utilized annealing temperatures. The nano-scale precipitation of ferromagnetic BCC α-Fe in the $Ni_{50}Fe_{25}Al_{25}$ alloy annealed at 673 K was confirmed by transmission electron microscopy.

Time–temperature dependence and kinetic aspects of α-phase precipitation in $Ni_{50}Fe_xAl_{50-x}$ alloys for x = 20, 25 and 30 were investigated by continuous heating and isothermal experiments in vibrating sample magnetometer. The α-phase precipitation process was treated by the JMA kinetic model where the time exponent for the process assumed values around n = 1, independent of the extent of precipitation, utilized isothermal temperature and alloy composition. The activation energies for the precipitation in three different alloy compositions were determined to range between 75 and 83 kJ/mol. It was concluded that the examined process is diffusion controlled growth with decreasing growth rate. Corresponding isothermal transformation diagrams, providing a general picture for the nano-sized BCC α-phase precipitation, were drawn by using magnetically assessed kinetic parameters.

Depending on the measured rates of magnetization at utilized temperatures in isothermal runs, remarkable precipitate growth rates were expected at annealing temperatures higher than around 750 K. It is intriguing that alloys annealed at 673 K presented a microstructure comprising of fine precipitates which provided ultimate hardening of the matrix involving

precipitates, in accordance with magnetic measurements. As opposed to that, a higher annealing temperature of 873 K resulted in a coarser microstructure accompanied by a corresponding reduction in the extent of precipitation hardening.

Microalloying Effects in Ni-Al-Fe Alloys

Influence of Co, Mn and V substitutions for 1 at.% Fe on the microstructure, magnetic properties and nanoscale precipitation was investigated in Ni-25Al-25Fe alloys. Modified alloys showed three phase microstructures consisting of dendritic β-phase and interdendritic β (ordered bcc) + γ (disordered fcc) + γ' (ordered fcc) phases in the as-cast state. Addition of Co and V decreased the volume fraction of interdendritic region while Mn had an opposite effect. High temperature (1073 K) annealing promoted needle-like disordered γ-phase precipitation in the β-phase dendrites for Mn- and Co-modified alloys. Dendritic microstructure disappeared and needle-like disordered γ-phase precipitates were formed within β-matrix in V modified alloy. After 1073 K annealing, all studied alloys demonstrated the dissolution of ordered γ'-phase into the γ (Ni,Fe) solid solution phase which facilitated the growth of β-phase particles embedded in the interdendritic region.

Mn and V additions decreased Curie transition temperature (T_C) while Co slightly increased T_C. These alterations of T_C were ascribed to changes in strength of exchange interactions in Mn- or Co-modified alloys, and antiferromagnetic alignment of magnetic moments of Fe and V in V-modified alloy.

Addition of Mn and Co caused softening of the β-phase dendrites whereas V had an opposite effect. In terms of compressive properties, V modification provided the greatest enhancement in yield strength. Ductility was decreased upon annealing at 673 and 873 K annealing and recovered by 1073 K

annealing due to increased volume fraction of the softer γ-phase. In conjunction with enhanced saturation magnetization, annealing of modified alloys at 673 K provided significant hardening of the β-phase and strengthening of the alloy which was attributed to the precipitation of a ferromagnetic second phase. TEM investigations revealed the precipitation of fine spherical disordered bcc α-phase within ordered β-matrix upon annealing. Ferromagnetic phase precipitation was verified by examining thermomagnetization behavior of alloys showing transient increases in magnetization at high temperatures. The temperature range of precipitation as monitored by magnetic measurements shifted to higher temperatures with V modification.

Isothermal kinetics of ferromagnetic phase precipitation was studied by a magnetic monitoring approach using Johnson-Mehl-Avrami model and it was found that V imparted a considerable suppression of precipitate growth particularly at high temperatures and large transformed fractions. Therefore, V substitution for Fe appears to be a promising approach to improve stability of the finely precipitated microstructure in Ni-Al-Fe alloys and deserves further studies to reveal NiAlFe-V alloys' promising high temperature structural properties.

Fe-based Bulk Amorphous Alloys

Cu-modified $Fe_{43}Co_{28-x}Ni_xB_{19}Si_5Nb_4$ alloys with varying Co/Ni ratio were prepared by arc melting and subsequent suction casting where best glass forming ability was attained at the lowest Ni content of 9 at.% (19 at.% Co). SEM images of suction-cast Cu-modified $Fe_{43}Co_{19}Ni_9B_{19}Si_5Nb_4$ alloy after convenient etching revealed featureless microstructure indicative of the amorphous state. Relatively slow-cooled Cu-modified $Fe_{43}Co_{19}Ni_9B_{19}Si_5Nb_4$

alloy displayed three distinguishable crystalline regions corresponding to α–(Fe,Co), (Fe,Co)NbB and $(Fe,Co)_2B$ phases.

Appropriate annealing of the amorphous precursor produced extremely fine microstructures containing uniformly distributed and densely dispersed α–(Fe,Co) nanocrystalline phase inside an amorphous matrix.

Kinetics of α–(Fe,Co) nanocrystallization was studied by DSC analysis which yielded activation barriers in the range 272–325 kJ/mol by different non-isothermal approaches. Using a direct extension of JMAK theory to non-isothermal regimes, local Avrami exponent, $n(X)$, was calculated for different heating rates. Temperature dependent Avrami exponent, $n(T)$, was also calculated from Ozawa analysis and shown qualitatively to be in good agreement with $n(T)$ derived from the direct extension of JMAK to non-isothermal kinetics at least for high crystallized fractions.

Thermomagnetizaton behavior of Cu modified FeSiB alloy revealed an increase in the magnetic moment above T_C of the amorphous phase which was related with the ferromagnetic character of α–(Fe,Co) nanocrystals. The course of α–(Fe,Co) nanocrystallization was tracked employing the magnetic response of alloys during annealing which revealed X dependent Avrami exponent, $n(X)$ and activation energy, $Q_a(X)$. The energy barrier for nanocrystallization was found to follow a decreasing trend as crystallization proceeds where the range of $Q_a(X)$ from isothermal magnetization was consistent with overall Q_a obtained from non-isothermal Kissinger analysis.

The local Avrami exponent, $n(X)$, extracted using classical JMAK theory as applied to isothermal magnetization provided a better understanding of the transformation mechanism as crystallization proceeds. Excellent agreement in local transformation kinetics was obtained between non-isothermal DSC analysis and isothermal magnetic monitoring. The early stages of crystallization follow abnormally low and increasing $n(X)$ due to non-steady state diffusion and transient nucleation effects. At the intermediate crystallization regime, $n(X)$ attains maximum values in the range n=1–1.2

which was attributed to diffusion controlled growth of instantaneously nucleated extremely fine crystalline regions. Later crystallization regime displays a gradual decrease of $n(X)$ to around 0.6–0.7 which was explained by diffusion controlled soft-impinged growth. A modified JMAK relation involving the impingement effect was used where it was found that $n(X)$ attains constant values verifying the soft-impingement diffusion mechanism for slowing down kinetics as transformation proceeds. The course of nanocrystallization examined through isothermal magnetic monitoring was verified with microstructural investigations on the amorphous matrix nanocrystalline alloys in each distinct transformation regime described in this study.

REFERENCES

[1] I. Akihisa, Stabilization of metallic supercooled liquid and bulk amorphous alloys, Acta Materialia 48 (2000) 279-306.

[2] C.J. Byrne, M. Eldrup, Bulk metallic glasses, Science 321 (2008) 502-503.

[3] W.L. Johnson, Bulk amorphous metal—an emerging engineering material, JOM Journal of the Minerals, Metals and Materials Society 54 (2002) 40-43.

[4] L. Jörg F, Bulk metallic glasses, Intermetallics 11 (2003) 529-540.

[5] C.A. Schuh, T.C. Hufnagel, U. Ramamurty, Mechanical behavior of amorphous alloys, Acta Materialia 55 (2007) 4067-4109.

[6] W. Wei Hua, The elastic properties, elastic models and elastic perspectives of metallic glasses, Progress in Materials Science (2012)

[7] I. Akihisa, Bulk amorphous alloys with soft and hard magnetic properties, Materials Science and Engineering: A 226-228 (1997) 357-363.

[8] F. Li, T. Zhang, A. Inoue, S. Guan, N. Shen, (Fe,Co)–Zr–Nd–B bulk amorphous alloys with good soft magnetic properties, Intermetallics 12 (2004) 1139-1142.

[9] S.J. Pang, T. Zhang, K. Asami, A. Inoue, Synthesis of Fe–Cr–Mo–C–B–P bulk metallic glasses with high corrosion resistance, Acta Materialia 50 (2002) 489-497.

[10] L. Wang, Y. Chao, Corrosion behavior of $Fe_{41}Co_7Cr_{15}Mo_{14}C_{15}B_6Y_2$ bulk metallic glass in NaCl solution, Materials Letters 69 (2012) 76-78.

[11] A. Inoue, B.L. Shen, C.T. Chang, Fe- and Co-based bulk glassy alloys with ultrahigh strength of over 4000 MPa, Intermetallics 14 (2006) 936-944.

[12] A. Inoue, B.L. Shen, C.T. Chang, Super-high strength of over 4000 MPa for Fe-based bulk glassy alloys in $[(Fe_{1-x}Co_x)_{0.75}B_{0.2}Si_{0.05}]_{96}Nb_4$ system, Acta Materialia 52 (2004) 4093-4099.

[13] R.W. Cahn, P. Haasen, Physical metallurgy, (1983)

[14] P. Nash, M.F. Singleton, J.L. Murray, Phase diagrams of binary nickel alloys (ed.), ASM international 1 (1991)

[15] G. Sauthoff, Intermetallics, (1995)

[16] R.C. Reed, The superalloys fundamentals and applications, (2006)

[17] J.H. Westbrook, R.L. Fleischer, Intermetallic compounds structural applications of intermetallic compounds, 3 (2000)

[18] C.L. Fu, M.H. Yoo, Deformation behavior of B2 type aluminides: FeAl and NiAl, Acta Metallurgica et Materialia 40 (1992) 703-711.

[19] T. Hong, A.J. Freeman, Effect of antiphase boundaries on the electronic structure and bonding character of intermetallic systems: NiAl, Physical Review B 43 (1991) 6446-6458.

[20] R. Rablbauer, R. Fischer, G. Frommeyer, Mechanical properties of NiAl-Cr alloys in relation to microstructure and atomic defects, Zeitschrift fuer Metallkunde/Materials Research and Advanced Techniques 95 (2004) 525-534.

[21] R.D. Field, D.F. Lahrman, R. Darolia, The effect of alloying on slip systems in 001 oriented NiAl single crystals, Acta Metallurgica et Materialia 39 (1991) 2961-2969.

[22] S. Guha, P.R. Munroe, I. Baker, Room temperature deformation behavior of multiphase Ni—20at.%Al—30at.%Fe and its constituent phases, Materials Science and Engineering: A 131 (1991) 27-37.

[23] J.D. Cotton, R.D. Noebe, M.J. Kaufman, The effects of chromium on NiAl intermetallic alloys: Part I. Microstructures and mechanical properties, Intermetallics 1 (1993) 3-20.

[24] D.B. Miracle, S.M. Russell, C.C. Law, High temperature ordered intermetallic alloys III, Materials Research Society Symposium Proceedings 133 (1989) 225.

[25] R. Darolia, D.F. Lahrman, R.D. Field, A.J. Freeman, High temperature ordered intermetallic alloys III, MRS Symposium Proceedings 133 (1989) 113.

[26] E.P. George, C.T. Liu, Brittle fracture and grain boundary chemistry of microalloyed NiAl, J. Mater. Res. 5 (1990) 754-762.

[27] L. Sheng, W. Zhang, J. Guo, F. Yang, Y. Liang, H. Ye, Effect of Au addition on the microstructure and mechanical properties of NiAl intermetallic compound, Intermetallics 18 (2010) 740-744.

[28] J. Zhou, J.T. Guo, Effect of Ag alloying on microstructure, mechanical and electrical properties of NiAl intermetallic compound, Materials Science and Engineering A 339 (2003) 166-174.

[29] B. Zeumert, G. Sauthoff, Intermetallic NiAl-Ta alloys with strengthening laves phase for high-temperature applications. I. Basic properties, Intermetallics 5 (1997) 563-577.

[30] L.Y. Sheng, J.T. Guo, W.L. Ren, Z.X. Zhang, Z.M. Ren, H.Q. Ye, Preliminary investigation on strong magnetic field treated NiAl–Cr(Mo)–Hf near eutectic alloy, Intermetallics 19 (2011) 143-148.

[31] L.Y. Sheng, W. Zhang, J.T. Guo, Z.S. Wang, V.E. Ovcharenko, L.Z. Zhou, H.Q. Ye, Microstructure and mechanical properties of Ni_3Al fabricated by thermal explosion and hot extrusion, Intermetallics 17 (2009) 572-577.

[32] M. Sherman, K. Vedula, High temperature dispersion strengthening of NiAl, Journal of Materials Science 21 (1986) 1974-1980.

[33] J.T. Guo, K.W. Huai, Q. Gao, W.L. Ren, G.S. Li, Effects of rare earth elements on the microstructure and mechanical properties of NiAl-based eutectic alloy, Intermetallics 15 (2007) 727-733.

[34] Q. Gao, J.T. Guo, K.W. Huai, J.S. Zhang, The microstructure and compressive properties of as-cast NiAl-28Cr-5.8Mo-0.2Hf containing minor Dy, Materials Letters 59 (2005) 2859-2862.

[35] Y. Xie, J.T. Guo, Y.C. Liang, L.Z. Zhou, H.Q. Ye, Modification of NiAl-Cr(Mo)-0.15Hf alloy by Sc addition, Intermetallics 17 (2009) 400-403.

[36] A. Albiter, E. Bedolla, R. Perez, Microstructure characterization of the NiAl intermetallic compound with Fe, Ga and Mo additions obtained by mechanical alloying, Materials Science and Engineering A 328 (2002) 80-86.

[37] J. Whittenberger, R. Noebe, Elevated temperature compressive properties of Zr-modified NiAl, Metallurgical and Materials Transactions A 27 (1996) 2628-2641.

[38] C.Y. Cui, J.T. Guo, H.Q. Ye, Effects of Hf additions on high-temperature mechanical properties of a directionally solidified NiAl/Cr(Mo) eutectic alloy, Journal of Alloys and Compounds 463 (2008) 263-270.

[39] D.B. Miracle, Overview no. 104 the physical and mechanical properties of NiAl, Acta Metallurgica et Materialia 41 (1993) 649-684.

[40] C.T. Liu, High-temperature ordered intermetallic alloys V, Materials Research Society (1993) 288.

[41] R. Bowman, R. Noebe, S. Raj, I. Locci, Correlation of deformation mechanisms with the tensile and compressive behavior of NiAl and NiAl(Zr) intermetallic alloys, Metallurgical and Materials Transactions A 23 (1992) 1493-1508.

[42] A. Misra, R. Gibala, Plasticity in multiphase intermetallics, Intermetallics 8 (2000) 1025-1034.

[43] D. Golberg, G. Sauthoff, Effects of ageing at 673 K on the compressive behaviour of 110 oriented (soft) NiAl single crystals and polycrystals with and without Ti additions, Intermetallics 4 (1996) 143-158.

[44] T. Hong, A.J. Freeman, High temperature ordered intermatallic alloys III, Materials Research Society (1989) 75.

[45] H. Vehoff, High temperature ordered intermatallic alloys V, Materials Research Society (1993) 71.

[46] A. Albiter, M. Salazar, E. Bedolla, R.A.L. Drew, R. Perez, Improvement of the mechanical properties in a nanocrystalline NiAl intermetallic alloy with Fe, Ga and Mo additions, Materials Science and Engineering A 347 (2003) 154-164.

[47] H. Bei, E.P. George, Microstructures and mechanical properties of a directionally solidified NiAl-Mo eutectic alloy, Acta Materialia 53 (2005) 69-77.

[48] J. Zhou, J.T. Guo, The phosphorus effect on the superplastic deformation of NiAl, Materials Science and Engineering A 360 (2003) 140-145.

[49] A. Mashreghi, M.M. Moshksar, Partial martensitic transformation of nanocrystalline NiAl intermetallic during mechanical alloying, Journal of Alloys and Compounds 482 (2009) 196-198.

[50] G. Smola, W. Wang, J. Jedlinski, B. Gleeson, K. Kowalski, A. Bernasik, M. Nocun, Mechanistic aspects of Pt-modified beta-NiAl alloy oxidation, Mater. High Temp. 26 (2009) 273-280.

[51] R.J. Thompson, J.C. Zhao, K.J. Hemker, Effect of ternary elements on a martensitic transformation in [beta]-NiAl, Intermetallics 18 (2010) 796-802.

[52] R. Darolia, D. Lahrman, R. Field, The effect of iron, gallium and molybdenum on the room-temperature tensile ductility of NiAl, Scr. Metall. Materialia 26 (1992) 1007-1012.

[53] S. Guha, P. Munroe, I. Baker, Room temperature tensile ductility in polycrystalline B2 Ni-30Al-20Fe, Scripta Metallurgica 23 (1989) 897-900.

[54] S. Guha, I. Baker, P.R. Munroe, J.R. Michael, The effect of annealing on Ni-Al-Fe B2 compounds, Materials Science and Engineering A 152 (1992) 258-263.

[55] R. Kainuma, S. Imano, H. Ohtani, K. Ishida, Microstructural evolution in ductile beta(B2)+gamma'(L1(2)) Ni-Al-Fe alloys, Intermetallics 4 (1996) 37-45.

[56] E.P. George, C.T. Liu, J.A. Horton, C.J. Sparks, M. Kao, H. Kunsmann, T. King, Characterization, processing, and alloy design of NiAl-based shape memory alloys, Materials Characterization 39 (1997) 665-686.

[57] A. Inoue, T. Masumoto, H. Tomioka, Microstructure and mechanical-properties of rapidly quenched L20 and L20+L12 alloys in Ni-Al-Fe and Ni-Al-Co systems, Journal of Materials Science 19 (1984) 3097-3106.

[58] A. Misra, R. Gibala, Room-temperature deformation behavior of directionally solidified multiphase Ni-Fe-Al alloys, Metallurgical and Materials Transactions a-Physical Metallurgy and Materials Science 28 (1997) 795-807.

[59] A.J. Bradley, A. Taylor, An X-ray study of the iron-nickel-aluminium ternary equilibrium diagram, Proceedings of the Royal Society of London. Series A, Mathematical and Physical Sciences 166 (1938) 353-375.

[60] S.M. Hao, T. Takayama, K. Ishida, T. Nishizawa, Miscibility gap in Fe-Ni-Al and Fe-Ni-Al-Co systems, Metallurgical Transactions A 15 (1984) 1819-1828.

[61] A.J. Bradley, Microscopical studies on the iron nickel aluminium system. Part II-The breakdown of the body-centred cubic lattice, Journal of the Iron and Steel Institute 168 (1951) 233-244.

[62] P.R. Munroe, M. George, I. Baker, F.E. Kennedy, Microstructure, mechanical properties and wear of Ni-Al-Fe alloys, Materials Science and Engineering A 325 (2002) 1-8.

[63] R. Zallen, The physics of amorphous solids, (1998)

[64] W.L. Johnson, Bulk glass-forming metallic alloys: Science and technology, MRS Bulletin 24 (1999) 42-56.

[65] J. Eckert, J. Das, S. Pauly, C. Duhamel, Mechanical properties of bulk metallic glasses and composites, J. Mater. Res. 22 (2007) 285-301

[66] W. Klement, R.H. Willens, P. Duwez, Non-crystalline structure in solidified gold-silicon alloys, Nature 187 (1960) 869-870.

[67] A.J. Drehman, A.L. Greer, D. Turnbull, Bulk formation of a metallic glass: Pd-40 Ni-40-P-20, Applied Physics Letters 41 (1982) 716-717.

[68] A. Inoue, Stabilization of metallic supercooled liquid and bulk amorphous alloys, Acta Materialia 48 (2000) 279-306.

[69] D. Turnbull, Under what conditions can a glass be formed, Contemp. Phys. 10 (1969) 473.

[70] A. Inoue, T. Zhang, K. Ohba, T. Shibata, Continuous-cooling-transformation (CCT) curves for Zr-Al-Ni-Cu supercooled liquids to amorphous or crystalline phase, Mater. Trans. JIM 36 (1995) 876-878.

[71] H.J. Güntherodt, H. Beck, Glassy metals I, (1981)

[72] I. Akihisa, Bulk amorphous and nanocrystalline alloys with high functional properties, Materials Science and Engineering: A 304–306 (2001) 1-10.

[73] Y. Li, Q. Guo, J.A. Kalb, C.V. Thompson, Matching glass-forming ability with the density of the amorphous phase, Science 322 (2008) 1816-1819.

[74] M. Matsuura, A. Ashfaq, M. Sakurai, Redistribution of Zr in nanocrystalline $Fe_{90}Zr_7B_2Cu_1$ and crystalline $Fe_{97}Zr_3$: Local structures around Zr by XAFS, Scripta Materialia 44 (2001) 2353-2356.

[75] J.S. Blázquez, S. Roth, C. Mickel, A. Conde, Partial substitution of Co and Ge for Fe and B in Fe–Zr–B–Cu alloys: Microstructure and soft magnetic applicability at high temperature, Acta Materialia 53 (2005) 1241-1251.

[76] D.H. Ping, Y.Q. Wu, K. Hono, M.A. Willard, M.E. McHenry, D.E. Laughlin, Microstructural characterization of $(Fe_{0.5}Co_{0.5})_{88}Zr_7B_4Cu_1$ nanocrystalline alloys, Scripta Materialia 45 (2001) 781-786.

[77] Y. Sun, L. Zhong, X. Bi, High temperature soft magnetic property of the nanocrystalline $Fe_{44}Co_{44}Zr_7B_5$ alloy arising from ge addition, Scripta Materialia 60 (2009) 814-817.

[78] M.E. McHenry, F. Johnson, H. Okumura, T. Ohkubo, V.R.V. Ramanan, D.E. Laughlin, The kinetics of nanocrystallization and microstructural observations in finemet, nanoperm and hitperm nanocomposite magnetic materials, Scripta Materialia 48 (2003) 881-887.

[79] M. Hagiwara, A. Inoue, T. Masumoto, Mechanical properties of Fe-Si-B amorphous wires produced by in-rotating-water spinning method, Metallurgical and Materials Transactions A 13 (1982) 373-382.

[80] Y. Yoshizawa, S. Oguma, K. Yamauchi, New Fe-based soft magnetic alloys composed of ultrafine grain structure, Journal of Applied Physics 64 (1988) 6044-6046.

[81] A. Makino, T. Hatanai, A. Inoue, T. Masumoto, Nanocrystalline soft magnetic Fe-M-B (M = Zr, Hf, Nb) alloys and their applications, Materials Science and Engineering: A 226–228 (1997) 594-602.

[82] P. Marin, M. Vázquez, A.O. Olofinjana, H.A. Davies, Influence of Cu and Nb on relaxation and crystallization of amorphous FeSiB(CuNb) wires, Nanostructured Materials 10 (1998) 299-310.

[83] F. Zhou, K.-Y. He, M.-L. Sui, Z.-H. Lai, Nucleation and growth characteristics of amorphous Fe-Si-B-(Cu)-(Nb) alloys during isothermal crystallization process, Materials Science and Engineering: A 181-182 (1994) 1419-1422.

[84] J.J. Ipus, J.S. Blázquez, V. Franco, A. Conde, Influence of Co addition on the magnetic properties and magnetocaloric effect of nanoperm $(Fe_{1-x}Co_x)_{75}Nb_{10}B_{15}$ type alloys prepared by mechanical alloying, Journal of Alloys and Compounds 496 (2010) 7-12.

[85] B. Shen, A. Inoue, C. Chang, Superhigh strength and good soft-magnetic properties of (Fe,Co)-B-Si-Nb bulk glassy alloys with high glass-forming ability, Applied Physics Letters 85 (2004) 4911-4913.

[86] M.A. Willard, D.E. Laughlin, M.E. McHenry, D. Thoma, K. Sickafus, J.O. Cross, V.G. Harris, Structure and magnetic properties of (Fe0.5Co0.5)88Zr7B4Cu1 nanocrystalline alloys, Journal of Applied Physics 84 (1998) 6773-6777.

[87] A. Inoue, B.L. Shen, A new Fe-based bulk glassy alloy with outstanding mechanical properties, Advanced Materials 16 (2004) 2189-2192.

[88] K. Hono, Nanoscale microstructural analysis of metallic materials by atom probe field ion microscopy, Progress in Materials Science 47 (2002) 621-729.

[89] M. Avrami, Kinetics of phase change. I General theory, Journal of Chemical Physics 7 (1939) 1103.

[90] M. Avrami, Kinetics of phase change. II Transformation-time relations for random distribution of nuclei, Journal of Chemical Physics 8 (1940) 212.

[91] M. Avrami, Granulation, phase change, and microstructure kinetics of phase change. III Journal of Chemical Physics 9 (1941) 177.

[92] W. Johnson, R. Mehl, Reaction kinetics in processes of nucleation and growth, Trans. Am. 135 (1939) 416.

[93] J.W. Christian, The theory of transformations in metals and alloys, (1981)

[94] K. Nakamura, K. Katayama, T. Amano, Some aspects of nonisothermal crystallization of polymers. II. Consideration of the isokinetic condition, Journal of Applied Polymer Science 17 (1973) 1031-1041.

[95] K. Nakamura, T. Watanabe, K. Katayama, T. Amano, Some aspects of nonisothermal crystallization of polymers. I. Relationship between crystallization temperature, crystallinity, and cooling conditions, Journal of Applied Polymer Science 16 (1972) 1077-1091.

[96] J.S. Blázquez, C.F. Conde, A. Conde, Non-isothermal approach to isokinetic crystallization processes: Application to the nanocrystallization of hitperm alloys, Acta Materialia 53 (2005) 2305-2311.

[97] T. Ozawa, Kinetics of non-isothermal crystallization, Polymer 12 (1971) 150-158.

[98] H.E. Kissinger, Variation of peak temperature with heating rate in differential thermal analysis, J. Res. Natl. Bur. Stand., Sect. A 57 (1956) 217.

[99] H.E. Kissinger, Reaction kinetics in differential thermal analysis, Analytical Chemistry 29 (1957) 1702-1706.

[100] Y.Q. Gao, W. Wang, On the activation energy of crystallization in metallic glasses, Journal of Non-Crystalline Solids 81 (1986) 129-134.

[101] J.A. Augis, J.E. Bennett, Calculation of the avrami parameters for heterogeneous solid state reactions using a modification of the kissinger method, Journal of Thermal Analysis and Calorimetry 13 (1978) 283-292.

[102] H.S. Ko, H.S. Park, K.T. Hong, K.S. Lee, M.J. Kaufman, The effects of the point defects on precipitation in NiAlFe alloys, Scripta Materialia 39 (1998) 1267-1272.

[103] K.Z. Rozman, P.J. McGuiness, B. Podmiljsak, M. Rajic, S. Kobe, Magnetic monitoring of the disproportionation behavior in Sm-Fe-based materials, IEEE Transactions on Magnetics 40 (2004) 2952-2954.

[104] M. Muñoz-Morris, N. Calderon, D. Morris, Coarsening kinetics of metastable nanoprecipitates in a Fe–Ni–Al alloy, Journal of Materials Science 43 (2008) 3674-3682.

[105] F.E. Luborsky, Kinetics for changes in anisotropy, coercivity, and argon content of transition metal-rare earth films, Journal of Applied Physics 57 (1985) 3592-3594.

[106] R.C. Agarwala, S. Ray, Crystallization behavior of electroless Ni-P films. Part II-A kinetics study, Z. Metallk. 83 (1992) 203-207.

[107] P.J. McGuiness, E.J. Devlin, M. Komelj, B. Podmiljsak, D. Niarchos, S. Kobe, Magnetic monitoring of the disproportionation process in Nd-Fe-B-based materials, Journal of Magnetism and Magnetic Materials 272-276 (2004) E1877-E1879.

[108] A. Hsiao, M.E. McHenry, D.E. Laughlin, M.J. Kramer, C. Ashe, T. Ohkubo, The thermal, magnetic, and structural characterization of the crystallization kinetics of $Fe_{88}Zr_7B_4Cu_1$, an amorphous soft magnetic ribbon, Magnetics, IEEE Transactions on 38 (2002) 3039-3044.

[109] L. Eleno, K. Frisk, A. Schneider, Assessment of the Fe-Ni-Al system, Intermetallics 14 (2006) 1276-1290.

[110] B.A. D'Santhoshini, S.N. Kaul, Site preference of ternary Fe addition in $Ni_{75}Al_{25}$, J. Phys.-Condes. Matter 15 (2003) 4903-4918.

[111] S.N. Kaul, B.A. D' Santhoshini, A.C. Abhyankar, L.F. Barquin, P. Henry, Thermoelastic martensitic transformation in ferromagnetic Ni-Fe-Al alloys: Effect of site disorder, Applied Physics Letters 89 (2006)

[112] Z.G. Liu, J.T. Guo, L.Z. Zhou, Z.Q. Hu, M. Umemoto, Mechanical alloying synthesis and structural characterization of ternary Ni-Al-Fe alloys, Journal of Materials Science 32 (1997) 4857-4864.

[113] L. Yang, X.L. Wang, C.T. Liu, J.A. Fernandez-Baca, C.L. Fu, J.W. Richardson, D. Shi, Neutron diffraction study of the structure and low-temperature phase transformation in ternary NiAl+M (M = Ni, Fe, Co) alloys, Scripta Materialia 56 (2007) 911-914.

[114] K. Oikawa, Y. Tanaka, Y. Sutou, T. Omori, F.H. Luo, R. Kainuma, K. Ishida, Effects of aging and Co addition on martensitic and magnetic transitions in Ni-Al-Fe beta-based shape memory alloys, ISIJ International 46 (2006) 1287-1291.

[115] K. Oikawa, T. Ota, Y. Tanaka, T. Omori, R. Kainuma, K. Ishida, Magnetic and martensitic phase transitions in the Ni-Al-Fe shape memory alloys Transactions of the Materials Research Society of Japan 28 (2003) 263-264.

[116] G.P. Cammarota, A. Casagrande, Effect of ternary additions of iron on microstructure and microhardness of the intermetallic NiAl in reactive sintering, Journal of Alloys and Compounds 381 (2004) 208-214.

[117] G.W. Smith, A method for determination of avrami parameters directly from isothermal calorimetry data, Thermochimica Acta 291 (1997) 59-64.

[118] S. Divinski, Y.-S. Kang, W. Löser, C. Herzig, Ni and Fe tracer diffusion in the B2-ordered $Ni_{40}Fe_{10}Al_{50}$ ternary alloy, Intermetallics 12 (2004) 511-518.

[119] G.H. Bozzolo, R.D. Noebe, C. Amador, Site occupancy of ternary additions to B2 alloys, Intermetallics 10 (2002) 149-159.

[120] Y.L. Hao, R. Yang, Q.M. Hu, D. Li, Y. Song, M. Niinomi, Bonding characteristics of micro-alloyed B2 NiAl in relation to site occupancies and phase stability, Acta Materialia 51 (2003) 5545-5554.

[121] C. Jiang, Site preference of transition-metal elements in B2 NiAl: A comprehensive study, Acta Materialia 55 (2007) 4799-4806.

[122] A.O. Mekhrabov, M.V. Akdeniz, M.M. Arer, Atomic ordering characteristics of Ni_3Al intermetallics with substitutional ternary additions, Acta Materialia 45 (1997) 1077-1083.

[123] Y. Song, Z.X. Guo, R. Yang, D. Li, First principles study of site substitution of ternary elements in NiAl, Acta Materialia 49 (2001) 1647-1654.

[124] M.A. Muñoz-Morris, D.G. Morris, Microstructure and mechanical behaviour of a Fe-Ni-Al alloy, Materials Science and Engineering: A 444 (2007) 236-241.

[125] H. Luo, F. Meng, Y. Cai, W. Hong, E. Liu, G. Wu, X. Zhu, C. Jiang, Effect of low-valent atom substitution on electronic structure and magnetic properties of $Fe_{1.5}M_{0.5}CoSi$ (M=V, Cr, Mn, Fe) heusler alloys, J. Magn. Magn. Mater. 323 (2011) 2323-2327.

[126] I. Akihisa, Bulk amorphous and nanocrystalline alloys with high functional properties, Materials Science and Engineering: A 304-306 (2001) 1-10.

[127] F. Kong, B. Shen, A. Makino, A. Inoue, Enhancement of soft magnetic properties of FeCoNbB nanocrystalline alloys with cu and ni additions, Thin Solid Films 519 (2011) 8280-8282.

[128] H. Ryusuke, Advances in amorphous and nanocrystalline magnetic materials, Journal of Magnetism and Magnetic Materials 304 (2006) 187-191.

[129] A. Inoue, B.L. Shen, C.T. Chang, Fe- and Co-based bulk glassy alloys with ultrahigh strength of over 4000 MPa, Intermetallics 14 (2006) 936-944.

[130] B. Shen, C. Chang, A. Inoue, Formation, ductile deformation behavior and soft-magnetic properties of (Fe,Co,Ni)–B–Si–Nb bulk glassy alloys, Intermetallics 15 (2007) 9-16.

[131] B.L. Shen, C.T. Chang, Z.F. Zhang, A. Inoue, Enhancement of glass-forming ability of FeCoNiBSiNb bulk glassy alloys with superhigh strength and good soft-magnetic properties, Journal of Applied Physics 102 (2007)

[132] S.H. Al-Heniti, Kinetic study of non-isothermal crystallization in $Fe_{78}Si_9B_{13}$ metallic glass, Journal of Alloys and Compounds 484 (2009) 177-184.

[133] D.S. dos Santos, D.R. dos Santos, Crystallization kinetics of Fe–B–Si metallic glasses, Journal of Non-Crystalline Solids 304 (2002) 56-63.

[134] J.S. Blazquez, C.F. Conde, A. Conde, Kinetics of nanocrystallization in FeCoNbB(Cu) alloys, Applied Physics a-Materials Science & Processing 76 (2003) 571-575.

[135] C.F. Conde, A. Conde, Crystallization of a finemet-type alloy: Nanocrystallization kinetics, Materials Letters 21 (1994) 409-414.

[136] B. Adnađević, B. Janković, D.M. Minić, Kinetics of the apparent isothermal and non-isothermal crystallization of the α-Fe phase within the amorphous $Fe_{81}B_{13}Si_4C_2$ alloy, Journal of Physics and Chemistry of Solids 71 (2010) 927-934.

[137] P.J. McGuiness, E.J. Devlin, M. Komelj, B. Podmiljšak, D. Niarchos, S. Kobe, Magnetic monitoring of the disproportionation process in Nd–Fe–B-based materials, Journal of Magnetism and Magnetic Materials 272-276, Supplement (2004) E1877-E1879.

[138] F.X. Qin, H.F. Zhang, B.Z. Ding, Z.Q. Hu, Nanocrystallization kinetics of Ni-based bulk amorphous alloy, Intermetallics 12 (2004) 1197-1203.

[139] H. Benaini, J.S. Blázquez, C.F. Conde, A. Conde, Kinetic and microstructural studies on the devitrification of $Fe_{60-x}Co_{18}Mn_xNb_6B_{16}$ amorphous alloys, Journal of Alloys and Compounds 454 (2008) 156-163.

[140] C.F. Conde, J.S. Blázquez, V. Franco, A. Conde, P. Švec, D. Janičkovič, Microstructure and magnetic properties of FeMoBCu alloys: Influence of B content, Acta Materialia 55 (2007) 5675-5683.

[141] C.F. Conde, J.M. Borrego, J.S. Blázquez, A. Conde, P. Švec, D. Janičkovič, Magnetic and structural characterization of Mo-hitperm alloys with different Fe/Co ratio, Journal of Alloys and Compounds 509 (2011) 1994-2000.

[142] J.S. Blazquez, C.F. Conde, A. Conde, Thermomagnetic detection of recrystallization in FeCoNbBCu nanocrystalline alloys, Applied Physics Letters 79 (2001) 2898-2900.

[143] M.C. Weinberg, D.P. Birnie III, V.A. Shneidman, Crystallization kinetics and the JMAK equation, Journal of Non-Crystalline Solids 219 (1997) 89-99.

[144] T. Pradell, D. Crespo, N. Clavaguera, M.T. Clavaguera-Mora, Diffusion controlled grain growth in primary crystallization: Avrami exponents revisited, J. Phys.-Condes. Matter 10 (1998) 3833-3844.

[145] M.T. Clavaguera-Mora, N. Clavaguera, D. Crespo, T. Pradell, Crystallisation kinetics and microstructure development in metallic systems, Progress in Materials Science 47 (2002) 559-619.

[146] T. Pradell, D. Crespo, N. Clavaguera, J. Zhu, M.T. ClavagueraMora, Kinetics of microstructural development in nanocrystalline materials, Nanostructured Materials 8 (1997) 345-357.

[147] J. Wang, H.C. Kou, X.F. Gu, J.S. Li, L.Q. Xing, R. Hu, L. Zhou, On discussion of the applicability of local avrami exponent: Errors and solutions, Materials Letters 63 (2009) 1153-1155.

[148] J.W. Edington, Practical electron microscopy in materials science, (1976)

[149] ASM Metals Handbook, Alloy Phase Diagrams, Volume 3.

APPENDIX A

KIKUCHI MAPS FOR CUBIC CRYSTALS

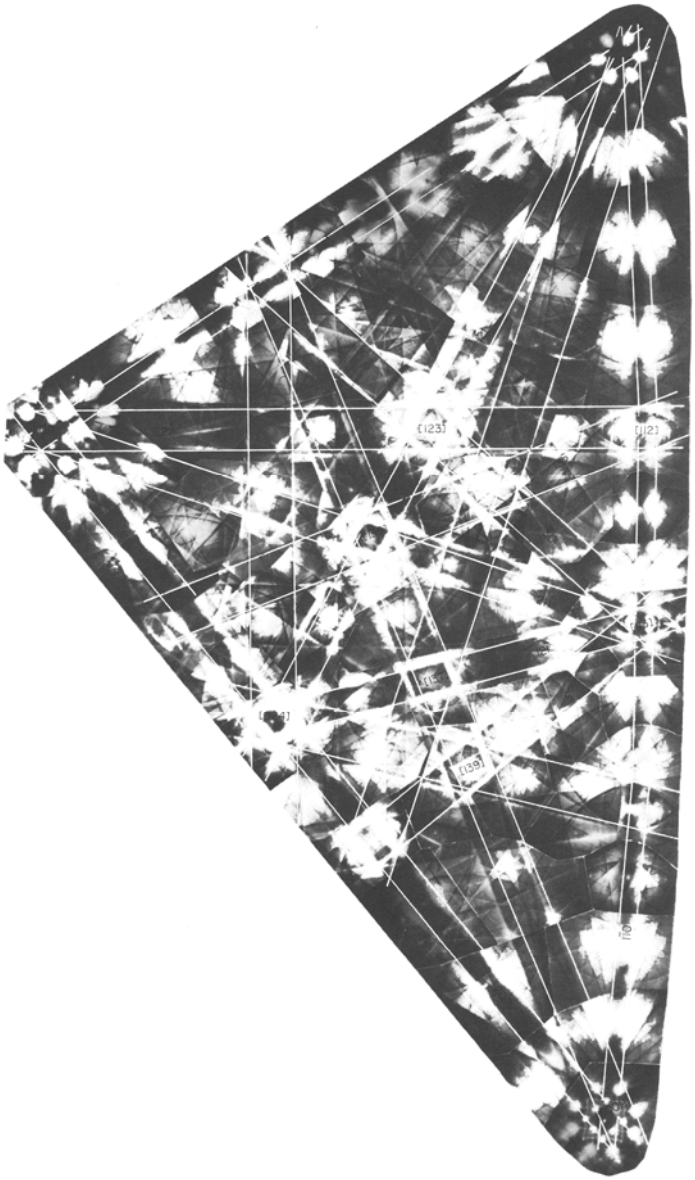

Figure A.1 Kikuchi map for BCC crystal structure [148].

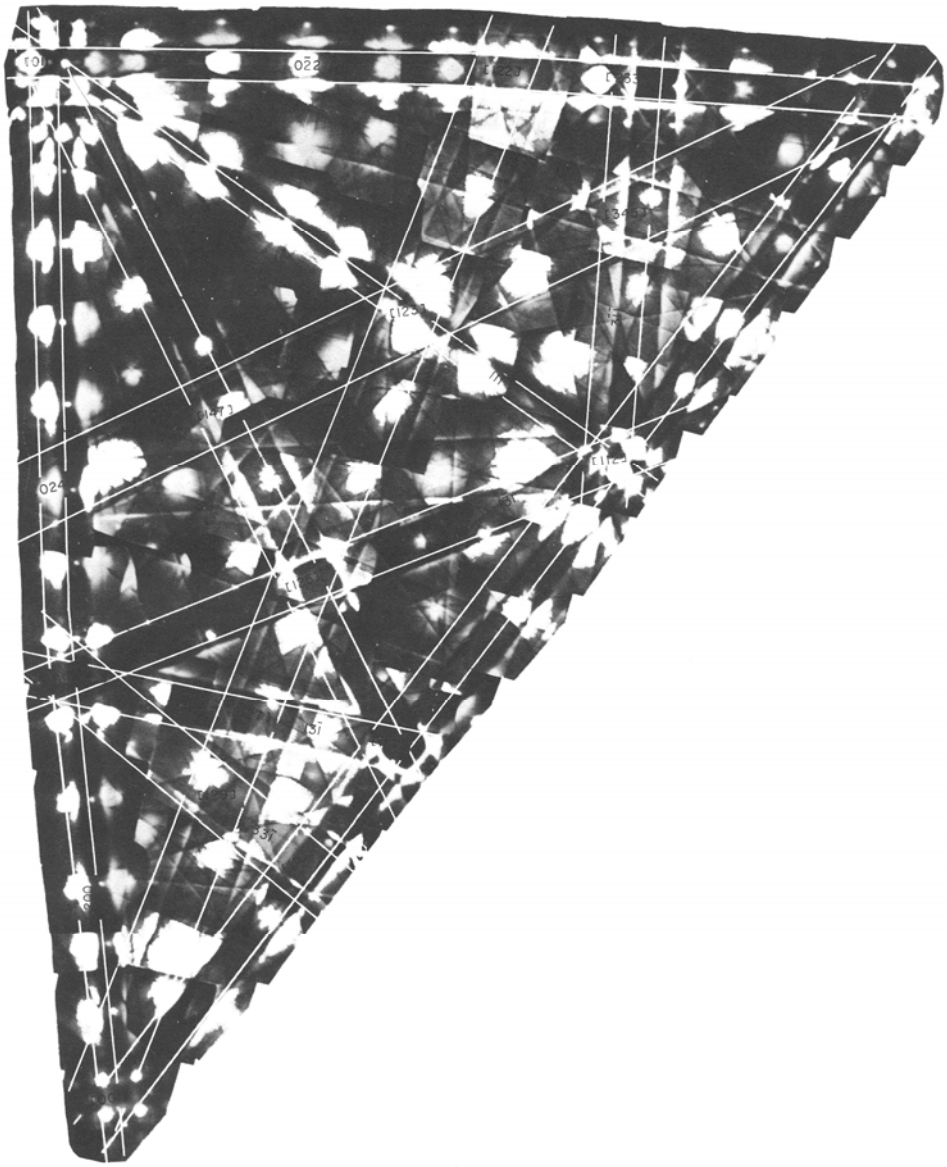

Figure A.2 Kikuchi map for FCC crystal structure [148]

APPENDIX B

STANDARD INDEXED ELECTRON DIFFRACTION PATTERNS FOR CUBIC STRUCTURES

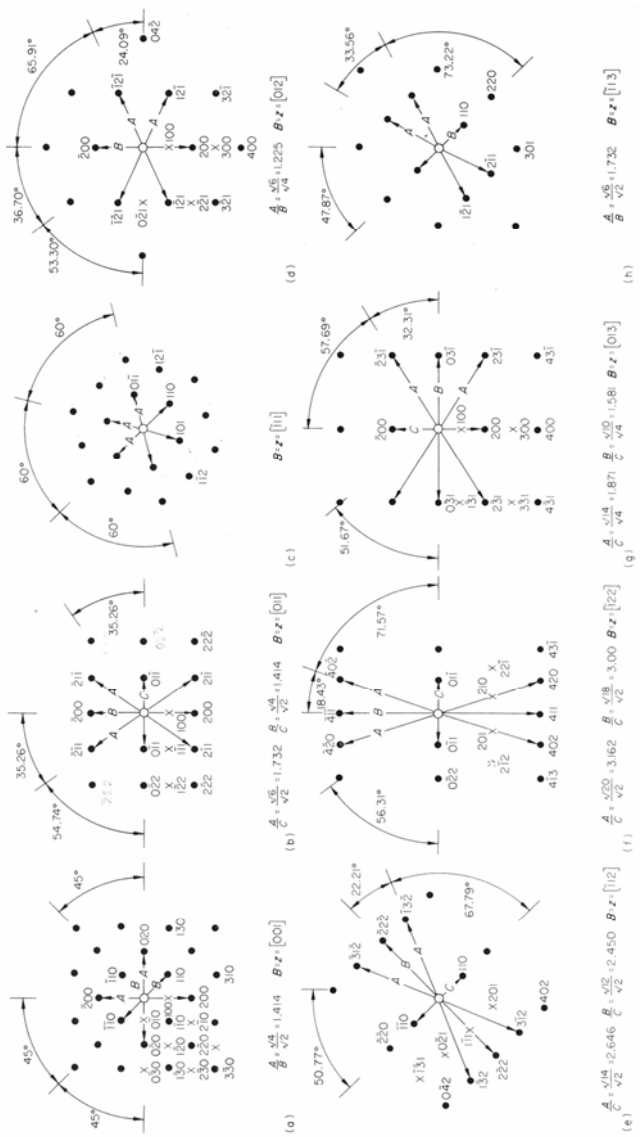

Figure B.1 Standard indexed electron diffraction spot patterns for BCC crystal [148].

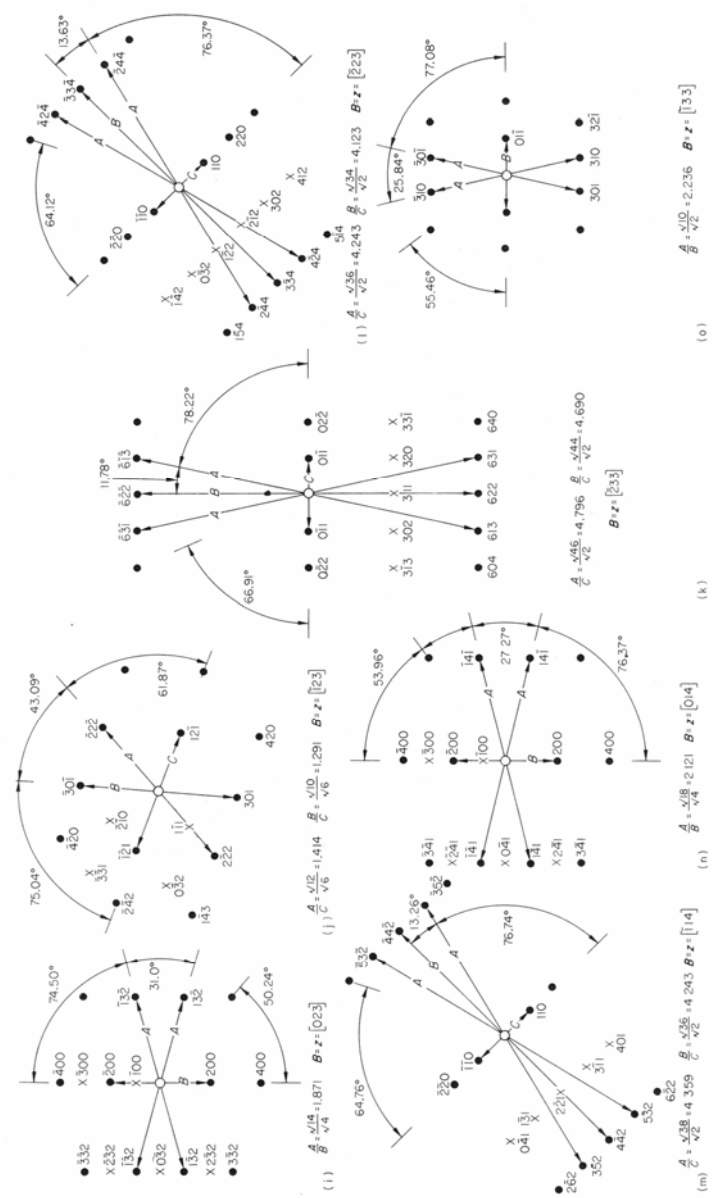

Figure B.1 (continued)

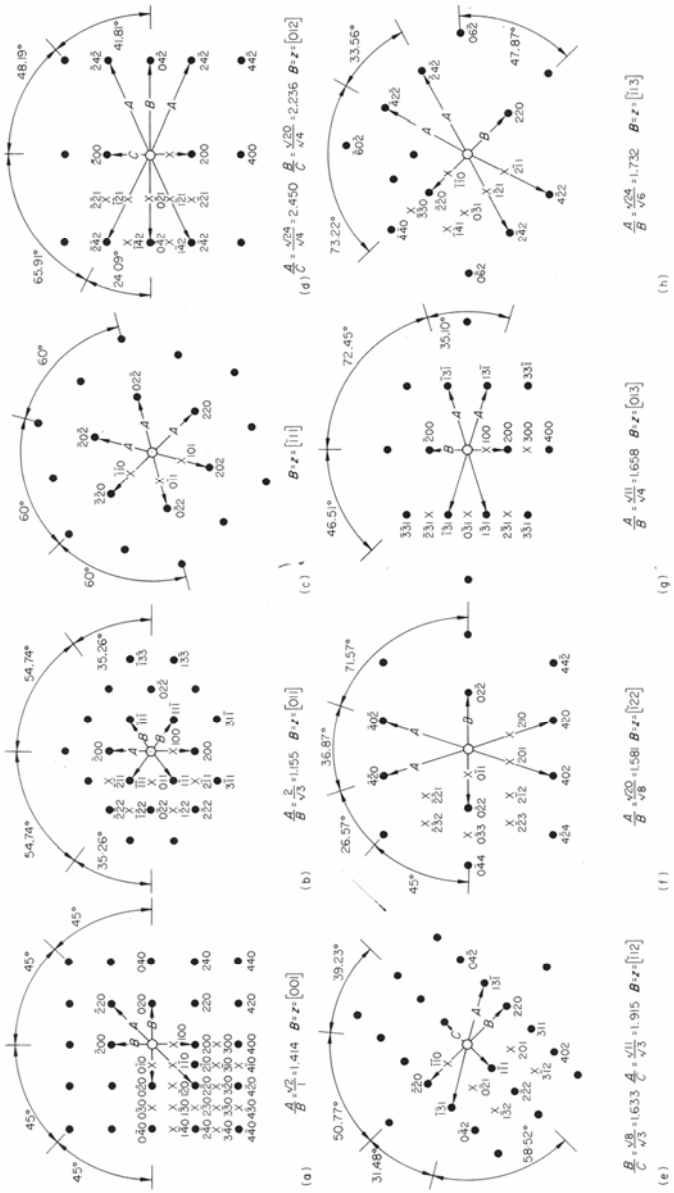

Figure B.2 Standard indexed electron diffraction spot patterns for FCC crystal [148].

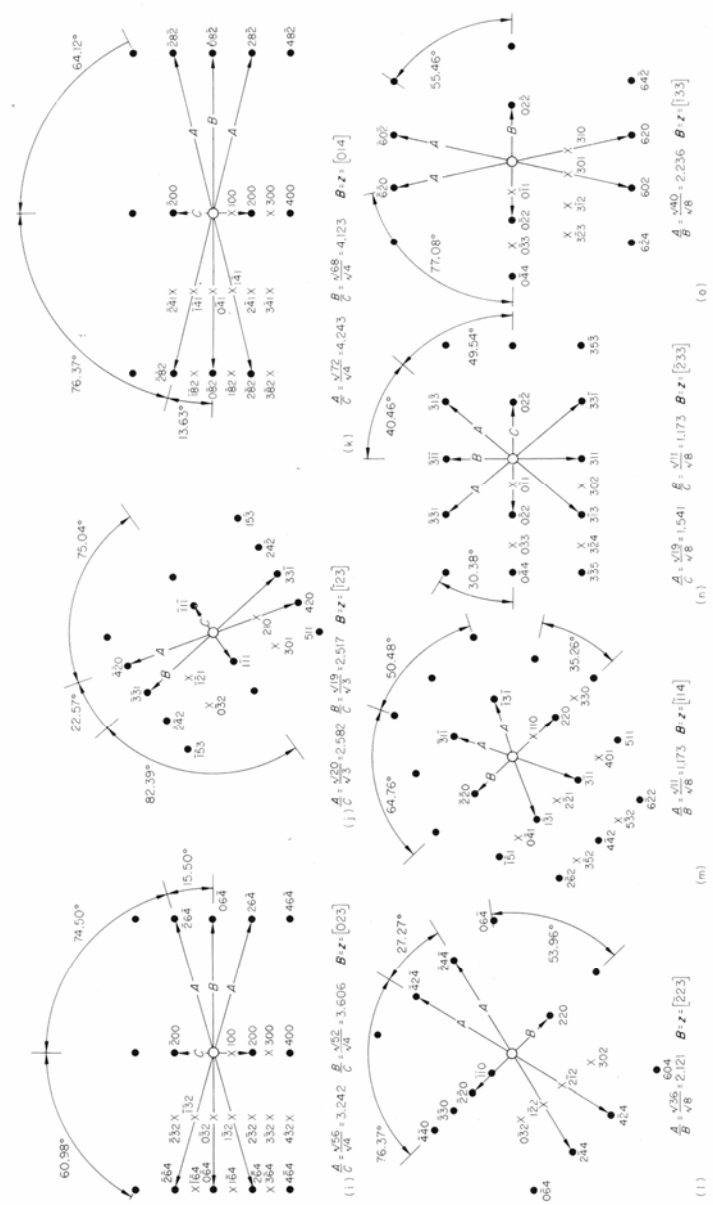

Figure B.2 (continued)

APPENDIX C

EQUILIBRIUM PHASE DIAGRAMS

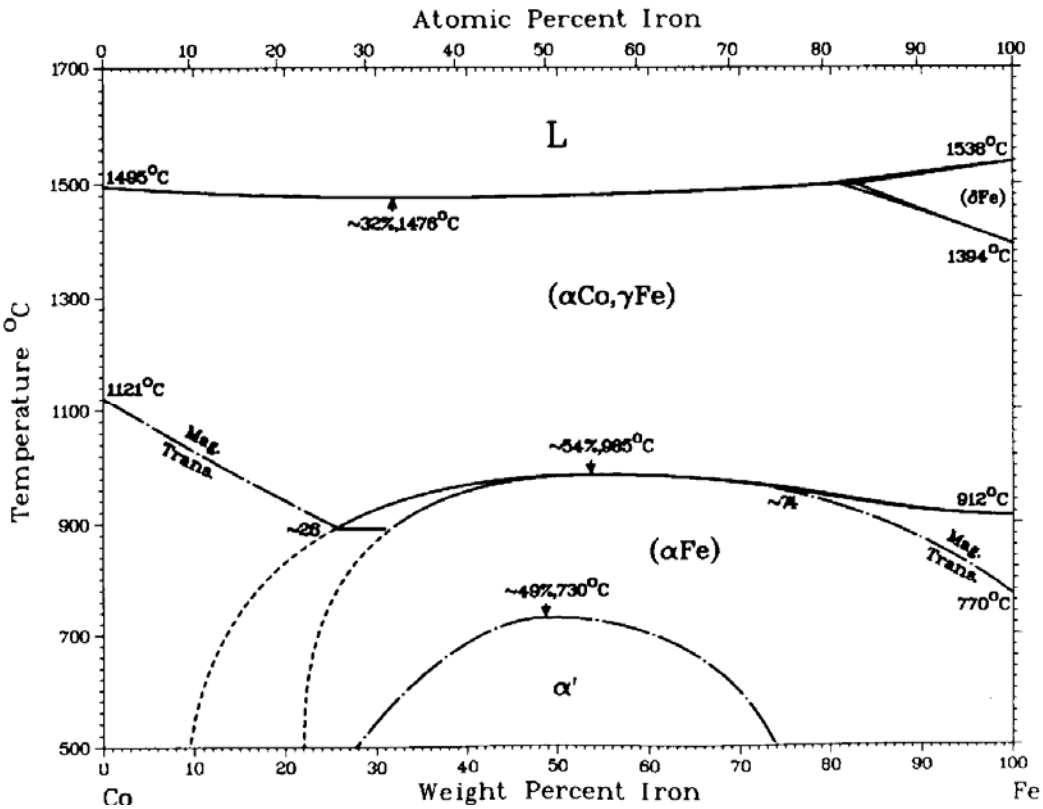

Figure C.1 Co-Fe equilibrium phase diagram [149].

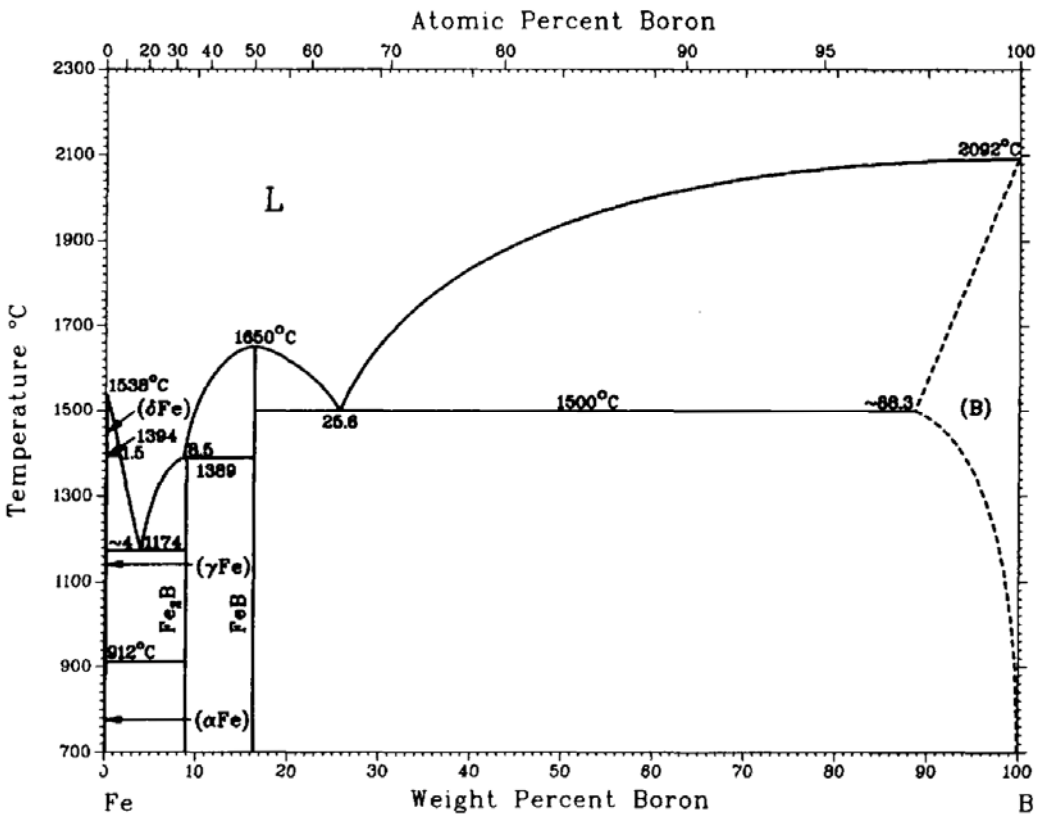

Figure C.2 Fe-B equilibrium phase diagram [149].

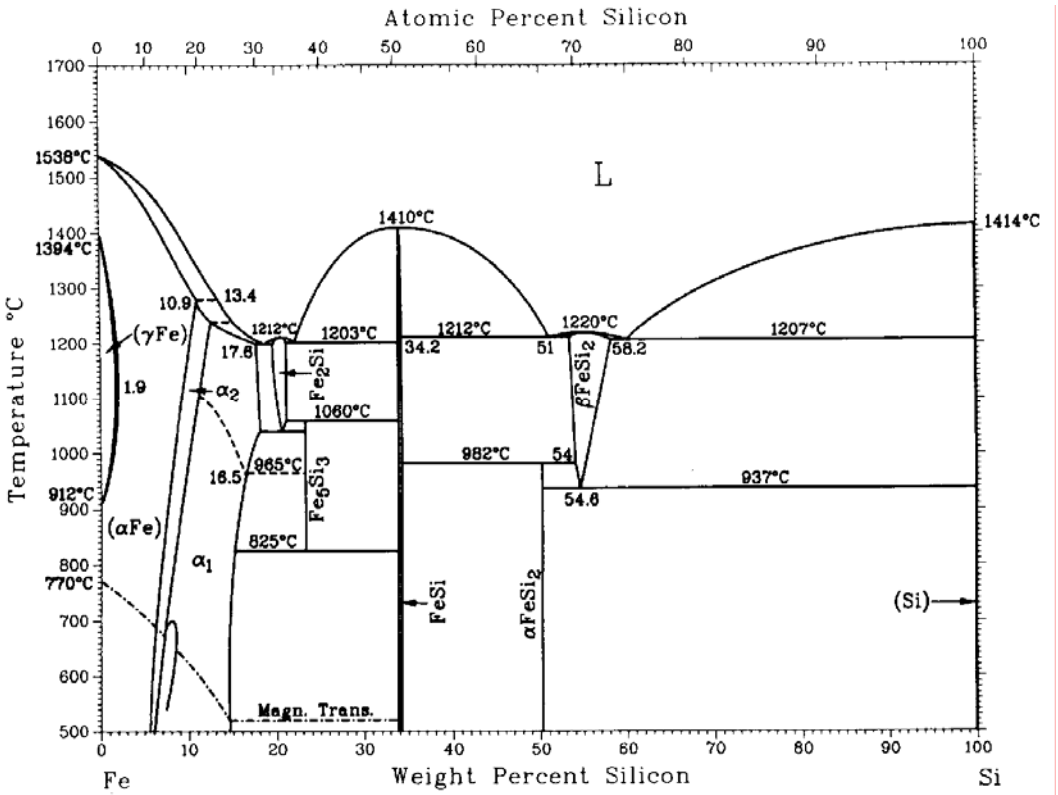

Figure C.3 Fe-Si equilibrium phase diagram [149].

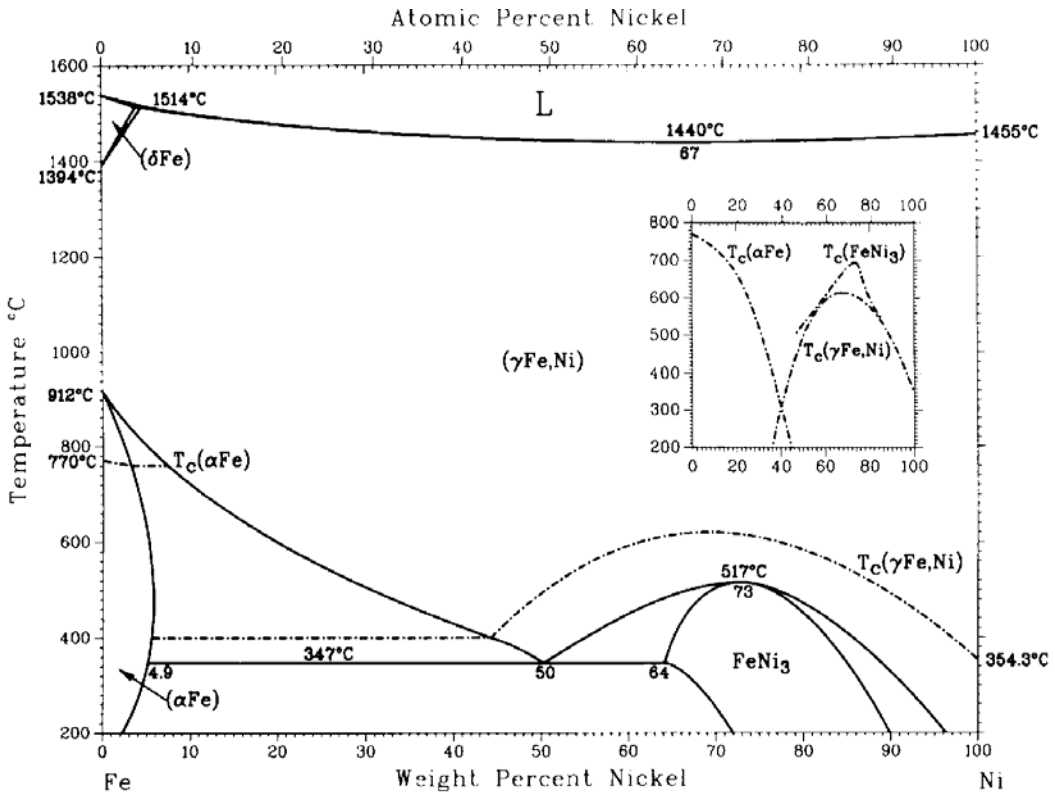

Figure C.4 Fe-Ni equilibrium phase diagram [149].

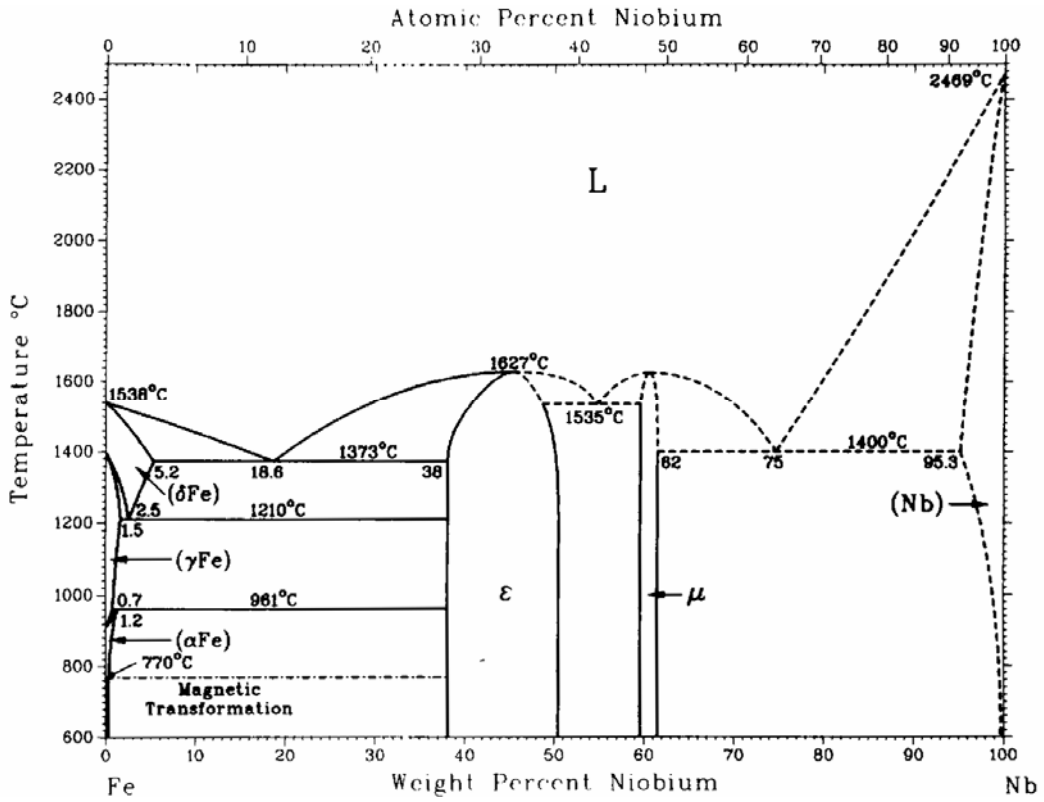

Figure C.5 Fe-Nb equilibrium phase diagram [149].

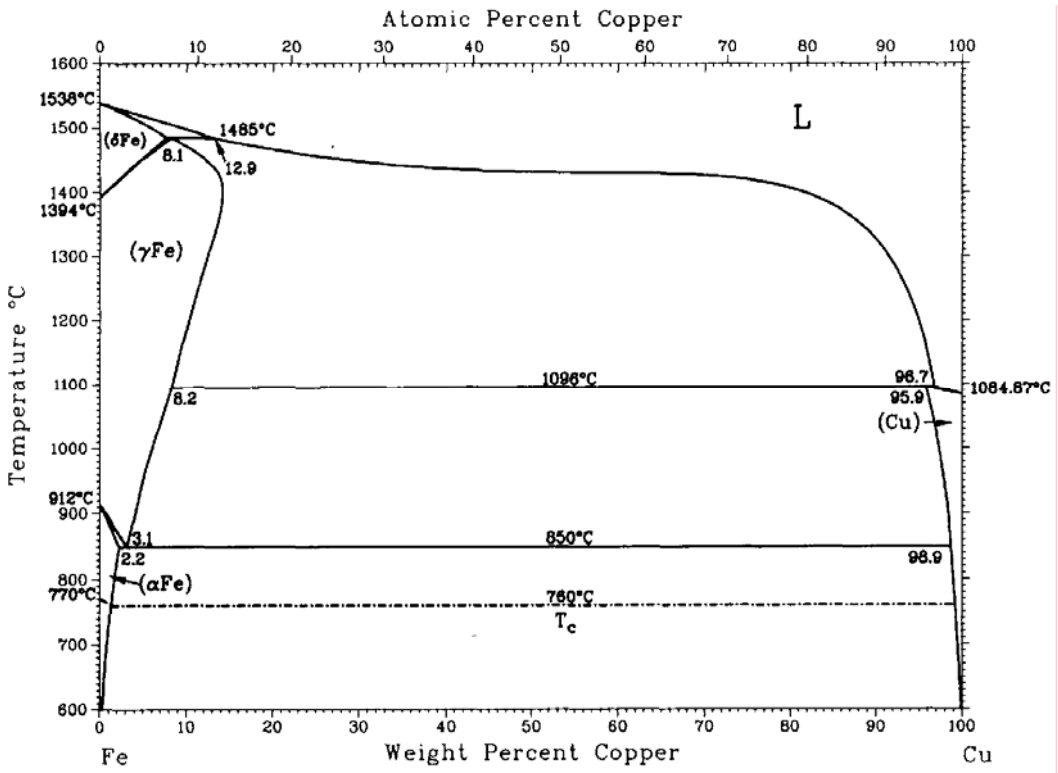

Figure C.6 Fe-Cu equilibrium phase diagram [149].

CURRICULUM VITAE

Nagehan Duman

Department of Metallurgical and Materials Engineering,
Middle East Technical University • Ankara, Turkey 06531
Tel: +90-312-210-2534 • Cell: +90-537-503-5008
Email: nagehanduman@gmail.com
Web: www.metu.edu.tr/~nduman

EDUCATION

- **Doctor of Philosophy in Metallurgical and Materials Engineering,** Middle East Technical University, Ankara, TR, 2012

- **Scientific Preparation Program in Metallurgical and Materials Engineering,** Middle East Technical University, Ankara, TR, 2007

- **English Preparation School in School of Foreign Languages, Department of Basic English**, Middle East Technical University, Ankara, TR, 2006

- **Master of Science in Metallurgical and Materials Engineering,** Yildiz Technical University, Istanbul, TR, 2005

- **Bachelor of Science in Metallurgical and Materials Engineering,** Eskisehir Osmangazi University, Eskisehir, TR, 2003

ACADEMIC HONORS AND AWARDS

- **The most successful in Ph.D. Program**, Graduate Courses Performance Award, Middle East Technical University, 2009

ACADEMIC / TEACHING EXPERIENCE

Teaching Assistant, Middle East Technical University, Department of Metallurgical and Materials Engineering, Ankara, TR,

- **MetE 222-Materials Science and Engineering** for Chemical Engineering undergraduate students

- **MetE 229-Materials Science and Engineering** for Electrical and Electronics Engineering undergraduate students

- **MetE 507-Advanced Crystallography and Diffraction** for Metallurgical and Materials Engineering graduate students

Research Assistant, Middle East Technical University, Department of Metallurgical and Materials Engineering, Ankara, TR, 2006 - On-going.

RESEARCH INTERESTS

- High temperature materials
- Intermetallics
- Bulk amorphous materials
- Nanocrystallization

PUBLICATIONS

Papers

- **N. Duman**, A.O. Mekhrabov and M.V. Akdeniz, "Magnetic Monitoring Approach to Nanocrystallization Kinetics in Fe-based Bulk Amorphous Alloy", (submitted, under review, 2012)

- **N. Duman**, A.O. Mekhrabov and M.V. Akdeniz, "Microalloying Effects on the Microstructure and Kinetics of Nanoscale Precipitation in Ni-Al-Fe Alloy", *Intermetallics* 23, 217-227, 2012

- **N. Duman**, A.O. Mekhrabov and M.V. Akdeniz, "Kinetics of Nanoscale Precipitation in Ni-Fe-Al Alloys: A Magnetic Monitoring Approach", *Journal of Alloys and Compounds* 509 (24), 6781-6786, 2011

- **N. Duman**, A.O. Mekhrabov and M.V. Akdeniz, "Microstructural and Magnetic Characterization of Iron Precipitation in Ni-Fe-Al Alloys", *Materials Characterization* 62 (6), 606-614, 2011

- I. Kucuk, M. Aykol, O. Uzun, M. Yildirim, M. Kabaer, **N. Duman**, F.Yilmaz, K. Erturk, M.V. Akdeniz and A.O. Mekhrabov, "Effects of (Mo, W) Substitution for Nb on Glass Forming Ability and Magnetic Properties of Fe-Co based Bulk Amorphous Alloys Fabricated by Centrifugal Casting", *Journal of Alloys and Compounds* 509 (5), 2334-2337, 2011

Presentations

- **N. Duman**, A.O. Mekhrabov and M.V. Akdeniz, *"Precipitation Kinetics of an Fe-Rich Phase in $Ni_{50}Al_{50-x}Fe_x$ Alloys Monitored by Magnetic Measurements"*, **Book of Abstracts of the Materials Research Society 2010 Fall Meeting**, Boston, USA (29 November-03 December 2010)

- **N. Duman**, A.O. Mekhrabov and M.V. Akdeniz, *"Farklı Demir Oranlarında Ni-Al-Fe Alaşımlarının Manyetik Özellikleri"*, **e-Proceedings of the 15th International Metallurgy & Materials Congress – IMMC 2010**, UCTEA Chamber of Metallurgical Engineers, Istanbul, Turkey, 8 pages on CD (11-13 November 2010)

- **N. Duman**, A.O. Mekhrabov and M.V. Akdeniz, *"Ni-Fe-Al Alaşımlarında Demir Çökelme Kinetiği"*, **e-Proceedings of the 13th International Materials Symposium – IMSP 2010**, Pamukkale University, Denizli, Turkey, 6 pages on CD (13-15 October 2010)

- **N. Duman**, A.O. Mekhrabov and M.V. Akdeniz, *"Magnetic Monitoring of Nano-Sized Iron Precipitation in $Ni_{50}Al_{50-x}Fe_x$ Alloys"*, **Book of Abstracts of the 10th International Conference on Nanostructured Materials – NANO 2010**, Rome, Italy (13-17 September 2010)

- **N. Duman**, A.O. Mekhrabov and M.V. Akdeniz, *"Nano-Sized Iron Precipitation in Ni-Al-Fe Alloys"*, **Book of Abstracts of the 6th Nanoscience and Nanotechnology Conference – NANO TR-VI**, Izmir Institute of Technology, Izmir, Turkey (15-18 June 2010)

- I. Kucuk, O. Uzun, M. Aykol, **N. Duman**, A.O. Mekhrabov, F. Yilmaz and M.V. Akdeniz, *"Effects of Mo and W on Soft Magnetic Properties of Melt-Spun Fe-Co-B-Si-Mo-W Amorphous Ribbons"*, **Book of Abstracts of the International Conference on Superconductivity and Magnetism ICSM-2010**, Antalya, Turkey (25-30 April 2010)

- **N. Duman**, A.O. Mekhrabov and M.V. Akdeniz, *"A Study on Magnetic Properties of $Ni_{50}Fe_xAl_{50-x}$ Alloys"*, **Book of Extended Abstracts Proceedings of the 6th Japanese-Mediterranean Workshop on Applied Electromagnetic Engineering for Magnetic, Superconducting and Nano Materials**, 2 pages, Bucharest, Romania, (27-29 July 2009)

- **N. Duman**, A.O. Mekhrabov and M.V. Akdeniz, *"An Investigation on Martensitic and Magnetic Phase Transition in Ferromagnetic Ni-Fe-Al Heusler Alloys"*, **Book of Abstracts of the Materials Research Society 2008 Fall Meeting**, Boston, USA (1-5 December 2008)

- **N. Duman**, A.O. Mekhrabov and M.V. Akdeniz, *"Simulation of Glass Forming Ability of Ni-Al Based Multicomponent Alloy Systems"*, **e-Proceedings of the 14th International Metallurgy & Materials Congress – IMMC 2008**, UCTEA Chamber of Metallurgical Engineers, Istanbul, Turkey, 7 pages on CD (16-18 October 2008)